VI INTERNATIONAL SCIENTIFIC CONFERENCE
WINTER SESSION

INDUSTRY 4.0

08 - 11 DECEMBER 2021, BOROVETS, BULGARIA

ISSN (Print) - 2535-0153
ISSN (Online) - 2535-0161

PROCEEDINGS

VOLUME II
TECHNOLOGICAL BASIS OF "INDUSTRY 4.0"
DOMINANT TECHNOLOGIES IN "INDUSTRY 4.0"

ORGANIZER
SCIENTIFIC-TECHNICAL UNION of MECHANICAL ENGINEERING "INDUSTRY 4.0"

VI INTERNATIONAL SCIENTIFIC CONFERENCE - WINTER SESSION

INDUSTRY 4.0

08 -11.12.2021, BOROVETS, HOTEL ELA

Year V Volume 2/12 DECEMBER 2021

ISSN (Print) - 2535-0153
ISSN (Online) - 2535-0161

TECHNOLOGICAL BASIS OF "INDUSTRY 4.0"
DOMINANT TECHNOLOGIES IN "INDUSTRY 4.0"

ORGANIZER

SCIENTIFIC-TECHNICAL UNION OF MECHANICAL ENGINEERING "INDUSTRY 4.0"

108 Rakovski str., 1000 Sofia
e-mail: office@industry-4.eu
www.industry-4.eu

INTERNATIONAL EDITORIAL BOARD

Co-Chairs:		
Prof. D.Sc. Georgi Popov, DHC, Technical University of Sofia, BG	Prof. Dr. Dr. Jivka Ovtcharova, DHC, Karlsruhe Institute of Technology, GE	
Members:		
Acad. Igor Bychkov	Institute for System Dynamics and Control Theory SB RAS	RU
Cor. member Alexey Beliy	National Academy of Sciences of Belarus	BY
Cor. member Svetozar Margenov	Bulgarian Academy of Science	BG
Prof. Alexander Afanasyev	Institute for Information Transmission Problems	RU
Prof. Alexander Guts	Omsk State University	RU
Prof. Andrzej Golabczak	Technical University of Lodz	PL
Prof. Andrey Firsov	Saint-Petersburg Polytechnic University	RU
Prof. Bobek Shuklev	Ss. Cyril and Methodius University of Skopje	NM
Prof. Boris Gordon	Tallinn University of Technology	EE
Prof. Branko Sirok	University of Ljubljana	SI
Prof. Claudio Melchiorri	University of Bologna	IT
Prof. Cveta Martinovska	Goce Delchev University, Stip	NM
Prof. Dale Dzemydiene	Mykolas Romeris University, Vilnius	LT
Prof. Dimitar Yonchev	Free Bulgarian University, Sofia	BG
Prof. Dimitrios Vlachos	Aristotle University of Thessaloniki	GR
Prof. Dragan Perakovic	University of Zagreb	HR
Prof. Galina Nikolcheva	Technical University of Sofia	BG
Prof. Galina Zhavoronkova	National Aviation University	UA
Prof. Gerard Lyons	National University of Ireland, Galway	IE
Dr. Giovanni Pappalettera	Politecnico di Bari	IT
Prof. Henrik Carlsen	Technical University of Denmark	DK
Prof. Idilia Bachkova	University of Chemical Technology and Metallurgy	BG
Prof. Idit Avrahami	Ariel Univerity	IL
Prof. Inocentiu Maniu	Politehnica University of Timisoara	RO
Prof. Iurii Bazhal	National University of Kyiv-Mohyla Academy	UA
Prof. Dr. Ivan Kuric	University of Zilina	SK
Prof. Jürgen Köbler	University of Offenburg	DE
Prof. Jiri Maryska	Technical University of Liberec	CZ
Prof. Katia Vutova	Institute of electronics, Bulgarian Academy of Sciences	BG
Prof. Lappalainen Kauko	University of Oulo	FI
Dr. Liviu Jalba	SEEC Manufuture Program	RO
Prof. Luigi del Re	Johannes Kepler University, Linz	AT
Prof. Majid Zamani	Technical University of Munich	DE
Prof. Martin Eigner	Technical University of Kaiserslautern	DE
Dipl.-Kfm. Michael Grethler	Karlsruhe Institute of Technology	DE
Prof. Michael Valasek	Czech Technical University in Prague	CZ
Prof. Milija Suknovic	University of Belgrade	RS
Prof. Miodrag Dashic	University of Belgrade	RS
Prof. Mladen Velev	Technical University of Sofia	BG
Prof. Murat Alanyali	TOBB University of Economics and Technology	TR
Prof. Nafisa Yusupova	Ufa State Aviation Technical University	RU
Prof. Nina Bijedic	Dzemal Bijedic University of Mostar	BA
Prof. Ninoslav Marina	University of Information Science and Technology – Ohrid	NM
Prof. Olga Zaborovskaia	State Inst. of Econom., Finance, Law and Technologies	RU
Prof. Pavel Kovach	University of Novi Sad	RS
Prof. Petar Kolev	University of Transport Sofia	BG
Prof. Peter Korondi	Budapest University of Technology and Economics	HU
Prof. Peter Sincak	Technical University of Košice	SK
Prof. Petra Bittrich	Berlin University of Applied Sciences	DE
Prof. Predrag Dasic	High Technical Mechanical School, Trstenik	RS
Prof. Radu Dogaru	University Politehnica of Bucharest	RO
Prof. Raicho Ilarionov	Technical University of Gabrovo	BG
Prof. Raul Turmanidze	Georgian Technical University	GE
Prof. René Beigang	Technical University of Kaiserslautern	DE
Prof. Rozeta Miho	Polytechnic University of Tirana	AL
Prof. Sasho Guergov	Technical University of Sofia	BG
Prof. Seniye Ümit Oktay Firat	Marmara University, Istambul	TR
Prof. Sreten Savicevic	University of Montenegro	ME
Prof. Stefan Stefanov	Technical University of Sofia	BG
Prof. Svetan Ratchev	University of Nottingham	UK
Prof. Sveto Svetkovski	St. Cyril and St. Methodius University of Skopje	NM
Prof. Tomislav Šarić	University of Osijek	HR
Prof. Vasile Cartofeanu	Technical University of Moldova	MD
Prof. Vidosav Majstorovic	Technical University of Belgrade	RS
Prof. Vjaceslavs Bobrovs	Riga Technical University	LV
Prof. Vladyslav Alieksieiev	Lviv Polytechnic National University	UA

CONTENTS

SESSION
TECHNOLOGICAL BASIS OF "INDUSTRY 4.0"
DOMINANT TECHNOLOGIES IN "INDUSTRY 4.0"

Cybersecurity of OPC ua based cyber-physical systems

Dr. Eng. Ivanova T.A., Eng. Belev Y. A., Prof. Dr. Batchkova I. A.
Dept. of Industrial Automation, University of Chemical Technology and Metallurgy
Bul. Kl. Ohridski 8, Sofia, Bulgaria

t.ivanova@uctm.edu, idilia@uctm.edu

***Abstract**: The IEC-62541 (OPC UA) standard is an important part of the Industry 4.0 reference architecture and is recommended as the only possible communication standard. A particularly important issue that is being addressed is the issue of security. Cyber security is one of the most important challenges for achieving the objectives of the Industry 4.0 initiative and of the associated cyber-physical systems (CPS). The paper analyzes the vulnerability of cyber-attacks and the main threats that threaten the security of OPC UA-based CPS and defines proven and sustainable recommendations for increasing the security of these applications.*

***Keywords**:* CYBER SECURITY, CYBER-PHYSICAL SYSTEMS, OPC UA, IEC 62541, INDUSTRY-4.0

1. Introduction

The rapid development and widespread penetration of information and communication technologies in the industry has led to the emergence of new strategies for the development of the industry in order to increase its competitiveness, such as the German initiative "Industrie 4.0" [1]. Standardization plays a central role in successfully tackling new challenges. The development and adoption of standards reduces the risk for enterprises and encourages the adoption of new technologies, products and production methods. The Industry Perspectives 4.0 study [2] confirms that the first major challenge related to the implementation of the vision is standardization. The main advantage of using standards is that they reflect the state of science and the development of technology and promote mutual understanding and consensus between partners.

Cyber-Physical Systems (CPS) are physical and engineered systems whose operations are monitored, coordinated, controlled and integrated by a computing and communication core [3]. Their components can be distributed both spatially and temporally, and include complex networks of feedback controllers and real time communication. These characteristics of CPS significantly complicate the cyber security of these systems and require the solution of a series of complex tasks with the application of a combination of various methods and techniques. Cyber security professionals are facing increasing challenges, both in terms of the frequency with which cyber threats occur and in terms of increasing their risk. The impact of malware and cyber-attacks can not only lead to denial of service or theft and diversion of information, but also affect the behavior of the object under control by causing it to behave in a dangerous manner, which can cause accidents and dangerous consequences. With the increasing complexity of cyber-physical systems and system of system, the issues of ensuring the security and safety of these systems are of global importance. There are three main approaches in achieving cyber security: (i) building and using reference architecture, (ii) developing cyber security standards and (iii) applying methods and tools in the field of automation in cyber security systems.

The basic requirement to the CPS for building fast, platform-independent, scalable and secure communications, which can be integrated horizontally and vertically, is fully met by the IEC-62541 standard (OPC UA) [4]. This standard defines a common infrastructure model for information exchange between components (sensors, mechanisms, control systems) and systems (MES, ERP) in the industry. OPC UA supports the following specifications: (i) information model for presenting structure, behavior and semantics; (ii) modeling of messages for interactions between applications and (iii) communication model for data transfer between endpoints. The IEC-62541 standard (OPC UA) is present in the reference architecture for Industry 4.0 - RAMI [5] and is listed as the only recommended communication standard for implementation. Two aspects are the focus of attention in this standard: the use of information modeling tools and the security issues that are covered in the standard. The paper focuses on Part 2 of IEC-62541 (OPC UA) standard [6], which addresses the security issues of OPC UA applications.

The main purpose of the paper is to analyze the vulnerability of cyber-attacks and the main threats that threaten the security of OPC UA based cyber-physical systems and to define proven and sustainable recommendations for increasing the security of these applications. These recommendations are essential for defining and using effective scenarios to increase the security of these applications and create a successful lifecycle model for the development of OPC UA based cyber-physical systems.

The paper is structured in 4 parts. Following the introduction, in part two, the IEC-62541 (OPC-UA) standard, the term security and the security model are briefly presented. Part 3 provides a brief analysis of cyber-attack threats that threaten the security of OPC UA applications. Part 4 systematizes the main recommendations for building secure OPC UA based cyber-physical systems, which can be used to improve their development lifecycle model.

2. OPC-UA and the security model

2.1. Summary of IEC-62541 standard (OPC-UA)

The IEC-62541 standard or also known as OPC-UA (Open Platform Communication - Unified Architecture) [4], which includes 14 parts, presents a new generation of OPC, which replaces TCP/IP communication protocols specific to DCOM, allowing: (1) the use of OPC applications on any operating system; (2) the implementation in all languages; (3) the use of OPC in devices (firmware); (4) to activate WAN (secure Internet/Intranet/Extranet) and (5) to improve the security management. OPC UA combines all previous protocols into a common, unified data model. It offers a complete networked, object-oriented concept for the namespace, including metadata for defining objects. The OPC UA specification defines a service-oriented architecture (SOA) with a set of services described in Part 4 of the standard [7]. The information models in OPC UA form a layered structure, shown in Fig. 1, where the basic information model is at the lowest level. Above the base model are service-specific extensions to the information model for data access, alarms and conditions, programs, historical access, and aggregates. The accompanying specifications are defined above the composition of the general information models. The next layer contains the accompanying specifications, which are domain-specific information models. At the top level of the OPC UA structure, highly refined information models from different companies or suppliers for use in their specific products are defined. The composition of information models can be extended. The information models are defined and explained in Part 5 of the standard [8].

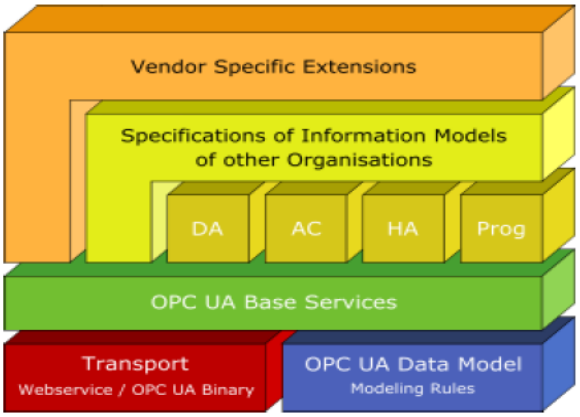

Fig.1: *Multilayer structure of models in OPC UA [8]*

With OPC UA, OPC Foundation makes the transition from object-oriented COM/DCOM technology to service-oriented architecture by integrating previous specifications into a single address space represented by a model for defining complex information in the form of objects consisting of nodes, connected with references. Different classes of nodes convey different semantics. For example, a variable node is a readable or writable value, which has an associated data type that can define the current value. The method node is a function that can be called to be executed. Each node is characterized by attributes, including a unique identifier.

2.2. On the definition of security

In the English technical literature, there are two terms for software security - "assurance" and "security". The term "assurance" looks at security in a broader sense, including its reliability, also known as software resilience, software safety, and its security as "Security", which is the ability of software to resist, tolerate and recovers from events that intentionally compromise its reliability. According to the US National Security Systems Committee's (CNSS) National Information Security Dictionary [9], software security is: "the degree of assurance that software is free of vulnerabilities, either intentionally designed in the software, or accidentally included in any time throughout its life cycle, and that the software functions as intended". Achieving software security affects all phases of the software development life cycle, and the goal of all integrated activities in this direction is to achieve software that shows:

- Trustworthiness - mainly related to the absence of malicious and/or unintentional operational vulnerabilities or weaknesses;
- Predictable execution - there is reasonable assurance that the software, when executed, functions only as intended;
- Conformance - where a planned and systematic set of multidisciplinary activities ensures that software processes and products meet the relevant requirements, standards and procedures.

2.3. Security objectives in OPC-UA

The security model is presented in Part 2 of IEC-62541 [6]. The security of industrial systems is achieved by achieving a set of objectives that are defined on the basis of many years of experience and remain unchanged over the years, despite the ever-changing set of threats to the systems. The main objectives of security are summarized as follows:

- Authentication (A1): Entities such as clients, servers and users must prove their identity. Authentication can be based on something that the entity is, possesses or knows;
- Authorization (A2): Access to read, write or execute resources should be allowed only for those objects that need this access within the system requirements;
- Confidentiality (A3): ensures that users without access rights do not have access to the information, i.e. the data is protected from passive attacks such as eavesdropping, whether the data is transmitted to be stored in memory or stored. To ensure confidentiality, data encryption algorithms using special data protection secrets are used, along with authentication and authorization mechanisms to access this secret;
- Integrity (A4): refers to maintaining the accuracy and integrity of the information, i.e. the recipients receive the same information as the original sender, without the data changing during transmission. Unauthorized changes by authorized organizations or any modifications by unauthorized entities, such as: overwriting, falsification, destruction, involuntary or malicious insertion of logic, deletion, etc. should not be allowed;
- Auditability (A5): actions taken by the system should be recorded to provide evidence to stakeholders that the system is working as intended (successful actions are tracked), to identify the initiator of certain actions (the activity of the user is tracked), to find that attempts to compromise the system have been denied (unsuccessful actions are tracked);
- Availability (A6): refers to the ability of authorized persons to have access to information and timely maintenance of information resources in a state in which they can be used without problems.
- Non-Repudiation (A7): non-repudiation ensures that something that actually happened cannot be said not to have happened. The security service that provides this protection can be one of two types: (1) the recipient of the data receives and stores information proving that the data came from the creator. This blocks the author from claiming that he never sent the data. (2) one in which the sender of the data receives confirmation that the data have been received by the recipient as intended.

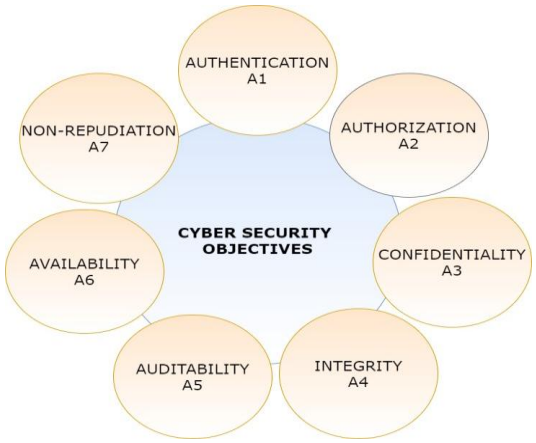

Fig.2: *Cyber security objectives*

Based on the requirements for confidentiality, integrity and availability, a classification of systems and data has been developed, and classes have been defined in accordance with the quality aspects of these requirements. Each class meets a minimum set of security requirements to be met and security measures to be taken. At the heart of this classification are the ISO27001 and ISO27002 standards. The ISO27001 standard refers to the requirements for information security management systems, preparation or selection of lists of known risks, based on various sources of good practice, such as CAPEC (contains a list of 1000 possible attacks), Microsoft's STRIDE, OWASP "Top 10" and many others.

Security is achieved through preventive methods used to protect information from theft, compromise or attack. This requires understanding potential information threats such as viruses and other malicious code. Security risk is a product of three elements: threat, vulnerability and impact. Risk refers to the possibility of loss or damage when a specific threat exploits a captured vulnerability. Risk can include financial losses as a result of business interruptions, damage to reputation, legal

consequences and even loss of life. Vulnerability refers to a specific weakness in assets (resources) that allows a particular attack to be successful.

2.4. OPC-UA security architecture

The standard provides a flexible set of security mechanisms. Client-server communication can be realized in two ways - through and without a session, as shown in Fig. 3. The session is organized in the application layer and in addition to the routine work of client and server applications. It has the task of managing the security, authentication and authorization objectives of the user. The session communicates through a security channel in the communication layer, which is organized in a very flexible way and must be activated. The communication layer provides security mechanisms to achieve confidentiality, integrity, and authentication of the application, using a secure channel that provides encryption to maintain confidentiality, signing messages to maintain integrity, and application authentication certificates. The security mechanisms provided by the Secure Channel services are implemented by a stack protocol that is selected for execution. When OPC UA (UACP) protocols are used, then the security functions are specified in the SSL/TLS mode.

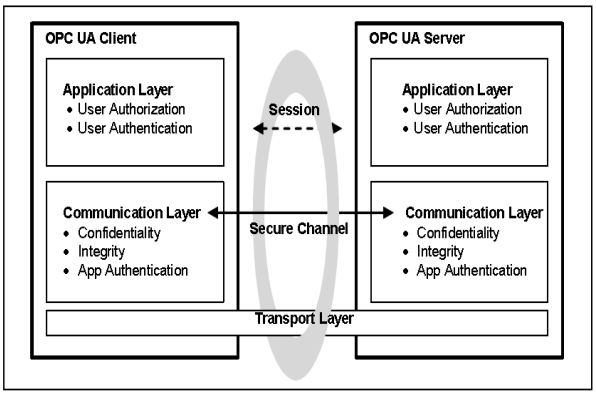

Fig.3: *OPC-UA security architecture for client-server applications [6]*

Communication between applications is based on messages, the parameters of which are defined in Part 4 of the standard and their format defined by *Data Encoding* and *Transport Protocol* (Fig. 4). A stack is a collection of software libraries that implement one or more *Stack Profiles*. The interface between the application and the stack hides the details of stack execution, depending entirely on the development platform used. Each OPC UA *Stack Profile* is a separate application protocol. Even when *Security Mode = None* is selected, i.e. security is not supported, the *Secure Channel* layer is present, supporting a logical channel with a unique identifier.

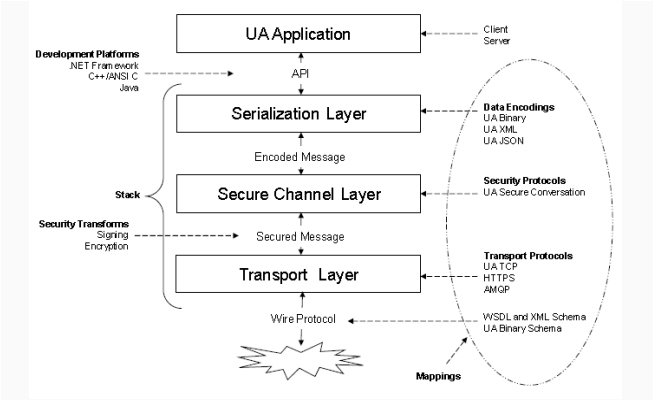

Fig.4: *OPC-UA security architecture for client – server applications*

3. Analysis of threats to OPC UA based CPS

3.1. Defining the main threats

The security of cyber-physical systems reduces the risk of damage caused by attacks. This includes: (1) identifying system threats, (2) identifying system vulnerabilities to those threats, and (3) providing countermeasures that directly reduce vulnerabilities, counter threats, or recover from successful attacks.

OPC UA applications can be used in a variety of operating environments. In some cases, they can be an attractive target for industrial espionage or sabotage, and they can also be exposed to threats through unobtrusive malware, such as worms circulating in public networks with different assumptions about threats and accessibility, as well as different policies for security and application modes. Some of the most common threats to OPC UA based CPS can be summarized as follows:

- Message Flooding: The attacker sends a sequence of requests to the system in an attempt to consume enough server resources to make the system insensitive to legitimate traffic.
- Eavesdropping: listening to other people's conversation or communication without their consent.
- Message Spoofing: A malicious party that impersonates another device or user on the network to launch attacks on network hosts, steals data, distribute malware, or bypass access controls.
- Message Alteration: during the attack, messages are intercepted in the communication environment, and certain information can be changed, or the call can be diverted, the service can be interrupted, etc.
- Message Replay: A network attack in which a valid data transmission is recorded and then played back to affect system operations.
- Malformed Messages: Also known as Protocol Fuzzing, the attack sends messages with the wrong syntax to the target server or client to interrupt the service.
- Server Profiling: Gathers information about the server or related equipment to explore what the core infrastructure is.
- Session Hijacking: When a TCP session is hijacked, the user session is attacked over a secure network. Session hijacking is also known as a "middle man attack" in which an attacker uses a computer program (sniffer) that detects and records a variety of limited information, especially secret passwords needed to access files or networks.
- Rogue Server: A rogue server is a network server that is not under the administrative control of network personnel.
- Compromised User Credentials: User credentials are available to others other than the user (without their knowledge or consent) and may be logged into the user's account.

3.2. Coordinating threats with OPC UA security mechanisms

The coherence achieved between the threats and the security mechanisms of OPC UA, presented in Table 1, links the security functions of OPC UA with specific threats. For example, the following cases are possible (1) OPC UA minimizes the loss of availability caused by flooding with messages by minimizing the processing of messages until they are authenticated, or (2) when eavesdropping occurs, OPC UA provides encryption to protect against eavesdropping, or (3) OPC UA counts threats to tamper with messages by providing the ability to sign messages, or (4) OPC UA counteracts session hijacking by setting a security context, i.e. security channel in each session, etc.

Table.1: *Consistency of threats and security functions*

Threats	A1	A2	A3	A4	A5	A6
Message Flooding						X
Eavesdropping			X			
Message Spoofing		X		X		
Message Alteration		X		X		
Message Replay		X				
Malformed Messages				X		
Server Profiling	X	X	X	X	X	X
Session Hijacking	X	X	X			
Rogue Server	X	X	X		X	X
Compromised User Credentials		X	X			

4. Safety recommendations when using OPC UA

As a result of a number of tests performed in accordance with the standard, the following recommendations have been identified and summarized with a view to the use of secure communications with the OPC UA protocol:

• Operation in "*SecurityMode*": This means that "*Sign*" or "*SignAndEncrypt*" mode must be selected. These modes ensure that, at the application level, authentication is mandatory. "*None*" security mode does not provide protection! The "*SignAndEncrypt*" security mode is used to protect the integrity of data and its confidentiality [10].

• Choice of cryptographic algorithms: "*Basic256Sha256*" must be selected as the *SecurityPolicy* [11], provided that the clients with which the server interacts support this policy. Security policies using outdated algorithms, such as "*SHA-1*", should not be used.

• User authentication: Logging in to the UA server with an "anonymous" ID should only be used when accessing non-critical resources, as in this case it is not possible to track by the server who is changing the data or configuration. Hackers can take advantage of these recommendations to use OPC UA with a Secure Way ID to read or write data in an unauthorized manner. This can happen if the restriction on the rights to work with the "anonymous" identifier is not configured adequately. [10]

• Storing certificates and private keys: The used private keys or certificate files should not be stored in an unencrypted file system. For this purpose, special certificates stores of the operating system and its capabilities for setting access rights must be used. It is recommended to use TPMs (Trusted Platform Modules) or external secure hardware, such as USB authentication tokens to store certificates and/or private keys.

• Use certificates: Connections that do not provide trusted certificates are not allowed. Self-signed certificates require additional verification. If the certificates are not self-signed, the establishment of a certification body is required, and the certificates of the certification body are signed independently or by another certification body. Certification bodies can be multi-layered [5].

• Certificate management and maintenance: It is recommended to use certificate trust lists and certificate revocation lists to manage only valid certificates. These lists are created by trusted users or processes. The lists must be updated regularly.

Conclusions

Digitalization and growing network structures and applications on the one hand, and increasing hacking attacks on critical infrastructures and industrial applications on the other, are placing the issue of network and application security increasingly on the agenda. The analysis and comparison of the capabilities of OPC UA presented in the paper show the ability to successfully deal with security issues at different levels in the automation pyramid. The defined objectives, potential threats and established compliance allow, according to IEC-62541 standard (OPC UA), the development of security profiles and models for individual areas of application.

Acknowledgment: The study was conducted within the National Research Program "Information and Communication Technologies for a Digital Single Market in Science, Education and Security (ICTinSES)", funded by the Ministry of Education and Science.

References

1. Kagermann H., Wahlster W., Helbig J., Recommendations for implementing the strategic initiative INDUSTRIE 4.0, Final report of the Industrie 4.0 Working Group, Akatech, April, 2013.
2. Forschungsunion, "Recommendations for implementing the strategic initiative Industry 4.0", Acatech, 2013.
3. Rajkumar, R., I. Lee, L. Sha, and J. Stankovic (2010), Cyber-physical systems: the next computing revolution, In Proceedings of the 47th Design Automation Conference, ACM, New York, 2010, pp. 731-736.
4. OPC Foundation (2017), OPC UA Specification, Part 1: Overview and Concepts, http://www.opcfoundation.org/UA/Part1/
5. DIN SPEC 91345, Reference architectural model Industry 4.0 (RAMI4.0), 2016, Berlin.
6. OPC Foundation (2018), OPC UA Specification, Part 2: Security model http://www.opcfoundation.org/UA/Part2/
7. OPC Foundation (2017), OPC UA Specification, Part 4: Services http://www.opcfoundation.org/UA/Part4/
8. OPC Foundation (2017), OPC UA Specification, Part 5: Information Model, http://www.opcfoundation.org/UA/Part5/
9. Committee on National Security Systems, National Information Assurance (IA) Glossary, CNSS instruction No. 4009 (revised June 2006). Available from: http://www.cnss.gov/Assets/pdf/cnssi_4009.pdf
10. Fiat, Störtkuhl, Plöb, Zugfil, Gappmeier and Damm, "OPC UA Security Analysis," Federal Office for Information Security, Bonn, Germany, 2017.
11. OPC Foundation (2017), OPC UA Specification, Part 7: Profiles, http://www.opcfoundation.org/UA/Part7/

A predictive maintenance application for band saw machines

Mahmut Berkan Alisinoglu[a], Kadir Cavdar[b]
[a] Beka-Mak R&D Center, Bursa, Turkey
[b] Bursa Uludag University, Department of Mechanical Engineering, Bursa, Turkey

ABSTRACT: Digitalization of production lines is the most important issue in the world in recent years. One of the most important issues of this digitalization for today's manufacturing enterprises is the need to update maintenance practices and maintenance work processes in production lines with technological developments. The fact that sawing machines are in the first part of the production lines shows that it is of critical importance. In this study, it is aimed to determine the necessary principles for digitizing sawing machines and integrating the predictive maintenance system into the machine. As a result of the evaluation, the necessity of real-time data collection, data analysis and artificial intelligence algorithms for predictive maintenance requirements has been determined.
KEY WORDS: *Manufacturing, Sawing Machines, Industry 4.0, Predictive Maintenance*

1. INTRODUCTION

Today's technological developments, increasing energy need, changing and developing competition conditions make maintenance and repair activities of enterprises even more important. In this direction, different maintenance strategies have been developed.
Maintenance is defined as ensuring that equipment and systems operate efficiently without malfunctions throughout their life cycle in order to maintain their functions with the best performance. Unexpected failures cause production losses and costly maintenance costs. In this direction, maintenance methods should be applied to ensure production and line efficiency. The fact that the saw machines are in the first part of the production lines shows that they are of critical importance.

Reactive maintenance occurs once a piece of machinery has already failed. In contrast to proactive maintenance, no analysis, tracking, or anticipation is required to carry it out. As the name implies, work is only completed in reaction to a breakdown, see Figure 1.

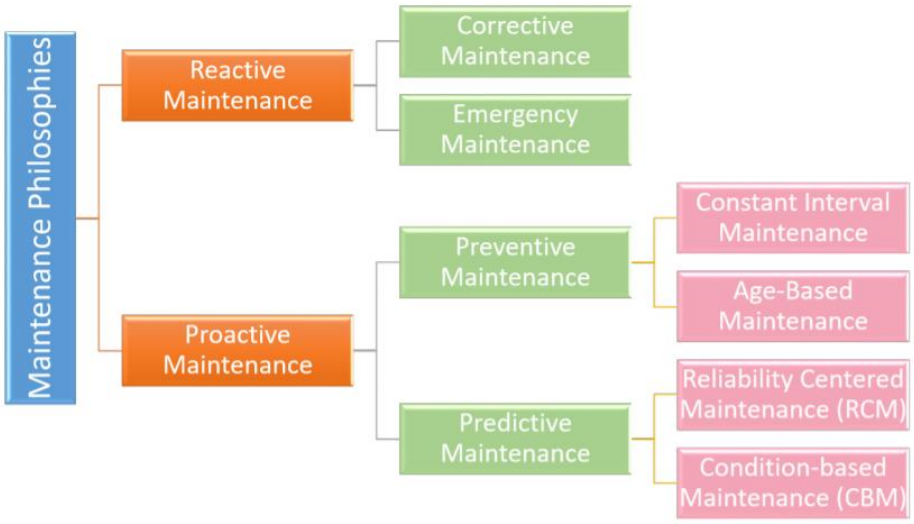

Fig 1. *Classification of Maintenance Philosophies [1]*

2. THE PREDICTIVE MAINTENANCE APPROACHES

In the predictive maintenance concept, a prerequisite for the condition of the system must be met to maintain the system. The aim is to keep the system at the highest level with the least number of maintenances required, thus reducing maintenance costs [2]. It consists of 2 main parts as Reliability Centred Maintenance (RCM) and Condition-Based Maintenance (CBM). RCM tries to improve the reliability and usability of the most crucial points in the system and minimize system failures and maintenance costs. The main aim is to find the optimum point where system reliability and profitability intersect with the number of maintenances [3]. CBM enables the maintenance decision to be performed in regard to the actual state of the equipment or system. CBM indicates that maintenance should be carried out when specific indications indicate the possibility of poor performance or unexpected failure. For a machine, these symptoms are detected by visual inspection, performance data, vibration data, and analysis of planned test results. A proper CBM plan reduce maintenance costs considerably as a result of avoiding unnecessary maintenance [4].

3. AN APPLICATION FOR BAND SAW MACHINES

3.1 The Band Saw Machines

Band saw machines are saws that consist of a continuous metal band (called the band saw blade) that rides on two wheels rotating in the same plane. A band saw machine contains a round and serrated blade, and can be used to process metal materials. Depending upon the lateral flexibility and the width of the band, a band saw machine can be used for straight, irregular or curved shape cuts. In a band saw, work pieces are fed into the cutting edge of the machine. The band saw machine cuts by drawing a continuous metal band across the work piece. The band saw blade is supported and driven by a drive wheel and an idler wheel. A sample of the band sew machine was given in Figure 2.

Fig 2. *A Band Saw Machine [5]*

3.2 The Predictive Maintenance Application

3.2.1 Current and Linearity Analysis for Band Saw

Among several techniques to detect cutting force during cutting process, driver current and deviation control low cost and high efficiency methods. Cutting force directly affects surface roughness and surface steepness are Surface roughness and surface steepness are important outputs of the cut quality in sawing. These outputs can be controlled with the current drawn by the cutting tool and the inductive distance sensor to be placed on the cutting tool.

Many engine data can be received via the EtherCat protocol. EtherCAT (Ethernet for Control Automation Technology) is an Ethernet-based fieldbus system invented by Beckhoff Automation. The protocol is standardized in IEC 61158 and is suitable for both hard and soft real-time computing requirements in automation technology. The goal during development of EtherCAT was to apply Ethernet for automation applications requiring short data update times (≤ 100 µs) with low communication jitter (≤ 1 µs) and reduced hardware costs [6].

Motor current set value is set as 3 amperes. With the real-time current information to be obtained from the saw motor, the motor speed can be reduced automatically in case of strain.

In addition to the current data, it is aimed to make straight cuts by checking the perpendicularity with the deviation sensor placed on the cutting tool. With the inductive displacement sensor to be placed in front of the cutting tool, linearity control is performed in real time at the time of cutting. Since high precision cutting perpendicularity is aimed, perpendicularity limits are set as ± 0.2 mm and the sensor is positioned at a distance of 1.2 mm.

Omron ZX-EM02HT inductive displacement sensor is used for deviation detection. Linearity and measurement distance graphic of the sensor is given in the Figure 3.

The current graph of the motor driving the cutting tool was drawn with 100ms sampling (Figure 4).

The deviation graph of the cutting tool was drawn with 100ms sampling (Figure 5).

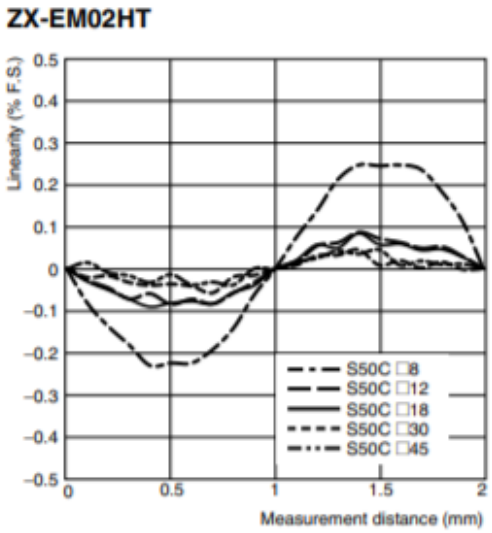

Fig 3. *ZX-EM02HT Linearity – Measurement Distance Graphic [7]*

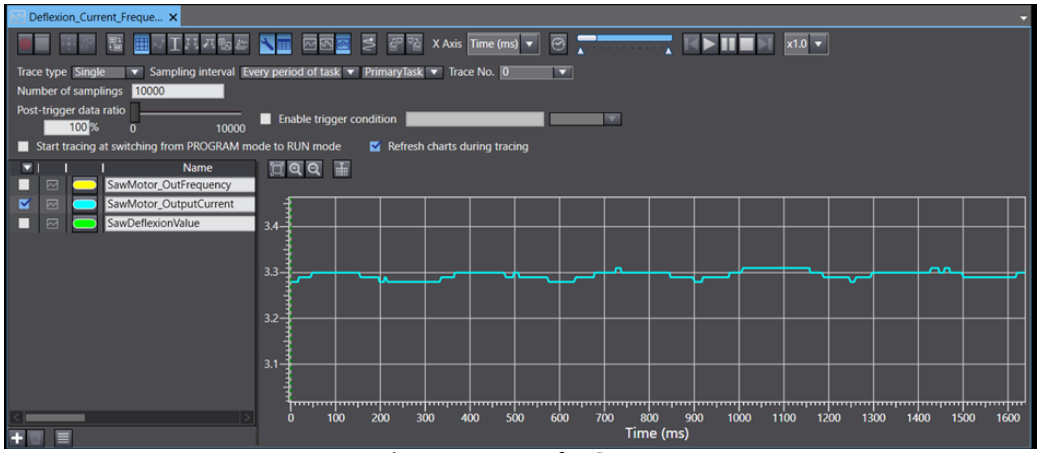

Fig 4. *Data Trace for Current*

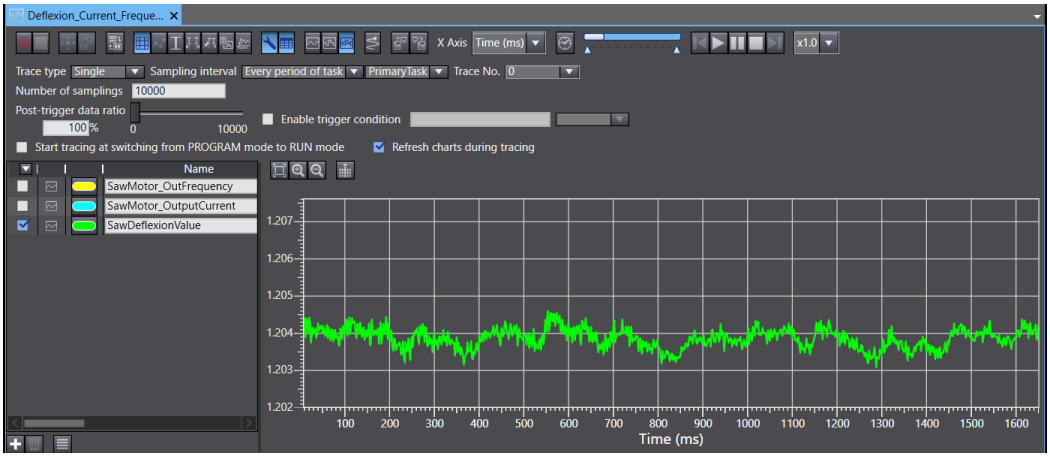

Fig 5. *Data Trace for Deviation*

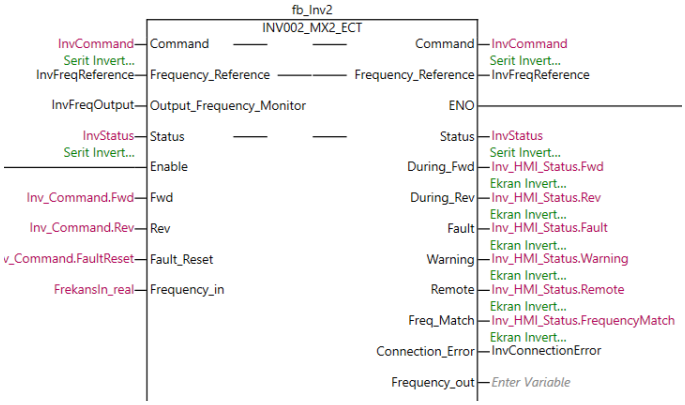

Fig 6. *Motor Driver Control Block*

3.2.2 Detection of Sensor Faults

Saw machines have many sensors to collect data. Conventional digital sensors produce zero or multiple signals for the situation. In order to design intelligent machines within the scope of Industry 4.0 transformation, it was felt that digital sensors should provide information to the user by creating additional data indicating the sensor operating status besides zero and one values [8]. For this reason, IO link sensors have started to be used frequently in the industry. IO-Link (IEC61131-9) is a point-to-point communication protocol that supports IO-Link and provides bidirectional exchange of data.

IO links series photoelectric and inductive sensors are placed on the band saw machine. Thus, two-way communication with the sensors is provided. For example, when the sensor's performance is degraded due to contamination, the sensor can issue an alarm so that the situation can be corrected without stopping the machine. The ability to send new parameters to sensors is particularly useful for machines working with multiple products; because this feature eliminates the need for manual intervention during changes in many applications.

Thanks to the IO link protocol, the detection data of the photoelectric sensor can be received from the PD0, while stable operation, warning and alarm information can be obtained from the PD1.
Bits and assignments are shown in Figure 7.

3.2.3 Vibration Analysis for Ball Screw

The ball screw is a transmission device that converts linear motion into rotary motion or rotary motion into linear motion, and it has the advantages of high position accuracy, load capacity and fatigue life. Ball screw systems (see Figure 8) generate vibration signals when they are operated. when the system runs continuously the various frequency components of vibration signals represent different characteristics pertinent to each mechanical and the amplitude of frequency changes.

The vibration analysis method is the most applied and the fastest method among predictive maintenance methods. In this method, with the help of a receiver that converts the vibrations into an electrical signal. The measurement is taken on the machine and the electrical signal formed as a result of this measurement is transferred to a device that processes it. This information is transferred to the controller, analysed with the help of an analysis software, and a conclusion is reached about the machines [10].

4. CONCLUSION

Studies on predictive maintenance are topics that are on the agenda of today's machinery manufacturing industry and user-friendly solutions can be produced in many areas. These studies can generally be summarized as detecting and interpreting vibrations on the machine and taking the necessary precautions.
In this study, the necessary criteria for predictive maintenance integration into the band saw machine were determined. Field tests and analyses related to current and deviation for the cutting tool, field tests and error analyses on the sensors used to collect data were carried out.
It has been observed that surface roughness and perpendicularity outputs can be obtained with current and deflection control in particular for band saw cutting machines. Apart from this, it has been determined that manual intervention is prevented with IO link sensors.
The ball screw part, which was briefly introduced in the article, was left to the next stage of the work.

Byte0 (PD0)								Assignment	Details
7	6	5	4	3	2	1	0	Monitor output	The Sensing data are output as eight bits (0-255).

Byte1 (PD1)								Assignment	Details
7	6	5	4	3	2	1	0	Control Output1	0:OFF 1:ON
								Control Output2	0:OFF 1:ON
								Reserved	0
								Instability Alarm(Non-Light Receiving)	0:Stable 1:Unstable
								Instability Alarm(Light Receiving)	0:Stable 1:Unstable
								Reserved	0
								Warning	Diagnostic output when the sensor cannot continue operation due to a recoverable factor such as a load short-circuit or a service data error 0:Normal (OFF) 1:Error (ON)
								Error	Diagnostic output when the sensor has an internal error such as the emitting circuit destruction and replacement is needed 0:Normal (OFF) 1:Error (ON)

Fig 7. *Process Data for Photoelectric Sensor [9]*

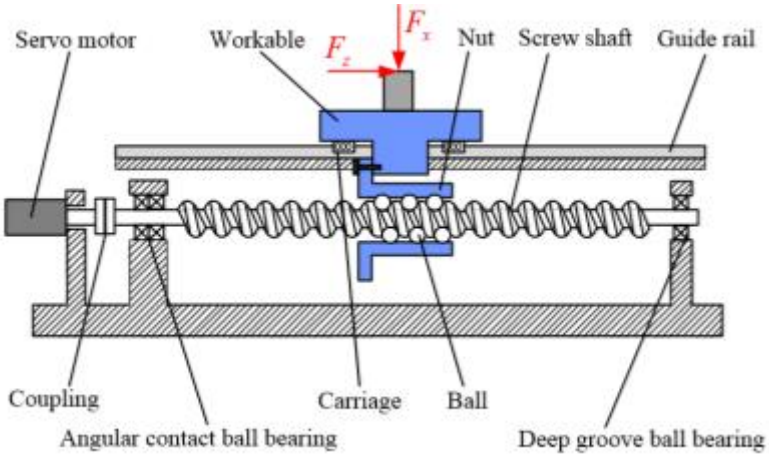

Fig 8. *Structure of Ball Screw Feed System [11]*

5. REFERENCES

[1] EVALUATION OF ALTERNATIVE MAINTENANCE STRATEGIES ON A COMPLEX SYSTEM IN THERMAL POWER SYSTEMS, Busenur Türkali,2017

[2] R. K. Mobley, An introduction to predictive maintenance. Elsevier, 2002.

[3] J. Moubray, Reliability-centred maintenance. Industrial Press Inc., 2001.

[4] A. K. Jardine, D. Lin, and D. Banjevic, "A review on machinery diagnostics and prognostics implementing condition-based maintenance," Mechanical systems and signal processing, vol. 20, no. 7, pp. 1483–1510, 2006.

[5] https://www.bekamak.com/urun/420-xs/

[6] https://en.wikipedia.org/wiki/EtherCAT

[7] https://assets.omron.eu/downloads/datasheet/en/v4/e331_zxe_smart_sensors

[8] Onur Çimen, INDUSTRY 4.0 APPLICATIONS IN WET WIPES MACHINES, INTERNATIONAL SCIENTIFIC JOURNAL INDUSTRY 4.0, 2020

[9] https://assets.omron.eu/downloads/manual/en/w570_io-link_system_users_manual_en.pdf

[10] Titreşim Analizi ile Pompalarda Arıza Tesbiti ve Kestirimci Bakım İçin Örnek Bir Çalışma, Gulsen Yaman:Sablon 26.03.2014

[11] Dynamic Analysis of Ball Screw Feed System with the Effects of Excitation Amplitude and Design Parameters Chang Liu, Chunyu Zhao *, Zhendong Liu and Shuai Wang, 2021

Improving the corrosion resistance of carbon steel cylindrical pipe by nano-materials coating, part -2

[1]Salloom A. Al-Juboori, and Dana Alshamaileh, M.Sc
[1]Professor in Mechanical Engineering, B.Sc, M.Sc, PhD, Leeds University, U.K
[1]Engineering Faculty /Mutah University / AlKark/ Jordan, Email: sajibury@mutah.edu.jo

Abstract: *This part is a continuation of Part-1, which was studying the effect of anti-corrosion nano-materials coating using zinc (Zn) and cobalt (Co) on corrosion resistance and its relationship with mechanical properties. While, part 2 was on studying the linear stresses resistance after coating by using the same nanomaterials of paret-1 of carbon steel pipe and their relationship with chemical corrosion resistance using finite element analysis (FEA). The coating was tested with different thicknesses of nano-layers (300 μm, 600 μm, 900 μm, 10 μm) on a thick-walled cylindrical pipe subjected to a uniformly distributed internal pressure of 4 bars. The results showed that the value of linear normal stresses did not change when coating with 300 μm for both nano-coating materials. However, it was started to decrease slightly when covered with 600 μm of cobalt and continues to decrease with increasing the coating thickness. In addition, the results have shown that the overall improvement in linearized normal stresses and corrosion resistance due to cobalt coating can be about (66 %) higher in comparison with Zinc at 10 μm thickness of coating*.

***KEYWORDS**: LINEAR STRESSES, NANO-COATING, ZN, CO, AND CARBON STEEL, CORROSION RESISTANCE, ANSYS-19.*

***Abbreviations:** ALD: Atomic Laser Deposition, CVD: Chemical Vapor Deposition, ISO: International Organization for Standardization, MWCNT: Multi-Wall Carbon Nanotubes, SEM: Scanning Electron Micrographs, SCC: Stress Corrosion Crack, Co: Cobalt, Ni: Nickel, μm : nanometer, Zn : Zinc, μ: surface Roughness, E: Modulus of elasticity, v: Poisson's ratio, σ: Sigma (tensile stresses),P: Fluid pressure*

Background: The relationship between corrosion and the degradation of metals' mechanical properties is very important factor affecting the metal life. The further corrosion the metal undergoes, and both the tensile strength and fracture strength of the metal are diminished by the corrosion [1,2]. Corrosive wear is also known as chemical wear or oxidation. Which is due to the chemical and electrochemical interaction of the surface and the environment. This form of wear can occur, inn corrosive wear, the fine corrosive products on the surface reflect the wear debris. As the shaped layer is broken or removed by sliding and abrasion because of corrosion, another layer starts to form, and the process of removing a new corrosive layer formation repeated. The most common corrosive media are water, seawater, oxygen, acids, chemicals, atmospheric hydrogen sulfide and sulfur dioxide.

Corrosion can have a variety of negative effects on metal. When metal structures suffer from corrosion, they become unsafe which can lead to accidents, such as collapses. Even minor corrosion requires repairs and maintenance. Corrosive wear can be minimized by selecting the right materials that will resist environmental attack, by applying different coating methods. This can controlling the environment, and reducing operating temperatures in order to lower the rate of chemical reaction [6,7]. Seawater distinguished by being a corrosive complex medium due to the high salt content, dissolved organic substances, such as carbohydrates and amino acids, and dissolved gasses such as (chiefly nitrogen, oxygen, argon, and carbon dioxide). The presence of carbonates, chloride and other component will influence seawater chemistry significantly and lead to the formation of scale at the membranes and in piping structures. This lead to severe corrosion of alloys, especially carbon steel, and with high level of presence of dissolved oxygen, corrosion will accelerate. Figure (1) shows an example of corrosion effect on bolts, valves, flanges, piping, and pipe support [8].

One of the most important problem of damage that contribute to reduce both the static and cyclic strength of a performance of thin-walled structures that immersed in seawater such as pipelines is corrosion problem. It is a process depend on a time, local environment inside or near the pipeline and occur on the internal and external surfaces in the pipe, in the base material and contact welding. As such, protection of metal equipment in a seawater environment will give prime consideration [9].

Predicting the rate of corrosion of a steel structure in seawater is one of the difficult tasks facing design and corrosion engineers. The main parameters that effect on the rate are dissolved oxygen, salinity, temperature, ph and Sulphur [10]. Protective coatings are one of the most important methods used to reduce metal waste caused by surface corrosion, which leads to extend the life of metal equipment. Example of these coatings are Chromized or Aluminized coatings [11]. Chromatid zinc deposits was given a better protection against corrosion compared to unprotected zinc that was corrodes quickly in chloride medium [12]. In present work a more advanced coating will be used which is a Nano-coating.

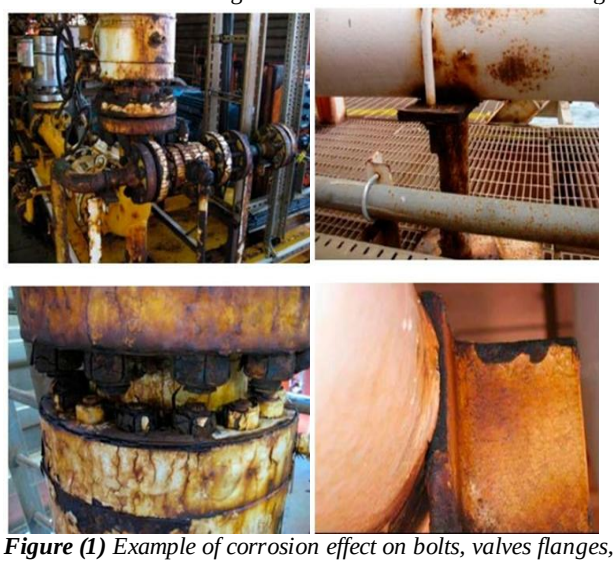

***Figure (1)** Example of corrosion effect on bolts, valves flanges, piping, and pipe support (Abdeen, et al., 2019).*

Corrosion and Nano-materials: The field of nanomaterial have found one of the most promising topics in different applications such as chemistry, engineering, physics, biology that will change the direction of nanotechnology advances in wide range of fields. The term "nano-materials" employed to describe of the creation and exploitation the materials where at least one dimension in the range from approximately 1-100 nanometer. Due to their unique properties in nanoscale, observations showed that nanomaterial's are different from their bulk moieties and cannot be studied as same as from their bulk molecules [13]. The use of nano-materials reduces the content of costly and toxic elements in alloy components, which gives high profitability in material cost, excellent performance, and enhances the mechanical properties of the coating. Electro-deposition and sol-gel chemistry method are attractive techniques in Nano-coatings applications, as it is cheaper and novel strategies [14,15]. Nano coatings have significant potentials to resistance the corrosion performance of surfaces compared to micro material coatings. Due to their fine grain sizes, nano-crystal line structures are superior over microstructures for corrosion resistance .where provide a better filling ,a higher integrity of the coated surface and it also called for the availability

of chromium-toxic coating replacements . However, the coating thickness and composition should optimize to avoid decrease its protective characteristics towards corrosive and eroding influences [16]. Corrosion induces changes in the composition of the elements and decreases in grain size, contributing to the deterioration of corroded materials' mechanical properties (yield strength, ultimate strength, and failure strain). Applied stress accelerates corrosion and the loss of ultimate strength and failure strain of corroded materials exacerbated by its interaction with corrosion [17]. Anti-corrosion nano-materials and their coatings play an important role in improving mechanical properties such as linear stresses, ductility, high hardness, etc. in addition to surface properties such as residual stresses, surface roughness and distribution of particles on surface [18].

Research Objectives:
The main objective of this part is to study and analyze the linearized stresses improvement and their effect on corrosion resistance due to the application of nano coating of pressurized carbon steel pipe by Cobalt and Zinc nano-particles separately of thickness of 300, 600, 900 μm and 10 micrometer [3].

Research Methodology: A comprehensive review of the literature pertaining to nano- materials and their applications in the field of corrosion has undertaken in order to achieve the above objectives for this research. Then a group of nano-material's with corrosion-resistant properties will be selected and simulated the effect of apply nano coating technology using ANSYS software on a thick-walled cylindrical pipe that carries salty water under internal pressure, using electro-deposition nano coating method. After that will study and analyze the results and compare the changes in linearized stresses and in corrosion mechanical properties before and after applying coating by nano-materials of different thickness.

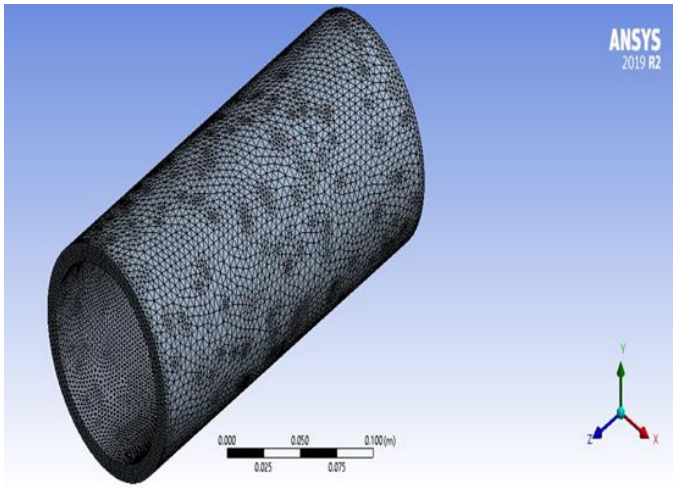

Figure (2) *Thick-walled cylindrical pipe with 4.5 mm on outer and side faces and 3.5 mm on inner face elements size of mish.*

The geometric modeling of the study: One finite element model has created. Thick walled cylindrical pipe coated with different nano thickness of Zinc and Cobalt materials separately, as in figures (2 to 5), which show the pipe specimen will analyze and coated during this work. At the beginning, the CAD geometry built using space claim in ANSYS with the given dimensions. Geometry transferred into ANSYS mechanical and thin nano layer defined on the inner surface wall using surface coating from ANSYS, [3,4].

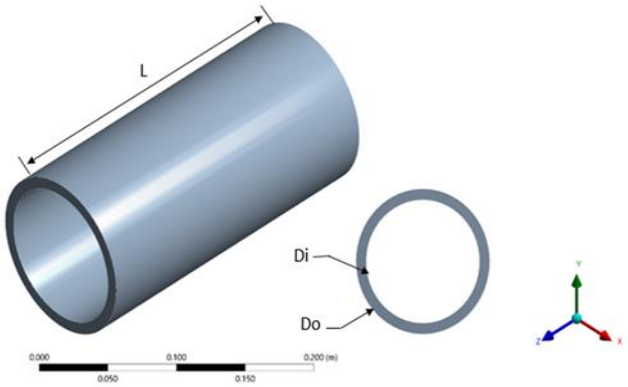

Figure (3) *Front and ISO views of thick-walled cylindrical pipe specimen with dimensions.*
Where:
L= 0.25m Do = 0.1143 m Di = 0.0971804 m

Mesh Details: Parts was converted to small elements in order to use FEA methods for solving the problem, refinement of mesh was done on the inner wall where the nano coating is located in order to get more accurate results, number of nodes is 143620 and elements is 71929 [3,4], as in figure-2

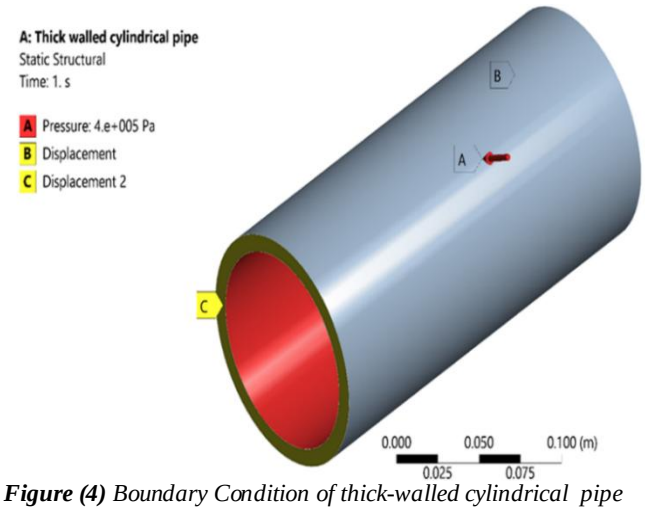

Figure (4) *Boundary Condition of thick-walled cylindrical pipe specimen.*

Materials: In the present work cobalt and zinc which are anticorrosion nano-material's will be used to apply coating on a thick-cylindrical pipe made from carbon steel, the physical, chemical and mechanical properties of the materials will be analysis before and after coating by nano-materials [4].

Carbon Steel: Carbon steels defined as those containing iron, carbon, and manganese. There are three type of carbon steel depend on the amount of carbon content is low carbon, medium carbon, and high carbon steel which contains 0.6–1.4% carbon. (Pressure System Design. 2012). It is the most widely used engineering material for service in seawater and many engineering applications in high temperature conditions such as power plant, chemical treatment, mining, mineral equipment Processing and other industrial fields, it offers many advantages of low price, easy availability, ease of fabrication, and a satisfactory rate of corrosion [19, 20, 21]. Carbon steel piping and tubing because of their

minimal resistance to corrosion there are limits on their operating time [22].

Zinc: Zinc is the fourth most used engineering metal in the world, a bluish-white metal, and one of the main uses for zinc is steel coating to protect against corrosion in the presence of an electrolyte such as moist soils or seawater [23].

Cobalt: Cobalt is one of the rare elements in the Earth's crust of about 0.1%, usually distributed in conjunction with nickel, lead, silver, iron, etc. It is a white, hard-bluish, ferromagnetic metal, relatively unreactive and slowly dissolves in mineral acids without union with hydrogen or nitrogen. Cobalt is now widely used in the production of alloy steel, which is the base metal in most of them. Cobalt alloys distinguished by being strength, high melting point, and high resistance to oxidation [24, 25].

Linearized Normal Stress: Stress linearization is the separation of stresses through a section into constant membrane. Linear bending stresses and total stress along a straight-line path, the linearized normal stress in (Y-axis) value and improvement represented in figures (5 to 10) and tables (1 to 4). Stresses along the thickness calculated through membrane stress for shell in the transverse direction, the longitudinal direction, and in plane shear. This theory applied only when shell bodies and solids that meshed with shell element. When highly localized stress occurs at a discontinuity in the load stress theory can apply. Most common example of peak stress when highly stress values on sharp edges as in figure-5 [3, 4, 5].

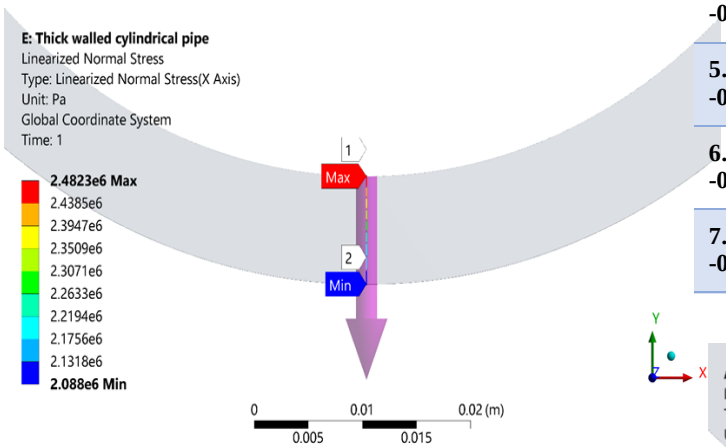

Figure (5) *Linearized Normal Stress (Y-axis) of Carbon steel (ASTM A53) pipe without coating*

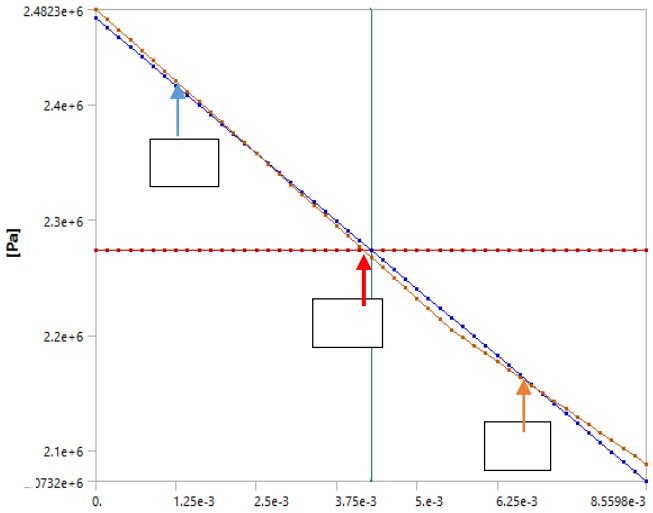

Figure (6) (a) *Membrane [Pa], (b) Membrane +Bending [Pa], (c) Total stress [Pa] without coating.*

Table (1) *Linearized normal stresses of carbon steel pipe without coating*

Length [m]	Membrane [Pa]	Bending [Pa]	Membrane +Bending [Pa]	Peak [Pa]	Total [Pa]
0.0000E+00	2.27E+06	2.0066E+05	2.4745E+06	7.8158E+03	2.4823E+06
1.7833E-04		1.9230E+05	2.4662E+06	7.2620E+03	2.4734E+06
3.5666E-04		1.8394E+05	2.4578E+06	6.7081E+03	2.4645E+06
5.3499E-04		1.7558E+05	2.4494E+06	6.1543E+03	2.4556E+06
7.1332E-04		1.6722E+05	2.4411E+06	5.6004E+03	2.4467E+06
8.9165E-04		1.5886E+05	2.4327E+06	5.0466E+03	2.4378E+06
1.0700E-03		1.5050E+05	2.4244E+06	4.4927E+03	2.4289E+06
2.1400E-03		1.0033E+05	2.3742E+06	1.1697E+03	2.3754E+06
3.0316E-03		5.8527E+04	2.3324E+06	-2.0267E+03	2.3304E+06
4.1016E-03		8.3610E+03	2.2822E+06	-5.5006E+03	2.2767E+06
5.1715E-03		-4.1805E+04	2.2321E+06	-8.9744E+03	2.2231E+06
6.0632E-03		-8.3610E+04	2.1903E+06	-6.3741E+03	2.1839E+06
7.1332E-03		-1.3378E+05	2.1401E+06	2.7006E+03	2.1428E+06

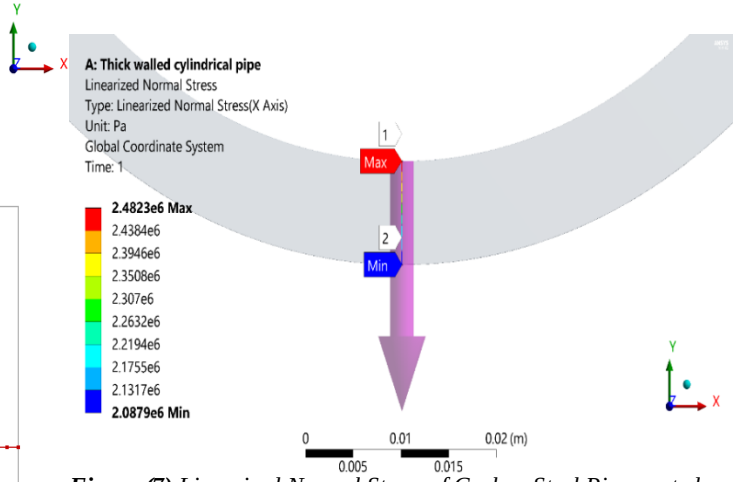

Figure (7) *Linearized Normal Stress of Carbon Steel Pipe coated with 300 Nanometer of Cobalt*

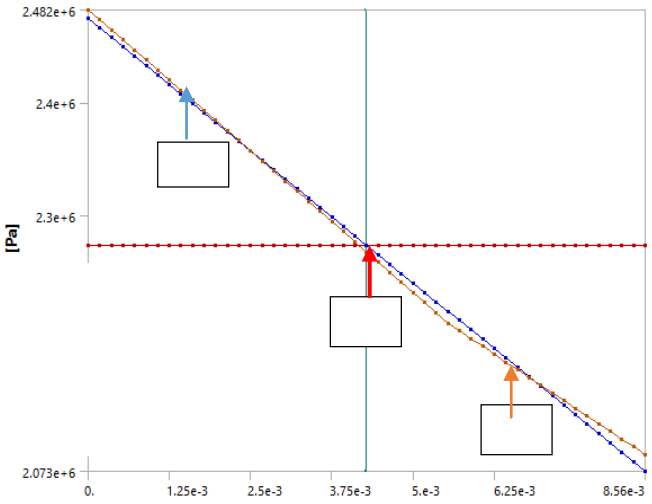

Figure (8) (a) *Membrane [Pa], (b) Membrane +Bending [Pa], (c) Total stress [Pa] coated with 300 Nanometer of Cobalt*

Table (2) *Linearized normal stresses of Carbon Steel Pipe coated with 300 Nanometer of cobalt*

Length [m]	Membrane [Pa]	Bending [Pa]	Membrane +Bending [Pa]	Peak [Pa]	Total [Pa]
0.00000 E+00	2.27E+06	2.00660 E+05	2.47440 E+06	7.81530 E+03	2.48230 E+06
1.78340 E-04		1.92300 E+05	2.46610 E+06	7.26150 E+03	2.47330 E+06
3.56670 E-04		1.83940 E+05	2.45770 E+06	6.70770 E+03	2.46440 E+06
5.35010 E-04		1.75580 E+05	2.44940 E+06	6.15390 E+03	2.45550 E+06
7.13340 E-04		1.67220 E+05	2.44100 E+06	5.60010 E+03	2.44660 E+06
8.91680 E-04		1.58860 E+05	2.43260 E+06	5.04630 E+03	2.43770 E+06
1.07000 E-03		1.50500 E+05	2.42430 E+06	4.49250 E+03	2.42880 E+06
2.14000 E-03		1.00330 E+05	2.37410 E+06	1.16970 E+03	2.37530 E+06
3.03170 E-03		5.85270 E+04	2.33230 E+06	-2.02650 E+03	2.33030 E+06
4.10170 E-03		8.36100 E+03	2.28210 E+06	-5.50010 E+03	2.27660 E+06
5.17170 E-03		-4.18050 E+04	2.23200 E+06	-8.97370 E+03	2.22300 E+06
6.06340 E-03		-8.36100 E+04	2.19020 E+06	-6.37440 E+03	2.18380 E+06
7.13340 E-03		-1.33780 E+05	2.14000 E+06	2.70030 E+03	2.14270 E+06
8.02510 E-03		-1.75580 E+05	2.09820 E+06	1.03010 E+04	2.10850 E+06

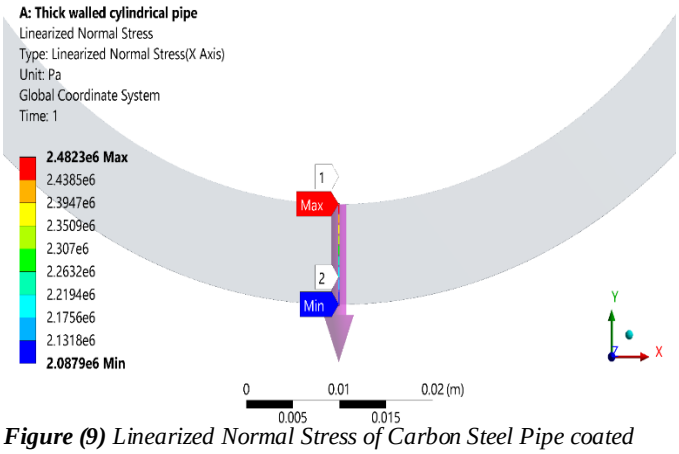

Figure (9) *Linearized Normal Stress of Carbon Steel Pipe coated with 300 Nanometer of Zinc*

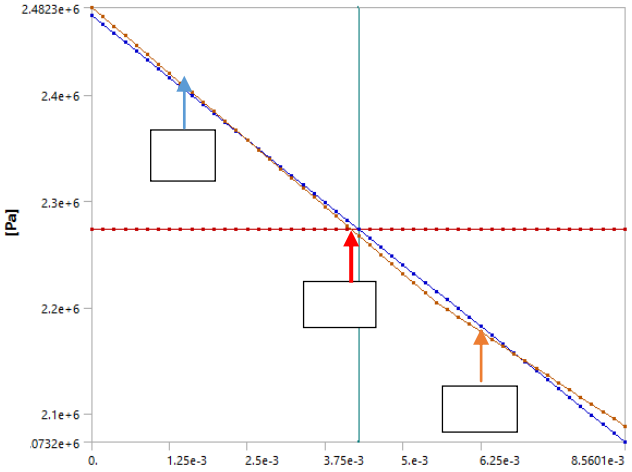

Figure (10) *(a) Membrane [Pa], (b) Membrane +Bending [Pa], (c) Total stress [Pa] coated with 300 Nanometer of zinc*

Table (3) *Linearized normal stress values of Carbon Steel Pipe coated with 300 nanometer of zinc*

Length [m]	Membrane [Pa]	Bending [Pa]	Membrane +Bending [Pa]	Peak [Pa]	Total [Pa]
0.00000 E+00	2.27E+06	2.00670 E+05	2.47450 E+06	7.81550 E+03	2.48230 E+06
1.78340 E-04		1.92310 E+05	2.46610 E+06	7.26170 E+03	2.47340 E+06
3.56670 E-04		1.83950 E+05	2.45780 E+06	6.70790 E+03	2.46450 E+06
5.35010 E-04		1.75590 E+05	2.44940 E+06	6.15410 E+03	2.45560 E+06
7.13340 E-04		1.67220 E+05	2.44110 E+06	5.60020 E+03	2.44670 E+06
8.91680 E-04		1.58860 E+05	2.43270 E+06	5.04640 E+03	2.43770 E+06
1.07000 E-03		1.50500 E+05	2.42430 E+06	4.49260 E+03	2.42880 E+06
2.14000 E-03		1.00330 E+05	2.37420 E+06	1.16970 E+03	2.37530 E+06
3.03170 E-03		5.85280 E+04	2.33240 E+06	-2.02650 E+03	2.33030 E+06
4.10170 E-03		8.36120 E+03	2.28220 E+06	-5.50020 E+03	2.27670 E+06
5.17170		-	2.23200	-	2.22310

E-03		4.18060 E+04	E+06	8.97390 E+03	E+06
6.06340 E-03		- 8.36120 E+04	2.19020 E+06	- 6.37460 E+03	2.18380 E+06
7.13340 E-03		- 1.33780 E+05	2.14010 E+06	2.70040 E+03	2.14280 E+06
8.02510 E-03		- 1.75590 E+05	2.09820 E+06	1.03010 E+04	2.10850 E+06

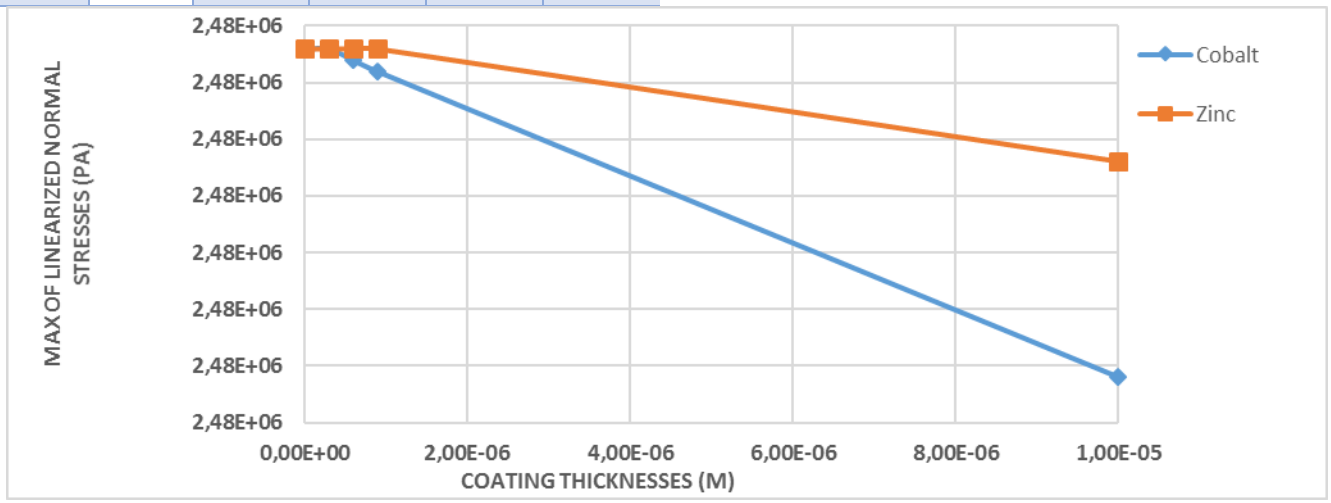

Figure (11) *Comparison of maximum Linearized Normal Stress (Y-axis) With Cobalt and Zinc of different nano coating thicknesses.*

Table (4) *Maximum Linearized Normal Stress value and percentage of improvement in corrosion resistance with different coating thickness (Y-axis).*

	Cobalt(Co)			Zinc(Zn)		
Coating thickness (m)	**Value (Pa)**	**Improvement %**	**Corrosion Resistance %**	**Value (Pa)**	**Improvement %**	**Corrosion Resistance %**
0	**2.48230E+06**	**0**	**0**	**2.48230E+06**	**0**	**0**
300 *nm*	**2.48230E+06**	**0**	**0**	**2.48230E+06**	**0**	**0**
600 *nm*	**2.48220E+06**	**0.004028522**	**0.635**	**2.48230E+06**	**0**	**0**
900 *nm*	**2.48210E+06**	**0.008057044**	**0.898**	**2.48230E+06**	**0**	**0**
10 *μm*	**2.47940E+06**	**0.116827136**	**3.418**	**2.48130E+06**	**0.040285219**	**2.007**

Results Discussion: Figure (11) shows a comparison of maximum linearized normal stresses (Y-axis) of a pressurized carbon steel (ASTM A53) thick-walled cylindrical pipe and the improvement due to coating with different nano thicknesses of Cobalt and Zinc separately. Starting with thickness (300, 600, 900 nanometers to 10 micrometer). It is clear that the linearized normal stress (Y-axis) did not change when coated with 300 nanometer for both coating materials, but it began to decrease slightly when coated with 600 nanometer of Zinc and fast decreasing with 10 microns. While, when coated with 600 and 900 Cobalt, can be noticed that there is a noticeable decrease on linearized normal stresses and become more sharply decreasing when the coating was 10 microns. The maximum improvement is (0.1168%) when coated with 10 µm of cobalt, which is (34. %) higher than zinc. The same behavior was found in the resistance of corrosion where the increase started at 600 µm of cobalt with value (0.635%) and it reached the highest value (3.418%).While coating by zinc nanoparticle at (10 mm) found to be (2.007%).

Conclusions: From the analysis of the above results, the following main points can extracted:

- The Carbon steel (ASTM A53) thick walled cylindrical pipe subjected to internal pressure was successfully coated theoretically with anticorrosion nano- particles of Cobalt and Zinc using ANSYS software (version.19 with different nano thicknesses of 300 µm, 600 µm, 900 µm and 10 µm separately.
- Coating with 300 nanometers of both Znic and Cobalt nano-particles, the linearized normal stresses (Y-axis) did not change but starts to decrease slightly when coated with 600 nanometers of cobalt and continues to decrease with 10 µm with greater than zinc. On the other hand, when coated with 600-µm and 900-µm zinc, it noticed that there is no difference in the linearized normal stresses.
- The value of improvement in the rate of corrosion resistance began to increase when coating with 600 µm of cobalt until became (3.418%).
- The overall improvement in linearized normal stresses and corrosion resistance due to cobalt coating can be about (66 %) higher in comparison with Zinc at 10 µm thickness of coating.
- Cobalt nano-coating has shown to be a promising technique to improve corrosion and linearized stresses resistance.

References:

[1] Abdeen, D., El Hachach, M., Koc, M., & Atieh, M. (2019). A Review on the Corrosion Behavior of Nano coatings on Metallic Substrates. Materials, 12(2)

[2] ASTM A53 / A53M-18, Standard Specification for Pipe, Steel, Black and Hot-Dipped, Zinc-Coated, Welded and Seamless, ASTM International, West Conshohocken, PA, 2018, www.astm.org).

[3] Al-Juboori, S., Albtoosh, M., 2019. Improving the Mechanical Properties of Conventional Materials by Nano-coating, part-1. V International Scientific Conference Mareria Science „Nonequilibrium Phase Transformations", Varna, Bulgaria.

[4] Al-Juboori, S., Albtoosh, M., 2019Improving the Linearized stresses resistance by Nano-Coating, Part-2 Proceeding of International Scientific Conference High Technologies. Business. Society09-11.03.2020, Borovets, Bulgaria, Year V, Issue 2 (8), Sofia, Bulgaria 2020

[5] Al-Juboori S. and Dana Alshamaileh, Improving the Corrosion Resistance by nano-Materials Coating, part-1, v international scientific conference material science no equilibrium phase transformations 09 - 12 September 2019, Varna, Bulgaria

[6] Beyene, F. (2016). A Review on nano-coating of Metallic Structures to Improve Hardness and Maintaining Toughness. I-manager's Journal on Material Science, 4(1), 32-40.

[7] Cosham, A., Hopkins, P., & Macdonald, K. (2007). Best practice for the assessment of defects in pipelines – Corrosion. Engineering Failure Analysis, 14(7), 1245–1265.

[8] CRC Handbook of Chemistry and Physics, Robert C. Weast, Ed. 62 Edition, Crc Press, Boca Raton, FL,1981. http://www.matweb.com/index.aspx

[9] Darvell, B. (2018). Corrosion. Materials Science for Dentistry, 382–398.Dhoke, S. Khanna, A. & Sinha, T. (2009). "Effect of nano-ZnO particles on the corrosion behavior of alkyd-based waterborne coatings." Progress in Organic Coatings, 64(4), 371–382.

[10] Farag, A. (2020). Applications of nanomaterials in corrosion protection coatings and inhibitors. Corrosion Reviews.

[11] Ferreira, M. Zheludkevich, M. & Tedim, J. (2011). Advanced protective coatings for aeronautical applications. Nanocoatings and Ultra-Thin Films, 235–279.

[12] Jose, R., Sakho, E. hadji M., Parani, S., Thomas, S., Oluwafemi, O. S., & Wu, J. (2019). Introduction to nanomaterials: synthesis and applications. Nanomaterials for Solar Cell Applications, 75–95.

[13] HEARN, E. (1997). THICK CYLINDERS. Mechanics of Materials 1, 215–253.

[14] Hou, Y., Lei, D., Li, S., Yang, W., & Li, C.-Q. (2016). Experimental Investigation on Corrosion Effect on Mechanical Properties of Buried Metal Pipes. International Journal of Corrosion, 2016, 1–13.

[15] Gao, Y., Ward, L., Fan, L., Li, H., & Liu, Z. (2019). A study of the use of polyaspartic acid derivative composite for the corrosion inhibition of carbon steel in a seawater environment. Journal of Molecular Liquids, 111634.

[16] Klarstrom, D., & Crook, P. (2001). Cobalt Alloys: Properties and Applications. Encyclopedia of Materials: Science and Technology, 1281–1288.

[17] Khodair, Z. Khadom, A. & Jasim, H. (2018). Corrosion protection of mild steel in different aqueous media via epoxy/nanomaterial coating: preparation, characterization and mathematical views. Journal of Materials Research and Technology.

[18] Lynch, R. (2001). Zinc: Alloying, Thermomechanical Processing, Properties, and Applications. Encyclopedia of Materials: Science and Technology, 9869–9883.

[19] Li, L., Li, C.-Q., & Mahmoodian, M. (2019). Effect of Applied Stress on Corrosion and Mechanical Properties of Mild Steel. Journal of Materials in Civil Engineering, 31(2), 04018375.

[20] Mutahhar, F., Aithan, G., Iski, E. V., Keller, M. W., Shirazi, S., & P. Roberts, K. (2017). Mechanistic modeling of erosion–corrosion for carbon steel. Trends in Oil and Gas Corrosion Research and Technologies, 749–763.

[21] Nguyen Tri, Nguyen, T. Rtimi, S., & Ouellet Plamondon, C. (2019). Nanomaterials-based coatings: an introduction. Nanomaterials-Based Coatings, 1–7.

[22] Païdoussis, M. (2016). Cylindrical Shells Containing or Immersed in Flow. Fluid-Structure Interactions, 1–141.
Pressure System Design. (2012). Lees' Loss Prevention in the Process Industries, 509–617.

[23] Qu, Z., Wang, L., Tang, H., Ye, H., & Li, M. (2019). Effect of Nano-SnS and Nano-MoS2 on the Corrosion Protection Performance of the Polyvinylbutyral and Zinc-Rich Polyvinylbutyral Coatings. Nanomaterials, 9(7), 956.

[24] Solatani, H., Tavoosi, M., & Loghman-Estarki, M. R. (2019). Fe-Ni composite coatings reinforced with SiC nanoparticles and carbon nanotubes: corrosion and tribological performance. Materials Research Express.

[25] Sankara, T. (2012). Nanocoatings to improve the tribocorrosion performance of materials. Corrosion Protection and Control Using Nanomaterials, 167–212.

Influence of filtering size on results in interpretation of Hopkinson-Kolsky bar signals

Rumen Krastev, Tatiana Simeonova, Vasil Kavardjikov
Institute of Mechanics - Bulgarian Academy of Science, Sofia, Bulgaria
R_krastev@imbm.bas.bg

Abstract: *The influence of registered signals smoothing on the calculated diagram of the test specimen was analysed for impact test using split Hopkinson-Kolsky pressure bar. Two methods are used to smooth the signals: low-pass filtering built into the software and arithmetic mean averaging. When determining the elastic modulus and the upper yield stress in these high-strain rate tests, it is concluded that more accurate values are obtained by filtering with a cut-off frequency in the range of 60 to 80 kHz. For the second method, it is concluded that it is best to average the curves with an amplitude of 3 or 4 microseconds. Attention is paid to the correct choice of the initial moments from which the reading of the signals begins because the wrong choice leads to inaccurate calculations and conclusions about the properties of the tested material.*

Keywords*: SPLIT HOPKINSON-KOLSKY PRESSURE BAR, SIGNALS, FILTERING, DATA TREATMENT*

1. Introduction

At the beginning of 2021, in implementation of a project BG05M2OP001-1.001-0008 "National Center for Mechatronics and Clean Technologies", a new experimental equipment was installed at the Institute of Mechanics at the Bulgarian Academy of Sciences – Split Hopkinson-Kolsky Pressure Bar (Fig. 1). This device is used for determination of materials properties at high deformation rates. It applies a load to the test specimen similar to that which the material would withstand in real situations like car accidents or other high-energy collisions. Modern implementations of these devices are used to study metals and metal alloys [1-4], concrete, foam concrete and reinforced concrete with different fibres [5-12], geological materials (marble, rocks) [13, 14], different 3D printing materials and products made by this technology [15, 16] and composite materials [17]. In addition to experiments with compressive impact deformation along the sample axis, shear deformation can also be realised [18]. Often modern devices of this type are equipped with high-speed cameras, which visualise the process of shock deformation, and/or determine the field of deformation of the observed surface of the sample by correlation analysis of the recorded images [19]. The results obtained from these measurements provide essential information about the properties of the tested materials for scientific and engineering applications. Researchers use them as input data in developing numerical models of structures from relevant materials and in basic research related to defining constitutive equations describing the behaviour of materials under dynamic loading [20].

Experiments are conducted by mounting a cylindrical test body between two rods, called *Incident Bar* (IB) and *Transmitted Bar* (TB). Strain gauges are glued in the middle of the two bars, and the machine is equipped with a computer and a recording device for the signals coming from these strain gauges.

There is a theoretical model for determining the compressive stress and strain of the crushed specimen, which uses the registered strain pulses in time.

The registered signals *strain-time* have fluctuations that affect the quality of the determined diagrams. To improve the results, a low-pass software filter is applied to the registered signals.

Accumulating experience, it became clear that the selected cut-off frequency of the filter not only smooths the resulting diagrams but also changes the slope of the observed mechanical diagram.

In this report, we analyse the influence of the selected cut-off filter frequency on the final shape of the obtained diagram (with the same output signals for all analyses). The aim is to find such cut-off frequency that will provide sufficient smoothing of the desired diagram and will have only a slight effect on its initial slope.

2. Test equipment, material and experimental plan

A pressure Hopkinson's bar, as modified by Kolsky (Fig. 1), contains a launching device (1) powered with compressed air. It can fire strikers at planned speed. The available strikers are 200 to 800 mm long and have a diameter of 20 mm, the same as the diameter of the main bars. After firing the selected striker, its impulse is passed to the incident bar (2), creating in it a longitudinal pressure wave that moves at the speed of sound. The test specimen (4) is deformed between the IB and the transmitted bar (5), as part of the impact wave is reflected (from the end of the bar 2) and is registered through the strain gauges (3), and another part is transmited through the test specimen and is registered by the strain gauges (6), located in the middle of the TB (5). Behind the last rod (7), there are devices (not visible in Fig. 1) for suppressing the movement after impact. The equipment works well when the system of bars are positioned with minimal deviations from a straight line.

Fig. 1 *Split Hopkinson-Kolsky pressure bar*
1- Launching device, 2-Incident bar, 3-Strain gauges in the middle of IB, 4-Test piece, 5-Transmitted wave bar, 6- Strain gauges in the middle of TB, 7-motion suppression bar.

IB and TB are made of "Maraging 300" steel with a diameter of 20 mm and a length of 2000 mm. A striker with 600 mm length was used for this experiment. There are disk anvils of the same diameter and 8 mm length on both sides of the test specimen. On the forehead of the incident bar is used a shaper - washer M4 according to DIN 9021 made of A2 steel.

The influence of filtering on the obtained results will be shown by processing the signals from one of the tsts in different ways. The test specimen is made of duralumin with initial dimensions: 5 mm diameter and 5 mm length. The speed of the striker before the impact with the IB is estimated as 13.3 m/s.

The experimental plan is expressed in signal processing and analysis of the results, as smoothing of the signals is done in different sizes and by two methods:

- Using the built-in filter, at the following cut-off frequencies: 40, 60 and 80 kHz.
- Using the averaging method described in section 3.4, at the following averaging amplitudes: 1, 2, 3, 4, 6, 8, 10 and 12 microseconds.

The results obtained without any signal smoothing are compared with the results obtained after smoothing.

3. Signal processing methods

3.1 Simplified analytical model

The mechanical diagram of the test specimen for the described Hopkinson-Kolsky bar is obtained by the following "simplified" system of equations [21, 22]:

$$\dot{e}_s(t) = \frac{-2c_b}{l_0}\varepsilon_R(t) \quad (1)$$

$$e_s(t) = \int_0^t \dot{e}_s(\tau)d\tau \quad (2)$$

$$s_s(t) = E_b \frac{A_b}{A_{s0}}\varepsilon_T(t) \quad (3)$$

Where:

t – Time

$\varepsilon_R(t)$ – Reflected (by the end of IB) signal

c_b – Propagation velocity of the deformation waves (pulses) in the bars, 4730 m/s

l_0 – Initial sample length

$\dot{e}_s(t)$ – Sample deformation rate

$e_s(t)$ – Nominal (engineering) deformation of the sample, calculated for moment *t*

$\varepsilon_T(t)$ – Passed through the sample (transmitted) deformation pulse

E_b – Elastic modulus of all bars, 181 GPa.

A_b – Cross-section of the bars

A_{so} – Initial cross-section of the sample

$s_s(t)$ – Nominal (engineering) stress in the sample for moment *t*.

It is accepted that stress and strain are considered as positive values even though the sample is subjected to compression [22]. Therefore, the signs of the recorded signals must be reversed.

During an impact deformation of the sample, its dimensions change significantly. Therefore, under compression and while the variables are positive, the true strain ε_s and the true stress σ_s are calculated by the formulas (4) – (6), [22]:

$$\varepsilon_s(t) = -\ln[1 - e_s(t)] \quad (4)$$

$$\dot{\varepsilon}_s(t) = \frac{\dot{e}_s(t)}{1-e_s(t)} \quad (5)$$

$$\sigma_s(t) = s_s(t)[1 - e_s(t)] \quad (6)$$

3.2 Start of signal reporting

The recorded signals are available in tabular form, every 1 microsecond. Before mathematical processing, the starting points in time must be chosen for both signals (reflected and transmitted). The machine is designed so that these two points coincide or at least be close enough to each other.

Our experience has shown that beginning of the signal $\varepsilon_T(t)$ is delayed by about 13 μs after the beginning of the signal $\varepsilon_R(t)$, as shown in Fig.2. We think this is due to the passage of the strain pulse through the sample and by removal of gaps between the sample, disk anvils and bars.

To obtain quality results, it is crucial the starting points of reading the signals $\varepsilon_R(t)$ and $\varepsilon_T(t)$ to be chosen correctly, using a theoretically and empirically justified method. In the presented calculations and results, the starting moments of reading the two signals were chosen to be (approximately) when $|\varepsilon_R(t)|$ = 10/100 * max($|\varepsilon_R|$) and $\varepsilon_T(t)$ = 10/100 * max(ε_T).

3.3 Signal filtering

The experimental equipment is provided with a computer and signal processing software developed by the manufacturer - THIOT INGENIERIE. The software contains an option for signals filtering where a "threshold frequency" is selected. In subsequent calculations, the software uses the filtered curves (Fig. 3).

3.4 Signal smoothing by averaging

The recorded signals are available in tabular form through 1 μs. The aim is to suppress unwanted signal fluctuations by averaging adjacent values. Select the *amplitude of averaging A*, μs, and determine *averaging period and frequency*.

$$T = 2A \quad \mu s, (7)$$

$$\nu = \frac{1}{T} \quad Hz, (8)$$

Example: A = 12 μs; T = 2A = 24 μs. ν = 1/ (24.10^{-6}) = 41.7 kHz. These parameters were introduced for comparison with the threshold frequency of the other method (section 3.3).

Formulas for smoothing signals and inverting signs

$$\bar{\varepsilon}_R(t) = -\text{Average}\,\varepsilon_R \begin{pmatrix} t-A \\ t+A \end{pmatrix} \quad (9)$$

$$\bar{\varepsilon}_T(t) = -\text{Average}\,\varepsilon_T \begin{pmatrix} t-A \\ t+A \end{pmatrix} \quad (10)$$

The function *Average* in Excel software is used to find the mean value at moment *t*, as the arithmetic mean of the values in the range from *t–A* to *t+A* inclusive. When processed in Excel tables, the time increases from top to bottom and, therefore, in Eqs. (9) and (10), the later value of the interval is written below. Index *R* refers to reflected pulse, and index *T* refers to the strain pulse transmitted through the sample. In Eqs. 9 and 10, the minus sign satisfies the requirement for stress and strain to be positive in subsequent calculations.

4. Experimental result and discussion

4.1 Recorded signals

The reflected strain pulse and the strain pulse passed through the sample are shown in Fig. 2. The duration corresponds to the 600 mm striker used, and the pulse shape is typical for the used shaper.

Several sharp pulsations of the signals are visible, the most drastic at the moment being 594 μs. These ripples affect 1 to 2 adjacent recorded values. The filtration techniques are mainly used to suppress such pulsations, which are not a property of the material under study, but have an electrical origin.

Before starting the calculations in accordance with Eqs. (1) - (6), the beginning points in the time must be selected, for both signals. The points when $\varepsilon_R(t)$ = 77 μm/m and $\varepsilon_T(t)$ = -27 μm/m were selected, and they are indicated in Fig. 2. The difference between them is 13 μs.

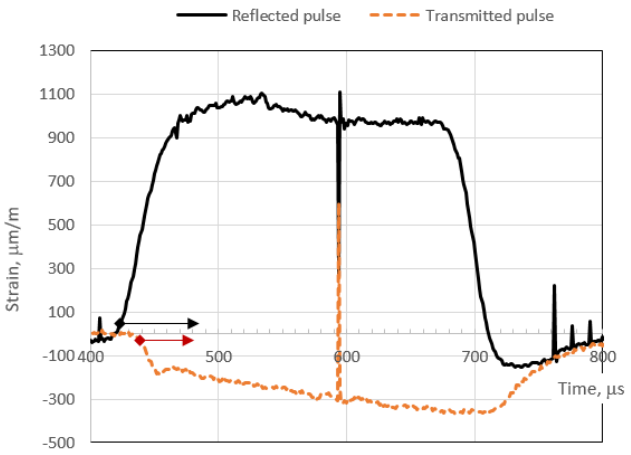

Fig. 2 *Recorded signals*

4.2 Smoothed signals

Figs. 3 and 4 show the signals smoothed by the two mentioned methods: with the built-in the machine's software low-pass filter at a threshold frequency of 40 kHz, and by averaging as described in section 3.4, at A = 12 µs.

The curves are visualised from the selected start times. It can be seen that the curves are smoothed similarly, but differences show that mathematical apparatuses of both methods are different.

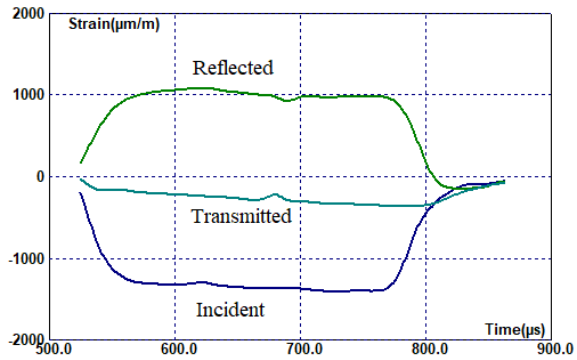

Fig. 3 *Filtered signals, threshold frequency = 40 kHz.*

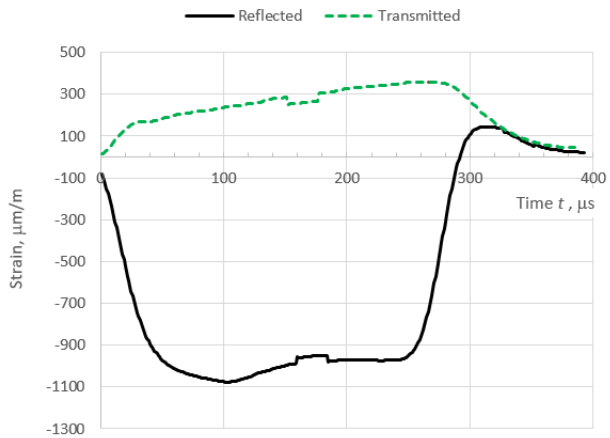

Fig. 4 *Averaged and reversed signals, A = 12 µs.*

4.3 Influence of the size of filtering (averaging) on the final diagram

Figure 5 shows how the selected cut-off frequency of the low-pass filter affects the calculated mechanical diagram.

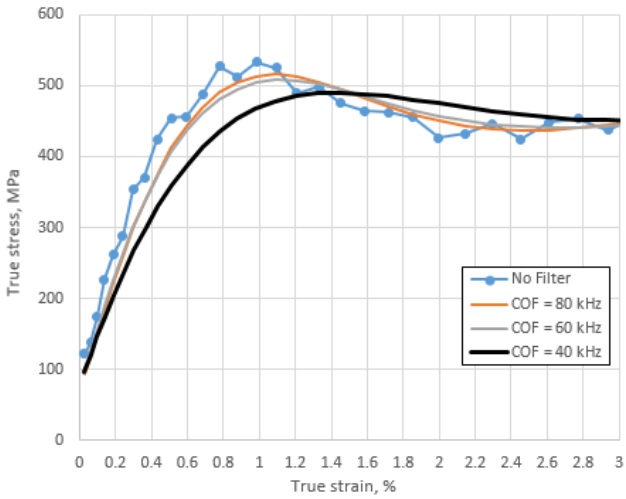

Fig. 5 *Diagrams of the test sample, calculated with the original equipment software at different sizes of filtration (cut-off frequencies: 40, 60 or 80 kHz).*

Fig. 5 shows that a filter with 40 kHz cut-off frequency has a noticeable effect on the initial slope of the curve and the upper yield strength. The reduction is 30% for the elastic modulus and 8% for the upper yield strength.

The elastic modulus is determined according to the average slope of the calculated curve for strain up to 0.2%.

The diagram obtained at 80 kHz is quite close to the raw diagram (obtained without filtering). The reduction in this case is 15% for the elastic modulus and 3% for the upper yield strength.

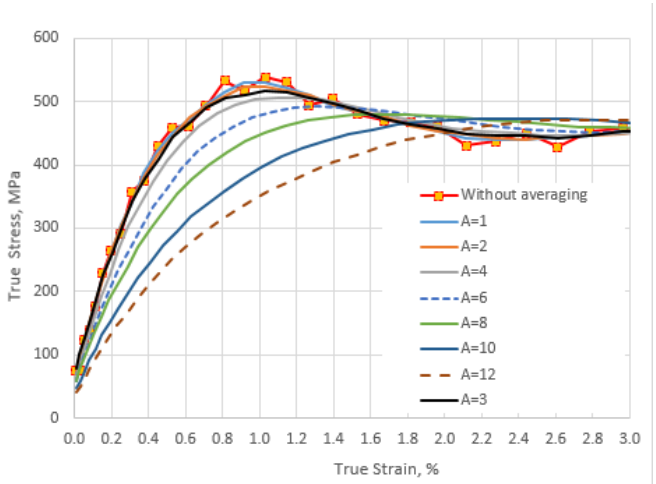

Fig. 6 *Test sample diagrams, calculated in Excel when smoothing signals with different averaging amplitudes.*

From Fig. 6 it is clear that the smoothing of the registered signals by averaging also leads to smoother diagrams and a decrease in the slope and height.

When averaging with an amplitude of 3 µs, the elastic modulus is obtained 6% smaller and the upper yield strength is obtained 4% smaller compared to the same indicators, determined without averaging the signals.

Averaging with an amplitude of 6 μs is similar to filtering with a 40 kHz cut-off frequency.

5. Conclusions

The influence of the amount of smoothing of the registered signals on the calculated diagram of the test body was studied using a Hopkinson-Kolsky bar impact test. Two methods have been used to smooth the signals: a low-pass filtering built into the software and arithmetic mean averaging.

It is shown (Figs. 5 and 6) that stronger smoothing leads to more significant changes in the initial slope of the calculated diagrams. It was found that both methods, filtering with 40 kHz cut-off frequency and averaging with an amplitude of 6 μs, have similar effect over the stress-strain diagram.

We concluded that filtering with a cutting frequency of 60 to 80 kHz and averaging with an amplitude of 3 to 4 μs leads to sufficient smoothing and neglectable deviation from the original (unfiltered) diagram.

6. Acknowledgments

This report is a research result of project BG05M2OP001-1.001-0008 "National Center for Mechatronics and Clean Technologies", funded by the Operational Program "Science and Education for Smart Growth" 2014-2020, co-financed by the European Union through the European Fund for Regional Development.

The authors express their gratitude to Prof. Dr. Dora Karagiozova for her assistance in introduction to the field of studies using Split Hopkinson-Kolsky Bar device.

7. References

1. Z. Li, Y. Wang, X. Cheng, J. Liang, S. Li, Mat. Sc. and Eng.: A, Vol. **772**, 138700 (2020)
2. M. Sedighi, M. Khandaei, H. Shokrollahi, Mat. Sc. and Eng.: A, Vol. **527**, Issue 15, pp. 3521-3528 (2010)
3. T. Zhou, J. Wu, J. Che, Y. Wang, X. Wang, Int. J. of Imp. Eng., Vol. **109**, pp. 167-177 (2017)
4. W. Wang, M. Li, C. He, X. Wei, D. Wang, H. Du, Mater. & Des., Vol. **47**, pp. 510-521 (2013)
5. Q. Fu, M. Bu, W. Xu, L. Chen, D. Li, J. He, H. Kou, He Li, Int. J. of Imp. Eng., Vol. **148**, 103763 (2021)
6. G. Liu, E. Bai, J. Xu, N. Yang, T. Wang, Constr. and Build. Mater., Vol. **261**, 119995, (2020)
7. Y. Guo, S. Xiao, J. Zeng, Yu Zheng, X. Li, F. Liu, Constr. and Build. Mater. **Vol. 260**, 120460 (2020)
8. J. Zhu, C. Sun, Z. Qian, J. Chen, Eng. Fail. Anal. Vol. **18**, Issue 7, pp. 1808-1817 (2011)
9. S. Cao, G. Xue, W. Song, Q. Teng, Constr. and Build. Mater., Vol. **247**, 118537 (2020)
10. X. Chen, X. Shi, J. Zhou, E. Li, P. Qiu, Y. Gou, Int. J. of Mining Sc. and Techn., Vol. **31**, Issue 3, pp. 387-399 (2021)
11. Z. Huang, L. Sui, F. Wang, S. Du, Y. Zhou, J. Ye, Comp. Str. , Vol. **244**, 112300 (2020)
12. S. Feng, Yu Zhou, Yu Wang, M. Lei, Int. J. of Imp. Eng., Vol. **140**, 103558 (2020)
13. R. Zwiessler, T. Kenkmann, M. H. Poelchau, S. Nau, S. Hess, J. of Str. Geol., Vol. **97**, pp. 225-236 (2017)
14. F. Wang, S. Liu, L. Cao, J. of Str. Geol., Vol. **138** , 104095 (2020)
15. J. Chen, H. Wei, K. Bao, X. Zhang, Y. Cao, Y. Peng, J. Kong, K. Wang, J. of Mat. Res. and Techn., Vol. **11**, pp. 170-179 (2021)
16. B. Nurel, M. Nahmany, N. Frage, A. Stern, O. Sadot, Vol. **22**, pp. 823-833 (2018)
17. P. Golewski, T. Sadowski, A. Rusinek, Mater.Today: PROCEED., Vol. **45**, Part 5, pp. 4275-4279 (2021)
18. B. Jia, A. Rusinek, R. Pesci, R. Bernier, S. Bahi, P. Wood, Int. J. of Solids and Str., Vol. **204–205**, pp. 153-171 (2020)
19 Gilat, A., Schmidt, T.E. & Walker, A.L., Exp. Mech., Vol. **49**, pp. 291–302 (2009)
20. M. Ruiz de Sotto, P. Longère, V. Doquet, J. Papasidero, Int. J. of Plast., Vol. **134**, 102777 (2020)
21. W. Chen, Bo Song, *Split Hopkinson (Kolsky) bar. Design, Testing and Applications*, Springer, Boston, MA, ISBN 978-1-4419-7982-7 (2011), p. 388
22. Ramesh K.T. High Rates and Impact Experiments. In: *Sharpe W. (eds) Springer Handbook of Experimental Solid Mechanics*. Springer Handbooks. Springer, Boston, MA. pp. 929-960 (2008)

Consistent Presentation of the Beam Deflection Theory Including Shear Correction

Rumen Krastev
Institute of Mechanics - Bulgarian Academy of Sciences
Email: r_krastev@imbm.bas.bg

Abstract: *This article explains a mathematically consistent approach for solving the equations of Timoshenko's beam theory for statically loaded beams. Theoretic sections 3.4 - 3.5 give a good description of the shear deformation and the primary approach for calculating deflections of beams under bending, taking into account both causes for deflection: bending moment and shear force. Values for the shear correction factor are discussed in section 4. This work was started to check the validity of an equation for deflection of a symmetrically loaded short rectangular beam with span/height ratio = 3 under four-point bending with upper-span/span ratio = 1/3. The exact solution is not presented here, but we can confirm that the presented theory, when applied for the mentioned loading scheme, leads to this equation using a shear correction factor k = 5/6.*
Keywords*: EULER-BERNOULLI, TIMOSHENKO BEAM THEORY, DEFLECTION, SHEAR DEFORMATION, SHEAR COEFFICIENT*

1. Introduction

Many structural members in working conditions are subjected to bending. Usually, the bending is not pure, i.e. the structural element endures both bending moment and shearing force. These internal forces cause deformation of the beam, i.e. its shape changes. The deviation of the centre of a cross-section from its original position is called *deflection*. It is known for slender beams that deflection caused by the shearing force is negligible.

A practical problem for determining the exact deflection of short rectangular beams under four-point bending raises the need to clarify the theory, more precisely, the theoretical base of the following equation, published in standard ASTM C1018-97.

$$f = \frac{23F}{1296EI} l^3 \left(1 + \frac{216(1+\nu)}{115}\left(\frac{h}{l}\right)^2\right) \tag{1}$$

Where f is the deflection of the neutral plane, F is the load, l is the span, E is the estimated elastic modulus, I is the second moment of area, h is the specimen height, and ν is the Poisson's ratio. The mentioned standard is related to the test method ASTM C78 that requires the span length to be three times the specimen depth (l/h = 3) and *upper-span/span* = 1/3.

2. Synopsis of the historical development

An approach is known for calculating the deflection caused by bending moment with main contributors of Jacob Bernoulli, Daniel Bernoulli and Leonard Euler, [1]. When considering deflection of a cantilever beam, loaded at the free end by force F, Euler [1, p. 45] reached the differential equation (2):

$$C\frac{w''}{(1+w'^2)^{3/2}} = Fx \tag{2}$$

Where x is the distance from the point of application of the force to a cross-section under consideration, C is constant, w is the deflection of the centre of the cross-section, $w' = \frac{dw}{dx}$ and $w'' = \frac{d^2w}{dx^2}$.

In the real constructions, small deflections are considered usually. In this case, the rotation angle is minimal, respectively $w' \ll 1$, and for engineering purposes, the simplified equation (3) is solved:

$$Cw'' = Fx \tag{3}$$

Later, Saint Venant carefully considered the hypotheses: 1. the cross-sections in the deformation remain flat, and 2. the adjacent longitudinal fibres do not influence each other, being in a state of tensile or compression [1, p. 164]. He shows that the initially plane cross-sections change their shape due to the tangential stresses acting in the cross-section [1, p. 165]. Saint-Venant has formulated a solution for bending a cylindrical cantilever beam of a constant cross-section by a terminal load [2, p. 316; p. 133].

D. Zhouravski had investigated how shearing stress is distributed by the height of the cross-section and derived a formula for its approximate assessment, see eq. 64 in [3, p. 111-113].

An elementary derivation of the effect of the shearing force on the curvature of the beam has been made by Grashof (1878) and W.J.M Rankine (1895), [2, p. 31].

J.W. Raleigh investigated vibrations of strings, rods, membranes, plates and shells. The author demonstrates some properties that an engineer can extract from the application of *generalised forces* and *generalised coordinates*. The idea of calculating frequencies directly from the energy condition without solving differential equations was subsequently developed by Walter Ritz. The *Rayleigh-Ritz method* is now widely used not only in the study of oscillations but also in solving problems of the theory of elasticity, theory of structures, not linear mechanics and other branches of physics, [1, p. 404].

In the early 20th century, S.P. Timoshenko proposed an approach as an adjunct to the Euler-Bernoulli theory in order to take into account the effect of the transverse force on the transverse vibrations of a cantilever beam [4]. According to it:

$$\frac{dw}{dx} = \varphi + \gamma \tag{4}$$

$$M = -EI\frac{d\varphi}{dx} \tag{5}$$

$$Q = kGA\gamma \tag{6}$$

Where φ is the angle of rotation of the cross-section due to the bending moment M, γ is the angle induced by the tangential force Q, EI is the flexural rigidity of the cross-section, A is the cross-section area, G is the shearing modulus of elasticity and k is "a constant which depend on the cross-section", [4]. This coefficient is introduced because the tangential stress is not distributed evenly along with the height of the cross-section. As it is well known, the tangential stress is zeroth at the upper and lower edge of the cross-section, and it is greatest near the neutral plane. The angle γ can be eliminated from Eqs. (4) and (6):

$$Q = kGA\left(-\varphi + \frac{dw}{dx}\right) \tag{7}$$

In his work [4], Timoshenko analyses the system of equations (5) and (7) in order to determine the effect of tangential force on the frequency of transverse vibrations of a rectangular beam.

In the textbook [3], Timoshenko presents eq. (6) otherwise:

$$\frac{dy_1}{dx} = \frac{cQ}{GA} \tag{8}$$

Where y_1 is *deflection due to shear* and respectively $\gamma = dy_1/dx$. The coefficient c is explained as "a numerical factor with which the average shearing stress (Q/A) must be multiplied in order to obtain the shearing stress at the centroid of the cross-section", [3, p. 170]. This definition "has been clearly shown to give unsatisfactory results" [5], but the main equations (3)-(7) are still applicable.

Many articles are aiming more precise definition for the shear coefficient and its determination. Based on the Jouravski's formula, one technique is published in the textbook [6] and is presented below in this article.

From the comparison of Eqs. (6) and (8) it can be seen that

(9) $$k = \frac{1}{c} = \frac{Q}{GA\gamma}$$

It should be noted that the term "shear correction factor" is not clearly defined. In most articles, [5, 10, 15 etc.], we could see that it refers to coefficient *k* and eq. (6), but in other works, [6, 11], it refers to the factor *c* and eq. (8). One should use some published shear coefficient with a clear idea for its proper place in the equation.

Most of the textbooks explain well how to calculate the deflection caused by the bending moment - "Euler-Bernoulli Method". However, the deflection caused by the tangential force is not commented or is indicated that it is negligible for long (slender) beams. For example, standard EN ISO 178, [7] requires the use of long specimens, with a *span/height* ratio = 16 for usual specimens. However, for tick fibre-reinforced specimens this ratio should be = 60; for thin specimens – it should be = 8, and for flexible materials it should be = 32.

When we need to work with short beams, the question about the magnitude of the tangential deflection cannot be neglected! Textbooks like [8] and [19] do not explain the Timoshenko beam theory.

There is a significant interest about vibrations of Timoshenko beams in several conditions, [10-15] etc. However, the mathematical apparatus in these publications is too complicated and it is not suitable for easy understanding and assessment of shear deflection of statically loaded beams.

Recently, Ke Gong [20], Ghugal et al. [21] suggested new theories about the deflection of thick beams.

With the purpose of clarifying and gathering on one place these accomplishments, there is a consistent presentation below of the static beam deflection theory, including shear correction.

3. Theoretical approach

3.1 Scheme and coordinate system

Consider a horizontal beam, somehow fixed in space and loaded with forces and distributed loads. We use a coordinate system with the *x*-axis to the right, *y* to us and *z* – downward (Fig. 1). We consider a situation in which the loads are directed in the vertical direction *z*.

3.2 Load and support reactions

The equilibrium conditions of the beam are considered. From these equations are find the support reactions, i.e. forces and moments at the anchorage points, depending on the loads applied to the beam.

3.3 Internal forces in the beam

The beam is divided into segments, with borders - where there is a concentrated load or at the ends of the distributed loads. These segments are examined sequentially. For each segment, a mental cut is made through the beam at a distance *x* from the end of the beam. Fig. 1 illustrate a beam segment under distributed load, mentally cut at distance *x*.

By applying the equilibrium conditions, we find the dependences of the tangential force Q_z on x and the bending moment M_y on *x*. The following dependencies apply in all cases:

(9) $$\frac{dQ_z}{dx} = -q(x)$$

(10) $$\frac{dM_y}{dx} = Q_z(x)$$

Here, q is the load distributed on the beam. For example, the load by the weight of the beam.

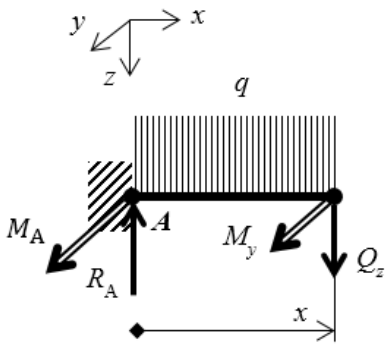

Fig. 1 *beam section under distributed load, fixed in point A and mentally cut at distance x.*

Equation (9) shows that the distributed load (in the *z*-direction) causes a tangential force in the beam. Concentrated forces cause the tangential force to jump in the applied points, so these points should be the boundaries of the segments considered.

The tangential force causes a bending moment in the beam, according to Eq. (10).

3.4 Deformation of the beam

The centre line of the beam in question coincides with the *x*-axis initially. The deformed state of the beam is described by the equation of the elastic line $w(x)$, which indicates the deflection, i.e. displacement of the centres of the cross-sections in the *z*-direction.

It is known that bending moment causes bending (flexure) of the beam, which changes its shape. This is expressed by a change in the slope and position of the cross-sections under consideration in the plane *xz*, Eq. (5).

It is known that tangential force causes a tangential displacement between adjacent cross-sections of the beam, increasing the rotation of the cross-sections by an angle γ, Eq. (6).

Timoshenko considers the bending as a sum of two components, Eq. (4). In integral form, the overall deflection also has two parts: deflection due to bending moment and deflection due to shear force.

(11) $$w = w_M + w_Q$$

Bernoulli-Euler's theory only considers deflection caused by the bending moment, and the second component is neglected. This is acceptable for slender beams.

3.4.1 Deflection due to bending moment

The bending moment M_y causes an elastic bending and rotation of the beam, which, for small deflections, is described by the equation:

(12) $$EI\frac{d\alpha}{dx} = M_y(x)$$

Where: $d\alpha$ is the angle between two initially collinear cross-sections, on a distance dx from each other, E – elastic modulus of the material, I – area moment of the cross-section. The solution of the differential equation (12) gives the angle of rotation α of the cross-section under consideration, generated by the bending moment, depending on the position *x* of the section.

Deflection of a section under consideration depends on its slope: $dw_M/dx = -\mathrm{tg}(\alpha)$. At small angles $\alpha \cong \mathrm{tg}(\alpha)$ and deflection due to bending moment can be sought according to equation (13):

(13) $$\frac{dw_M}{dx} = -\alpha(x)$$

After the determination of the internal forces, by integrating Eqs. (12) and (13) one can find the deflection caused by the change in beam shape due to the bending moment.

(14) $$w_M(x) = -\int \alpha(x)dx$$

3.4.2 Deflection due to shear force

The tangential force Q_z causes a displacement of adjacent cross-sections in a tangential direction, known as shearing or sliding. It is known that tangential stress has some distribution $\tau_{xz}(y,z)$ over the cross-section – Fig. 2 B). However, if we do not know the exact distribution, or it is too complicated, we could use a simplified - rectangular distribution of the stress (or average shear stress):

(15) $$\tau_R = \frac{Q_z}{A}$$

in combination with some correction factor. Here A is the cross-sectional area. In this case (of rectangular distribution), for the elastic angular deformation of an elementary volume with thickness dx, the Hooke's law is:

(16) $$\frac{Q_z}{A} = -G\gamma = G\frac{dw_Q}{dx}$$

Where G is the shear modulus of elasticity and dw_Q is the tangential displacement between the two sides of this volume. These ideas are visualised in Fig. 2. The angle γ presents the difference between deformed shape by Q (DS Q) and un-deformed shape by Q (UDS Q). The angle γ here is assumed as negative and therefore (-γ) is positive when $Q_z > 0$. This section is in equilibrium because the shearing force generates a bending moment, $dM_y = Q_z dx$, but near cross-sections hold it.

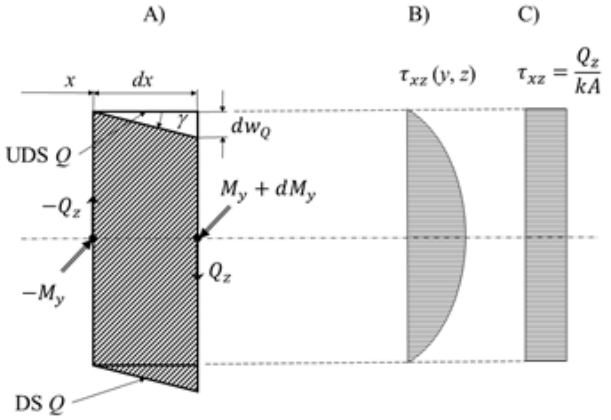

***Fig.2** Simplifying the scheme for shearing. A) Angular deformation of cross-section by transverse shear force. B) Real distribution of the shear stress. C) An assumption for simplified and corrected – rectangular distribution of the shear stress.*

In his paper [4], S.P. Timoshenko does not discuss a hypothetic rectangular distribution that should generate the same deflection as the actual distribution of tangential stresses. However, he introduced a correction factor k (Shear correction factor, Timoshenko shear coefficient) in Eq. (6). It takes into account the fact that used average shear stress (Q_z/A) must be corrected so that it has the same effect as the actual distribution of the stress (as shown in Fig. 2 C).

In the present work, the shear force is considered as known, and the shear displacement is sought:

(17) $$\frac{dw_Q}{dx} = \frac{Q_z(x)}{kGA}$$

Shearing deflection of a beam with variable cross-section is found by solving Eq. (18):

(18) $$w_Q(x) = \int \frac{Q_z(x)}{kGA(x)}dx$$

When considering beams with constant cross-section and using eq. (10), the equation (19) holds:

(19) $$w_Q(x) = \frac{1}{kGA}M_y(x) + C$$

Therefore, the sag pattern is similar to the bending moment diagram for beams with a constant cross-section. The integration constant C is determined according to a known boundary condition.

3.5 Calculation of the shear correction factor

For beams subjected to bending, in the Timoshenko's equation (6), the Q/A ratio represents some mean tangential stress of the section. However, it is known that the actual tangential stress is zero at the upper end and at the lower ends of the section, and it is maximal at the neutral line. To express the dependence of the tangential stresses τ_{xz} on the coordinate (height) z, for a cross-section of arbitrary shape, one usually uses the approximate formula proposed by D. Zhuravskii:

(20) $$\tau_{xz} = \frac{Q_z S_y(z)}{b(z).I_y}$$

Where:

Q_z – Shear force for the cross-section under consideration with coordinate x,

I_y – The second area moment with regard to y-axis.

$b(z)$ – Length of the dense part of the cross-section with coordinate z. For a rectangular section, b is constant.

$S_y(z) = \int_z^{zc} z.dA$ – Static moment of the dense part of the cross-section, bounded by the straight-line $b(z)$ and the outer contour (zc) of the cross-section.

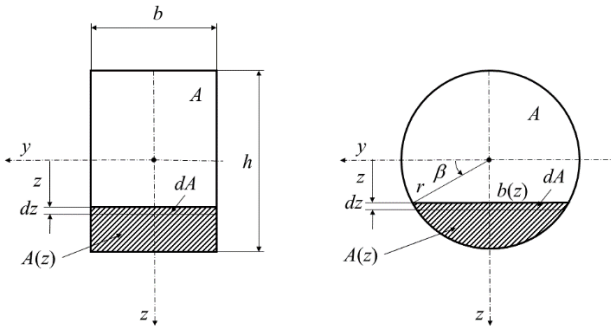

***Fig. 3** Schemes for rectangular cross-section and circular cross-section, explaining the variables in Zhuravskii's formula and Eq. (23), [6, p. 295].*

If we consider a hypothetic situation in which the tangential force is evenly distributed in a cross-section with area A and thickness dx, then the accumulated (specific) potential energy in this section would be:

(21) $$\frac{dU_Q}{dx} = \frac{Q_z^2}{2GA}$$

When considering the same cross-section, but using a distribution of the shear stress according to the Zhuravskii's formula, then this potential energy is given by Eq. (22), [6, p. 294]:

(22) $$\frac{dU_Q}{dx} = \frac{cQ_z^2}{2GA}$$

Formula (23) is obtained for the correction coefficient c.

(23) $$c = \frac{A}{I_y^2}\int_A \frac{S_y^2(z)}{b^2(z)}dA$$

As it was stated above, the static moment is calculated for the dense part of the cross-section bounded between line $b(z)$ and the outer contour.

The correction coefficient *c*, obtained by Eq. (23), could be used in Eq. (8) and other related equations. If one prefers to use the original definition of the Timoshenko's correction factor, Eq. (9) will help.

3.5.1 Correction coefficient for rectangular cross-section

We consider a rectangular section of width b and height h, [6, p. 295] and apply Eq. (23):

$$A = bh,\ I_y = \frac{bh^3}{12},\ b(z) = const.$$

$$S_y(z) = b\left(\frac{h}{2} - z\right).\left(\frac{h}{2} + z\right)/2,\ dA = bdz$$

(24) $$c_{\blacksquare} = \frac{144.bh}{b^2h^6}\,2\int_0^{h/2}\frac{b^2}{4b^2}\left(\frac{h^2}{4} - z^2\right)^2 bdz = \frac{6}{5} = \frac{1}{k_{\blacksquare}}$$

3.5.2 Correction coefficient for circular cross-section

We consider a circular cross-section of radius *r*, [6, p. 295] and find the shear correction factor by Eq. (23):

$$A = \pi r^2, I_y = \pi r^4/4, z = r\sin\beta, b(z) = 2rcos\beta,$$

$$S_y(z) = \frac{2}{3}r^3cos^3\beta,\ dA = b(z)dz = 2r^2cos^2\beta d\beta$$

(25) $$c_{\odot} = \frac{16}{\pi r^6}\,2\int_0^{\pi/2}\frac{1}{9}r^4cos^4\beta.2r^2cos^2\beta d\beta = \frac{64}{9\pi}\frac{5}{16}\frac{\pi}{2} = \frac{10}{9} = \frac{1}{k_{\odot}}$$

4. The shear correction factor, according to some authors

There are other suggestions in the literature for these coefficients, which have been obtained when considering hypotheses for a more complex and probably more accurate distribution of the tangential force in the cross-section.

According to Cowper [16], the shear correction factor for rectangular cross-section depends on the Poisson's ratio in conformance with Eq. (26) and for circular cross-section – by Eq. (27).

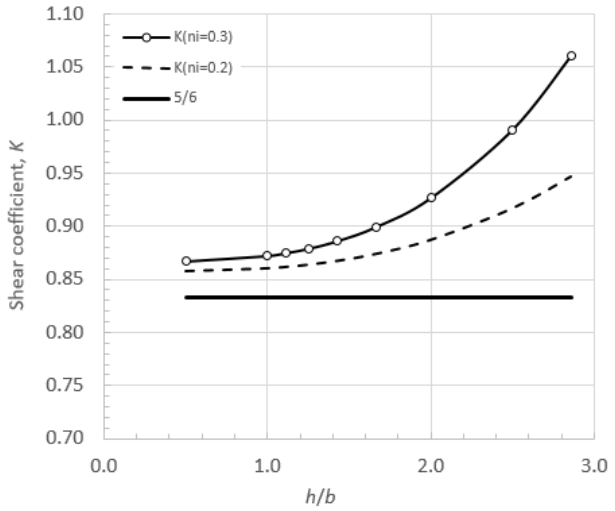

(26), (27) $$k_{\blacksquare} = \frac{10(1+\nu)}{12+11\nu} \qquad k_{\odot} = \frac{6(1+\nu)}{7+6\nu}$$

Fig. 4. *The shear coefficient for rectangular cross-section depends on the shape (h/b) and on the Poisson's ratio.*

More precise values for the shear correction factor of rectangular and circular cross-sections are suggested by Kaneko [17]:

(28), (29) $$k_{\blacksquare} = \frac{5+5\nu}{6+5\nu} \qquad k_{\odot} = \frac{6+12\nu+6\nu^2}{7+12\nu+4\nu^2}$$

For circular cross-section Stephen [5] gives Eq. (29). However, for rectangular cross-section, the chosen distribution of the stress is more complicated and Stephen obtained a relationship [5] that depends not only on the Poisson's ratio but also from the aspect ratio (h/b , height/width). It is shown in Fig. 4 for two typical values for Poisson's ratio and is compared there with the reference coefficient k = 5/6. According to this relationship, $k_{\blacksquare}$ = 0.860 for material with $\nu = 0.20$ and square cross-section.

5. Conclusion

This article explains a mathematically consistent approach for solving the Equations (4), (5), (6) in Timoshenko's beam theory. It is based on separate integration of both terms in the right side of eq. (4). In this integration, the functions for the bending moment and shear force are used.

Theoretic sections 3.4 - 3.5 give a good description of the shear deformation and the theory for calculating deflections of beams under bending, taking into account both causes for deflection: bending moment and shear force. Fig. 2 visualises the shear-deflection and shear-correction method in a new way.

This work has been started with an aim to check the validity of Eq. (1). An exact solution is not presented here, but we can confirm that the presented here theory leads to this equation for short rectangular beams with shape as specified in the mentioned standards and subjected to four-point bending when a shear correction factor k = 5/6 is accepted.

The Stephen's approach suggests probably more accurate value for mortar and concrete: $k_{\blacksquare}$ = 0.860 for materials with $\nu = 0.20$ and square cross-section.

6. References

1. S.P. Timoshenko, *History of Strength of Materials*. State publ. house for technical-theor. Literat. Moscow. (1957) (in Russian)
2. S.P. Timoshenko, J.N. Goodier, *Theory of Elasticity*. McGraw-Hill Book company Inc, (1951).
3. S.P. Timoshenko *Strength of Materials. Part I. Elementary theory and problems*. Publ. D. van Nostrand company. II ed. (1948)
4. S.P. Timoshenko, Phil. Mag. **41**, 744-746 (1921).
5. N.G. Stephen, J. Appl. Mech. *Mar*., **47** (1): 121-127 (1980)
6. I. Kisiov, *Strength of materials, III ed*. Technika. (1963) (in Bulgarian "Съпротивление на материалите")
7. EN ISO 178:2019. *Plastics – determination of flexural properties*
8. G.M. Gere, B.G Goodno, *Mechanics of materials 8-th ed., SI.* Cengage Learning (2013)
9. S.P. Mandgakov, Mandichev GI, Veselinov KV et. al. *Collection of Problems and Methodological Guidelines on Strength of Materials*. Ed. by S.P Nedelchev. Technika. (1989) (in Bulgarian "СБОРНИК от задачи и методически указания по съпротивление на материалите")
10. K.T. Chan, K.F. Lai, N.G. Stephen, K. Young. J. of Sound and Vibr. **330** (14), pp. 3488-3497 (2011)
11. H. Hadavinia, K. Gordnian, J. Karwatzki and A. Aboutorabi, SDHM, **2** No 4, pp.197-206 (2006)
12. N.G. Stephen, J. of Sound and Vibr. **292**, pp. 372–389 (2006)
13. X.-F. Li, J. of S. and Vibr. **318** No 4-5, pp. 1210–1229 (2008)
14. Jae-Hoon Kang, J. of Sound and Vibr. **333** No 14, pp. 3332–3337 (2014)
15. Marie Brons, J.J. Thomsen, J. of Sound and Vibr. **459**, 114856 (2019)
16. G.R. Cowper, J. Appl. Mech., **33** No 2, pp. 335–340 (1966)
17. T. Kaneko, J. Phys. D (Appl. Phys.) **8,** No 16, pp. 1927-1936 (1975).
18. A. Dı´az-de-Anda, J. Flores, et al., J. of Sound and Vibr. **331,** No 26, pp. 5732–5744 (2012)
19. T.H.G. Megson *Aircraft Structures for engineering students. IV ed*. ELSEVIER (2007)
20. Ke Gong, Appl. Math. and Mech. (Engl. Ed.), **21**, No 9 pp. 1091-1098 (2000)
21. Yuwaraj M.Ghugal, Rajneesh Sharma, Lat. Amer. J. of Solids and Structures, **8,** No 2, pp. 183 – 195 (2011)

Nanosized ZnO and ZnO@zeolite composite prepared via sonication method

Gospodinka Gicheva, Neli Mintcheva, Marinela Panayotova
University of Mining and Geology "St. Ivan Rilski", Sofia, Bulgaria
g.gicheva@mgu.bg

Abstract: *ZnO nanosized materials are well known for their photocatalytic and antibacterial properties. Their implication in water treatment and environmental protection, especially as a part of composite materials, has been an object of study of a great number of researchers working in the field. Zeolites are excellent candidates for support of composites preparation with semiconductor oxides since they are non-hazardous, non-expensive and naturally abundant materials. In order to synthesize nanosized ZnO with well-developed surface area and uniform size distribution in pristine form and supported on zeolite, we applied the method of precipitation assisted by sonication. As prepared ZnO nanoparticles and the composite ZnO-zeolite were characterized by XRD, SEM and UV-Vis spectroscopy. The ZnO crystalized in wurtzite structure in both materials. The morphology of ZnO nanoparticles was affected by the zeolite framework, as in the composite the ZnO was formed in-situ at the presence of zeolite. The ultrasonic irradiation during the precipitation of $Zn(OH)_2$ and aging of the reaction mixture causes activation of the zeolite surface and prevents the aggregation of ZnO particles. In result evenly distributed ZnO nanoparticles were obtained in the composite.*

Keywords*: ZnO NANOPARTICLES, SYNTHESIS, NANOCOMPOSITES, ZEOLITE*

1. Introduction

Zinc oxide (ZnO) is well-known and widely used material as an active ingredient in paints, plastic, cosmetics, medicine (common brand name(s): Aquaphor, Balmex, Medi-Paste, etc). It is a II-VI semiconductor with energy band gap of ~3.3 eV at room temperature. ZnO is non-toxic and non-expensive material which makes it very convenient for a large scale application. With the intensive development of nanotechnologies, ZnO found some new areas of application by using its nanosized form, namely ZnO nanoparticles (ZnONPs). Based on the fact that by changing the morphology, surface area, particle size and distribution, the properties of the same chemical compound can be varied, the antibacterial [1,2,3] and photocatalytic properties [4,5] of ZnONPs as well as their application for solar cells fabrication [6,7] have been extensively explored.

Promising results in each of the listed areas have been reported so far. Beek et al. [6] have described new hybrid bulk-heterojunction solar cells based on nanocrystalline ZnO with 5 nm diameter as the n-type semiconductor, which were prepared via hydrolysis and condensation of zinc acetate dihydrate. The ZnO nanoparticles were dispersed in a semiconducting polymer thus forming the active layer of the solar cell. This model cell demonstrated up to 40 % conversion of solar energy into electrical current proving the effectiveness of synergism of organic and inorganic materials in photovoltaics.

The photocatalytic activity of ZnONPs have been studied for years and the research is still ongoing due to the promising results. Weerathunga et al. [5] showed very interesting results from their latest study which suggests a relationship between the morphology of ZnO nanoparticles and their photocatalytic activity. Three types of shapes (rods, plates and cones) have been tested in the reaction of benzyl alcohol oxidation. The experimental data revealed that ZnO nanocones resulted in higher benzyl alcohol conversion compared to nanorods and nanoplates. This was explained by the crystal structure of ZnO nanocones and the orientation of undercoordinated O atoms towards the species in reaction medium. The authors are hopeful that their findings will provide useful insights how to optimize reaction conditions in other heterogeneous photocatalytic reactions involving oxidation reactions activity.

The antibacterial activity of ZnO is another area of interest of researchers. Bhuyan et al. [**Грешка! Показалецът не е дефиниран.**] used 25% (w/v) of *Azadirachta indica (Neem)* leaf extract for biosynthesis of ZnO nanoparticles. They tested the antibacterial and photocatalytic activity of ZnO obtained. By shake flask method different concentrations of ZnO nanoparticles (20 mg/mL, 40 mg/mL, 60 mg/mL, 80 mg/mL and 100 mg/mL) were used against Gram-positive and Gram-negative bacteria: *Staphylococcus aureus, Streptococcus pyogenes* and *Escherichia coli*. The authors found that increase in nanoparticle concentration leads to decrease in bacteria growth and Gram-positive bacteria were more sensitive to ZnO nanoparticles than Gram-negative bacteria. As an additional benefit, biosynthesized ZnO nanoparticles demonstrated activity in the photocatalytic degradation of methylene blue (MB) under the UV light.

Other authors also reported biosynthesis using plant extract for nanosized ZnO preparation. [8, 9, 10]. Salam et al. [10] have showed the synthesis of ZnONPs using *Ocimum basilicum L. var. purpurascens Benth.-Lamiaceae* leaf extract and zinc nitrate. The obtained ZnONPs had hexagonal (wurtzite) shape and size about 50 nm.

Other widely applied method for preparation of ZnONPs is by precipitation reaction under ultrasonic irradiation that allows a control over the size and morphology of the formed nanoparticles. This fact is of significant importance because some studies suggest that photocatalytic properties of ZnO strongly depend on their morphology [**Грешка! Показалецът не е дефиниран.**,11,12]. The effect of ultrasonic irradiation was confirmed by other research teams as well [13]. Meronia et al investigated an ultrasound-assisted synthesis of ZnO-based photocatalysts for the removal of NOx. They found enhanced surface area under sonication in comparison with samples from conventional synthesis. . The main experimental parameter affecting the structure of obtained ZnONPs was pH and the reaction temperature, as both influenced the precipitation of $Zn(OH)_2$ and its subsequent conversion to ZnO phase. Other important founding was that the counter-ion in the zinc precursor influence the morphology (star-shaped, flower-like, platelets), as well as the surface area [13].

In order to improve the antibacterial and photocatalytic properties of ZnONPs some authors suggest to immobilize the ZnO onto a support aiming a synergetic effect of action and easier recovery of the nanocomposite material. Zeolite is very beneficial support for ZnONPs because zeolite itself is used in water treatment as a sorbent and ion exchanger [14,15]. Shaw et al., demonstrated the efficiency and specificity of ZnO-zeolite core-shell composite in the removal of heavy metal ions and organic pollutants in neat, multi and mixed system [14]. It was established that the adsorption by the nanocomposite follows the order Pb(II) > Fe(III) > Cd(II) and MB dye > p-nitrophenol > Aniline. In addition, it was also demonstrated that the adsorption on zeolites is slower chemisorption compared to the faster physi-chemisorption in core-shell particles contributing to the rapid and enhanced adsorption posessed by the composite. ZnO-zeolite has also proven to be very effective photocatalyst and a multifunctional adsorbent with high specificity towards Pb(II), Fe(II), MB dye and p-nitrophenol.

For preparation of nanocomposite materials containing ZnONPs the ultrasonication method was chosen by researchers [16]. Heidaria et al. [17] used sonoprecipitation for in-situ preparation of Zn-zeolite nanocomposites resulting in novel ZnO nanorods over ion

exchanged clinoptilolite. This material was found to be efficient catalyst for the photocatalytic degradation of the drug furosemide (FRS). The higher surface area of the composite resulted in an enhanced photocatalytic activity in comparison to pristine ZnONPs prepared by conventional precipitation method. By means of various analytical methods (TEM, EDX, BET, UV-visible spectroscopy techniques, XRD, etc.) it was shown that the average particle size of ZnO in ZnO/clinoptilolite composite prepared by sonoprecipitation was 20.5 nm, while without sonication the size increased up to 34.8 nm. Aside from that, the sonication of the reaction mixture during the precipitation process prevented the agglomeration of nanoparticles. The effects of different parameters such as amount of ZnO on the zeolite, catalyst dosage, initial FRS concentration, pH of reaction media on the photocatalytic degradation were investigated.

ZnO-based composites are also known for their antibacterial properties against bacterial growth in wastewater.

Having in mind the above-described we have decided to use natural zeolite clinoptilolite for immobilization of ZnO and to study the potential of composites obtained for reduction of organic pollutants and inhibition of bacterial growth in wastewaters. In order to synthesize nanosized ZnO with well-developed surface area and uniform size distribution in pristine form and supported on zeolite, we applied the method of precipitation assisted by sonication. The present paper describes the preparation of ZnO nanoparticles and composite ZnO-zeolite and the characterization of as prepared materials by XRD, SEM and UV-Vis spectroscopy. The physicochemical parameters of these materials were examined and compared in respect to their morphology, composition and nanoparticles distribution.

2. Materials and methods

Zinc acetate dihydrate ($Zn(CH_3COO)_2 \cdot 2H_2O$) was purchased by Merck KGaA, sodium hydroxide (NaOH) from Valerus, Bulgaria. All reagents were used without any further purification. A natural zeolite (clinoptilolite) from the region of East Rhodopes, Bulgaria, was washed and modified by turning it to its sodium form, by placing the clinoptilolite in contact with 2 M NaCl as described in our previous paper [18]. The ultrasonic bath (SIEL UST7.8-200, with an ultrasound energy of 250 W) was used to generate the ultrasonic waves in the reaction mixture. The crystalline structure of the samples was determined by X-ray diffraction (XRD) Empyrean (PANalytical). UV–vis Diffuse Reflectance Spectroscopy (DRS) analysis was carried out on an Evolution 300 UV-Vis Spectrophotometer (Thermo Fisher Scientific), at room temperature in the wavelength range of 200–1100 nm). Scanning electron microscopy (SEM) was performed on JEOL 6390 и INCA Oxford element analyzer.

2.1 Synthesis of pristine ZnO nanoparticles by sonication

The experimental setup used is shown in Fig. 1. ZnO nanoparticles were synthesized by precipitation reaction between zinc acetate solution and sodium hydroxide solution under ultrasound irradiation. Overall amount of 12.5 cm^3 NaOH solution (0.1M) and 6.5 cm^3 $Zn(CH_3COO)_2$ solution (0.1M) were simultaneously added dropwise to a 50 cm^3 pure water and mixed under constant sonication for 30 min to form a precipitate. Prior to mixing of both solutions, the flask was immersed in the ultrasonic bath. . The resulting dispersion containing ZnONPs went further aging process for 1 h at 80°C under sonication, after that the precipitate was filtered and washed with distilled water several times. The product was dried for 12 h at 120 °C and the resulting ZnONPs were further analyzed.

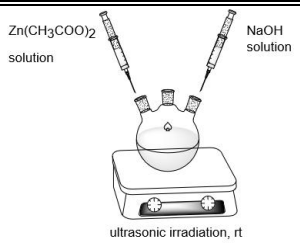

Fig. 1 *Schematic representation of experimental setup for ultrasonic synthesis of ZnONPs and ZnO-zeolite nanocomposites.*

2.2 Synthesis of ZnO-zeolite nanocomposite by sonication

ZnO-zeolite nanocomposite was prepared following the above described procedure and experimental setup shown inFig.1. Sodium form of clinoptilolite with a mass 0,5 g was dispersed in 60 cm^3 distilled water and sonicated for 15 min for surface groups activation. After that following the previously described procedure, 62.0 cm^3 NaOH solution (0.1M) and 31.0 cm^3 $Zn(CH_3COO)_2$ solution (0.1M) were added dropwise to the zeolite dispersion under constant ultrasonic irradiation for 30 min. The resulting reaction mixture was left to age for 1 h at 80 °C under sonication, after that the precipitate was filtered and washed with distilled water several times. The nanocomposite product was dried for 12 h at 120 °C and the resulting ZnO-zeolite was further analyzed.

3. Results and discussion

3.1 Materials characterization

We have successfully prepared ZnONPs and ZnO-zeolite nanocomposite by controlled precipitation reaction between $Zn(CH_3COO)_2$ and NaOH solutions under ultrasonic irradiation of the reaction mixture. The XRD crystalline analysis (Fig. 2) of the composite material confirmed the formation of ZnO nanoparticles with hexagonal wurtzite structure. The XRD patterns revealed that clinoptilolite was the major crystalline phase (82 wt.% clinoptilolite) and some cristobalite (2 wt.%) also existed as a naturally occurring inclusion. The ZnO phase was detected by its low intensity peaks showing that ZnONPs are part of the composite material. The percent of ZnO determined was 16 wt.%. The XRD data indicated that clinoptilolite is monoclinic phase, cristobalite is tetragonal and ZnO nanoparticles have hexagonal wurtzite structure.

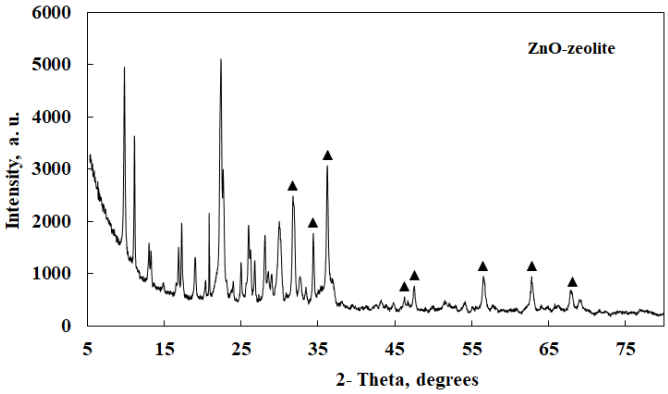

Fig. 2*. X-ray diffraction patterns of ZnO-zeolite nanocomposite. The peaks of ZnO phase are denoted with a black triangle. Detailed XRD analysis revealed the following composition: 82% clinoptilolite , 16% ZnO - and 2% cristobalite -.*

The surface morphology of ZnONPs and ZnO-zeolite nanocomposite was studied by SEM. Selected images of both materials are shown in Figure 3. SEM analysis revealed that the

ZnO has a flake like morphology (Fig. 3a). The nanocomposite ZnO-zeolite demonstrated that ZnO is evenly distributed onto the zeolite surface and the average size of the particles is about 100 nm (Fig. 3b).

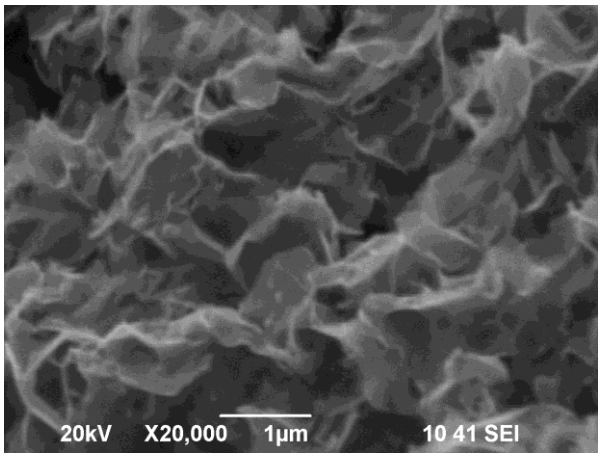

(A)

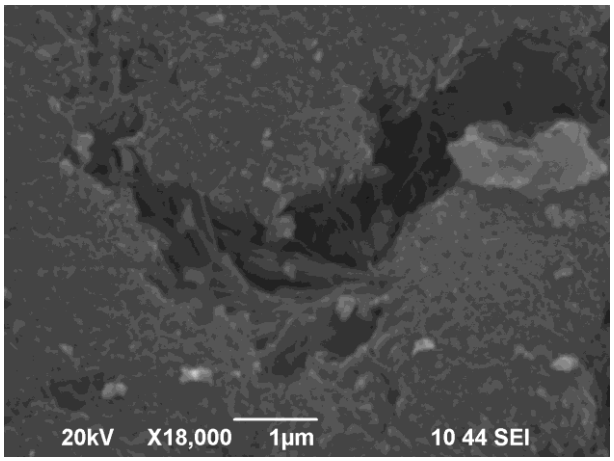

(B)

***Fig. 3**. SEM images of sample of ZnONPs (A) and ZnO-zeolite nanocomposite (B).*

The SEM images strongly suggest that the presence of zeolite affects the formation and morphology of ZnO nanoparticles loaded on zeolite. In the case of ZnONPs, a flake-like nanomaterial (Fig. 3a) was obtained and in the case of ZnO-zeolite, when the zeolite was present in the reaction mixture spherical shaped nanoparticles were formed.

The results from EDX elemental analysis were summarized in Table 1. The estimated element composition in ZnO-zeolite nanocomposite revealed a ratio Al:Si equal to 1:5 that is typical for the studied natural clinoptilolite. The high percent of Zn (30.73) suggest that not only ZnO present but also Zn^{2+} ions might be exchanged with the zeolite prior precipitation and remained in the zeolite. .

***Table 1:** Element composition (in wt. %) of ZnO-zeolite nanocomposite as determined by EDX probe.*

Elements	O	Al	Si	K	Zn
ZnO-zeolite	39,71	4,66	23,63	1,26	30,73

Another evidence for Zn^{2+} ion exchange is the fact that no Na^{+} ions were detected by EDX. It is because the Na^{+} ions had been replaced by Zn^{2+} ions. It is also possible the Zn^{2+} ions adsorbed on the zeolite to react with OH^{-} ions from solution to form $Zn(OH)_2$ which further converts to ZnO nanoparticles that indicates the active role of zeolite support in the formation of ZnONPs on the zeolite surface.

UV–vis Diffuse Reflectance Spectroscopy analysis was carried out to characterize the optical properties of ZnO-zeolite composite. The spectrum is shown in Fig. 4. The weak band at 257 nm is due to zeolite framework and it originated from the charge transfer from O^{2-} to Al^{3+} ions at specific locations such as surface defects, corners, etc [19]. The intensive band at 360 nm is assigned to ZnO nanoparticles and confirms the nanosized ZnO on the clinoptilolite [20].

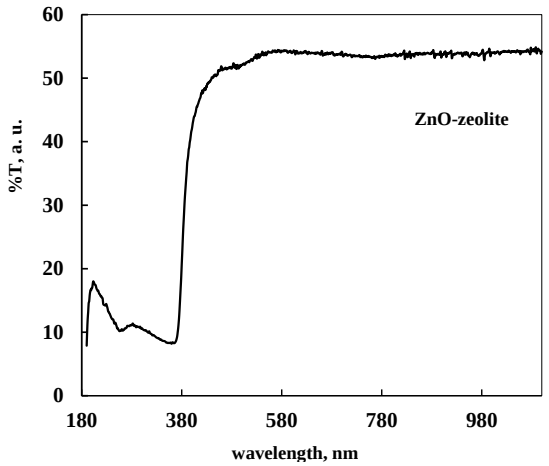

***Fig. 4**. UV–vis Diffuse Reflectance Spectrum of ZnO-zeolite nanocomposite.*

4. Conclusions

We have successfully prepared ZnO nanoparticles and ZnO-zeolite nanocomposite via precipitation reaction of $Zn(CH_3COO)_2$ and NaOH solution under ultrasonic irradiation. The XRD analysis confirmed that ZnO nanoparticles in the nanocomposite have hexagonal wurtzite structure.

The SEM images revealed different morphology of the prepared ZnONPs and ZnO-zeolite. The ZnONPs have flake-like shape while ZnO nanoparticles in the nanocomposite are spherical with average size of 100 nm. This observation suggests that zeolite plays an active role in the process of formation and nucleation of ZnONPs. The EDX element analysis showed an absence of Na^{+} ions suggesting that they had been replaced by Zn^{2+} ions. It suggested electrostatic interaction or partial coordination bonding between the active sites in zeolite and ZnO nanoparticles in the composite.

In conclusion, the obtained ZnO-zeolite nanocomposite may be considered as a promising candidate material for water treatment. Such materials will be further tested for their photocatalytical and antibacterial activity.

4. Acknowledgements

The authors express gratitude to The Bulgarian National Science Fund (BNSF) for the financial support under Project DN-17/20.

5. References

1. A. C. Janaki, E. Sailatha, S. Gunasekaran, Spectrochim Acta A, 144, 17 (2015)

2. M. Sundrarajan, S. Ambika, K. Bharathi, Adv Powder Technol ., 26(5), 1294 (2015)

3. T. Bhuyan, K. Mishra, M. Khanuja, R. Prasad, A. Varma, Mater Sci Semicond Process, 32, 55 (2015)

4. S. Dey, S. Das, A. K. Kar, Mater. Chem. Phys., 270, 124872 (2021)

5. H. Weerathunga, C. Tang, A. J. Brock, S. Sarina, T. Wang, Q. Liud, H. Zhu, A. Du, E.R. Waclawik, J. Colloid Interface Sci., 606(1), 588 (2022)

6. W. J. E. Beek, M. M. Wienk, R. A. J. Janssen, Adv.Mater, 16(12), 1009 (2004)

7. M. Saeidi, M. Abrari, M. Ahmadi, *Appl. Phys. A* **125,** 409 (2019).

8. F.T. Thema, E. Manikandan, M.S. Dhlamini, M. Maaza, Mater. Lett., Volume 161, 24 (2015)

9. G. Yashni, A. Al-Gheethi, R. M. S. R. Mohamed, N. Vo Dai-Viet, A. A.Al-Kahtani, M. Al-Sahari, N. J. N. Hazhar, E. Nomand, S. Alkhadher, Chemosphere, 281, 130661 (2021)

10. H. A. Salam, R. Sivaraj, R. Venckatesh, Mater. Lett, 131, 16 (2014)

11. S.R. Veerabhadraiah, S. Maji, A. Panneerselvam, J. Cryst. Growth, 14, 126430 (2021)

12. Z. Sharifalhoseini, M. H. Entezari, R. Jalal, Ultrason Sonochem 27, 466 (2015)

13. D. Meronia, C. Gasparini, A. Di Michele, S. Ardizzone, C. L. Bianchi, Ultrason Sonochem 66, 105119 (2020)

14. R. Shaw, T. Mittal, S. Tiwari, S. K. Tiwari, J. Environ. Chem. Eng. 6, 1424 (2018)

15. V. R. Batistela, L. Z. Fogaca, S. L. Fávaro,W. Caetano, N. R. Camargo Fernandes-Machado, N. Hioka, Colloids Surf. A: Physicochem. Eng. Asp. 513, 20 (2017)

16. X. Li, H. Li, X. Wang, D. Xu, T.g You, Y. Wu, F. Xu, Int. J. Biol. Macromol. 183, 760 (2021)

17. Z. Heidaria, R. Alizadeha, A. Ebadia, N. Oturan, M.A. Oturan, M. Sep. Purif. Technol., 242, 116800 (2020)

18. M. Panayotova, N. Mintcheva, G. Gicheva, L. Djerahov, N. Mirdzveli, Proceedings of 20th International Multidisciplinary Scientific GeoConference SGEM 2020, Albena, Bulgaria, 18 - 24 August 2020; p. 77-84

19 I. Rodríguez Iznaga, V. Petranovskii, G. Rodríguez Fuentes, C. Mendoza, A. Benítez Aguilar, J. Colloid Interface Sci. 316, 877 (2007).

20 T.B. Ivetic, M.R. Dimitrievska, I.O. Guth, Lj.R. Dacanin, S.R. Lukic-Petrovic, J. Phys. Res. 36 (1), 43 (2012)

Technology for production of technical products with fixed thickness and made of quartz ceramics by means of a moulding matrix with a silicone insert

Gabriel Peev, Lyuben Lakov, Gergana Mutafchieva*, Mihaela Aleksandrova
Bulgarian Academy of Sciences, Institute of Metal Science, Equipment, and Technologies with Center for Hydro- and Aerodynamics "Acad. A. Balevski", cl.creativeline@gmail.com

Abstract: *Molding of technical products with fixed thickness by casting quartz ceramics, based on pure quartz glass, requires specific technological regulations both in the preparation of the ceramic mass and in the process of molding itself. Due to the specific characteristics of the colloidal system such as low shrinkage and viscosity, casting in molds made only of gypsum is practically unworkable. A solution lies in developing a technology in which the dismantling of the die is supported so that the molded product can be easily removed. Proposed here is a gypsum mold developed in such a way that a silicone insert is mounted where the lower part of the cast product will be. The technological process presented here in detail includes the main stages of preparing a model according to pre-set parameters, making a gypsum mold consisting of two-parts and with a silicone insert, casting and high-temperature synthesis of the finished product made of quartz ceramics. The development is suitable for complex and large-size technical products made not only of quartz ceramics, but also of other silicate colloidal systems characterized by low and almost zero air shrinkage.*
Keywords*: QUARTZ GLASS-CERAMICS, SILICONE MOULD, INOVATIVE QUARTZ CERAMIC'S MOULDING*

1. Introduction

The development refers to the moulding of technical products with fixed thickness, for which there exist specific requirements for thermal resistance. Presented below are all the stages of the whole technological process: development of constructive documentation for building a model, taking into account the shrinkage of the material; preparing the complete moulding equipment which consists of a gypsum mould and a silicone insert; moulding of the product; high-temperature synthesis and finally, obtaining a finished product. As an example, we present a product with thick walls and with a certain depth, shaped as a truncated quadrangular pyramid with external dimensions of 205 x 105 h x 75 mm and wall thickness of 16 mm. The product is a refractory container used in the synthesis and melting of high-temperature steels. Other suitable examples are the production of equipment for pouring receivers (cups and crucibles) for steel melts, as well as saggars for the synthesis of zirconium cermets. The ceramics from which these products are made must meet certain requirements such as resistance to high-temperature shock, refractoriness and resistance to aggressive metals. One of the best ceramics meeting the above requirements is quartz glass ceramics. The refractory vessel can be developed from two products – mullite quartz and quartz ceramics. In the present study we consider the technological process of casting the second product. The casting of products with a complex shape from pure quartz glass ceramics requires a precise and specific technological process for their preparation, depending on the indicators and characteristics of the used ceramic composition in a colloidal state. An aqueous colloidal system based on amorphous SiO_2 from ground quartz glass consisting of two fractions in a 1:1 ratio a) 0.3-0.15 mm and b) <125 μm is used. Homogenization and grinding is carried out by wet mixing in a mill unit (ball mill) by a single-stage technique in the conditions of an exothermic process, in which higher indicators of the final suspension are achieved. In the process of obtaining an aqueous colloidal system of quartz glass powders, the water exerts an active surface influence on the amorphous SiO_2 . In order to obtain a suspension with low humidity, an additional 5% of the powder mixture is added to the aqueous colloidal mixture 3–4 times before the final completion of the processes in the system, the process of stirring and final grinding taking approximately 2 hours. As a result of the water grinding of the quartz powders, a specific surface of 600–900 cm² per g is achieved. Initially, 25% distilled water is added to the system, and at the end of the process the amount of water is reduced to 22%. The duration of the water grinding before the additional activation with small portions of powder is 25–26 h. The resulting suspension quickly shapes the body of the raw product, and the products have a low shrinkage – up to 0.05%. The activation of the system is associated with the hydration of SiO_2 and the formation of surface tetrahedra due to the coupling of solid particles of SiO_2 with ionized silicic acid which is obtained in the process of the water grinding with water playing an active role. An important requirement in the preparation of the slip is to monitor the pH of the suspension, where the optimal pH value is 4.5. Adjustment of the pH is done using HCl for lowering and VH_4 OH for raising it. The high-temperature synthesis is performed at a temperature from 1,230°C to 1,260°C [1-2]. In the experimental part we present a modern technology for moulding ceramic products, whose mould includes a silicone insert in addition to the gypsum part. The approach is entirely innovative due to the specific behavior of the particular ceramic material in the process of slip casting, as the gypsum mould avoids absorbing the water contained in the material.

2. Experiments

The experimental part includes several main stages, starting with the preparation of instrumental equipment and ending with the moulding and high-temperature synthesis of technical products made of quartz glass ceramics. The first step in the preparation of the instrumental equipment is the compiling of technical documentation that specifies the entire set of the necessary parameters relating to products made of special ceramics. Figure 1 shows a cross section of the refractory vessel, subject to the present development, with specific parameters excluding compressibility.

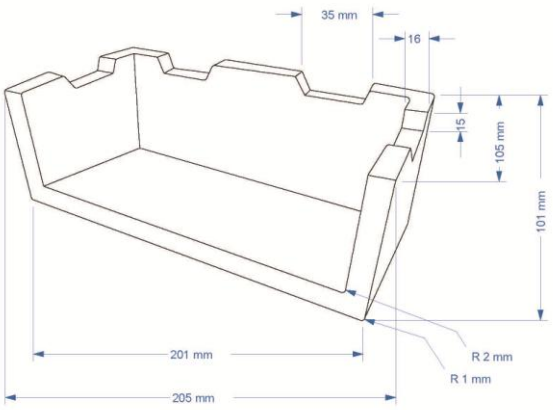

Fig. 1. *Cross section of a fixed-thickness refractory container for melting high-temperature steels. The set parameters refer to the finished product, to which should be added an increase relative to the mass used, which for quartz ceramics is 0.2%.*

After the requirements regarding the dimensions and the compressibility relative to the mass used are specified, the process of making the actual model with the necessary magnification is started. The next stage is preparing the moulding equipment – a gypsum mould with a silicone insert – which is the main tool in the moulding process. The material used for the model and the base of the casting mould is moulding gypsum, a hemihydrate with the chemical formula CaSO45H2O mixed during casting in a weight ratio of dry matter to water of 1:1.5 [3]. The silicone insert uses a

two-component elastomer ZA22 by the Italian company Zhermack, with polymerization at room temperature and a Shore A hardness of 22. The characteristics of the material depend on the properties of the product in the course of all processes after vulcanization [2]. Among the main properties of ZA22 are high chemical resistance to aggressive components; high tensile strength and high elasticity; high reproduction accuracy, listed in detail in Table 1 [6].

Table 1: *Chemical and physical properties of the silicone elastomer used in the making of the polymer insert in the casting mold.*

Mixing ratio	1 : 1
Viscosity of pre-catalyzation mixture	4000 ± 300 cP
Density of the Base component (g/cc)	1,13
Density of the Catalyst component (g/cc)	1,13
Colour	Blue
Working time at 23 °C (73 °F)	WT=14' – 17'
Setting time at 23 °C (73 °F)	ST= 60
Vulcanized product:	
Shore A hardness after 24 hours	21 ± 2 ShA
Breaking load	4.0±0.2 N/mm2
Elongation at break	380 ± 20 %
Tear strength	>20 N/mm
Reproduction of details	2 µm
Dimensional variation after 24 hours	< 0.05 %

An elastomer with suitable hardness was selected according to the Shore durometer, which refers to the stability of the polymers subjected to plastic deformation. The elastic performance of the silicone used allows flexible disassembly without tearing either the insert itself or the moulded product [4-5].

The making of a model depends on the shape and cross-section of the product as set in the drawing. In the case of the refractory container, the model is made by hand in several stages. Specific for products with a fixed thickness is that the model must match on its inside the shape of the finished product, as opposed to those with an arbitrary thickness. For this purpose, a negative auxiliary part is initially made, through which the core is formed. The auxiliary part is machined according to all the necessary slopes and set radii, so that after casting the base, no subsequent work on the inside of the model will be required. The outer contour with the set obligatory thickness (in this case 16 mm + 0.2% increase to take into account the shrinkage of material at high temperature) is enclosed around the core and prepared for casting. The model is given a final shape externally according to the slopes and the set radii, after which the casting mould can begin to be made.

The making of a two-part gypsum mould with a silicone insert begins with the first gypsum part, which forms the outer part of the product, and the sprues. The first part also serves as a base on which an auxiliary plate will be built together with the model. This plate will subsequently shape the silicone insert and determine its thickness according to the necessary technical parameters. It should be of equal thickness of approx. 7 mm, except for technological slopes for disassembly, so that the product can be removed without a problem. The second gypsum part occupies the space above the auxiliary base and it is a required mould thickness which is of approx. 35 - 40 mm for technical products. After the second part of the mould is ready, the auxiliary plate is removed and in its place is poured elastomer using the pourers additionally formed in it. It is desirable, after homogenizing the two components of the polymer, to perform a deaeration in a vacuum environment. The time required for complete vulcanization of the silicone is not longer than 24 hours, after which the material acquires all the necessary elasticity and strength. Figure 2 shows the parts of the mould die together with the silicone insert.

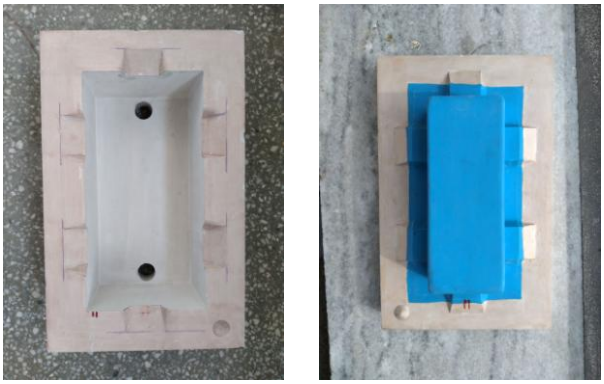

Fig. 2. *Two-part gypsum mould with silicone insert. The first part, together with the sprues, forms the outer shape of the moulded article, while the silicone insert forms the inside.*

3. Conclusion

A successful experiment was performed using an innovative approach for moulding a technical product with a fixed thickness made of quartz glass ceramics. The topical importance of the development is twofold. Firstly, it lies in the authors' original recipe composition of an aqueous colloidal system of ground quartz glass based on amorphous SiO_2 , which allows the finished products to meet the specific requirements for thermal stability at high temperature. The low shrinkage of 0.2% and the water saturation of the suspension of 22%, in turn, requires the development of a specific process to facilitate the moulding stage, which leads to the second main innovative feature – the development of a gypsum mould with a silicone insert. The use of elastomer for the moulding parts for casting ceramic products is not a common practice due to the high water content in the ceramic colloidal compositions and the requirements for water absorption by the matrix mould. The selected polymer meets the necessary conditions after its complete vulcanization and especially those for elasticity, due to the depth of the final product and the relatively small degree of internal slopes. Figure 3 shows the final result for three samples of a refractory container after high temperature synthesis at 1,250°C and retention at a final temperature for 60 minutes.

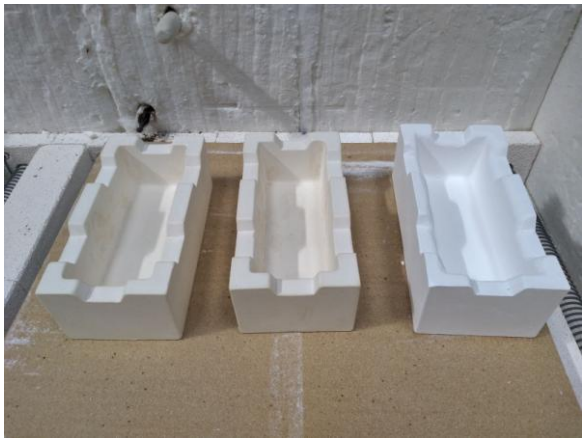

Fig. 3. *High temperature synthesis of technical products with fixed thickness – refractory containers made of quartz glass ceramics, moulded in a gypsum mould with a silicone insert.*

The experimental development shows the successful realization of thick-walled deep products made of special ceramics with low air shrinkage and moisture content of the initial mass. The study may be applicable to all similar masses meeting these requirements.

Acknowledgement

The authors are grateful to the financial support of the Bulgarian National Science Fund at the Ministry of Education and Science, Contract No КП-06-ОПР 03/4 14.12.2018, for carrying out the necessary research.

4. References

1. Gerasimov E., A. Gerasimov, A. Atanasov, V. Toshev, D. Petkov, D. Ivanov, L. Georgieva, L. Pavlova, H. Drenska, P. Vinarov, P. Petrov, S. Bachvarov, S. Panova, S. Bagarov, S. Serbezov, S. Stefanov, S. Dzhambazov, T. Stojkova, T. Datskova, H. Berlinov., *Technology of Ceramic Products and Materials*, Edited by Prof. Bachvarov S. (Saraswati press, Sofia 2003), pp 889-995.

2. Callister, William D., D. G. Rethwish., *Materials Science and Engineering: an introduction*, **8th** (Wiley 2009), pp588-600.

3. Mutafchieva, Gergana., L. Lakov., M. Aleksandrova., *Silicate Design of Hollow Ceramic Book to Illustrate Scientific and Secular Events*, NDT **IV** (2021), pp 286-287.

4. Tahir, Irfan., *Development of Silicone Mold Tool for Injection Molding Plastic Parts*, Degree of Master of Science in Mechanical Engineering University of Minnesota (2020), pp 6-8.

5. Mutafchieva, Gergana., *Modern Trends and Development of Lighting Fixtures in the Field of Silicate Design*, (National Academy of Arts Sofia, section Porcelain and Glass 2020, pp 100-116

6.https://www.zhermack.com/en/product_category/industrial/mould-making-industrial-en/master-mould/

Physicochemical and technological researches of marls from the area of the village Lovets related to the production of the new "Yellow paving stones"

Lyuben Lakov, Gergana Mutafchieva*, Gabriel Peev, Mihaela Aleksandrova , Bojidar Jivov
Bulgarian Academy of Sciences , Institute of Metal Science, Equipment, and Technologies with Center for Hydro- and Aerodynamics "Acad. A. Balevski", cl.creativeline@gmail.com

Abstract: *Due to force majeure circumstances, new researches of marls from the Alexandra deposit to the village of Lovets (Shumen region) were carried out to replace the marls from the village Svetlen (Targovishte region), which are part of a plastic mass for the production of large, fine-ceramic parts (yellow paving stones) from peturgical phases. Marls are characterized in terms of mineral and chemical composition. Their properties, characterizing them as a ceramic raw material, have been determined. Three test masses with a chemical composition similar to the one with the participation of marls from the village of Svetlen were developed. The test specimens are characterized in terms of sintering and strength characteristics. It has been established that the marls can be used to repla ce the marl from the village Svetlen in the composition of the plastic fine-ceramic masses for the production of yellow pavers.*
Keywords*: MARBLE CLAYS, NEW YELLOW COATS, PHYSICOCHEMICAL STUDIES OF MARBLE*

1. Introduction

Due to the bankrupt of the company "Rodna Industria" Popovo, using the concession of the marl deposit in the village Svetlen in obligations to the state, insolvency and lack of prospects for future cooperation, it was necessary to urgently conduct current research to find new alternative raw materials.

2. Representation

Both the marl from the village Svetlen and the marl from the village Lovets are used for coarse ceramic products - bricks. As marls are suitable for the production of high quality majolica tiles, they can easily be used as a raw material for the production of fine ceramic products, because clay marls contain a larger amount of fine fractions than typical brick clays [1]. The carbonates in the marls are more evenly distributed. Table 1 shows the chemical composition of marl from the village Lovets, and Figure 1 shows a radiograph of the raw material and the content of mineral phases in it. Table 2 presents the grain size distribution in% by weight.

Table 1: *Chemical composition of marl clay from the Alexandra deposit, Lovets village*

Composition	Quantity %
Na_2O	0,7
MgO	2,24
Al_2O_3	11,36
SiO2	35,19
$P2O_5$	0,1
K2O	2
CaO	19,58
TiO_2	0,47
MnO	0,11
Fe_2O_3	4,85
LOI	23,21
Σ	99,82
Cu	0,06
Zn	0,073
Sr	0,053

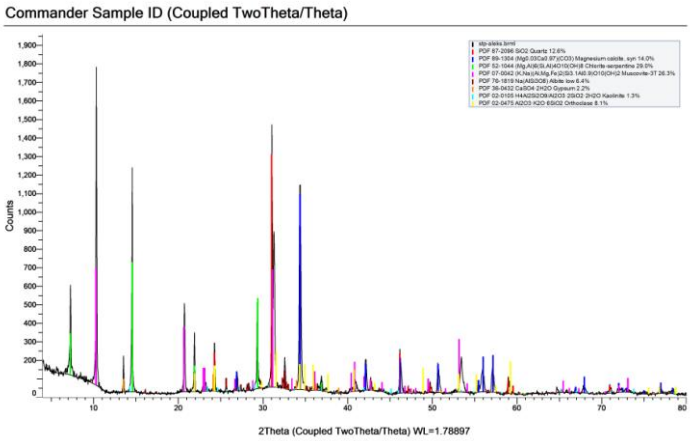

Fig. 1. *Phase analysis of dried marl clay from the village of Lovets at t =1140°C and retention at a final temperature of 80 minutes.*

Table 2: *Grain size distribution of marl clay as a percentage of particle size.*

Grain size distribution	Weight %
Faction under 0,005	45
Faction 0,005 - 0,05	42
Faction over 0,05	13

According to the standards, the studied clay belongs to the marls of group III - acidic below 15% Al_2O_3 high-carbonate, over 17 - 18% alkaline earth oxides and high content of coloring Fe_2O_3 - over 3%. According to the classification of Sitin, the clay marl used by us from the area of the village Lovets, the amount of alkaline earth oxides is 21.82% by weight. This implies a relatively narrow firing interval and difficulty in obtaining fine ceramic products. The DTA curve of marl showed a characteristic endoeffect at 800°C associated with the decomposition of $CaCO_3$ and $MgCO_3$. The weight reduction is 22.57%, which coincides with the determined by chemical analysis A.L.(annealing losses). 23.71%. From the DTA curve shown in fig. 2, it has surprisingly been found that the melting interval begins with the appearance of small amounts of liquid phase as early as approximately 1000°C before the actual melting point at 1137-1140°C. This suggests that a practical temperature regime for marl firing could be established.

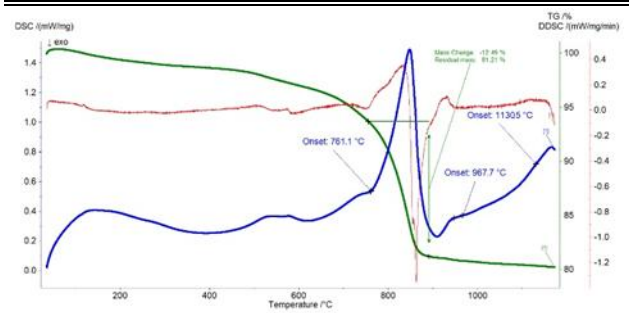

Fig. 2: *DTA-DSC analisys of the test samples*

X-ray phase analysis shows that marl contains, in addition to calcite ($CaCO_3$), chloride, mica such as musk quartz, feldspar, plagioclase, gypsum and kaolin. The content of clay substance is in accordance with the fractional composition (fraction below 0.005 - 45%) fig. 1.

Marl has the following properties, characterizing it as a ceramic raw material:

- Normal molding humidity - 20.5%;
- Plasticity according to Pfefferkorn - 29%;
- Critical humidity - 17.3%;
- Coefficient of sensitivity to drying - 0.18.

The clay marl used in plastic plastics has a favorable high critical humidity and is slightly sensitive to drying. This is in accordance with its mineral, chemical and fractional composition, which determines a simplified drying regime and the possibility of forming according to the classical technologies of ceramic technology. The recipe composition of the working tables used is presented in Table 3.

Tabl. 3. *Prescription composition of working tables*

Raw materials	Composition of test masses by weight %			
Marl from the village of Lovets	25	30	30	30
Fireclay from marl in the village of Lovets	55	55	60	70
Washed kaolin, dried at 120°C	20	15	10	-

The calculated chemical composition of the test masses is given in Table 4.

Tabl. 4. *Prescription composition of work tables*

Оксиди	M1	M2	M3	M4
Na_2O	0,60	0,66	0,67	0,70
MgO	2,16	2,14	2,14	2,24
Al_2O_3	12,60	13,00	13,10	11,36
SiO_2	41,30	39,98	40,10	37,19
P_2O_5	0,07	0,072	0,73	0,10
K_2O	1,80	1,85	1,90	2,00
CaO	16,70	17,32	19,30	20,58
TiO_2	0,33	0,34	0,34	0,47
MnO	0,10	0,11	0,11	0,11
Fe_2O_3	4,75	4,80	4,83	4,85
A.L.	19,425	20,90	21,00	20,21
Cu	0,05	0,06	0,06	0,06
Zn	0,066	0,069	0,068	0,073
Sr	0,049	0,051	0,052	0,053
	100,00	100,00	100,00	100,00

Slips with a humidity of 60% are prepared from the work tables. The plastic mass for the test samples was obtained by dehydrating the slip in gypsum forms to normal molding humidity, which for all four masses was 22%. The obtained samples from the plastic masses are tiles with dimensions 56.5 x 56.5 x 5.65, dried to a residual humidity of 2-3%.

The properties of the obtained water-dispersed colloidal systems (slips) are presented in Table 5.

Tabl. 5. *Properties of the four slips obtained from clay*

Properties	M1	M2	M3	M4
Liter weight g/l	1490	1485	1480	1492
Viscosity, Pas	2,30	2,25	2,23	2,22
Dry matter in the dispersed system , kg/l	0,80	0,79	0,78	0,77
Sieve residue in the sieve 0.063 mm g / l	0,09	0,10	0,11	0,25

The firing mode is determined by the DTA curve and is as follows: heating rate 3°C / minute; delay at 112°C and 148° C for 30 minutes; retention at 576°C, 687°C and 800°C - 20 minutes and retention at final temperature 1130°C - 60 minutes. The cooling rate is 3°C / minute and a hold at 576°C and 687°C for 30 minutes.

The results of the degree of sintering of the test samples up to 1160°C are presented in Table 6, and the mineral phases in the synthesized mass sample №4 are presented in Figure 3.

Tabl. 6. *Characteristics and degree of sintering of the test specimens at three temperature processes*

Maca	T°C calcination	contrastility	Water absorption	Appearant density
M1	1000	5,0	22,0	1,70
	1130	7,0	12,0	1,72
	1160	8,0	0,2	1,85
M2	1000	6,5	24,5	1,65
	1130	7,9	0,06	1,67
	1160	melt	0,0	-
M3	1000	6,0	20,2	1,63
	1130	8,0	0,04	1,65
	1160	melt	0,0	-
M4	1000	7,1	14,8	1,80
	1130	8,4	0,02	1,85
	1160	melt	0,0	-

Samples of mass M4 at annealing temperature of 1130°C and mass M1 at annealing temperature of 1160°C are best sintered, in

which the water absorption is 0 and 0%, respectively, and the apparent density of both samples is 1.85 g / cm³

The higher content of $CaCO_3$ reduces the viscosity of the mass during sintering, respectively the interval of sintering. The M4 mass burns the fastest and at the lowest temperature, which is due to the larger amount of melt formed. At a temperature of 1130°C the water absorption is 0%, but the baking interval - 15/20°C is the narrowest.

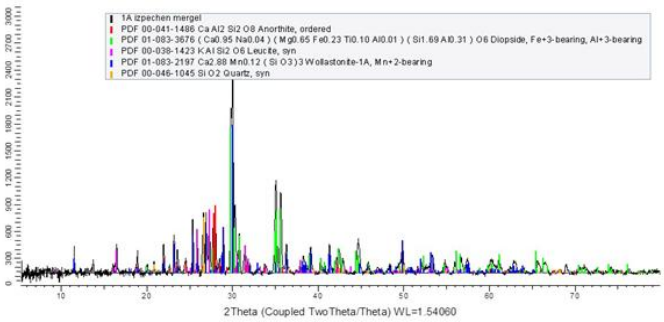

Фиг. 3. *Radiograph of a high-temperature synthesized sample of mass №1 shows the presence of peturgical phases anortite and diopside, which predetermine the good physico-chemical and mechanical parameters of the finished products shown in table. 7.*

The strength characteristics of the samples of test masses M1, M2, M3 and M4 are presented in Table 7.

Tabl. 7. *Compressive strength and bending strength of test specimens at different temperatures*

Indicators	M1	M2	M3	M4	T°C firing temperature
compressive strength, MPa	800 1000 1200	900 1100 -	950 1150 -	1000 1250 -	1000 1130 1160
Bending strength, MPa	116 140 460	120 400 -	125 420 -	140 470 -	1000 1130 1160

3. Conclusion

The results of the research confirm the possibility of using the marl from the Alexandra deposit to the village of Lovets, Targovishte district. However, the use of marl clay from this deposit requires a change in the technological process, which is the main goal in the present development.

Acknowledgement

The authors are grateful to the financial support of the Bulgarian National Science Fund at the Ministry of Education and Science, Contract No КП-06-ОПР 03/4 14.12.2018, for carrying out the necessary research.

All equipment and experimental units used in this work was funded by the European Regional Development Fund within the OP "Science and Education for Smart Growth 2014 - 2020", project CoE "National center of mechatronics and clean technologies", № BG05M2OP001-1.001-0008-C08

References

1. Gerasimov, E., Bachvarov, S., at al, "Technology of ceramic products and materials", 2003, Sarasvati, Handbook, ISBN 954-9841-15-4.
2. Berger, I. at al, "Freiformen und freidrehen, Handbuch der keramik, Gruppe ID2.7. Freburg.V. Schmid, 1991.
3. Bachvarov. S., at al, "Guide for laboratory experiments on the silicate technology", Handbook, pp159-192.
4. Lipinski, F. Das Keramische Laboratorium, Verlang Knapp, Halle (Saale), 1969.
5. Callister, William D., D. G. Rethwish., Materials Science and Engineering: an introduction, 8th (Wiley 2009).

Технологични особености при получаване на компакти от алуминиеви сплави

Доц . д-р Ангел Великов, гл. ас. д-р Цветан Точев, гл .ас .д-р Веселин Петков

Институт по металознание, съоръжения и технологии с Център по хидро- и аеродинамика „Академик Ангел Балевски“, Българска академия на науките

Резюме: Разработена и изработена е специализирана пресформа за компактиране на стружки. Създадена е технология за компактиране, включваща вариране на температурата на пресформата, обмазки, скорост и усилие на пресата при едностранно и двустранно пресоване и др .Изработени са компакти от четири вида алуминиеви сплави.

Ключови думи*: алуминиеви сплави, стружки, компактиране, пресформа.*

Technological features in the production of compacts from aluminum alloys

Assoc. Prof. PhD. Angel Velikov,
Senior assistant, PhD. Tsvetan Tochev, Senior assistant, PhD Veselin Petkov

Institute of Metal Science, Equipment and Technologies “Akad. A. Balevski“ with Hydroaerodynamics Center - Bulgarian Academy of Sciences

Abstract: A specialized pressing mold for chippings compaction has been developed and made. Compaction technology has been created, including variation of the pressing mold temperature, coatings, speed and force of the press in one-sided and two-sided pressing, etc. It has been made compacts of four types of aluminum alloys.

Key words: *aluminum alloys, chippings, compaction, pressing mold.*

1. Въведение

Алуминиевият материал може да бъде произведен по два начина: от първично или вторично производство. Вторичното производство е процес от рециклиране на алуминиеви отпадъци [1,2]. Технологията за рециклиране е способна да спести производствени разходи. Почти 95% от енергията може да бъде спестена от технологията за рециклиране от колкото при първичното производство[3]. Вторичното производство включва процеса претопяване, но като проблем трябва да се отчете по-високите загуби на материал [4]. Известен е екологичният проблем, който създават отпадъците от механичната обработка на метали и сплави. Тези отпадъци са основно във вид на стружки. За индустрията отдавна има няколко проблема с преработката на алуминиевите стружки, тъй като са обемисти и трудни за транспортиране. Също така е трудно да се премахне охлаждащата течност, която машините използват по време на обработката на материала.

Преработката на тези стружки се извършва основно чрез претопяване. Тази технология, обаче, е икономически неизгодна поради високата си енергоемкост и неефективност, тъй като голяма част от стружките изгарят в процеса на леене. Изгарянето от своя страна се дължи на интензивното окисляване при високите температури на топене поради голямата повърхност на стружките. За да се избегнат загубите от изгаряне се прилага брикетиране на стружките [5].

Брикетирането се използва повече от 50 години, като технологията се е развила значително през годините. Първите брикетиращи машини са големи и с високи разходи за поддръжка [6]. Днес системите за компактиране са надеждни, ефикасни, високо производителни и икономични. Брикетирането е процедура която компресира алуминиевите стружки в компактни и лесни за обработка кръгли блокове [7]. То намалява загубите на метал при претопяване, но пък увеличава енергийните разходи при преработката на отпадъчните стружки, а от там и икономическата рентабилност на процеса. Брикетите са с правилна форма, размер и тегло и така те са лесни за подреждане и транспортиране.

Процесът на директното рециклиране на алуминиеви стружки и скрап е екологично решение, което свежда до минимум проблема с разходите за обработка. За да се получат най-високи качества на продукта от директния метод за рециклиране трябва да се обмислят няколко фактора по време на обработката . Стружките се получават най-често от процесите струговане или фрезоване. Почистването на стружките е процес, който ги подготвя за метода на директното рециклиране (брикетиране). Те обикновено са замърсени от смазочно-охлаждащите течности, които се използват по време на машинната обработка. Емулсията може да бъде отстранена по термичен или химичен начин [8,9]. ϖ Термичен метод за почистване на алуминиеви стружки На всяка термична почистваща система целта е да се отстранят органичните съединения от повърхността на стружката, така че, когато материалът бъде брикетиран, да се постигнат най-добри качества на продукта [10,11].

Химическото почистване е процес, който основно използва химически разтвори за отстраняване на повърхностните окиси от алуминия . Тази почистваща операция често се извършва като: баня с натриева основа (NaON) при 65-77°C, изплакване с гореща вода, накисване в хромова киселина и изплакване с гореща вода. Почистените алуминиеви стружки се сушат при температура 80-100°C в пещи и се съхраняват в сушилни .

2. Разработка на конструкция и технология

Компактирането на алуминиеви стружки е процес, при който с прилагане на натиск върху матрица се получава определена форма на заготовката, с плътност, порьозност и уплътняване . Съществуват два начина за компактиране – студено и горещо.За осъществяване на гореказания процес е конструирана специализирана пресформа (фиг.1).

Фиг. 1. Специализирана пресформа

Пресформата се състои от вътрешен (работен) пресечен конус, който има проходен отвор с размер 40 мм. Върху конуса е монтирана втулка, чието предназначение е стабилизиране и уякчаване на работния възел. Към така изработената пресформа са приспособени два броя поансони- горен и долен, за да има възможност за едностранно или двустранно пресоване. Пресформата е съоръжена с нагревател, с цел осъществяване на процес на компактиране при повишени температури (горещо компактиране). Всички съставни на пресформата, както и поансоните са изработени от стомана 3Х3М3В. След изработката детайлите са термообработени. Работната повърхност на проходния отвор е йонно азотирана , с цел намаляване на възможността за задиране по време на работа, а оттам и накърняване на работния цилиндър.

За експерименти са използвани четири вида алуминиеви сплави:

- две леярски- EN AC-48000(EN AC-AlSi12CuNiMg) и EN AC-42000(EN AC-AlSi7Mg). Сплав EN AC-48000 е евтектична, а сплав EN AC-42000-подевтектична.

- две пластично деформируеми - EN AW-2024(EN AW-AlCu4Mg1) и EN AW-6082(EN AW-AlSi1MgMn). Двете сплави са сравнително широко използвани за изработка на детайли, което от своя страна предполага получаването на отпадъчен материал, след механична обработка.

Технологичният процес за получаване на опитни образци (компакти) включва следните операции:

1. Студено компактиране на алуминиеви стружки
2. монтиране на пресформата и поансоните към универсална хидравлична преса PYE-250 SS;
3. подгряване и обмазване на системата с различни видове обмазки;
4. насипване на заготовъчния материал;
5. пресоване – едностранно или двустранно;
6. отваряне и избиване на получения компакт.
7. Горещо компактиране на алуминиеви стружки
8. монтиране на пресформата и поансоните към хидравличната преса;
9. подгряване и обмазване на системата с различни видове обмазки;

10. подгряване на пресформата до предварително определена температура;

11. насипване на заготовъчния материал;

12. пресоване – едностранно или двустранно;

13. отваряне и избиване на получения компакт.

В технологичната разработка съществена част са следните фактори:

1. Експериментирано е с различни обмазки (дайкот, волфрако и др.), до достигане на желания резултат.
2. При горещо компактиране се варираще с различни по стойност температури.
3. Изследва се влиянието на едностранното и двустранното пресоване, както при студено, така и при горещо компактиране.
4. На фиг. 2 са показани получени образци от използваните четири вида алуминиеви сплави.

Фиг. 2. Получени образци от използваните четири вида алуминиеви сплави.

3. Заключение

Конструирана и изработена е екипировка за компактиране на стружки от алуминиеви сплави. Разработена е технология за получаване на компакти, която е съобразена с различни фактори (вид на материала, използвани обмазки, вид и сила на пресоване, температурни вариации на пресформата), влияещи върху крайния резултат. Изследванията ще се съсредоточат върху получените качества на изработените образци.

4. Благодарности

Тази разработка е осъществена благодарение на дог. КП-06-Китай/14(МОН 08/20/4). Оборудването и експериментални единици, използвани в тази работа, бяха финансирани от Европейският фонд за регионално развитие в рамките на ОП „Наука и Образование за интелигентен растеж 2014 - 2020”, проект СЕ „Национален център по мехатроника и чисти технологии“, №BG05M2OP001-1.001-0008-C08

5. Литература:

[1] ttp://www.dnr.state.oh.us/recycling/awareness/facts/benefits.htm
[2] afsinc.org. afsinc.org
[3] J. Gronostajski, A. Matuszak (1999). The recycling of metal by plastic
deformation: an example of recycling of aluminium and its alloys chips.
Journal of Materials Processing Technology, 92-93:35-41.
[4] Rombach, G.,1998," Aluminium in open and closed loops,"AluminiumDusseldorf, 74(6),pp421-424.

[5] Констадинов К. Г. И др., Влияние условий брикетирования на физико
– механические свойства брикетов полученных из стружек алюминиевого сплава, Обраб. Металлов давлением в машиностр., №26,
1990, 26 – 28.
[6] Mark E. Schlesinger. Aluminum Recycling, Taylor & Francis Group,
CRC Press; 2007.
[7] Misiolek, W. Z., Haase, M., Ben Khalifa, N., Tekkaya, A. E., Kleiner, M.,
2012. High quality extrudates from aluminum chips by new billet compaction
and deformation routes. CIRP Annals Manufacturing Technology, 61, 239-
242.
[8]] https://aljazarilab.weebly.com
[9] Nowalid W., Shaharun M., Effect of Lubrication Conditions to the
Cutting Force Coefficients in Machining Process. Advanced Materials
Research Vol. 1115 (2015) pp 55-58.
[10] Khalid S. Mechanical strength of as – compacted aluminium alloy waste
chips. A project report submitted in partial fulfillment of the requirement for
the award of the Master's Degree of Mechanical Engineering. Faculty of
Mechanical and Manufacturing Engineering Universiti Tun Hussein Onn
Malaysia - Janury 2013.
[11] Pdtidar D., Tiwari Er., Patidar P., „Recycling of aluminium by extrusion
process with annova or taughi design approach". November 2016, Volume 3,
Issue 11.

Разработване на технология за получаване на порести отливки от алуминий и алуминиева сплав А356

А. Великов, Б. Кръстев, Р. Димитрова, В. Петков, С. Станев, В. Манолов
Институт по металознание, съоръжения и технологии с Център по хидро- и аеродинамика "Акад. А. Балевски" Българска академия на науките, София, България

Резюме: Разработена е методика за получаване на порести отливки от Al и алуминиева сплав А356. Методиката включва въвеждане в стопилката на Ca за повишаване на вискозитета и хомогенизация чрез механично разбъркване. Следва добавяне на TiH_2 , хомогенизация, последващо формиране на порестата структура и кристализация. Проведени са изследвания на материала от отливките, включващи металография и SEM микроскопия. Определена е плътността и порестостта на метала. Те са в интервала от 337 до 536 kg/m^3 и от 80% до 87% съответно. Получените нови резултати имат значение за развитието на разработваната технология.
Ключови думи: *порести отливки, хомогенизация*

Development of technology for production of porous castings from aluminum and aluminum alloy A356

A. Velikov, B. Krastev, R. Dimitrova, V. Petkov, S. Stanev, V. Manolov

Institute of Metal Science, Equipment and Technologies with Centre of Hydroaerodynamics "Acad. A. Balevski"- Bulgarian Academy of Sciences (IMSETCH-BAS)

Summary: A methodology for obtaining of porous castings from Al and aluminum alloy A356 has been developed. The methodology involves the introduction of Ca into the melt for increasing of the viscosity and homogenization by mechanical stirring. This is followed by the addition of TiH_2, homogenization, subsequent formation of the porous structure and crystallization. Investigations of the material of castings, including metallography and SEM microscopy, have been carried out. The density and porosity of the metal were determined. They range is from 337 to 536 kg / m^3 and from 80% to 87%, respectively. The obtained new results are of importance for the developed technology.

Key words: porous castings, homogenization

1. Въведение

Производството на алуминий и алуминиеви сплави с висока порестост или наричани още пени е предмет на работата на редица изследователи. Тези материали имат ниска плътност с голямо количество разпределени пори. Намират приложение за топлоизолация и за защита при пожар, а също така за звукоизолация и за филтриране на течности. В настоящата работа са представени резултати от разработване и изследване на технология за получаване на високопорести отливки или пени от алуминий и алуминиева сплав А356.

2. Експериментална методика

2.1. Изходни материали

В експериментите са използвани блоков Al, блокова сплав А356 и прах TiH_2 за газообразовател със среден размер на частиците 20µm. TiH2 е произведен от AG Materials Inc., Taiwan. Направени са изследвания на разпределението на частиците на праховите материали, също така са заснети техните SEM изображения. TiH_2 е окислен в съпротивителна пещ във въздушна среда при температура 673 K в продължение на 24h..Окисления прах има по-ниска скорост на разлагане и отделяне на водород, с помощта на който се формира порестата структура. Извършен е диференциален термичен и термогравиметричен анализ с детекция на отделящия се газ чрез масспектрометър. Термоаналитичните криви (ТГ и ДТА) са снети при скорости на нагряване 10 °C/мин до 1073 K. Получени са следните интервали на разлагане на TiH_2 и отделяне на H_2 за неокисления TiH_2 697 K -940 K, а за окисления 782 K-967 K.

2.2. Метод за получаване на порести отливки

Използван е метод за получаване на порести отливки от стопилка на алуминий или сплав А356. Той включва стопяване на блоков метал в тиглова съпротивителна пещ, при T=953 K. В сплавта се въвежда 1 Wt % Ca и се извършва механично разбъркване. Следва преливане на стопилката в подгрята тънкостенна метална форма, въвеждане на 1.6 Wt % окислен TiH_2, интензивно механично разбъркване, пенообразуване и охлаждане на пеноматериала. На фиг.1 и фиг.2 са показани снимки на пещите и устройствата за хомогенизация съответно на Ca и на TiH_2.

Получените порести отливки са показани на фиг.3 и фиг.4 съответно от Al от А356. От фигурите се вижда, че и в двете отливки има област в която е формирана силно развита пореста структура и област от плътен или слабо порест метал. Това се дължи на ниската скорост на кристализация на отливките поради високата порестост. В резултат на това започва движение на течната фаза в стените на мехурчетата към дъното на отливката. Процесът е наречен дренаж и е характерен при кристализацията на по-големи обеми на порестите отливки.

***Фиг. 1**. Хомогенизация на Ca въведен в съпротивителна пещ*

***Фиг.2**.Хомогенизация на TiH_2 в съпротивителна пещ.*

***Фиг.3** Пореста отливка от Al*

***Фиг.4** Пореста отливка от A356*

3. Изследване на получените порести материали

3.1. Плътност и порестост

Направено е изследване на плътността и порестостта на пробни тела изрязани от получените отливки. В табл. 1 са показани получените резултати за Al и за сплав A356.

***Табл.1:** Плътност и порестост на порести отливки от Al и A356*

№ по ред	сплав	Тегло [g]	Обем [cm^3]	Относително тегло,[g/cm^3]	Порестост [%]
1	AlSi7Mg	3.73	6.97	0.536	80
2	AlSi7Mg	2.38	6.47	0.368	86
3	AlSi7Mg	2.23	6.60	0.399	85
4	Чист Al	2.57	6,15	0.418	84
5	Чист Al	2.20	6.53	0.337	87

3.2. Металографски и томографски изследвания

За металографски и томографски (3D) анализ са използвани порести образци от сплав AlSi7Mg. Томографското изследване е проведено чрез пролъчване с микротомограф (μCT) SkyScan 1272, Bruker. Образецът е подготвен като металографски шлиф като е шлайфан на шкурки до №1200 и механично полиран с диамантена паста. Проявен е с 0.5% воден разтвор на HF.

След извършване на първоначални настройки на μCT са избрани следните параметри на пролъчване: разделителна способност 2452x1640 pxl, големина на pxl: 10.8 μm, филтър Al 1mm, разстояние на образеца до рентгеновия източник: 200.399 mm, напрежение на източника 80 kV, ток на източника 125 μA, стъпка на пролъчване: 0.2˚, 360˚ пролъчване (пълно завъртане на образеца), експозиция 1400 ms. След приключване на пролъчването е направена 3D - реконструкция чрез обработка на получените графични изображения със софтуер NRecon v. 1.7.4.2. За визуализация на 3D – моделът и получаване на разрези в различни сечения е използван софтуер CTVox v.3.3.0r1403.

На фиг. 5 е показан 3D–моделът на порест образец AlSi7Mg (A356), като координатната система е в долният ляв ъгъл.

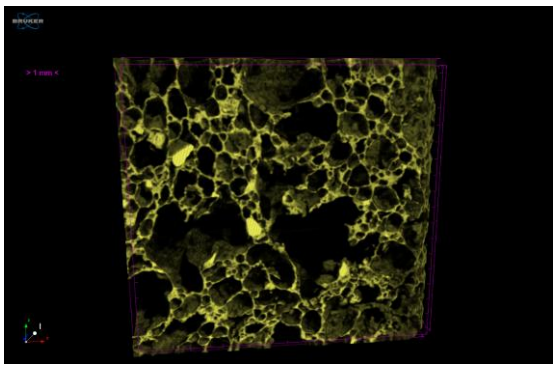

***Фиг. 5.** 3D–модел на на порест образец от AlSi7Mg*

След обработка на реконструирания модел чрез софтуер CTAn за бинаризиране на изображенията са направени изчисления на порестостта. Резултатите са дадени в табл.2.

Табл. 2: Порестост на изследваната проба

Отворена порестост, %	Затворена порестост, %	Обща порестост, %
79.4	0.793	79.6

На фиг. 6 е показана микроструктурата на порест образец от AlSi7Mg. Микроструктурата на образеца се състои от α-твърд разтвор с дендритен строеж и интерметални съединения. При измерване на диаметрите на порите в 10 полета на образеца са получени следните стойности: min diameter – 40.66 μm; max diameter - 1260.72 μm; average diameter - 296.33 μm.

3.3. Изследвания с използване на SEM

SEM-EDS изследванията на порист образец от AlSi7Mg бяха проведени с помощта на сканиращ електронен микроскоп HIROX SH-5500P с EDS система за микроанализ QUANTAX 100 Advanced (Bruker) при следните условия: (1) Използвани детектори: SE (secondary electrons) и BSE (back-scattered electrons); (2) Използвано ускоряващо напрежение: 20 kV.

На фиг.7 е показана част от микроструктурата на образеца при увеличение 250 x. Тази част обхваща пространството между големи пори (означени на снимката). За целите на EDS анализ маркираната с червено зона е увеличена до 500 x и показана на фиг.8. На нея ясно могат да бъдат различени (като нюанси на сивия цвят) следните фази: Al матрица (анализи 1 и 2); Al-Si-Ca (анализи 3 и 4) и нереагирали частици TiH_2 или само Ti (анализ 5). Резултатите от EDS анализи на отделните фази са представени под фиг.8, табл.3 .

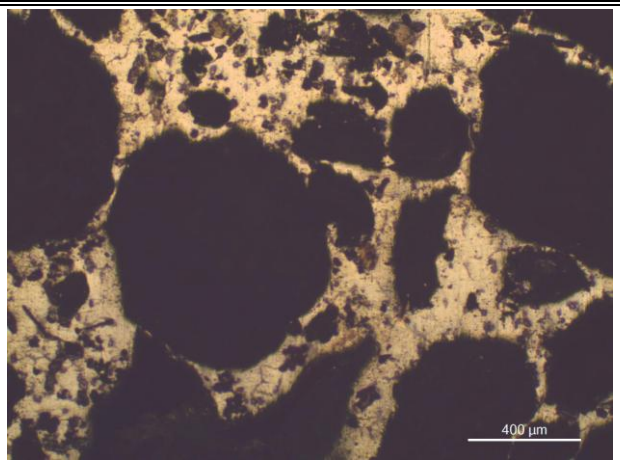

Фиг. 6 *Микроструктура на порест образец от сплав AlSi7M*

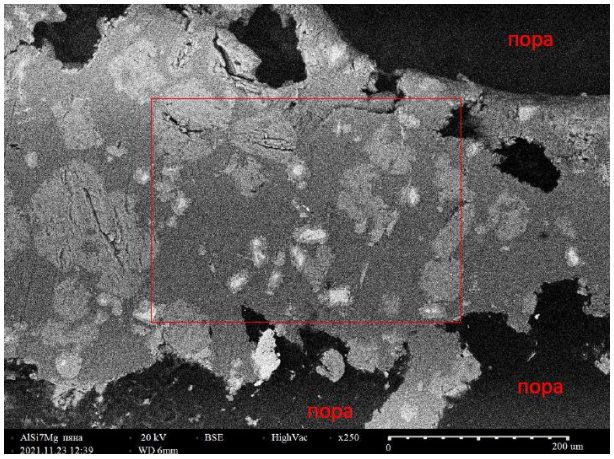

Фиг. 7. *Микроструктура на порист образец от AlSi7Mg при увеличение .250 х*

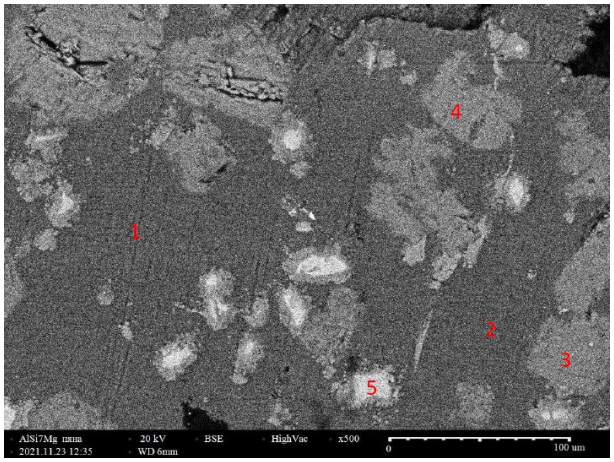

Фиг. 8 . *Микроструктура на порист образец от AlSi7Mg при увеличение 500 х*

Табл.3: EDS анализи на химичните елементи, съдържащи се в порестия образец в точките от 1 – 5 съгласно Фиг.8

1

Element	At. No.	Netto	Mass [%]	Mass Norm. [%]	Atom [%]	abs. error [%] (1 sigma)	rel. error [%] (1 sigma)
Al	13	39817	72.08	98.15	98.54	3.51	4.86
Si	14	128	0.76	1.04	1.00	0.11	14.60
Ti	22	136	0.59	0.81	0.46	0.08	13.76
		Sum	**73.44**	**100.00**	**100.00**		

2

Element	At. No.	Netto	Mass [%]	Mass Norm. [%]	Atom [%]	abs. error [%] (1 sigma)	rel. error [%] (1 sigma)
Al	13	26815	73.24	98.82	99.10	3.58	4.89
Si	14	51	0.44	0.60	0.58	0.10	21.98
Ti	22	62	0.43	0.58	0.33	0.08	19.42
		Sum	**74.11**	**100.00**	**100.00**		

3

Element	At. No.	Netto	Mass [%]	Mass Norm. [%]	Atom [%]	abs. error [%] (1 sigma)	rel. error [%] (1 sigma)
Al	13	7354	35.20	40.30	45.20	1.81	5.15
Si	14	3973	26.34	30.15	32.49	1.29	4.90
Ca	20	4390	25.80	29.54	22.31	0.91	3.51
		Sum	**87.34**	**100.00**	**100.00**		

4

Element	At. No.	Netto	Mass [%]	Mass Norm. [%]	Atom [%]	abs. error [%] (1 sigma)	rel. error [%] (1 sigma)
Al	13	8066	34.39	40.56	45.52	1.76	5.13
Si	14	4356	25.20	29.72	32.04	1.23	4.86
Ca	20	4599	25.19	29.71	22.44	0.88	3.49
		Sum	**84.77**	**100.00**	**100.00**		

5

Element	At. No.	Netto	Mass [%]	Mass Norm. [%]	Atom [%]	abs. error [%] (1 sigma)	rel. error [%] (1 sigma)
Ti	22	13192	96.12	97.92	96.37	2.85	2.97
Al	13	231	2.04	2.08	3.63	0.22	10.87
		Sum	**98.16**	**100.00**	**100.00**		

4.Заключение

Разработена е методика за получаване на порести отливки от Al и A356 с използване на TiH_2 за порообразовател .За повишаване вискозитета в стопилката се въвежда Ca. Хомогенизацията на стопилката се извършва чрез механично разбъркване. Получени са отливки с добре развита порестост. Проведени са изследвания на плътността, порестостта, томографски, металографски и SEM изследвания на образци, изрязани от получените отливки. Определени са порестостта, относителната плътност, микроструктурата на стените на порите, наличието на открита и закрита порестост. Резултатите от SEM и EDS анализите дават възможност да се изясни механизма на взаимодействие при формиране на порите.

Работата е подкрепена от проект по договор №КП-06-Н47/12 / от 03.12.2020 г., финансиран от Фонд за научни изследвания, Р. България. Оборудването и експериментални единици, използвани в тази работа, бяха финансирани от Европейският фонд за регионално развитие в рамките на ОП „Наука и Образование за интелигентен растеж 2014 - 2020”, проект CE „Национален център по мехатроника и чисти технологии“, №BG05M2OP001-1.001-0008-C08

I4.0 Component Models based on IEC/EN 62264

Plamen Vasilev, Vasil Metodiev
Industrial Automation Dept.,
University of Chemical Technologies and Metallurgy Sofia, Bulgaria
plamen.vasilev@uctm.edu, metodiev@uctm.edu
https://orcid.org/0000-0001-6493-402X

Abstract: *Laying the foundations on which to build the cyber-physical world of the Fourth Industrial Revolution comes down to creating a unified platform for transforming existing information solutions to ones, that meet the requirements and capabilities of the new integrated world. The RAMI 4.0 standard aims to introduce the concept of "asset" as part of the cyber-physical world, as well as to describe the hierarchical structure of assets in an industrial enterprise during their life-cycle. A similar purpose has another standard - IEC/EN 62264, which describes the operations resources as objects for integration of information between information systems of different hierarchical levels, as well as models of operational activities for definitions, planning, execution and collecting and analyzing information on these resources.*

Keywords: *CYBER-PHYSICAL SYSTEMS, RAMI 4.0, IEC/EN 62264, ASSET, B2MML, WEB SERVICE*

1. Introduction

In the field of industrial solutions, the building foundation of the Fourth Industrial Revolution was released in 2016, in the form of the DIN SPEC 91345 standard - Reference Architectural Model for Industry 4.0 (RAMI 4.0) [1]. Its main purpose is to present a complete description of cyber-physical entities' (assets) architecture as a standardized reference model built on three fundamental standards [2,3,4] and referring four others [5,6,7,8], all of them, either in the field of industry or ICT, or interdisciplinary, in the area between the two. This is why the presumption in this article is that the aim of the RAMI 4.0 standard is to encompass, summarize and enhance the knowledge covered by the mentioned standards in a different perspective. The novel part in the model is introduced with the Architecture axis, describing the role of on asset or entity, hence the name. The standard RAMI 4.0 explicitly states that the layers in the Architecture axis should not be confused with information systems hierarchy layers, rather than describe structural properties of asset or assets. Layers also do not always have to have content. [1]

Second assumption given in the article is that the structure of the administration shell of an I4.0 component may be implemented by the use of standardized industrial models, such as the ones presented in the IEC/EN 62264, along with the B2MML XML Schema Definition (XSD) that accompany the standard. This common statement is used in cases where the asset does not posses embedded intelligence.

2. Reference Architecture Model for Industry 4.0

According to RAMI 4.0, the term "asset" means anything, physical or logical, that has value for the company. The asset can be part of the physical or information world, be tangible (sensor, engine, device, installation, etc.) or not (idea, service, software program). Depending on its role in the organization, the asset can perform a certain function of the "Architectural Axis" - Asset (the artifact itself, represented in the physical world); Integration function (the means by which the physical world cooperates with the information world); Communication function (represents who-where-when information through which the asset is represented in the information world); Information function (represents data processing modified by the event / model and verification of information); Functionality (describes the function of an activity in terms of its role in the 4.0 system); Business function (describes the commercial perspective of the asset).

The remaining "Life cycle and value flow" "represents the lifetime of the active and the value-added process based on the IEC 62890 standard. In this axis, the asset is secured with its condition at a certain point in time. [2]

The levels of the "Hierarchy" axis in the Reference Architectural Model Industry 4.0 (Fig. 2) is a modification of the model of the hierarchy of equipment from the standard IEC / EN 62264 (ANSI / ISA-95), thus suitable for defining assets compatible with I4.0. [3]

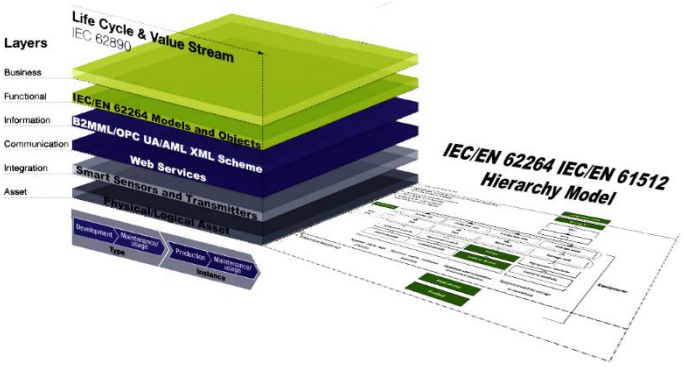

Fig. 1 *Hierarchy Model in the scope of RAMI 4.0.*

Another important aspect addressed in the RAMI 4.0 standard is the presentation and communication capabilities of the assets from the point of view of Industry 4.0. The presentation capacity of an asset refers to the extent to which it is represented and administered in an information system. From this point of view, the assets can be: Unrepresented; Anonymously submitted; Individually presented; Administered as an object.

From the communication point of view, the capabilities of the assets, may be: No communication capabilities; Passive; Active; I4.0 compatible. Assets of this type have an Administrative Shell, which contains a Manifest and a "Component Manager". Through the Administrative Shell accompanying the asset, the information system can access and request information about various functions and states of the I4.0 component (Fig.2).

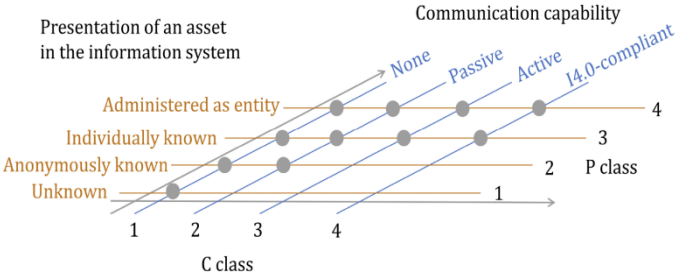

Fig. 2 *Communication and Presentation capabilities of an asset.* [1]

3. IEC/EN 62264

The main purpose of the standard is to provide a framework for integrating information from information systems at different hierarchical levels. This is necessary for several reasons: the different goals that systems at different levels have; the complexity of the tasks that the systems perform; time period or frequency of transactions execution and data aggregation. The information incompatibility may be overcome by defining the models and objects for transmission and aggregation of information between the different information levels.

The standard describes the models of the main resources used at operational level of management, on which information is collected and aggregated: Equipment Model, Materials Model Personnel Model and the logical union of personnel, equipment and materials – the model of Process Segment (workplace). These resources are the basis of the models of the definition of operation, in the sense of a series of operational activities (product production, maintenance, quality management or inventory), Production Capacity, Planning and Response.

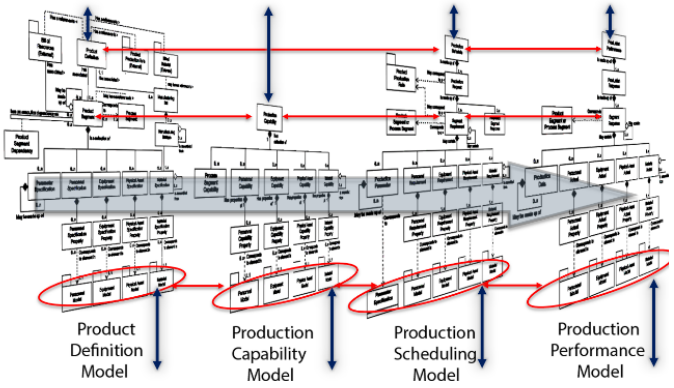

Fig. 3 *Manufacturing life-cycle and information integration in IEC/EN 62264*

The Operations Definition model introduces the term Operations Segment (or Operation) which represents a logical union of Equipment, Material and Personnel Specifications (specifies what type of Equipment, Material and Personnel that should be involved in the operation). The Operations Definition is associated with a list of Operations Segments (list of Operations). The Operations Segment corresponds to a Process Segment i.e., a given Operations should be executed on a particular workplace. Similar to the Operations Segment Specifications, there are Process Segment Specifications i.e., there must be a specific Equipment, Material with some characteristics and Personnel with particular qualification on a given workplace. The Operations Schedule, made up of Operations Requests consists of Requirements for each Operation – Equipment Requirement, Material Requirement and Personnel Requirement. Operations Capability Model is defined by the capabilities of Equipment, Material and Personnel, which corresponds to their availability in a particular time interval. The Operations Response Model is made up of responses of the scheduled operations and contain the Actual Equipment, Actual Material Consumed, Produced and/or Consumables and the Actual Personnel involved. These four models refer to Production, Maintenance, Quality and Inventory Management operations.

Figure 3 represents the four Production models as an example. The upper red arrow in the figure represent transition between production manufacturing operations of Definition of a product, Production scheduling and Production response. The lower red arrow aims to present that the Product Segment (respectively Process Segment) is related to Production Capability, Production Requirements and Production Response. The drilldown relation is expressed as Product / Process Segment Personnel / Equipment / Material Specification – Personnel / Equipment / Material Requirements – Personnel / Equipment / Material Capabilities – Personnel / Equipment / Material Actual used. The last ones from the four manufacturing models refer to same Personnel / Equipment / Material Information Models (the red ellipses). The blue arrows aim to pinpoint the objects, for which information may be transferred between different hierarchy level information systems.

Transferring of information through the use of the IEC/EN 62264 framework of models and objects allows tracking and tracing throughout the life-cycle of operational activities related not only with the product production, but to maintenance, quality and inventory operations (Fig. 4). [10].

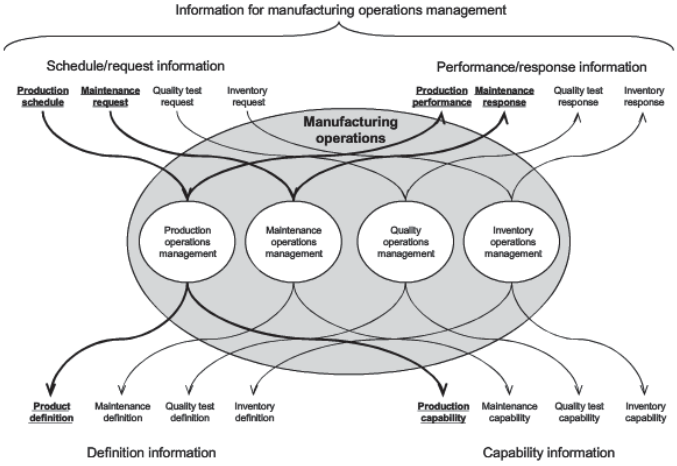

Fig. 4 *Information model of manufacturing operations.[10]*

4. I4.0 Component Models based on IEC/EN 62264

I4.0 compatible assets or I4.0 components are assets that have at least passive communication capabilities and are administered as an entity in an information system by an administration shell. There are a number of requirements for the administration shell, that are as follows:

a) The administration shell consists of the body and the header.
b) The body contains information on the asset in question.
c) The header contains information on how the asset is used.
d) The administration shell contains the key elements, the manifest and the component manager.
e) The information in the administration shell must be accessible using service-oriented architecture (SOA) and must take the corresponding security requirements into account.
f) The administration shell represents information on application aspects.
g) The administration shell is structured using views.
h) The administration has a unique ID.
i) The asset has a unique ID.
j) Even a factory can be an asset that has an administration shell and can be addressed using its ID. It should be possible to apply the concept of nesting.
k) Types and instances must be indicated as such.
l) The administration shell can contain references to other administration shells or I4.0 information.
m) Additional properties, such as manufacturer-specific ones, must be possible.
n) A reliable minimum set of properties must be defined for each administration shell. [1, 11, 12]

MES/MOM systems are industrial information systems that handles the models described in the standard IEC/EN 62264 and administer the whole information about manufacturing resources throughout their operations life-cycle. Following the standard objects allows the ease of integration with other information systems. Figure 5 presents a UML structural class diagram of the IEC/EN 62264 material model used in the MES/MOM system MOM4. Each class contains attributes from [9] and basic functionality applied with the help of methods: OnCreate(); OnRerieve(); OnUpdate(); OnDelete();

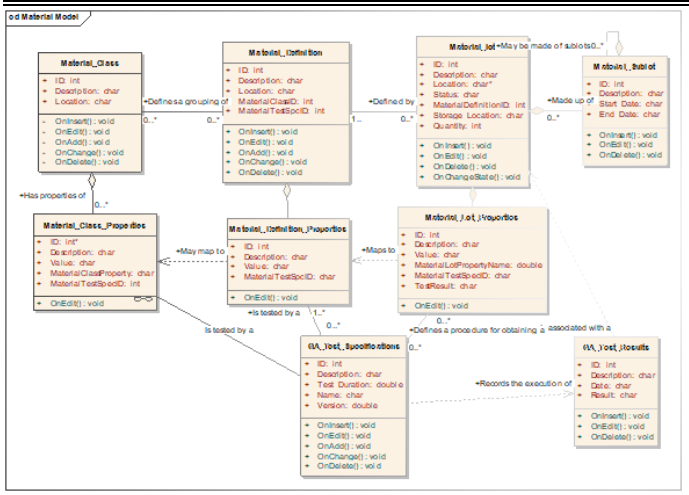

Fig. 5 *UML Class Diagram of the IEC/EN 62264 Material Model*

The Material Model represents a form of classification of materials used for the purpose of defining, scheduling and execution of manufacturing activities. All tangible piece of material is presented and described by the object Material Lot. The Material Lot is defined by a Material Definition, which describes the lot in all aspects needed. The Material Lot consists attributes as: ID, Location, a reference to a Material Definition ID, State, Storage Location and Quantity. The Material Lot has properties, the restriction count of which may depend e.g., on maximum capacity specification of a table in SQL Server [17].

Material Definitions have properties that describe them uniquely. A logical grouping of Material Definitions with similar characteristics for the purpose of scheduling is referred as Material Class. The Material Class has properties that describe it. Both the Material Class and Material Definition properties may be tested by a QA Test Specification which has to define a procedure for the Material Lot to obtain a property. Every QA Test Specification made creates a Material Lot Quality Test Result, which may have relation to the Material Lot current quality state. The Material Model is referred from every operations model in the form of Specifications, Requirements, Capabilities or as Actual Consumed, Produced or Consumable materials.

The information integration between industrial systems from different or same informational layer is made with the use of common XSD (XML Schema Definition), which represents a formal description of elements in an XML document. This formal description may refer models, as it is in B2MML (Fig. 6) [13] referring IEC/EN 62264 models (Fig), OPC UA [14,15] and AutomationML (AML) [16].

As shown in Figure 1, the meanings of communications function, as described in the RAMI 4.0 standard are performed in the form of web services. The web service technologies allow platform-independent communication through World Wide Web in a standard data format, such as plain text, HTML, JSON (REST) or XML (REST or SOAP services).[18]

The following piece of code is presented as a functional illustration in WSDL (Web Service Definition Language) of the web service operation “Create”:

```
<wsdl:portType name="IB2MMLService">

<wsdl:operation name="Create">

<wsdl:input
wsaw:Action="http://tempuri.org/IB2MMLService/Create"
message="tns:IB2MMLService_Create_InputMessage"/>

<wsdl:output
wsaw:Action="http://tempuri.org/IB2MMLService/CreateResponse
" message="tns:IB2MMLService_Create_OutputMessage"/>

<wsdl:fault
wsaw:Action="http://tempuri.org/IB2MMLService/CreateWCFServ
iceExceptionFormFault" name="WCFServiceExceptionFormFault"

message="tns:IB2MMLService_Create_WCFServiceException
FormFault_FaultMessage"/>

</wsdl:operation>
```

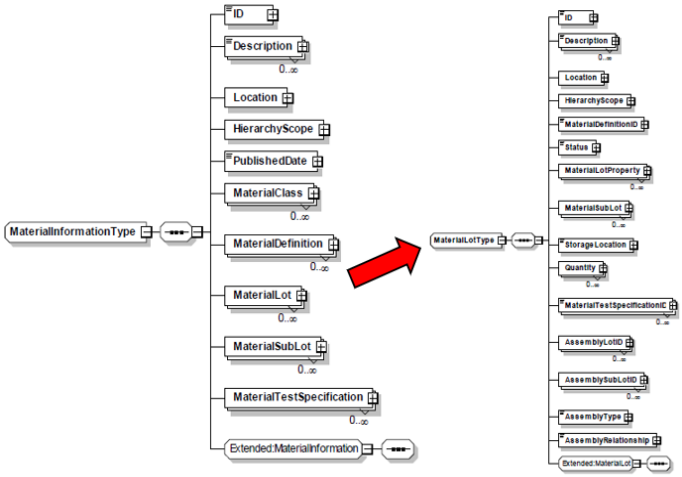

Fig. 6 *B2MML Material Information and Material Lot Schema [13]*

All the models described above have the following characteristics while interacting with each other:

a) The combination of all models is used for establishment of a logical, virtual representation of a given resource in an administrating information system.

b) The resource is described in all necessary aspects by properties.

c) Involving the resource in activities, covered by the models of definition, scheduling, capability and performance represents information of the usage of a resource.

d) The models define a meta-information of properties of the resource and description of operations that can be invoked through external interface.

e) The information described in the models is accessible using service-oriented architecture (SOA) [18] and take the corresponding security requirements into account.

f) The models represent information on application aspects.

g) The models are structured using views.

h) The models have a unique ID.

i) The resources have unique ID.

j) The Equipment hierarchy model is native to IEC/EN 62264 and comprise Enterprise, Site and Area, all of which may refer to a Factory.

k) Each resource is an instance of its class or definition.

l) Operations Models refer to resource models.

m) Additional properties, such as manufacturer-specific ones, are possible through Property classes.

n) A reliable minimum set of properties must be defined for each resource (attributes).

These fourteen assumptions, along with the definitions of the Manifest and Component Manager substantiate that IEC/EN 62264 standard models, B2MML XML Schema Definition and web services may be used as a suitable solution for building Administration shell for assets – I4.0 Components, when no embedded intelligence is applicable.

5. *Conclusions*

The Fourth Industrial Revolution is yet in its beginning and there are still many concepts to be clarified. The DIN SPEC 91345 standard - Reference Architectural Model for Industry 4.0 (RAMI 4.0) is a basis for future science and industry development. Although there are every day examples of Cyber - Physical Systems

that include assets with embedded intelligence, most of the assets in manufacturing production don't have any presentation capabilities at all. A small part of all assets is being administered as an entity by information systems and has Communication capabilities – I4.0 Components. The meanings by which the Administration shell of an I4.0 Component may be realized, must be standardized model-based descriptions of structure and behavior that follow all stages during the asset's life cycle.

Among others, IEC/EN 62264 standard models and objects may be used as a functional, information and communication architecture structure, together with the accompanying B2MML XML Schema Definition and the use of Web Service technologies.

Acknowledgment: This research is supported by two projects: the National Scientific Program "Information and Communication Technologies for a Single Digital Market in Science, Education and Security (ICTinSES)", which is gratefully acknowledged by the author.

6. References

1. DIN SPEC 91345:2016-04 Reference Architecture Model Industrie 4.0, DIN Deutsches Institut für Normung e. V., Berlin. Beuth Verlag GmbH, 10772 Berlin, Germany

2. IEC 62890:2020 ED1 Industrial-process measurement, control and automation - Life-cycle-management for systems and components, IEEE

3. IEC/EN 62264-1:2013 Enterprise-control systems integration – Part 1: Models and Terminology, CENELEC, Brussels, 2013

4. IEC/EN 61512-1:1999 Batch control – Part 1: Models and Terminology, CENELEC, Brussels, 1999

5. IEC/EN 61360-1, Standard data element types with associated classification scheme for electric components — Part 1: Definitions — Principles and methods (IEC 61360-1)

6. IEC/EN 61360-2, Standard data element types with associated classification scheme for electric components — Part 2: EXPRESS dictionary schema (IEC 61360-2)

7. IEC/TR 62794, Industrial-process measurement, control and automation — Reference model for representation of production facilities (Digital Factory)

8. IEC/TS 62832-1, Industrial-process measurement, control and automation — Digital Factory framework — Part 1: General principles

9. IEC/EN 62264-2:2013 Enterprise-control systems integration – Part 2: Objects and Attributes for Enterprise-control system integration, CENELEC, Brussels, 2013

10. IEC/EN 62264-3:2007 Enterprise-control systems integration – Part 3: Activity Models of Manufacturing Operations Mangement, CENELEC, Brussels, 2007

11. Details of the Asset Administration Shell, Part 1 - The exchange of information between partners in the value chain of Industrie 4.0 (Version 2.0.1), Federal Ministry for Economic Affairs and Energy (BMWi) Public Relations 10119 Berlin, V2.0.1 May 2020

12. Structure of the Administration Shell Continuation of the Development of the Reference Model for the Industrie 4.0 Component, Working paper, Federal Ministry for Economic Affairs and Energy (BMWi) Public Relations 10119 Berlin, April 2016

13. Manufacturing Enterprise Solutions Association (MESA), B2MML v.0700 - Business To Manufacturing Markup Language

14. International Electrotechnical Commission (2016) OPC unified architecture—part 1: Overview and concepts (IEC 62541-1)

15. Ivanova T., Batchkova I., Belev Y., INFORMATION MODELING OF INTELLIGENT AND SECURE CYBER-PHYSICAL PRODUCTION SYSTEMS USING OPC UA, Machines, Technologies. Materials, Vol. 13 (2019), Issue 12

16. AutomationML The Guide for Seamless Automation Engineering Interrelation of Asset Administration Shell and AutomationML Position paper State: May 2021

17. https://docs.microsoft.com/en-us/sql/sql-server/maximum-capacity-specifications-for-sql-server?view=sql-server-ver15

18. https://www.service-architecture.com/

Some robotics concepts for the Industry 4.0 applications

Nataša Popović[1], Božidar Popović[1]
University of East Sarajevo, Republic of Srpska, Bosnia and Herzegovina[1]
natasa.popovic@etf.ues.rs.ba

Abstract: *The advancement in Information and communication technologies has created conditions for using these technologies in many applications including the industry ones. Robotics has been traditionally present in industries, especially in manufacturing. Development of cyber-physical systems, artificial intelligence, smart sensors, Internet of Things, and other relevant technologies enabled certain transformation in the field of robotics which resulted in new robotics concepts that lead towards smart factories and fulfilment of Industry 4.0 requirements. This paper deals with some of these concepts such as cloud robotics, Internet of Robotics Things and collaborative robotics giving their main characteristics and possibilities of application in Industry 4.0 domain.*
Keywords*: ROBOTICS, INTERNET OF THINGS, CLOUD ROBOTICS, INTERNET OF ROBOTIC THINGS, INDUSTRY 4.0*

1. Introduction

The Industry 4.0 concept was first introduced at the Hanover Fair in 2011 with the aim of presenting a new strategic initiative of the German government witch task was creating new industrial production systems that would be based on modern information and communication technologies [1]. This concept and the American concept of the Industrial Internet of Things (IIoT) from 2012 initiated the emergence of other similar concepts such as French Industrie du futur, and Chinese Made in China 2025 [2]. Industry 4.0 is often identified as the fourth industrial revolution, which was initiated by the development of information and communication technologies. Cyber-physical systems, with decentralized control paradigm and advanced techniques for connecting a large number of devices enabled by the advent of the Internet of Things (IoT), are the core of the fourth industrial revolution. This results in the transformation of the classical hierarchical structure of industrial production systems into self-configuring cyber-physical production systems that enable flexible and adaptive mass production. Cyber-physical production systems provide smart manufacturing and smart factories as one of goals of Industry 4.0.

Robotic systems have been used for decades for various purposes, in industry, in everyday life, for entertainment and other. Industrial robots perform specific tasks and replace humans in difficult and dangerous operations. Robotic technology has given substantial contribution in modern industry and plays one of the key roles in Industry 4.0. It is predicted that next generation of robotics and its associated technologies will play more significant role to meet the dynamic needs of collaborative and intelligent manufacturing within the context of Industry 4.0 and Industrial Internet of Things [3].

Traditionally, to perform specific tasks, robots had to be programmed first. The emergence of cloud computing, Internet of Things, intelligent connectivity, artificial intelligence, machine learning and human-robot interaction, to name a few, enabled robots to be much more than preprogrammed machines. Cloud computing enabled robots to share the resources and to use the infrastructure of a cloud. Internet of Things allowed the robots to act as things and using intelligent connectivity to interact with each other. Artificial intelligence and machine learning gave the robots capability to operate using learning algorithms and cognitive decision-making. Robot-human interaction is becoming more and more sophisticated. Now robots can, practically, be connected at any time and anywhere, not just with each other but with anything. All these technologies led to significant transformation in the field of robotics over last decade creating the suitable environment for Industry 4.0 applications.

The advancement in computing, information and communication technologies emerged different robotics concepts such as: networked robotics, cloud robotics, collaborative robotics, cognitive robotics, swarm robotics. All these concepts led to Internet of Robotic Things (IoRT) as the most recent state-of-the-art concept in the smart manufacturing [4].

This paper deals with some robotics concepts giving their main characteristics and possibilities of application in Industry 4.0 domain. In section two, networked robotics, cloud robotics, collaborative robotics, cognitive robotics and Internet of Robotic Things are discussed, and section three considers their applications in Industry 4.0 domain. At the end, some conclusions are given.

2. Robotics Concepts in Industry 4.0

The era of industrial robotics has started in 1960s when robots were used to perform difficult tasks, mostly repetitive ones. This early robotics was enabled with key technologies such as servo and stepper motors, motor drivers and controllers. Introduction of concepts of feedback control systems, data acquisition and networking technologies in the field of robotics provided conditions for appearance of new robotics concepts. These concepts were based on various sensors, embedded and real-time systems, Ethernet and data processing. Today robotic systems relay on deep learning, human-robot interaction, system interoperability, real-time image recognition, voice communication, digital twinning for cyber-physical systems, collaborative cyber-physical systems, human friendly cognitive robots, cloud technologies, and so on. Future robotics needs to fit in the idea of Industry 4.0 using artificial intelligence, machine learning, integration of robots' cognitive skills, virtual/augmented reality and swarm technologies [3]. Nowadays, robotics is a multidisciplinary field in which different control, communication, information and computing technologies combine together with the goal of creating advanced robotic systems that will be capable to meet the requirements of the fourth industrial revolution. Some of these advanced systems are referred to as networked robotics, cloud robotics, collaborative robotics and Internet of Robotic Things, and are briefly described as follows.

2.1 Networked Robotics

When robots are required to perform complex operations that can only be realized by collaboration of a large number of robots, networking technologies are introduced into robotic systems, creating networked robotic systems. Networked robotic systems refer to a group of robots that are interconnected by wired and/or wireless communication. Such systems can perform teleoperations in a way that the operator manages and manipulates robots from a remote location, or they can act as multiagent systems in which a group of networked robots perform certain tasks together (Fig. 1). The first approach gives the teleoperated robots, and the second one gives autonomous robots. In networked robotics, multiple robots operate in a wide range of environments performing tasks that require them to coordinate with other robots, cooperate with humans, and act on information derived from multiple sensors [5]. These systems are related to networked control systems and are subject to many communication constraints. These constraints, expressed in terms of network delay, jitter, data dropouts, data loss, etc., disable reliable and continuous communication between robots. Networked robotics was the first step towards the collaborative robotics creating autonomous networked robots capable to act in a group.

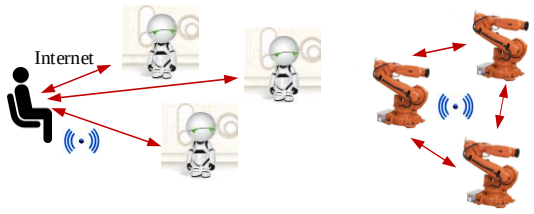

Fig. 1 *Networked robotics concept*

2.2 Cloud Robotics

The limitations of networked robotic systems can be overcome using cloud computing technologies in robotic system. This results in appearance of the concept of cloud robotics [6]. The main goal of cloud robotics is to transfer complex computing from microprocessors embedded into the robots to the cloud using communication technologies. Thus, robots no longer perform complex computing related to signal processing and execution of control algorithms locally, but in the cloud. This significantly relieves the microprocessor resources of the robot and leaves them the possibility of more efficient operation. The concept of cloud robotics was first introduced in [7]. It was preceded by the RoboEarth project, which had a vision of creating a WWW for robotic applications, i.e. large networks and databases in which robots can share information and learn from each other, and which would be available to robots from around the world. In achieving this vision, cloud computing and cloud infrastructure were used, and the results were 3-D models of different environments, speech and face recognition, etc.

The cloud robotics concept framework is given in Fig. 2. [8], where two basic parts can be identified. These are the cloud with its infrastructure (servers, databases, data centers) and networked robots of various types (mobile robots, drones, navigation robots). Communication between networked robots is realized on the M2M (Machine-to-Machine) principle, and between robots and cloud on the M2C (Machine-to-Cloud) principle. At the level of M2M communication, robots communicate with each other wirelessly and thus create a collaborative network of robots. In this way, the computing capabilities of individual robots are combined and dynamic sharing of resources between them is enabled, as well as collaborative decision-making. At the M2C communication level, robots are given access to cloud computing and memory resources, bringing together the big data needed in specific robotic applications in one place, and creating databases that store skills acquired in some previous robotic tasks that facilitate future tasks in a way that robots do not have to acquire skills from the beginning but use those already present in the cloud [9]. Networked robots communicate with each other if they are within range, and to communicate with cloud servers they need to be close to an access point which is an integral part of the cloud infrastructure. Wireless data protocols (ZigBee, Bluetooth, WiFi) are used for communication of networked robots at short distances, and radio and microwave communication at longer distances.

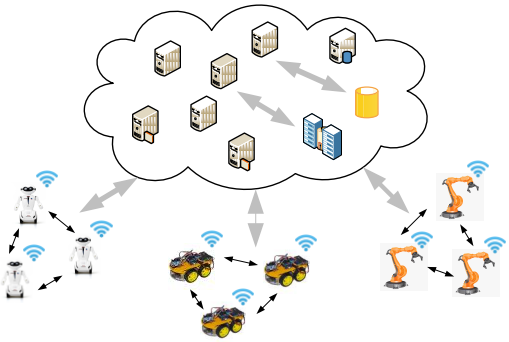

Fig. 2 *Cloud robotics concept*

2.3 Collaborative Robotics

A collaborative robot or a cobot is a robot which has the ability to safely work directly along-side human workers to complete a task [10]. It is specifically designed for direct interaction with a human within a defined collaborative workspace [11]. This workspace is safeguarded space where the robot and a human can perform tasks simultaneously during automatic operation. Human-robot interaction is defined as a state in which robots can safely work in direct cooperation with a human within a defined workspace. The concept of a collaborative robot was first introduced by Colgate as an Intelligent Assist Device (IAD) which manipulates objects in direct collaboration with a human operator [12]. The concept of collaborative robotics is given in Fig. 3. The collaboration between humans and cobots can be achieved in four ways [13]:

- a human operator and a cobot work on separate workpieces, independently, and for their individual manufacturing processes,
- a human operator and a cobot operate on separate manufacturing processes at the same workpiece at the same time,
- a human operator and a cobot perform sequential manufacturing processes on the same workpiece,
- a human operator and a cobot work on the same process on the same workpiece interactively.

Independent and simultaneous collaboration are mostly present in existing industrial applications, while sequential and supportive collaboration are subject to more advanced applications which will be part of future smart manufacturing environments. To achieve the aims of collaborative robotics, cobots need to have improved semantic understanding of the task goal and the actions as well as intents of its human co-workers. This means that cobots need to have cognitive capabilities which enable them to behave in intelligent manner as response to complex goals in a complex working environment. Similarly, the human workforce needs to be able to communicate with the cobots in intuitive way.

Collaborative robotics brings many advantages especially in production systems where cobots provide efficient production by supporting workers with both physical and cognitive tasks [14]. Introduction of cobots changes the role of humans in all areas of their collaborative work. Therefore, the fifth industrial revolution, which should be based on the complete collaboration of people and machines, has already been announced [15].

Fig. 3 *Collaborative robotics concept* [12]

2.4 Internet of Robotic Things

The combination of the Internet of Things and classical robotics emerged the Internet of Robotic Things in which the Internet of Things provides information services necessary for sensing, tracking and monitoring of objects while robotics allows objects to take appropriate actions, interact and behave autonomously [16, 17]. The Internet of Robotic Things represents a new field in

robotics that has emerged through various stages of robotics development from networked robotic systems, ubiquitous robotics to cloud robotics. The term IoRT was first introduced in 2014 in ABI's technical report [18], and was referred to a concept in which sensor data obtained from many sensors are combined, processed in local or distributed processors and used to control or manipulate physical objects. Today, the term IoRT is also used to denote multi-agent robotic systems with robust team communication as well as IoT systems in which robots act as sensors.

Internet of Robotic Things in a broader way combines autonomous robotic systems with Internet of Things, intelligent connectivity, distributed and federated edge/cloud computing, artificial intelligence, digital twins, virtual/augmented reality and swarm technologies [19]. Things in IoRT are intelligent objects that interact and communicate using Internet and standard protocols used in wired and wireless networks. Robotic things have the abilities of interaction and cognitive abilities. Interaction between things is obtained with M2M communication, and IoT technologies provide the interaction between things and human. Cognitive abilities are referred to the abilities of robotic things to understand the connections between them and between the environment in which they are located, to understand the relations between objects and to estimate the impact that these relations have on the actions that robots take themselves. Cognitive abilities are obtained by ontologies used within the Internet of Things (semantic sensor networks, semantic web technologies), and Ontologies for Robotics and Automation (ORA) are widely used in the Internet of Robotic Things.

The IoRT concept implies the existence of distributed robotic systems organized in three basic layers (Fig. 4), in which exist wired and/or wireless intelligent connectivity networks, network controller nodes that collect, analyze and send data to other networks, processors that process data and algorithms, and cloud infrastructure.

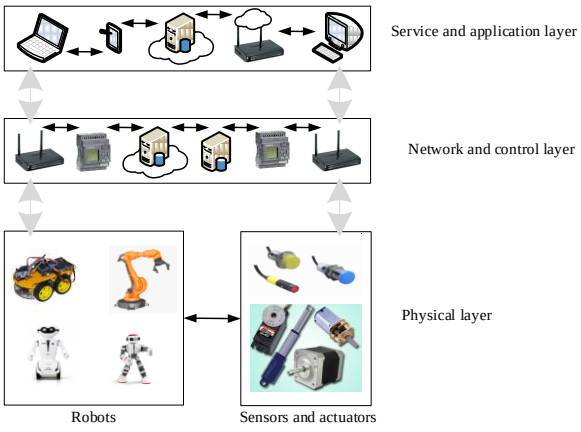

Fig. 4 *Internet of Robotic Things concept*

Future autonomous and connected IoRT systems must be able to sense, locate, think, connect, collaborate, learn and act, as shown in Fig. 5 [19]. All these are necessary for IoRT devices to properly detect, perceive and interpret the environment in which they operate, and to decide what actions to take and how to behave. In the scope of Industry 4.0 IoRT devices should be autonomous robotic systems capable of forming collaborative groups of heterogenous devices to be used in different applications. Here, concepts of networked, cloud and collaborative robotics are combined with each other. Features of Tactile Internet of Things (TIoT) and Internet of Things Senses (IoTS) enable IoRT devices to better interact with humans and cyber world. These features provide IoRT devices to become assistive robotics devices.

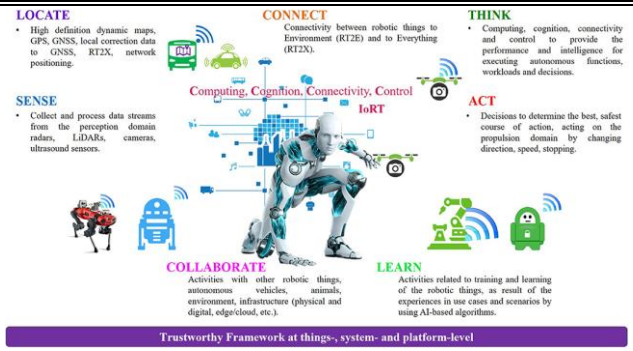

Fig. 5 *Future autonomous and connected IoRT systems* [19]

3. Robotics Concepts in Industry 4.0 Applications

Industry 4.0 concept has nine key technologies [20]: cloud, additive manufacturing, augmented reality, big data analysis, autonomous robots, simulation, horizontal and vertical system integration, Industrial Internet of Things, and cybersecurity. As concepts of networked, cloud and collaborative robotics, as well as IoRT fall under the Industry 4.0 domain, they can be used in various applications. The basic ideas of the Industry 4.0 concept are to take advantage of the global availability of the Internet and the use of the Internet of Things, to integrate technical and business processes, to perform digital mapping and virtualization of the real world, and to build smart factories that combine smart manufacturing and smart products. Smart manufacturing can fully be achieved using different robotics concepts.

Cloud robotics can be efficiently used within smart factories where autonomous robots connected to the cloud perform various tasks. In this sense, the concept of context-aware cloud robotics, which integrates Industrial Internet of Things and cloud robotics, has been proposed in [21]. When autonomous robots have to move around their workspace, they should be provided with navigation abilities. Navigation is a problem that has long been present in robotic systems. It concerns the problems of mapping (exploring the environment using sensors placed on the robot and obtaining the map of it) and localization (the ability of the robot to know its position in the environment it operates in). The use of cloud robotics provides enough space to store big data generated in the mapping process as well as computing resources to process that data while creating maps and searching existing ones. Cloud robotics enables changings in assembling process where robots manage to perform tasks previously performed by humans [22]. It also changed flexibility and extensibility of task scheduling in manufacturing [23].

Collaborative robotics is one the fundamental part of smart factories and smart production. The synthesis of cobots in the industry is underway in many different fields. Faster response time, more accurate patterns of movement, alignment capacity, human imitation capability - all of these factors lead to the advancement of cobot production [24]. Human-robot interaction in smart manufacturing should enable stable and cost-effective production. Collaborative robotics has already found its place in automotive industry. The leading automotive manufacturers use the cobots in the repetitive and precise task of equipping the inside of car doors, to apply an adhesive on a car roof, to perform screwing on a drive train in locations that are inconvenient to reach by a human operator, to loosen bolts and carry heavy components to relieve the workforce of these arduous tasks and speed up the manufacturing process, to work alongside humans in the production of direct-shift-gearboxes [25]. Universal Robots as one of the leaders in the cobot market listed the most common tasks that cobot can be used in: pick and place tasks, machine tending, packaging and palletizing of products, process tasks (gluing processing, dispensing, welding), finishing tasks (polishing, grinding, deburring), quality inspection of parts [10].

Internet of Robotic Things is the main enabler of manufacturing change, through which manufacturing is embracing the concepts of Industry 4.0 [23]. Internet of Things paradigm in the robotic systems enabled heterogeneous collaborative context aware robotic things to be used in many smart manufacturing applications. Using artificial intelligence, smart connectivity and interaction, robotic things behave more intelligently than robots belonging to collaborative or cloud robotics. Industrial operations that use information and operational technologies integrate supervisory control and data acquisition (SCADA) systems and programable logical controllers (PLC) connecting them with intelligent connectivity networks. Industrial robotics applications of IoRT include assembly, fault-finding, painting/varnishing, welding/soldering and delivery tasks [19]. All of them need to be performed precisely and in a case of an error, they have to be capable of doing corrections in a real-time. Assembly, painting, welding and delivery tasks require robotic things to have self-localization, navigation and path-planning abilities [4]. Robotic things can be used for logistics, delivery and moving objects (boxes, pallets, tools) between machines or storage areas. Collaborative mobile robotic things such as automated guided vehicles or lightweight mobile platforms can be used as fleets in warehouses and distribution centers and manufacturing intralogistics [19].

4. Conclusion

In this paper, some robotic concepts for Industry 4.0 applications are described. Networked robotics, cloud robotics, collaborative robotics and Internet of Robotic Things were studied as well as possibilities of their use in smart manufacturing. All of these concepts possess specific features which can be used on the way of meeting the requirements of the fourth industrial revolution. They provide flexible mass production without increasing costs, flexible and worker-friendly work environment, efficient use of natural resources and energy, and reduced production, logistics and quality management costs. The most promising concept on this way is Internet of Robotics Things. Although there are numerous examples of using IoRT concept in different application, there are a lot of challenges and difficulties to be resolved before it can be used in future Industry 4.0 applications. Some of the difficulties are related to communication technologies and 5G networks are seen to be a good solution to overcome them. This is the reason why the researchers in the field of IoRT and other advanced robotics concepts are very interested in resolving the problems. Intensive research on these topics is expected to continue in future, as well, and in that way come closer to realization of smart factories and smart manufacturing.

5. References

1. L. D. Xu, E. L. Xu L. Li, *Industry 4.0: state of the art and future trends*. International Journal of Production Research, (2018) 56:8, 2941-2962
2. A. Rojko, *Industry 4.0 Concept: Background and Overview*. iJIM, Vol. 11, No. 5, 2017, 77 – 90
3. Z. Gaoa, T. Wanyamaa, I. Singha, A. Gadhrria, R. Schmidt, *From Industry 4.0 to Robotics 4.0 - A Conceptual Framework for Collaborative and Intelligent Robotic Systems*, INTER-ENG 2019, Elsevier Procedia Manufacturing 46 (2020) 591–599
4. L. Romeo, A. Petitti, R. Marani and A. Milella, *Internet of Robotic Things in Smart Domains: Applications and Challenges*, Sensors 2020, 20, 3355
5. V. Kumar, D. Rus, G. S. Sukhatme, *Networked Robots*, Mobile and Distributed Robotics, 2008, DOI: 10.1007/978-3-540-30301-5_42
6. G. Hu, W.P. Tay, Y. Wen, *Cloud robotics: Architecture, challenges and applications*. IEEE Netw. 2012, 26, 21–28.
7. J. Kuffner, *Cloud-Enabled Robots*, in IEEE-RAS International Conference on Humanoid Robots, 2010.
8. J. Wan, S. Tang, H. Yan, D. Li, S. Wang, A.V. Vasilakos, *Cloud robotics: Current status and open issues*. IEEE Access 2016, 4, 2797–2807.
9. A.K. Bozcuoğlu, G. Kazhoyan, Y. Furuta, S. Stelter, M. Beetz, K. Okada, M. Inaba, *The Exchange of Knowledge Using Cloud Robotics*. IEEE Robot. Autom. Lett. 2018, 3, 1072–1079.
10. Universal robots, *An Introduction to Common Collaborative Robot Applications*, https://www.universal-robots.com/academy
11. M. Beaupre, *Collaborative Robot Technology and Applications*, Robotic Industry Assosiation - RIA, https://www.robotics.org/userAssets/riaUploads/file/4-KUKA_Beaupre.pdf
12. A. A. Malik, A. Bilberg, (2017). *Framework to Implement Collaborative Robots In Manual Assembly: A Lean Automation Approach*, Proceedings of the 28th DAAAM International Symposium, pp.1151-1160, B. Katalinic (Ed.), Published by DAAAM International, ISBN 978-3-902734-11-2, ISSN 1726-9679, Vienna, Austria, DOI: 10.2507/28th.daaam.proceedings.160
13. M. Knudsen, J. Kaivo-Oja, *Collaborative Robots: Frontiers of Current Literature*, Journal of Intelligent Systems: Theory and Applications 3(2) 2020: 13-20.
14. S. Bragança, E. Costa, I. Castellucci, & P. M. Arezes, (2019). *A Brief Overview of the Use of Collaborative Robots in Industry 4.0: Human Role and Safety*. Wandel Durch Partizipation, 641–650. doi:10.1007/978-3-030-14730-3
15. M. H. Miraz, M. Ali, P. S. Excell, R. Picking, *Internet of Nano-Things, Things and Everything: Future Growth Trends*. Future Internet 2018, 10, 68
16. P. P. Ray, (2016). *Internet of Robotic Things: Concept, Technologies, and Challenges*. IEEE Access, **4**, 9489–9500.
17. P. Simoens, M. Dragone, and A. Saffiotti, *The Internet of Robotic Things: A review of concept, added value and applications*, Internat. Journal of advanced Robotic Systems, 2018: I-II, doi: 10.1177/1729881418759424
18. D. Kara and S. Carlaw, *The Internet of Robotic Things. Technical Report*, ABI Research, 2014.
19. O. Vermesan, R. Bahr, M. Ottella, M. Serrano, T. Karlsen, T. Wahlstrøm, H. E. Sand, M. Ashwathnarayan and M. T. Gamba (2020) *Internet of Robotic Things Intelligent Connectivity and Platforms*. Front. Robot. AI 7:104. doi: 10.3389/frobt.2020.00104
20. M. Rüßmann et al., *Industry 4.0: The future of productivity and growth in manufacturing industries*, report Boston Consult. Group **9**(1), 54-89, (2015)
21. J. Wan, S. Tang, Q. Hua, D. Li, C. Liu, J. Lloret, *Context-aware cloud robotics for material handling in cognitive industrial internet of things*. IEEE Internet Things J. 2017, 5.
22. S. J. Khalid, *Internet of Robotic Things: A Review*, JASTT, Vol. 02, No. 03, pp. 78-90 (2021)
23. L. Romeo, A. Petitti, R. Marani and A. Milella, *Internet of Robotic Things in Industry 4.0: Applications, Issues and Challenges*, 7th International Conference on Control, Decision and Information Technologies (CoDIT'20), 2020, 177-182
24. M. Javaid, A. Haleem, R. P. Singh, R. Suman, *Substantial capabilities of robotics in enhancing industry 4.0 implementation*, Cognitive Robotics 1 (2021) 1–18, https://doi.org/10.1016/j.cogr.2021.06.001
25. S. El Zaataria, M. Mareia, W. Lia, Z. Usmanb, *Cobot programming for collaborative industrial tasks: An overview*. Robotics and Autonomous Systems, 2019 DOI: 10.1016/j.robot.2019.03.003

COMPARATIVE ANALYSIS OF HYDRAULIC SYSTEMS WITH ADAPTATION TO THE LOAD OF MOBILE MACHINES

СРАВНИТЕЛЬНЫЙ АНАЛИЗ ГИДРОСИСТЕМ С АДАПТАЦИЕЙ К НАГРУЗКЕ МОБИЛЬНЫХ МАШИН

Ph. D. in Eng. Assoc. Prof. Stasenko Dmitriy[1], Chief Designer Hinzburh Aleksander[2], Khazeyeu Yahor[3]
Pavel Sukhoi State Technical University of Gomel, Gomel, Republic of Belarus[1, 3]
OJSC "Gomel Special Design and Technical Bureau of Hydro-Pneumatic Automation", Gomel, Republic of Belarus[2]
E-mail: stasenko@gstu.by, ginsburg.gsktb@tut.by, hazeev@tut.by

Abstract: *The proposed comparative analysis of hydraulic systems of mobile machines allowed us to identify the advantages and disadvantages of the considered systems in terms of energy efficiency, which lays the foundation for further research of load-sensing hydraulic systems, and the analysis also allows us to develop a methodology for optimal selection of the type of hydraulic system for a particular type of mobile machine.*
KEYWORDS*: HYDRAULIC SYSTEMS, LOAD-SENSING, ENERGY EFFICIENCY, ENERGY BALANCE.*

1. Введение

В последнее время в области машиностроения появляется большое количество машин, гидравлические системы которых основаны по принципу адаптации к нагрузке, которые решают ключевую проблему одновременного дроссельного регулирования скоростей нескольких рабочих органов гидравлического привода – проблему излишнего уровня потерь мощности в гидросистеме. В гидравлических системах с адаптацией к нагрузке для управления входным давлением системы используется наибольшее давление на рабочем органе, таким образом, что за счет изменения давления на наиболее нагруженном рабочем органе, настроенном на постоянную величину контролирует входное давление гидравлической системы. Достоинствам гидросистем с адаптацией к нагрузке являются экономичность, низкие потери энергии, больший срок эксплуатации рабочей жидкости по сравнению с системами с дроссельным управлением. Недостатком таких систем является высокая стоимость элементов, а также трудности при ремонте и диагностике данных гидросистем [1].

Целью настоящей работы является сравнительный анализ эффективности систем с адаптацией к нагрузке различного типа.

2. Основная часть

2.1 Анализ гидросистемы с объемной адаптацией к нагрузке мобильных машин

Одним из видов широко применяемых гидросистем с адаптацией к нагрузке являются гидросистемы с объемной адаптацией к нагрузке. Массовость использования таких систем обусловлена тем, что по уровню потерь мощности данные гидросистемы являются более эффективными, нежели системы с дроссельным регулированием или системы с клапанной адаптацией к нагрузке. В качестве рассматриваемого примера гидросистемы с объемной адаптацией к нагрузке представлена гидросистема энергонасыщенного трактора «*Belarus 3022B*» [2].

В гидросистеме трактора «*Belarus 3022B*» Рис. 1, применяется регулируемый аксиально-поршневой насос. Секционный распределитель управляет подачей насоса, а для подпитки основного насоса используется шестеренный насос. Расход рабочей жидкости в гидросистеме трактора «*Belarus 3022B*» регулируется объемным способом при помощи аксиально-поршневого насоса с регулятором подачи. В результате чего максимальный расход, поступающий, к потребителю ограничивается за счет снабжения регулятором расхода 18 рис. 1, каждой рабочей секции распределителя гидросистемы [3].

Принцип действия гидросистемы трактора «*Belarus 3022B*» выполняется следующим образом: при нейтральном положении распределителя (секции 11,12,13) и не включенных магнитах канал *T*, давлением жидкости смещается золотник регулятора 2 основного насоса 1, таким образом обеспечивая подачу рабочей жидкости в цилиндр управления положением наклонной шайбы насоса 1, в итоге угол наклона становится меньше и производительность насоса падает до минимальных значений (с помощью пружины регулятора насоса 2 давление составляет около 1,5 МПа).

При смещении одного из золотников секционного распределителя в рабочее положение, давление также подается в канал управления *T*. В итоге возникает давление в правой полости регулятора 2 и золотник смещается влево, таким образом, под действием пружины поршень цилиндра управления положением шайбы перемещается, вправо увеличивая угол наклона, что приводит к повышению подачи насоса.

Поскольку перепад давления поддерживается постоянным определять подачу можно при помощи проходного сечения на золотнике распределителя. В фиксируемой позиции золотника (крайней правой) становится возможным «плавающее» положение рабочего органа машины, со сливом соединяется канал управления *T*, дающий возможность работы, на минимальных значениях подачи, насосу 1. При одновременном включении двух и более потребителей, система наибольшей нагрузки давления, подает сигнал по каналу *T* к регулятору насоса, при помощи которого повышается подача и давление в напорной гидролинии и становится равным суммарному. В результате возникает перепад давления, установленный пружиной регулятора 5, на проходном сечении золотника менее нагруженного потребителя, и к менее нагруженному потребителю поступает поток рабочей жидкости. Для ликвидации данного эффекта используется редукционный клапан 19, в каждую секцию напорной гидролинии *P*, который на золотнике менее нагруженного потребителя уменьшает перепад давления. Если подача основного насоса 1 и насоса подпитки 3 при одновременной работе потребителей превышает их суммарный расход, то одинаковый перепад давления будет сохраняться на всех золотниках, а размером проходного сечения распределительной секции будет определяться величиной расхода. Для того чтобы уменьшить утечки из закрытой полости гидроцилиндра при перемещении трактора установлены управляемые обратные клапаны 14, в рабочих гидролиниях. Обратный клапан 14 является необходимым для секций, рассчитанных для систем автоматического регулирования положением навесного оборудования, так как защищает от частого срабатывания системы позиционного регулирования. В сравнении с вариантами, где только при помощи золотника обеспечивается герметичность рабочей гидролинии в нейтральной позиции, при добавлении в систему обратных клапанов утечки рабочей жидкости уменьшаются более, чем в 4 раза. Для ограничения максимального расхода в систему установлены дроссели 18 [3].

Таким образом в тракторе «*Belarus 3022B*», установлена универсальная гидросистема управления рабочими органами с

регулирующим насосам, с объемной адаптацией к нагрузке управляемая при помощи пропорциональных и логических клапанов сравнивающих давление по сливу и напору.

Основным достоинством данной гидросистемы трактора является ее энергетические возможности таблица 1. Гидросистема работает с различными системами трактора независимыми друг от друга с гидравлической запиткой от одного насоса с регулируемым расходом. Такими системами в частности являются автоматическая система регулирования положения навесного орудия и система управления бортовыми, выносными гидроцилиндрами.

Таблица 1: *Параметры гидросистемы трактора*

Показатель	Значения
Мощность трактора	220 кВт
Максимальное давление	20 МПа
Максимальный расход	120 л/мин

Сравнительный анализ систем с адаптацией к нагрузке, возможно, выполнить, используя известные зависимости:

$$\Delta N_o = \Delta p_{LSO} \sum_{i=1}^{n} Q_i + \sum_{i=1}^{n} (\max(p_i) - p_i) Q_i$$

где: Δp_{LSO}– разность давлений между входным давлением гидросистемы и давлением на наиболее нагруженном рабочем органе (*LS*-перепад) для гидросистем с объемной адаптацией к нагрузке; p_i– давление в рабочей полости *i*-го исполнительного органа; Q_i – расход на *i*-м исполнительном органе.

Величина Δp_{LSO}, в гидросистемах с объемной адаптацией к нагрузке, задается настройкой регулятора насоса и регулятора разности давлений, входящего в состав гидросистемы. Значения настроенного *LS*-перепада для современных насосов различных производителей представлены в таблица 2, [4].

Таблица 2: *Значения настроенного LS-перепада для насосов различных производителей*

Тип насоса	*Производитель*	Δp_{LS}, *МПа*
A10VCO	*Bosch Rexroth AG*	1,8
HR02	*Linde Hydraulics*	2,0
VP1	*Parker Hannifin*	2,5

Таким образом, для гидросистем с объемной адаптацией к нагрузке характерной величиной *LS*-перепада согласно данным табл. 2 должно считаться значение Δp_{LS} = 1,8–2,5 МПа.

В гидроприводах с объемной адаптацией к нагрузке характерным уровнем максимального давления составляет от 10 до 25 МПа, но среднее значение максимального давления в гидросистеме p_0 за цикл является меньшим. Такие гидросистемы подразделяются на системы низкого (p_0<12 МПа), среднего (12 <p_0 <20 МПа) и высокого (p_0>20 МПа) давления [4].

Исходя из того, что гидросистема с адаптацией к нагрузке трактора «*Belarus 3022B*» является системой среднего давления, что требует использования в них дорогих аксиально-поршневых регулируемых насосов, которые конкурируют с нерегулируемыми шестеренными насосами. Стоит отметить, что шестеренные насосы отличаются низкой стоимостью и неприхотливостью в работе. Это означает, что без анализа факторов, влияющих на энергоэффективность и анализа рабочего цикла системы, применение гидросистем с объемной адаптацией к нагрузке, приводит к значительному повышению стоимости гидропривода.

Отметим, что в гидросистеме трактора «*Belarus 3022B*» не применяется регулируемый самовсасывающий насос, так как в реальных условиях эксплуатации регулируемый насос нуждаются в установке фильтра тонкой очистки на входе, поскольку гидропривод является требовательным к чистоте рабочей жидкости. Так же высокие требования к чистоте рабочей жидкости связаны с обеспечением защиты регулятора насоса от загрязнения. В результате насос лишается возможности самовсасывания, из-за установки на входе, фильтра тонкой очистки, это связано с большим гидравлическим сопротивлением фильтра, сопровождающееся падением абсолютного давления на входе в насос, до критически малых значений, следовательно, быстрый износ элементов насоса. В результате использование самовсасывающих насосов в гидросистеме трактора «*Belarus 3022B*» нежелательно, что подтверждается анализом гидросистем мобильных машин [1].

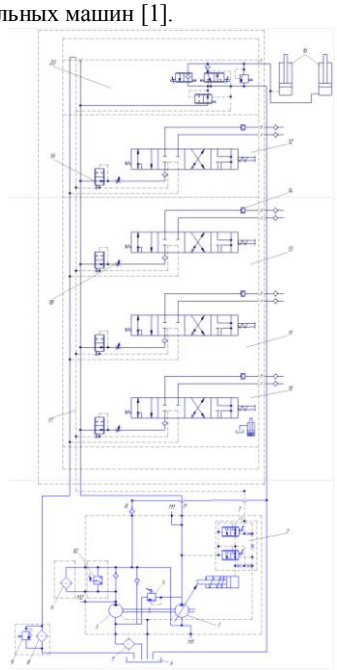

Рис. 1. *Схема принципиальная гидравлическая трактора «Belarus 3022B»: 1 – насос аксиально-поршневой; 2 – регулятор аксиально-поршневого гидронасоса; 3 – насос подпитки; 4 – масляный бак; 5 – клапан редукционный; 6,7,8 – фильтры; 9 – предохранительный клапан; 10 – реле давления (датчик засорения фильтра); 11,12,13 – секции выносных гидроцилиндров; 14 – обратный клапан; 15 – секция подъемника; 16 – гидроцилиндр подъемника; 17 – линия клапана управления; 18 – регуляторы расхода (дроссели); 19 – клапаны редукционные; 20 – регулятор; p – магистраль нагнетания; R – магистраль слива; T – магистраль управления; M1,M2,M3 – отверстия (порты) для подключения манометра*

Использование в гидросистеме трактора «*Belarus 3022B*» несамовсасывающего насоса, следовательно, подключение контура подпитки в гидросистему, ведет к возникновению дополнительных потерь мощности в сравнении с определяемым выражением (1), которое приобретает вид:

$$\Delta N_o = \Delta p_{LSO} \sum_{i=1}^{n} Q_i + \sum_{i=1}^{n} (\max(p_i) - p_i) Q_i + p_p Q_p$$

где: p_p и Q_p – давление в контуре подпитки и подача насоса.

В результате, чтобы трактора «*Belarus 3022B*» с объемной адаптацией к нагрузке был энергетически эффективным, необходимо, чтобы в среднем за рабочий цикл на исполнительных органах расход изменялся на величину, примерно превышающую на 13–15 % величину для систем среднего давления (12–20 МПа).

Данные результаты анализа показывают, что применение в тракторе «*Belarus 3022B*» гидросистемы с объемной адаптацией к нагрузке при реальных условиях эксплуатации разумное решение и применение другого типа гидросистем не рационально в данном случае.

2.2 Анализ гидросистемы с клапанной адаптацией к нагрузке мобильных машин

Другим типом, гидросистем с адаптацией к нагрузке, получивших широкое применение являются гидросистемы с клапанной адаптацией к нагрузке. В гидросистеме с клапанной адаптацией к нагрузке для поддержания постоянной разности давлений между входным давлением системы и наибольшим давлением на рабочих органах используются гидравлические клапана разности давлений. Примером гидросистемы с клапанной адаптацией к нагрузке является гидросистема машины рубильной *«Belarus MP-40»* [1].

В гидросистеме рубильной машины *«Belarus MP-40»* Рис. 2, применяется нерегулируемый аксиально-поршневой насос. Пропорциональные распределители *PVG 32* является чувствительным к нагрузке. Расход рабочей жидкости в гидросистеме машины рубильной *«Belarus MP-40»* регулируется клапанным способом с адаптацией к нагрузке при помощи данных пропорциональных распределителей [5].

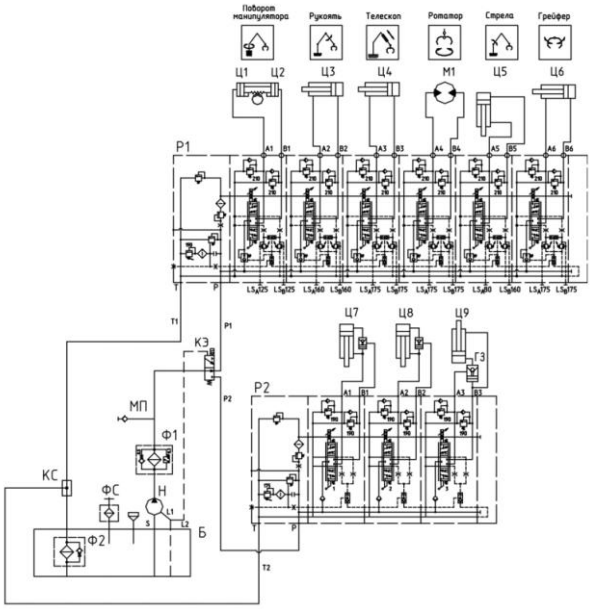

Рис. 2. *Схема принципиальная гидравлическая гидроманипулятора, аутригеров и кабины машины рубильной «Belarus MP-40»:*
Н – насос аксиально-поршневой; Б – бак; КЭ – клапан электромагнитный; КС – колодка сливная; М1 – гидромотор ротора; Р1, Р2 – распределители; Ф1, Ф2, ФС – фильтры; Ц1, Ц2 – гидроцилиндры поворота манипулятора; Ц3 гидроцилиндр рукоятки; Ц4 гидроцилиндр телескопа; Ц5 гидроцилиндр стрелы; Ц6 гидроцилиндр грейфера; Ц7, Ц8 гидроцилиндры аутригеров; Ц9 гидроцилиндр кабины; ГЗ гидрозамок

Ключевой особенностью работы гидросистемы рубильной машины *«Belarus MP-40»* является работа установленных в нее чувствительных к нагрузке распределителей Рис. 3. При включении насоса в нейтральном положении находятся золотники рабочих секций 1, следовательно, рабочая жидкость от насоса по подводу *P* через редукционный клапан 2 поступает в бак. Давление насоса (давление разгрузки), определяется расходом рабочей жидкости проходящей через клапан регулирования давления, то есть через редукционный клапан 2. При смещении одного или более золотников рабочих секций в пружинной полости золотника редукционного клапана 2 через контур логических клапанов «ИЛИ» 3 создается максимальное давление нагрузке, в результате чего прекращается подача рабочей жидкости в бак. В результате давление насоса смещает золотник редукционного клапана 2 влево. Если давление в системе превысит установленную величину, то открывается предохранительный клапан 4, и подача рабочей жидкости поступает от насоса обратно в бак. При включении рабочей секции с большей нагрузкой или при изменении нагрузки в системе, поддерживается перепад давления на главном золотнике в рабочей секции с компенсатором давления 5. Для защиты отдельных исполнительных органов машины от перегрузки в канале распределителя *A* используется подпиточный клапан *PVLA* 6, а в линии *B* рабочей секции с компенсатором давления встроен регулирующий *LS*-давление предохранительный клапан 7. Если давление в системе превысит заданную величину, то включается предохранительный клапан 7, регулирующий *LS*-давление, и поток рабочей жидкости, приблизительно 2 л/мин, через данный клапан направится в бак [6].

В гидросистеме рубильной машины *«Belarus MP-40»* Рис. 2. применяется два данных типа распределителей. Для аутригеров и кабины машины 3-х секционный пропорциональный распределитель «*PVG32»* и для манипулятора 6-ти секционный пропорциональный распределитель «*PVG32»*. Это позволяет обеспечить в гидросистеме отсутствие взаимных помех при совмещении рабочих операций нескольких исполнительных органов и индивидуально устанавливать величину давления для каждой рабочей гидролинии. Так же при работе системы наблюдается быстрое реагирование на требования системы к расходу и давлению, и питание нескольких исполнительных механизмов от одного нерегулируемого насоса.

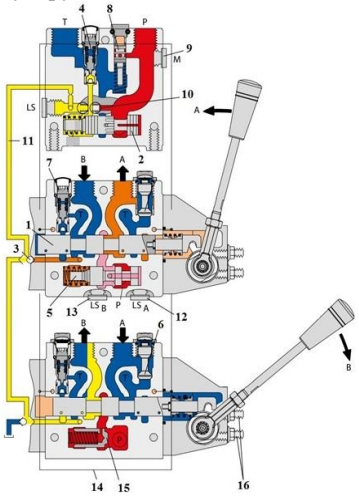

Рис. 3. *Чувствительных к нагрузке распределителей «PVG32»:*
1 главный золотник; 2 редукционный клапан; 3 логический клапан «ИЛИ»; 4 клапан ограничения давления; 5 компенсатор давления; 6 подпиточный клапан PVLA; 7 клапан, ограничивающий LS-давление; 8 редукционный клапан для подачи рабочей жидкости в контур управления; 9 порт для датчика давления; 10 заглушка; 11 LS-сигнал; 12 LS-соединение, порт A; 13 LS-соединение, порт B; 14 гидравлический контур управления PVE; 15 обратный клапан в линии P рабочей секции; 16 винты, регулирующие максимальный расход для портов A/B

Основные параметры работы гидросистемы рубильной машины «*Belarus MP-40*» представлены в табл. 3.

Таблица 3: *Параметры гидросистемы рубильной машины*

Показатель	Значения
Мощность рубильной машины	156 кВт
Максимальное давление	21 МПа
Максимальный расход	100 л/мин

Анализ систем с клапанной адаптацией к нагрузке по уровню потерь мощности, возможно, выполнить, используя известные зависимости [4]:

$$\Delta N = \Delta p_{LSK} \cdot Q_0 + \max(p_i) \cdot \left(Q_0 - \sum_{i=1}^{n} Q_i \right) + \sum_{i=1}^{n} (\max(p_i) - p_i) Q_i$$

где: Δp_{LSK} – разность давлений между входным давлением гидросистемы и давлением на наиболее нагруженном рабочем органе (*LS*-перепад) для гидросистем с клапанной адаптацией к нагрузке; p_i – давление в рабочей полости *i*-го исполнительного органа; Q_i – расход на *i*-м исполнительном органе; Q_0 – входной расход гидропривода (подача насоса) однопоточной системы с клапанной адаптацией.

Величина Δp_{LSK}, в гидросистемах с клапанной адаптацией к нагрузке, задается настройкой клапана разности давлений, входящего в состав пропорционального распределителя *PVG 32*. Значения настроенного *LS*-перепада для современных гидроаппаратов различных производителей представлены в табл. 4, [4].

Таблица 4: *Значения настроенного LS-перепада для гидроаппаратов различных производителей*

Тип гидроаппарата	Производитель	Δp_{LS}, МПа
РАМ	ОАО «ГСКТБ ГА»	не менее 0,6
M4-12	*Bosch Rexroth AG*	0,85-2,2
PVG32	*Danfoss*	0,5-1,5

Таким образом, для гидросистем с клапанной адаптацией к нагрузке характерная величина *LS*-перепада согласно данным табл. 4. должна считаться Δp_{LSK} = 0,7–1,8 МПа.

Применение в рубильной машине «*Belarus MP-40*» гидросистемы с клапанной адаптацией к нагрузке является разумным решением, поскольку показатель потери мощности в данной машине играет не ключевую роль. Для данной машины важным требованием является быстродействие, а по этому показателю гидросистемы с клапанной адаптацией к нагрузке являются одними из лучших на данный момент.

2.3 Сравнительный анализ гидросистем с адаптацией к нагрузке мобильных машин

Сравним энергетический баланс систем клапанной и объемной адаптации к нагрузке при полезной мощности [7,8]:

$$N_{пол} = \frac{85л/мин \cdot 12МПа}{60} = 17кВт;$$

Система с клапанной адаптацией к нагрузке:

$$N_{потр} = \frac{100л/мин \cdot 15МПа}{60} = 25кВт$$

Система с объемной адаптацией к нагрузке:

$$N_{потр} = \frac{85л/мин \cdot 15МПа}{60} = 21{,}2кВт$$

Энергетический баланс системы с клапанной и объемной адаптацией к нагрузке представлен на Рис. 4.

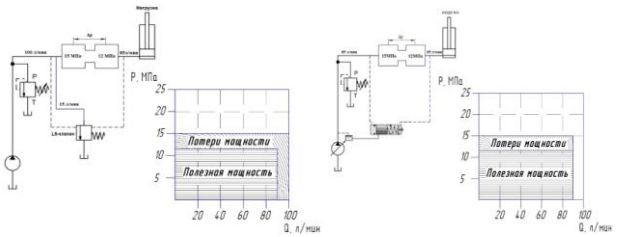

Рис. 4. *Энергетический баланс гидросистем: а) - гидросистема с клапанной адаптацией к нагрузке; б) - гидросистема с объемной адаптацией к нагрузке*

В результате сравнения гидросистема с объемной адаптацией к нагрузке имеет преимущество перед гидросистемой с клапанной адаптацией к нагрузке по уровню потерь мощности. Однако достоинством гидросистемы с клапанной адаптацией к нагрузке, является ее быстродействие (пример клапан разности давлений, регулирующий *LS*-перепад давления, значительно превосходит по параметру быстродействия машины использующие объемную адаптацию к нагрузке). Данный фактор позволяет системам с клапанной адаптацией к нагрузке составлять конкуренцию системам с объемной адаптацией к нагрузке. Дополнительным достоинством реализации принципа клапанной адаптации в гидросистемах по примеру рубильной машины «*Belarus MP-40*» является стоимость гидроаппаратов, которые стоят на порядок ниже, чем в системах с объемной адаптацией к нагрузке, но при этом стоит отметить, что машины с объемной адаптацией к нагрузке при более высокой величине давления работают более стабильней. Таким образом выбор применения в мобильной машине того или иного типа гидросистемы с адаптацией к нагрузке должен исходить из конкретных задач и функций мобильной машины.

3. Заключение

1. Анализ гидросистемы трактора «*Belarus 3022B*» показал, что применение принципа объемной адаптацией к нагрузке по показателю энергетической эффективности является весьма разумным решением нежели применение иных типов гидросистем. По показателю потерь мощности системы с объемной адаптацией к нагрузке являются одними из лучших систем, представленных в современном машиностроении, при соблюдении некоторых условий. В нашем случае выполнение условия изменения величины расходы, для системы среднего давления (12-20 МПа), на 13–15 % в среднем за рабочий цикл на исполнительных органах. Недостатком данного типа систем является высокая стоимость и сложность элементов системы.

2. Анализ гидросистемы рубильной машины «*Belarus MP-40*» показывает, что применение принципа клапанной адаптацией к нагрузке по показателю энергетической эффективности является не самым удачным решением по сравнению с объемной адаптацией к нагрузке. Однако по показателю быстродействия гидросистемы с клапанной адаптацией к нагрузке являются одними из лучших гидросистем, представленных в современном машиностроении, и для рубильной машины «*Belarus MP-40*» являются оптимальным решением на данный момент. Недостатком данного типа гидросистем является существенная ограниченность заданных параметров работы, при работе в системах со средним и высоким давлением, где клапанная адаптация к нагрузке проигрывает объемной по множеству факторов.

3. Мобильные машины использующие гидросистемы с адаптацией к нагрузке, меньше загрязняют окружающую среду и потребляют меньше топлива. Срок службы данных машин, до следующего ремонта на порядок выше. Также данные машины обеспечивают хорошую управляемость в широком диапазоне параметров. Однако на повсеместное внедрение данного типа систем до сих пор влияет существенным образом их динамические характеристики, которые требуют дальнейших исследований, так как при динамической работе гидросистемы с адаптацией к нагрузке склонны к нестабильной работе, следовательно, это приводит к увеличению риска внезапного торможения рабочих органов гидросистемы.

4. Литература

1. Гинзбург А.А. Дроссельное регулирование в гидросистемах и адаптация гидропривода к нагрузке (LS-принцип): курс лекций для студ. специальности 1-36 01 07 «Гидропневмосистемы мобильных и технологических машин» / А.А. Гинзбург. – Гомель: Издат. центр УО «ГТТУ им. П.О. Сухого», 2007. – 77 с.
2. Рунов А.В. Руководство по эксплуатации «Беларус 2522В/2522ДВ 2822ДЦ /3022В/3022ДВ» / А.В. Рунов – Минск: РУП «Минский тракторный завод», 2008. – 395 с.
3. Горин Г.С., Захаров А.В. Гидрооборудование тракторов «Беларус»: лабораторный практикум. В двух частях / Г.С. Горин, А.В. Захаров.–Минск: БГАТУ, 2008.– 60 с.
4. Гинзбург А.А., Стасенко Д.Л. Сравнение однопоточных гидросистем с объемной и клапанной адаптацией к нагрузке по уровню потерь мощности / А.А. Гинзбург, Д.Л. Стасенко – Минск: журнал «Механика машин, механизмов и материалов» 3-й выпуск, 2018. – С. 67–74.
5. Машина рубильная «Belarus MP-40». Руководство по эксплуатации «МР40-00010» РЭ – Мозырь: ОАО «Мозырский машиностроительный завод», 2009. – 129 с.
6. Technical information. Proportional distributors «PVG 32» Danfoss Power Solutions / Company Catalog «Danfoss Power Solutions» – Copenhagen, 2016. – 78.
7. Хазеев Е. В., Рогов С. А., Стасенко Д. Л. Анализ гидравлической системы с клапанной адаптацией к нагрузке // Исследования и разработки в области машиностроения, энергетики и управления: материалы XXI Междунар. науч.-техн. конф. студентов, аспирантов и молодых ученых, Гомель, 22–23 апр. 2021 г. В 2 ч. Ч. 1 / М-во образования Респ. Беларусь, Гомель. гос. техн. ун-т им. П. О. Сухого; под общ. ред. А. А. Бойко. – Гомель: ГГТУ им. П. О. Сухого, 2021. – с. 27.
8. Хазеев Е. В., Стасенко Д. Л. Анализ гидравлической системы с объемной адаптацией к нагрузке // Исследования и разработки в области машиностроения, энергетики и управления: материалы XXI Междунар. науч.-техн. конф. студентов, аспирантов и молодых ученых, Гомель, 22–23 апр. 2021 г. В 2 ч. Ч. 1 / М-во образования Респ. Беларусь, Гомель. гос. техн. ун-т им. П. О. Сухого; под общ. ред. А. А. Бойко. – Гомель: ГГТУ им. П. О. Сухого, 2021. – с. 31.

Selected manufacturing difficulties encountered during setup of machining on cnc multi-axis linear automatic lathe and on cnc multi-spindle turning centers

Piotr Sender
Faculty of Mechanical Engineering and Shipbuilding, Institute of Machines and Materials Technology,
Department of Machine Technology and Production Automation, ul. Gabriela Narutowicza 11/12, 80-233 Gdańsk, Poland
E-mail: piosend1@pg.edu.pl

Abstract: *The article presents the observed manufacturing technology implementation difficulties in workshop practice, resulting from the construction and principles of operation on the DMG's SPRINT 32/5 CNC linear automatic lathe and on the Mazak's HQR 150 MSY and QTN 200 MS CNC turn - mill centers, and discusses possible rules for solving the production problems encountered. The article also discusses the principles of dividing the machining process and working steps on multi-spindle CNC turn - mill centers. It is worth to build a system supporting the selection of the sequence of treatments [1], taking into account the frequency of natural vibrations and stiffness obtained after each single machining operations.*
The article shows the method of verification of the selection of the machining planning method on CNC multi-spindle lathes.
KEYWORDS*: CNC, MULTI-AXIS, MULTI-SPINDLE, MACHINING, LINEAR AUTOMATIC LATHE*

1. Introduction

Machine tool selection and part machining method can be a complex technological issue. Depending on the shape, quantity, dimension tolerance, and the geometrical dependence of the machining features, the workpiece made on multi-spindle turning centers can be produced in various ways. If you can choose a machine tool for conducting of machining, it is worth analyzing the benefits of using a specific type of machine tool.

The number of degrees of freedom and the length of machining features affect the choice of machine tool and machining method. The article describe the conclusions from the implementation of the CNC machining by the Author in Radmor S.A., and in Mechanika Radmor Sp. z o.o. in Gdynia in Poland, on a multi-axis machine tool, the commissioning of which eliminated the use of conventional cam lathes from production. The differences in starting production on CNC multi-axis linear machines and on the CNC milling-turning centers, which was discussed in article [2], were described.

The workpieces shown in the article were made on machine tools:

- Mazak QTN 200 MS - one turret, two spindles CNC turning center
- Mazak HQR 150 MSY - two turrets, two spindles CNC turning center
- DMG Sprint 32/5 – CNC linear automatic lathe, slider and stationary rail with tools, two spindles and the workpiece performs a work movement in the axial of manufactured bar direction (in the spindle Z axis)

It is worth to build a system supporting the selection of the sequence of treatments [1], taking into account the frequency of natural vibrations and stiffness obtained after each single machining operations. One of the key issues is to carry out the machining in an economic manner and to ensure that the required dimensional and shape tolerances are achieved.

Before machining, the workpieces should be classified in terms of:
the number of workpieces performed in machining series, workpiece's shape, type, size and machining tolerance of machined features.

For machine tools with the possibility of simultaneous machining on both sides of the turned workpiece, it is possible to divide the machining in a way that allows maximum length of the external feature with a diameter different from that of the input bar with length greater than 3 times bar's diameter to perform on CNC multi-axis linear automatic lathes with dividing of machining for MAIN and SUB spindles and additional with regarding to the feature shape and dimensions between different kind of CNC centers type.

2. Description and characteristics of the dual-flow dissymmetrical low pressure steam turbine

Fig. 1 shows elements made by Autor on the DMG Sprint 32/5 CNC linear automatic lathe, characterized by various degrees of machining difficulty, the number of necessary tools to perform the machining and the requirement to apply the required machining strategy, including the machining strategy consisting in dividing the machining area into sections shorter than the length of the guiding part of the carbide guide bush.

Fig. 1. *Workpieces made on CNC turning centre*

Important principles of turning on CNC multi-spindle turning lathes:
1. After fixturing of the workpiece on a CNC multi-axis linear automatic lathe, the length of the protruding length of machined object from the face of the collet of the auxiliary SUB spindle should be as short as possible
2. The length of the turned step of the workpiece on the MAIN spindle, with a few passes of the tool, cannot be longer than the length of the leading part of the guide sleeve, for multi steps machining on the whole length (without dividing of machine feature on shorter machining lengths)
3. The turned workpiece's machining side requiring more machining tools is machined on the MAIN spindle
4. If the length of the part machined on the MAIN spindle is longer than the leading part of the guiding collet, but it is possible to process it with one pass, this machining is performed as the last machining operation on the MAIN spindle
5. If the length of the turned feature on the MAIN spindle isn't shorter than the length of the guiding part of the guide sleeve, it should be capable of turning during one pass
6. If the length of the outside turning feature machined on the MAIN spindle is longer than the leading part of the guiding collet, and it isn't possible to process it with one pass, because the depth of

cut is too large, this machining have to be performed with shorter length in Z-axis direction, than the length of machined feature is

7. For linear machines with a rigid guide sleeve (set on one diameter dimension), bars with the smallest possible cylindricity deviation should be used - a very important parameter for setup of machining

8. The length of the turned-milled workpiece that can be transported after machining with the conveyor belt is limited and is less than the length of the workable part described as maximum length of turning

9. The constant value of the rotational speed for individual tools (the same for machining the entire workpiece), if possible allows to shorten the machining time

10. When extending the bar onto the bumper, the amount of pressure force against the bumper should be reduced for smaller bar diameters

Fig. 2 shows workpieces with different machining features. The workpiece shown in Fig. 2a has turning features: outer diameter, faces, axial hole, slots. The workpiece shown in Fig. 2b has turning features: outer diameter, center and off-center holes, slot, faces.

Workpiece shown in Fig. 2c requires, during turning on CNC automatic linear lathe, conducting of turning with a very long guide of guiding bush, the length of which, even in a special version, is too short to perform machining of the feature in several passes along the entire length in the direction of the Z axis (in the workpiece's and spindle's Z axis).

The following symbols will be used throughout the rest of this article: MAIN - main spindle, SUB - auxiliary (second) spindle.

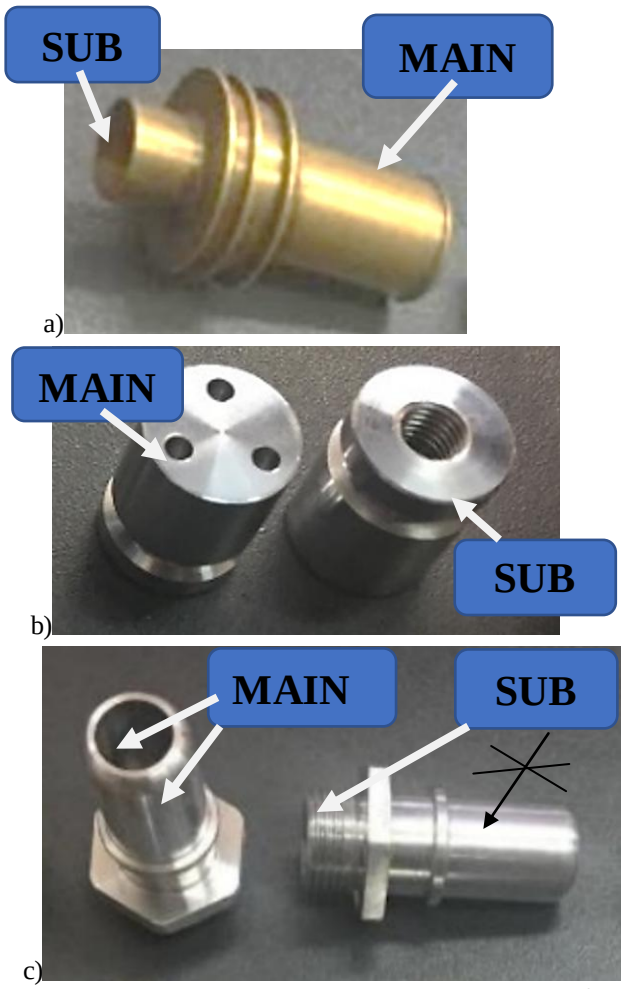

Fig. 2. *Turned workpieces: a) there is interchangeability of the MAIN and SUB machining sides, b) interchangeability of machining possible only when the SUB has the Y axis, c) the milled feature requires driven tools*

The individual workpieces shown in Fig. 2 represent a possible spectrum of items manufactured on CNC multi-spindle automatic lathes and on CNC multi-axis linear automatic lathes. Objects can be classified by weight and it can be assumed that Fig. 2a shows the workpiece of medium complexity and the most frequently made ones, Fig. 2b shows the objects that require the least amount of work to perform, while Fig. 2c shows the representative of the workpiece requiring the greatest amount of work, and the greatest amount of preparation time needing to start the machining on selected machine tool.

Figure 2c also shows the inability to process the indicated feature due to the inability to catch the workpiece for processing.

The most important thing regarding the issue of CNC turning linear automation lathe programming is verification of the possibility of guiding the bar through the carbide guide sleeve and the analysis of the possibility of symmetrically dividing the machining for both spindles MAIN and SUB that can be possible to simultaneously performing machining on both lathe's spindles.

Fig. 3 shows a sketch of the machining space of the DMG Sprint 32/5 machine tool.

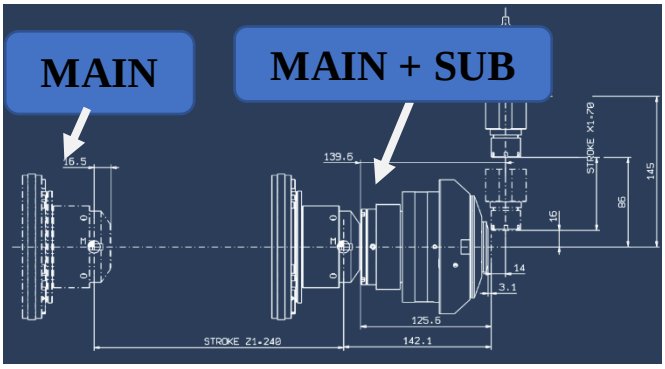

Fig. 3. *Working space of the DMG Sprint 32/5 linear automat*

Fig. 4 shows the 3D solid model of the Mazak's HQR 150MSY CNC multi-spindle lathe, which was implemented in the EdgeCAM software. The key issue before preparing of CNC program is to prepare the 3D solid model of a machine tools in a way to show the machining space with very high precision (no more than a few hundredths of a mm). Making a 3D solid of a CNC lathe with greater tolerance can cause a collision during machining. Attention should be clearly focused on the reliable preparation of the 3D machine tool body, especially of the machining space.

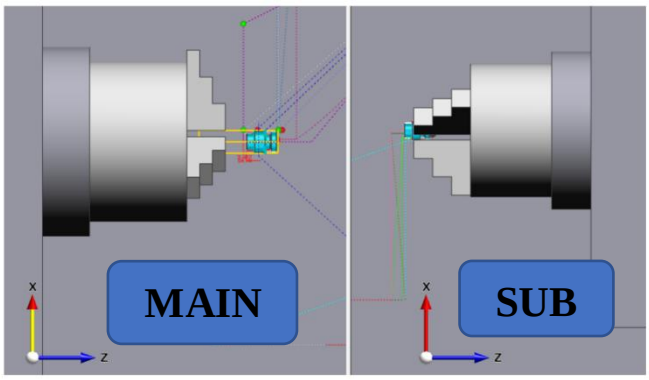

Fig. 4. *Machining space - view of the main spindle "MAIN" and the auxiliary spindle "SUB" of MAZAK HQR 150 MSY*

3. Preliminary analysis of the manufacturing method

When planning the machining process on a CNC multi-spindle turning center or on a CNC multi-axis automatic linear lathe, you should pay attention to several factors:

- Number of tools mounted in the MAIN spindle slide: C_1

- Number of tools mounted on the additional MAIN spindle holder: C_2
- Number of rotary tools for the MAIN spindle: C_3
- Number of rotary tools for SUB spindle: C_4
- Number of machining tools for the SUB spindle: C_5
- Total length of machined workpiece: L
- Length of the guide part of the guide sleeve in MAIN spindle: L_1
- Maximum length of insertion of the part into the SUB spindle: L_2
- Length of the part that can be ejected into the auto-feeder: L_3
- Length of the turning feature on the MAIN spindle: L_4
- Length of the turning feature on the SUB spindle: L_5
- Overhang of the part from the auxiliary SUB spindle: A
- Number of machining features for the MAIN spindle: X_1
- Number of machining features for the SUB spindle: Y_1
- Number of machining features requiring separate tools for machining features on the MAIN: X_2
- Number of machining features requiring separate tools to machine features on the
- SUB: Y_2

If is possible to manufacturing the workpiece, after checking $C_1 \div C_5$, X_1, X_2, Y_1 and Y_2 we should check further aspects:

If "A" is less than "L_3" it is possible to automatically collect machined workpieces by using a machined parts ejector and a conveyor belt.

Is there a machining feature length greater than the length of the guide part of the guide sleeve:
Z_1 = 0 NO (you can turn in traditional meaning of turning but with movement in Z direction of a machined bar)
Z_1 = 1 YES (you can turn only after dividing turning features on shorter length than the guiding part of guiding bush have)

Is there a turning feature length greater than the lead length of the guide sleeve and that requires turning in several passes:
Z_2 = 0 NO (you can turn on DMG SPRINT 32/5)
Z_2 = 1 YES (you can't turn on DMG SPRINT 32/5)

If Z_1 = 1 you can use Mazak's HQR 150MSY or QTN 200MS however, it should be remembered that in the case when the overhang of machined workpiece is longer than 3 diameters, it is necessary to support it with the tailstock of the lathe. The necessity for using of the tailstock will be when Z_2 parameter value is equal: Z_2=1.

4. Modal analysis - introduction

Analytical and numerical tests clearly show a change in the value of the natural frequency depending on the amount of material removed during turning process. On Fig. 5 shown simple sketch of turning process.

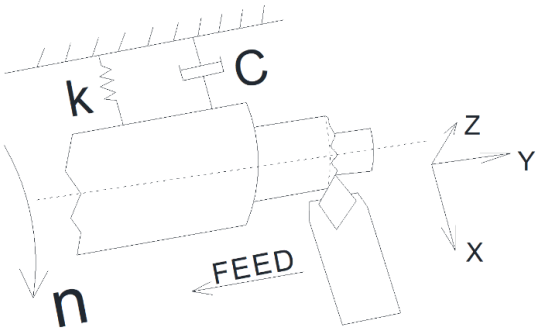

Fig. 5. Sketch of the turning process

Machining process, for example turning process, produces a machining force that is proportional to the chip thickness and chip width.

The machined tool used in turning process is stiff, but it is not infinitely stiff. The vibrating tool changes the chip thickness. Varying cutting forces due to varying chip's depth during turning produce vibrations of the turning tool. Variable forces cause vibrations and vibrations cause wavy surfaces, and than consequently wavy surfaces cause vibrations.
During turning, a very important phenomenon is the formation of self-excited vibrations, where, as we know, a slight change in parameters (the number of rotations) can drastically improve the course of the turning process. The knowledge of stability lobe diagrams and the problem of reduction or elimination of the formation of self-excited vibrations during the implementation of turning machining may determine the machining, e.g. in half the previously planned time value, with obtaining better parameters of the roughness profile of the machined surface (e.g. parameter Ra).

The time dependent chip thickness h(t) is determined as (formula 1):

$$h(t) = h_o + y(t - \mathrm{T}) - y(t) \quad (1)$$

where:
T – time for one rotation
y(t) – positive value current vibration of cutting tool
y(t – T) - positive value previous vibration of cutting tool

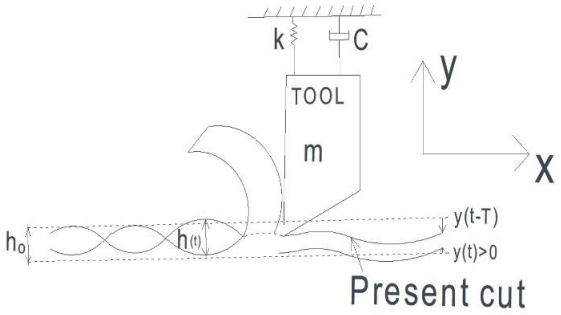

Fig. 6. *Sketch of the turning process (m – mass of the machining tool)*

Total cutting force received in turning process (Fig. 6) is described by formula 2.

$$F_n = k_s \cdot A = k_s \cdot b \cdot h_m \quad (2)$$

where: b – width of chip

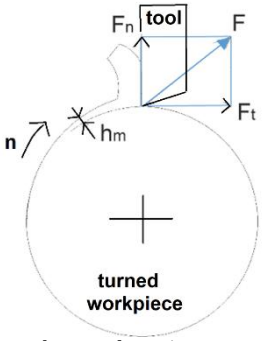

Fig. 7. *Sketch of the orthogonal turning operation*

Normal force F_n depends i.e. from the chip thickness h(t), and during turning (Fig. 7) the value of h(t) is changing its value (formula 3).

$$F_n = k_n \cdot b \cdot \mathrm{h(t)} = k_n \cdot b \cdot (h_m + \mathrm{y(t-\tau)} - \mathrm{y(t)}) \quad (3)$$

where: τ – time of one rotation

5. Modal analysis – numerical simulations

You can help with numerical finite element analysis FEA of turning process, which can help in finding, for example, the value of the natural frequency of a turned object. One possibility is to carry out several numerical analyzes for several production stages, after the turning operations of machining the turning features in a different sequence.

Characteristic data of the performed numerical FEA analysis are presented on Fig. 8.

Study Property	Value
Study name	Modal Study 1
Study Type	Normal Modes
Mesh Type	Tetrahedral
Iterative Solver	On
Number of modes	10
Frequency Range	Minimum: 0 Hz Maximum: 1e+04 Hz
NX Nastran Geometry Check	On
NX Nastran command line	
NX Nastran study options	
NX Nastran generated options	
NX Nastran default options	
Surface results only option	On

Aluminum, 6061-T6

Property	Value
Density	2712,000 kg/m^3
Coef. of Thermal Exp.	0,0000 /C
Thermal Conductivity	0,180 kW/m-C
Specific Heat	920,000 J/kg-C
Modulus of Elasticity	68947,570 MegaPa
Poisson's Ratio	0,330
Yield Stress	275,790 MegaPa
Ultimate Stress	310,264 MegaPa
Elongation %	0,000

Constraint Name	Constraint Type	Degrees of Freedom
Fixed 1	Fixed	FREE DOF: None

Mesh Information

Mesh type	Tetrahedral
Total number of bodies meshed	1
Total number of elements	55 449
Total number of nodes	82 269
Subjective mesh size (1-10)	10

Fig. 8. *Input data for modal analysis performed in SolidEdge*

The weight and stiffness of a turned workpiece changes during machining and depending on the machining method.

If we know the mass, stiffness, and the initial vibration conditions of the turned workpiece, we can describe how the workpiece will behave during turning operation.

Displacement Results

		Result component: Total Translation		
Extent	Value	X	Y	Z
		Mode 1, 2,996e+04 Hz		
Minimum	0 mm	6,250 mm	10,825 mm	-18,810 mm
Maximum	1,55e+04 mm	1,951 mm	9,808 mm	0,000 mm
		Mode 2, 2,996e+04 Hz		
Minimum	0 mm	6,250 mm	10,825 mm	-18,810 mm
Maximum	1,55e+04 mm	-9,808 mm	1,951 mm	0,000 mm

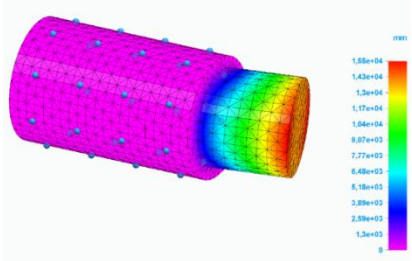

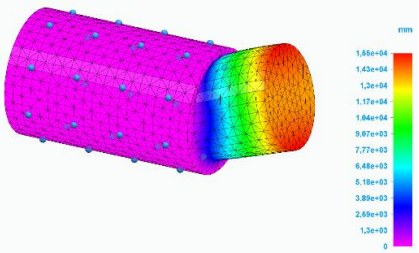

Fig. 9. *Natural frequency for the initial stage of turning*

Comparing the data shown in Fig. 9 and Fig. 10, it can be noticed that depending on the amount of material removed in turning process, different stiffnesses and different natural frequencies were obtained.

Displacement Results

		Result component: Total Translation		
Extent	Value	X	Y	Z
		Mode 1, 8,578e+03 Hz		
Minimum	0 mm	12,310 mm	-2,171 mm	-49,444 mm
Maximum	1,09e+04 mm	-3,701 mm	-9,290 mm	-0,000 mm
		Mode 2, 8,580e+03 Hz		
Minimum	0 mm	12,310 mm	-2,171 mm	-49,444 mm
Maximum	1,09e+04 mm	-9,076 mm	4,199 mm	-0,000 mm

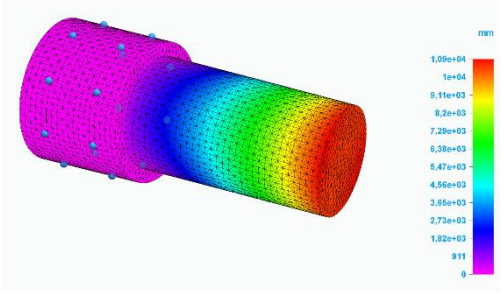

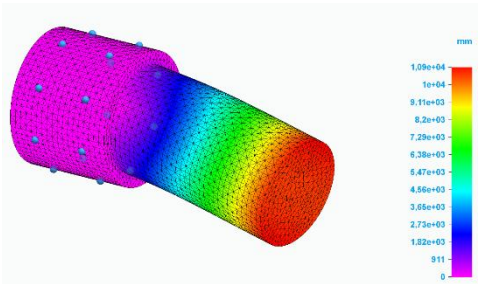

Fig. 10.*Natural frequency for the final stage of turning*

Different natural frequencies means different optimal value of machining parameters recommended for machining on turning centers.

7. Conclusions

In the case when it would be possible to machine the workpiece on different type of CNC lathes, for example on MAZAK QTN 200 MS (single-head, two-spindle machine), on the MAZAK HQR 150 MSY (two-head, two-spindle machine) but the FEA numerical simulations carried out will indicate that it is possible that the machining will not be stable (self-excited vibrations will develop), in this case it is worth to consider machining on e.g. CNC linear such as DMG SPRINT 32/5 multi-axis and multi-spindle linear lathe.

After each single machining and after each machining operation, the stiffness of the machined workpiece, and thus the natural frequency, changes.

It is worth to build a lathe system supporting the selection of the sequence of treatments, taking into account the frequency of natural vibrations for individual shapes and stiffness obtained after each single machining operations. Such a system could take into account, for example, what sequence of machining the features allows for machining with the greatest depth and the greatest feed, i.e. how to machine features successively so that the gradually changing

stiffness of the workpiece would allow maintaining a high value of machining parameters as long as possible.

In subsequent tests, experimental research will be carried out for turning with a constant and with variable rotational speed.

8. References

[1] Barylski, Adam; Sender, Piotr: The Proposition of an Automated Honing Cell with Advanced Monitoring. Machines 8, (4), 2000; pp. 70. DOI: 10.3390/machines8040070, 2020

[2] Barylski, Adam; Sender Piotr: The Production on Conventional and CNC Machines on the Example of the mill-turned workpiece, Mechanik (Poland) 07/2012, ISSN 0025-6552

Motorized low-cost 3d structured light scanning system for reverse engineering

Erald Piperi[1, *], Ilo Bodi[1], Luigi Maria Galantucci[2], Jorgaq Kaçani[3]
Polytechnic University of Tirana, Albania[1]
Politecnico di Bari, Italy[2]
Academy of Science, Albania[3]
epiperi@fim.edu.al

Abstract: *Recently, development in the 3D technology is becoming more evident. The diffusion of the acquisition systems is helped from the rapid evaluation of the information technology and Mechatronics, permitting low-cost system by using off-the-shelf hardware (webcam, projectors, etc.) for 3D scanning. This paper is focused on the development, implementation and testing of an automated low cost motorized active 3D structured light scanning system (SLS). The scanner is based on the software platform of the DAVID Laser Scanner Vision Systems GmbH's. Advanced of basic technologies for comparing the scanned data, will show the differences in performance of the 3D data acquisition with a test to reference approach with a commercial scanning system.*
KEYWORDS*: 3D SCAN, STRUCTURED LIGHT SCAN, REVERSE ENGINEERING, OPEN-SOURCE, CODED STRUCTURAL LIGHT*

1. Introduction

Nowadays, 3D technology has gained attention in different areas. The main scope is creating a replica of the 3D object. The generation of 3D CAD models is usually the first step in a rapid prototyping (RP) system [1]. The term rapid prototyping (RP) refers to a class of technologies that are used to produce physical objects layer-by-layer directly from CAD data [2].

There are various scanning systems used for 3D scanning. The diffusion of the acquisition systems is helped from the rapid evaluation of the information technology and Mechatronics, permitting low-cost system by using off-the-shelf hardware (webcam, projectors, etc.) for 3D scanning [3]. Of the many available techniques, Structured-light Scanning (SLS) systems have emerged as the most cost-effective and accurate method to capture the 3D geometry and appearance of a real object [4]. Structured light triangulation has become the method of choice for shape measurement in several applications including industrial automation, graphics etc [5]. Scanners that use structured light are in general faster than laser based devices but require longer signal processing [6]. In these systems, specific light patterns are projected onto the object and at least one camera in applied to observe these distorted patterns of object surface [7]. Different calibration approaches have been developed for this type of systems, which computes the intrinsic parameters of the perspective camera and light emitter as well as the relative position with respect to one another [8].

Compared to passive image-based approaches, active sensors provide directly and quickly 3D information of the surveyed object in form of range data (point clouds) [9].

2. Materials and methods

Structured light systems are used for different type of 3D object reconstruction. The scanning systems used in our work, use the triangulation principle for capturing scan data Fig. 1. David structured light scanning system (SLS) use Binary code and Phase shifting. It projects multiple phase shifting patters of a single frequency. David we use the Random Sample Consensus (RANSAC) based algorithm for coarse registration combined with a subsequent ICP for fine registration (optimizing the coarse solution). In coming sections, we are going to present a more detailed explanation of the possibilities that David software has for individual customizations.

3. Experimental work

Our scanning system consists of a low-cost 3D structured light system (SLS) based on the software platform of the DAVID Vision Systems GmbH's DAVID-Laser Scanner. The shelf hardware and equipment's as light projector, web camera and also open-source software can be used for 3D scanning systems [11]. The video projector TOSHIBA TDP S8 (resolutions 1400x1050) was used to project a number of stripe patterns onto the object. To obtain a higher resolution of single scans, we used "Default" pattern parameter, with 26 number of patterns both horizontals and vertically. The camera used has a CMOS sensor model uEye UI-1480-C (5MPixel, 6f/s, CE class A of regulation) and the optic lenses used is Fujinon 1: 1.4/12.5 mm HF12.5HA-1B. Once, the camera and structured light emitter (projector) is calibrated, the field of view of the sensor remains fixed by maintaining constant the distance R from the object Fig. 1. This range will be always in the depth of field of the sensor.

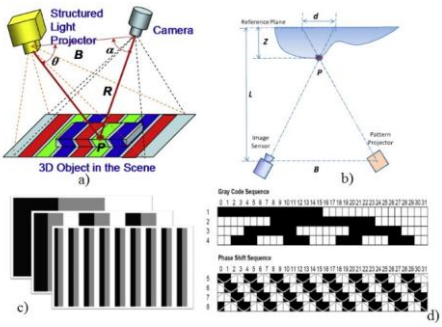

Fig. 1. *a) Illustration of structured light; b) calculation of the Z depth; c) gray level coding patterns; d) combining gray code with phase shift [10]*

David 3D scanning software has the capability to send and receive commands through a serial port using letters or numbers. This allows to simply create different inputs and outputs for the other control software. Customizing the Command options, it is possible to execute by David software an action connected with that command sending to the serial port special codes represented by letters identifying various commands [3] Fig. 2.

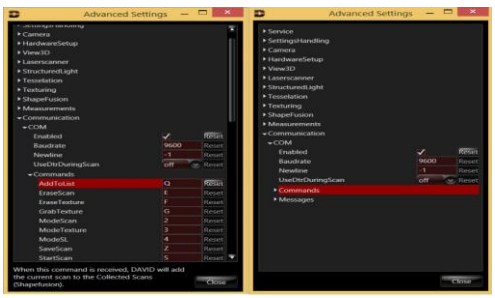

Fig. 2 *Advanced setting in David software*

The setup performed is:

1. Enable the port communication and the "Baudrate" to 9600.

2. Define in "Commands"

a. the letter code "Q" to perform "AddToList"

b. the number code "4" to prepare the system for structured light scanning (SLS) in "ModeSL"

3. Define in "Message"

a. "N" code letter the field "NextSLPattern"; this is necessary for the counting of the number of patterns that David send out for scanning.

Before starting the scanning process, we need to choose the resolution and the parameters in the hardware setup. For having a full scan, we need to rotate the motor 6 time by 60 degrees. For our scans we used a non-standard calibration board with 108.233 mm calibration scale.

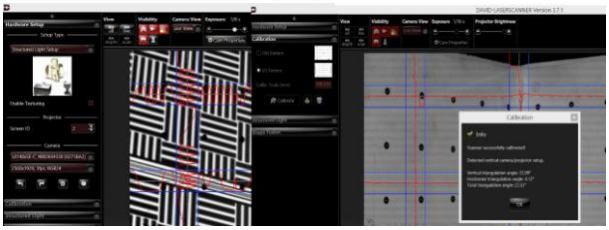

Fig. 3 *Hardware setup and calibration procedures*

After the calibration process results successfully completed, we are ready to perform the full scans process. The schematic setup and the real scanning process of David laser scan is show in Fig. 4 .

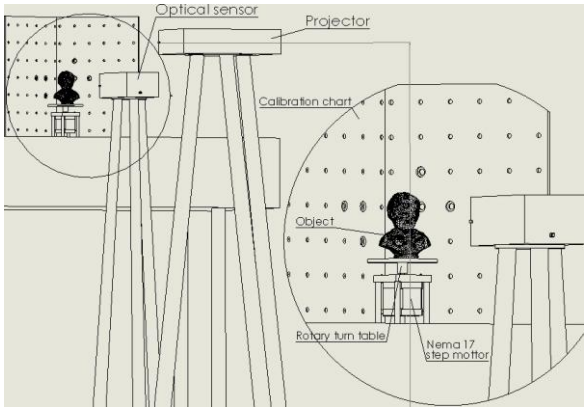

Fig. 4 *David SLS schematic view*

3.1 Rotary table configuration and setup

For performing a full scan, we have built a simple computer controlled rotary table, based on a stepper motor and an open-source Arduino single-board microcontroller. The hardware Arduino Mega 2560 can take inputs from a variety of switches or sensors, and controlling a variety of lights, motors, and another physical sensor. Arduino projects can communicate with software running on the PC [12]. We need to use a breadboard for circuit designed, a L293D quadruple high-current half-H drives for driving the stepper motor. A NEMA 17, 2 phase step motor power 5VDC 0.5A with a steep angle 3.75° was used to rotate the object on the turntable. For a 360° full scan we need 96 steps. As a power source, we used of the shelf hardware, an old PC power supply unit. The schematic connection with all input and outputs pins are shown in Fig. 5. For communicating and controlling David SLS scan and the motor a program inside the Arduino has been compiled.

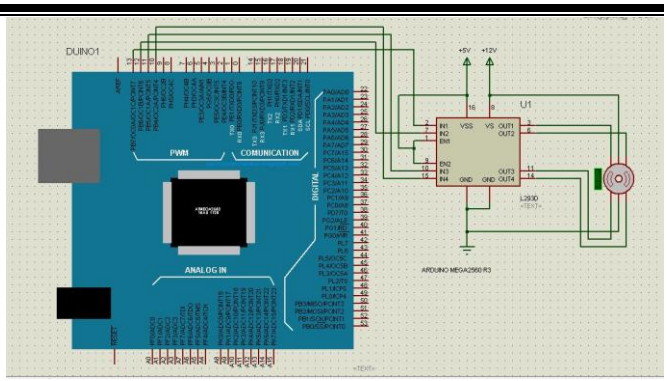

Fig. 5 *Schematic connection for controlling the turntable by Arduino Mega*

4. Results

A qualitative analyze, based on indirect comparison shows the performance of our implemented scanning systems. A test-to-reference data analyze is performed for two complex parts. The first model used for data comparison is a small medium size artistic ceramics statue with 100 mm height, representing freeform geometry Fig. 6 (A). The second model used, is pyramid 60x60x32mm made by resin for molds, and produced in a CNC milling machine, by having same incorrectness from production Fig. 6 (B). Its geometry represents plane parallel surfaces, holes, step planes, end gauges which are some of the main characteristics of artifacts for reference objects used in metrology.

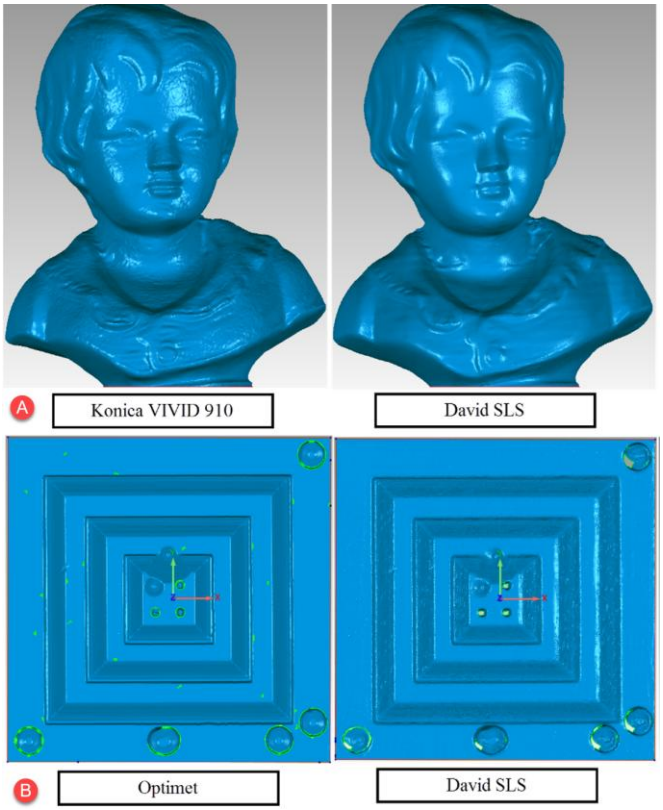

Fig. 6 *A) David Statue figurine; B) Pyramid*

A quantitative comparison of 3D models of the same objects taken by reference systems Optimet ConoScan 3000 and Konica VIDID 910 , was done using Geomagic Studio™ software [13]. The results of the Pyramid comparison between David SLS and Optimet are shown in Fig. 7 and data comparison for the David statue figurine in Fig. 8.

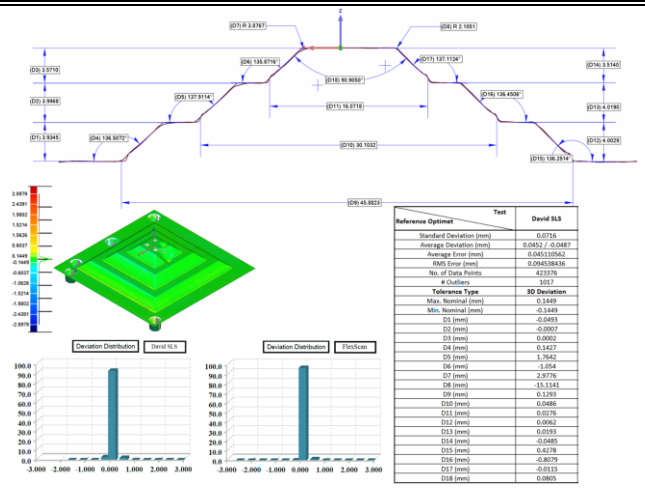

Reference Optimet \ Test	David SLS
Standard Deviation (mm)	0.0716
Average Deviation (mm)	0.0452 / -0.0487
Average Error (mm)	0.045110562
RMS Error (mm)	0.094538436
No. of Data Points	423376
# Outliers	1017
Tolerance Type	**3D Deviation**
Max. Nominal (mm)	0.1449
Min. Nominal (mm)	-0.1449
D1 (mm)	-0.0493
D2 (mm)	-0.0007
D3 (mm)	0.0062
D4 (mm)	0.1427
D5 (mm)	1.7642
D6 (mm)	-1.054
D7 (mm)	2.9776
D8 (mm)	-15.1141
D9 (mm)	0.1293
D10 (mm)	0.0486
D11 (mm)	0.0276
D12 (mm)	0.0062
D13 (mm)	0.0193
D14 (mm)	-0.0485
D15 (mm)	0.4278
D16 (mm)	-0.8079
D17 (mm)	-0.0115
D18 (mm)	0.0805

Fig. 7 *Data analyze for pyramid*

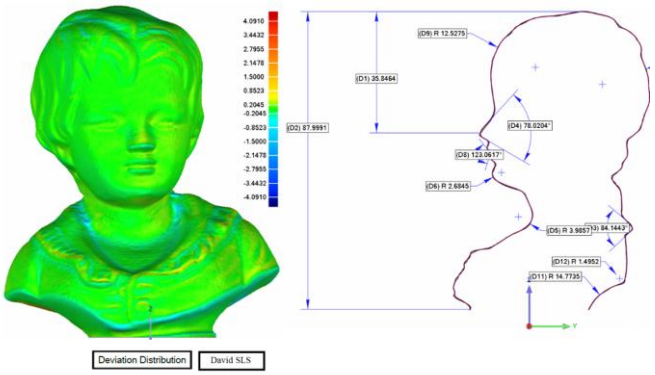

Reference Konica VIVID \ Test	David SLS
Standard Deviation (mm)	0.1698
Average Deviation (mm)	0.1047 / -0.1277
Average Error (mm)	0.099956793
RMS Error (mm)	0.174175365
No. of Data Points	475255
# Outliers	150
Tolerance Type	**3D Deviation**
Max. Nominal (mm)	0.0859
Min. Nominal (mm)	-0.0859
D1 (mm)	0.1119
D2 (mm)	-0.186
D3 (mm)	9.4251
D4 (mm)	3.9571
D5 (mm)	-1.513
D6 (mm)	-0.0267
D8 (mm)	33.8588
D9 (mm)	0.3206
D10 (mm)	0.412
D11 (mm)	2.4596
D12 (mm)	1.3841

Fig. 8 *Data analyze for statue figurine*

5. Discussion

The creation of semi-automatic low cost SLS system based on open-source hardware/software can permit users to create powerful algorithm codes for fast data capture and why not to be fully automatic process. David software is user friendly and can be modulated in different ways regarding its possibilities of sending and receiving command to different hardware/software connected to the systems. The time needed for David SLS system for data acquisition and processing (in default mode) is more than 90 sec. Especially when a high level of smooth average and quality check is chosen in David the tame for data processing can be higher. The time needed by our semi-automatic system for six single scans data acquisition and processing was 6.5min. The system resulted to have no problems working in laboratory condition with normal lights illumination.

6. Conclusions

The scope of our work was creation of semi-automatic low cost SLS system based on open-source hardware/software. In further publication by author David laser scan scanning software resulted do integrate very well with not only open-source software but even with standard equipment which have a motorized movement system as CNC machines [3]. Using low-cost systems for digitizing 3D object offer the potential for users to construct and implement a scanning system which has good performance with semiprofessional ones. These to be clear not that these user-build system are going to substitute the commercial scanning system in the dedicated areas. But with a good know-how experience users can obtain adequate results in the range of microns to millimeters.

From the results taken, we did not encountered problem with medium reflective surface, but problems can occur when dealing with metallic objects because of their higher reflective surface.

7. References

[1] D. Page, A. Koschan, S. Voisin, N. Ali and M. Abidi, "3D CAD model generation of mechanical parts," Assembly Automation, vol. 25, no. 3, p. 230–238, 2005.

[2] V. Raja and K. J. Fernandes, Reverse engineering : an industrial perspective, Springer Series in Advanced Manufacturing, 2009.

[3] L. M. Galantucci, E. Piperi, F. Lavecchia and A. Zhavo, "Semi-Automatic Low cost 3D Laser scanning systems for reverse engineering," in 3rd CIRP Global Web Conference, 2014.

[4] K. Herakleous and C. Poullis, "3DUNDERWORLD-SLS: An Open-Source Structured-Light Scanning System for Rapid Geometry Acquisition," Immersive and Creative Technologies Lab, Cyprus University of Technology, 2014.

[5] M. Gupta, A. Agrawal, A. Veeraraghavan and S. G. Narasimhan, "Structured Light 3D Scanning in the Presence of Global Illumination," in IEEE Computer Society Conference on Computer Vision and Pattern Recognition (2011), 2011.

[6] I. Stanc˘ic´, J. Music´ and V. Zanchi, "Improved structured light 3D scanner with application to anthropometric parameter estimation," Measurement, vol. 46, no. 1, p. 716–726, 2013.

[7] H. Cui, Y. Li and C. Li, "Strategy for 3D Reconstruction of Industrial Rubber Part," JOURNAL OF COMPUTERS, vol. 7, no. 2, pp. 458-463, 2012.

[8] C. Paniagua, L. Puig and J. J. Guerrero, "Omnidirectional Structured Light in a Flexible Configuration," Sensors 2013, vol. 13, pp. 13903-13916, 2013.

[9] D. Akca, "3D MODELING OF CULTURAL HERITAGE OBJECTS WITH A STRUCTURED LIGHT SYSTEM," Mediterranean Arhaeology and Archaeometry, vol. 12, no. 1, pp. 139-152, 2012.

[10] J. Geng, "Structured-light 3D surface imaging: a tutorial," Advances in Optics and Photonics 3, p. 128–160 , 31 March 2011.

[11] T. Spahiu, J. Kacani, E. Shehi and E. Piperi, "3D Body Scanning Technique for Anthropometric Measurements and Custom Clothing Design," in U3M-AL, 2014.

[12] "Arduino," Interaction Design Institute Ivrea, Italy, [Online]. Available: www.arduino.cc/en/Guide/ntroduction. [Accessed 11 November 2014].

[13] 3D. System, 333 Three D System Circle, [Online]. Available: http://www.3dsystems.com/about-us. [Accessed 10 11 2014].

Impostation of an experimental design for studying the optimization of artificial aging process for the aluminium alloys

Irida Markja
Faculty of Mechanical Engineering, Polytechnic University of Tirana, Albania
*imarkja@fim.edu.al ; irida.markja@gmail.com

Abstract: *New area industry of Albania, in recent years, factories with closed cycle of production and processing of aluminium alloys are being targeted. In Albania about 25,000 tons of aluminum alloys per year are produced and there is a tendency to increase this production. This reality has encouraged us to undertake a number of studies with the primary objective for optimizing the parameters of the basic process of this industry. In this article we focus on the process of artificially aging aluminum alloys. From early and newer studies [2], the importance and delicacy of temperature-time parameters in the evolution of microstructure and in the mechanical properties of the final product are recognized and underlined. We have impost an experimental planning based on the Response Surface Method by choosing Central Composite Design to optimize the temperature and time parameters for the artificial aging with the objective of maximizing the process indicator - mechanical properties, hardness in our case. The plan includes 13 tests with 5 replicas in the center of the experiment, built with the help of Design-Expert DX7 and DX13 software. The focus of our attention was the assesment of the design, analysis of residuals and diagnostic diagrams and forms of presentation of results: mathematical model, 3D response surface, isocontours and* effects *of interaction between factors. In the future works we will present the experimental results of the optimization of the artificial aging process for different aluminium alloys produced in Albania.*
Keywords*: RSM, CCD, ALUMINIUM ALLOY, AGING, OPTIMIZATION, DESING EXPERT*

1. Introduction

On the production and processing industry of aluminum in Albania

Starting from the 90s and especially after the 2000s in Albania, many factories and companies have been set up with the main object of processing aluminum and its alloys, mainly for the production of aluminum profiles. Today there are several dozen of them. Some of the largest companies have included in their production scheme the foundry line for the production of aluminum alloys based on recycled materials. Each of these companies produces from the foundry approximately five thousand tons per year. The aluminum produced is processed almost entirely in the country. To respond to the challenges of meeting the ever-increasing demands of quality products as most of them are mainly destined for export to developed countries. This industry is turning its attention to the university unlike what happened before. To respond to this new industrial reality we have planned and are undertaking a series of researches starting with the optimization of the parameters of artificial aging of aluminum alloys.

On the importance of the process of artificial aging of aluminum alloys

The industry of production and processing of aluminum alloys in Albania is in the early stages of its development and as such feels the need for studies in support of it and especially for the optimization of key processes. One of the processes that gives the impront to the mechanical properties of products made of aluminum alloys is that of artificial aging, as the final process of thermal processing. From earlier, but also newer studies, the importance and delicacy of artificial aging of aluminum alloys is recognized and underlined. Indeed, it is a process of strengthing oo the alloys by managing the transformation of a supersatureted solid solution. During this process, the formation and growth of precipitate particles of the second phases from the supersaturated solid solution occurs. It is a process that is controlled by the diffusion of atoms of dissolved elements and as such significantly influenced by the parameters of the process temperature and time, for a given chemical composition of the alloys and a optimized homogenization annealing. The characteristics of precipitated particles depend on the temperature and time parameters of artificial aging: size, distribution, relative quantities which determine the degree of strengthening of the alloy. Precisely for these reasons, we are undertaking a series of studies to optimize the parameters of the artificial aging process of aluminum alloys produced in Albania with the objective of maximizing mechanical properties, starting from hardness.

2.Choosing the Experiment Plan

Among the plans that offer optimization of the indicators we have chosen the Response Surface Method - **RSM**, and Central Composite Design - **CCD**. The CCD plan offers more experiment points compared to the simple factorial plan, while maintaining a minimum total number of tests. The CCD plane also offers the rotary property, which means that the same error is stored at a certain distance from the center of the experiment. The response surface method, as an optimization method, was developed in the 1950s and was first applied in the process industries (chemical, metallurgical, etc.). This method constitutes the optimization technique based on the programming of the most widespread and successful experiments even today. [5] Our e experimental plan was draft on recent industrial development in which was applied this experimental plan and also on the latest articles, scientific research regarding the experimental plan. [6]

3. Impostation of our CCD experimental plan

The primary objective of this study is to optimize the process of artificial aging of aluminum alloys, in order to maximize the mechanical properties, strength, tensile strength, hardness. For the construction of the plan we have chosen as the center of the experiment the value of the process parameters, temperature and aging time, approximate to the values applied by the manufacturers for some aluminum alloys: temperature T = 185 ^{o}C, time t = 8h. As a step value for these two parameters we have chosen: $\Delta T = 15\ ^{o}C$, $\Delta t = 3h$. These step values provide approximately the same change / effect on the process indicator (hardness), considered different bibliographic sources (Fig.1).

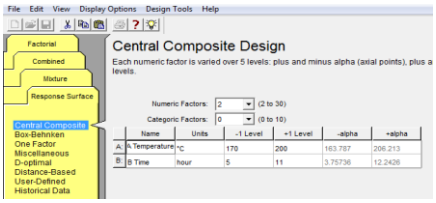

Fig.1 *From application to software for imposting the experiment plan*

For the star points arm, based on the recommendation in the Desing Expert tutorial, we have accepted the value +/- √2 (α = +/- 1.4214).

By entering this data, for *Factor A - Temperature* and *Factor B - Time*, in the software Design - Expert (RSM Method, CCD Plan), we obtain the Experimental Plan Table (Tab.1). In the experimental plan table are presented according to the factor combination and according to the order of the performing tests: *run*.

Table 1: *Experimental plan table for the experiment*

	Std	Run	Block	Factor 1 A: Temperature °C	Factor 2 B: Time h	Response 1 Hardness HBN
	5	1	Block 1	163.7867966	8	
	4	2	Block 1	200	11	
	1	3	Block 1	170	5	
	7	4	Block 1	185	3.757359313	
	8	5	Block 1	185	12.24264069	
	13	6	Block 1	185	8	
	3	7	Block 1	170	11	
	6	8	Block 1	206.2132034	8	
	12	9	Block 1	185	8	
	10	10	Block 1	185	8	
	11	11	Block 1	185	8	
	2	12	Block 1	200	5	
	9	13	Block 1	185	8	

In the experimental plan table all the tests are presented according to the combination of factors as well as according to the order of performing the tests (run). To demonstrate the method, we have obtained, for the indicator *"hardness-HRB"*, approximate results from various bibliographic sources and our unpublished works.

4. Analysis of Variance, ANOVA

The result of the analysis of variance (ANOVA) processed by the software is given in the following table (Tab.2)

Table 2: *Anova for response surfare quadratic model*

Transform | Fit Summary | Model | ANOVA | Diagnostics | Model Graphs

Use your mouse to right click on individual cells for definitions.

Response 1 Hardness

ANOVA for Response Surface Quadratic Model

Analysis of variance table [Partial sum of squares - Type III]

Source	Sum of Squares	df	Mean Square	F Value	p-value Prob > F	
Model	967.41	5	193.48	30.17	0.0001	significant
A-A Temperatur	*101.93*	*1*	*101.93*	*15.89*	*0.0053*	
B-B Time	*272.59*	*1*	*272.59*	*42.50*	*0.0003*	
AB	*182.25*	*1*	*182.25*	*28.41*	*0.0011*	
A²	*151.23*	*1*	*151.23*	*23.58*	*0.0018*	
B²	*308.79*	*1*	*308.79*	*48.14*	*0.0002*	
Residual	44.90	7	6.41			
Lack of Fit	*36.10*	*3*	*12.03*	*5.47*	*0.0671*	*not significant*
Pure Error	*8.80*	*4*	*2.20*			
Cor Total	1012.31	12				

Interpretation of ANOVA table for our ezperimental data: The Model F-value of 30.17 implies the model is significant. There is only a 0.01% chance that a "Model F-Value" this large could occur due to noise. Values of "Prob > F" less than 0.0500 indicate model terms are significant. In this case A, B, AB, A2, B2 are significant model terms. Values greater than 0.1000 indicate the model terms are not significant. If there are many insignificant model terms (not counting those required to support hierarchy), model reduction may improve your model. The "Lack of Fit F-value" of 5.47 implies there is a 6.71% chance that a "Lack of Fit F-value" this large could occur due to noise. [1,2,3]

5. Analysis of residuals and diagnostic diagrams

Before we can see and evaluate the results, we have to verify/diagnose the model. The assumptions and assertions made in the theory of Analysis of Variance must be fulfilled by the results of the experiment. As an illustrative example, we bring one of the assumptions made, that regarding to the "normality of the random size of residuals". For this, in the following we are bringing, the dependence on our experiment as well as two versions of this behavior (when not fulfilled and when the assumption is fulfilled) offered by the tutorial of Design - Expert 7 and 13.

5.1 Normal probability plot of the studentized residuals to check for normality of residuals.

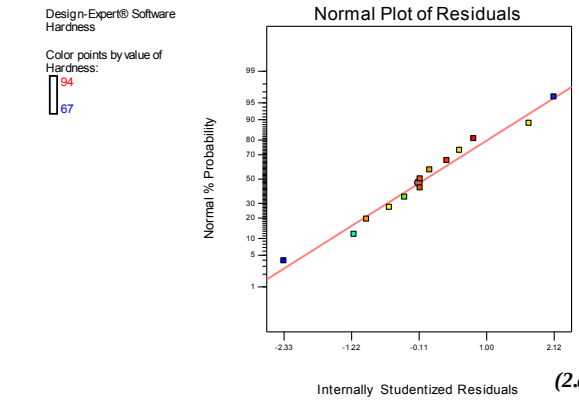

(2.a)

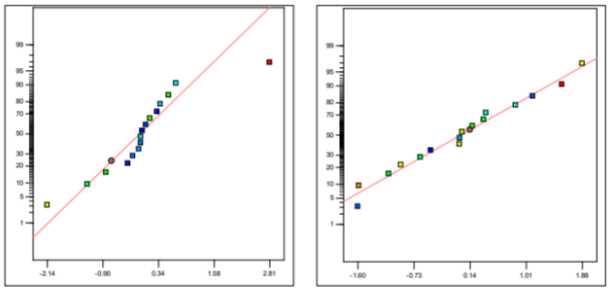

(2.b)

Fig. 2 *Normal Plot of residuals a) from our experiment b) from the DX software*

If the test points are placed in the form of an "S" the normality is not met (Fig. 2.b on the left) and when they are placed by random distribution around a straight line, the normality is met (Fig 2.b on the right). By carefully observing the graphs (Fig. 2a) it is concluded that in our experiment the assumption on the Normality of the random size of the residuals is fulfilled.

In the following we are bringing the diagnostic graphs for two other assumptions for which the same reasoning logic is followed also the graph for the power of transformation.

5.2 Studentized residuals versus predicted values to check for constant error.

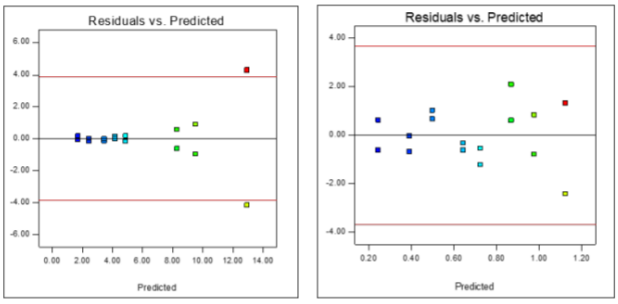

(3.a)

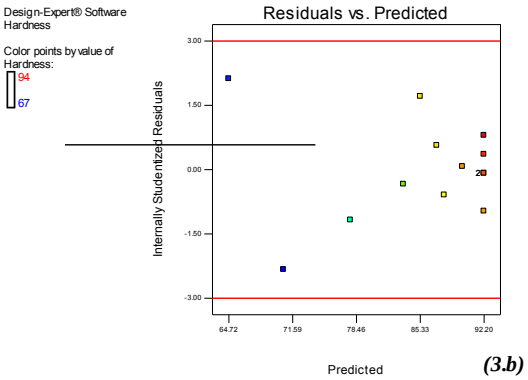

(3.b)

Fig. 3 *Residuals vs Predicted a) from the DX software b) from our experiment*

If the test points are distributed randomly, within the limit limits, the assumption is met and if the distribution gains certain geometry (megaphone in this case) the assumption is not met (Fig. 3.a). By carefully observing the graphs it is concluded that in our experiment the assumption on constant error is fulfilled (Fig. 3.b).

5.3 Externally Studentized Residuals to look for outliers, i.e., influential values.

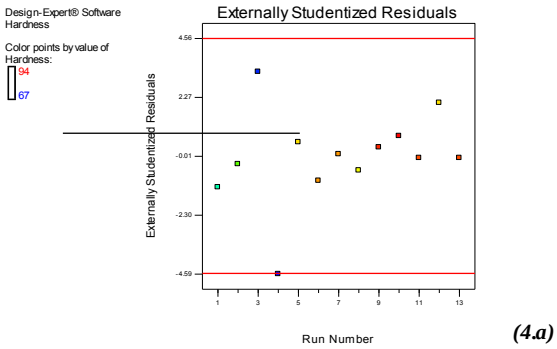

(4.a)

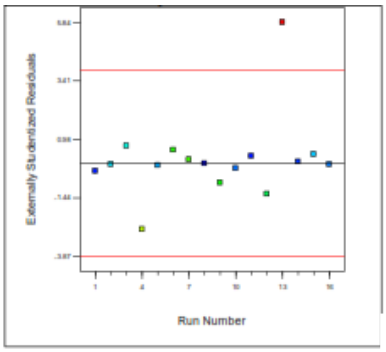

(4.b)

Fig. 4 *Externally Studentized Residuals vs Run : a) from our experiment b) from the DX software*

By carefully observing the graphs it is concluded that in our experiment the assumption on the affected values is fulfilled, we have no evidence points outside the limits (Fig.4.a).

5.4 Predicted vs. Actual

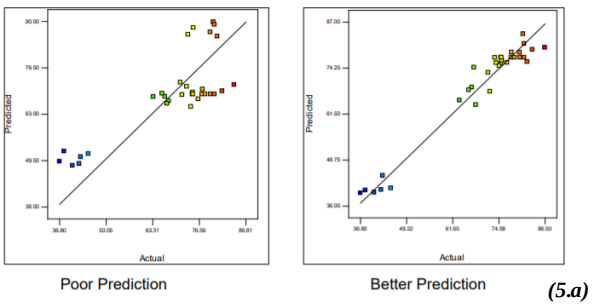

(5.a)

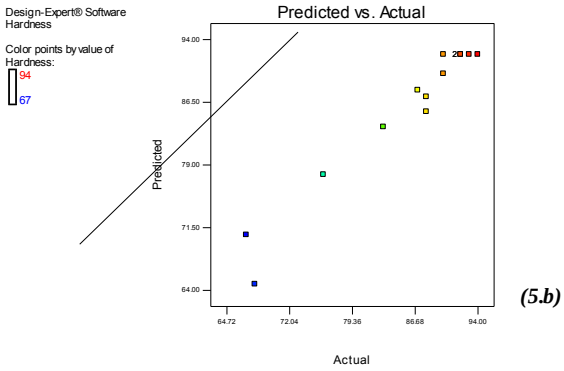

(5.b)

Fig. 5 *Predicted vs. Actual: a) from the DX software b) from our experiment*

The test points should be randomly distributed around the straight line at an angle of 45°, if clusters of points above or below the straight line are observed this indicates high or poor predictability (Fig. 5.a). By carefully observing the graphs it is concluded that in the experiment the predictability from the mathematical model is satisfactory (Fig. 5.b).

5.5 Box-Cox plot for power transformations.

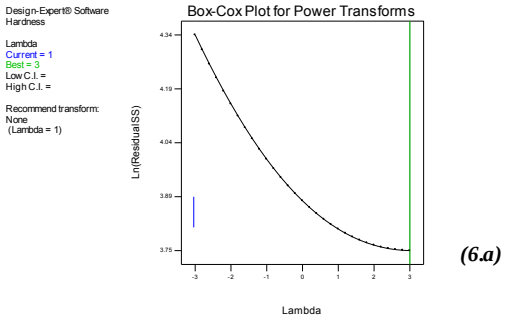

(6.a)

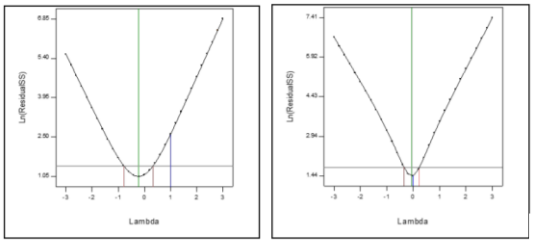

(6.b)

Fig. 6 *Box-Cox plot for power transformations a) from our experiment b) from the DX software*

When the ratio $y_{max}/y_{min} > 10$ usually indicates a transformation is required. For raport $y_{max}/y_{min} < 3$ the power transforms have little effect (Fig.6.a).

By carefully observing our experiment (Fig.6.b) the ratio is 1.4099 that means it is not necessary the power transform: $y^{(\lambda=1)}$.

6. Results

Below we are shown the data generated from the DX software:

a. Mathematical model equations
b. Response Surface Method - RSM
c. Isocontours of the Indicator of Process (hardness, HBN)
d. Effects of interaction between factors (temperature-time)

a) Mathematical model equations for our experiment

Mathematical model equations: is a quadratic polynomial which expresses the process indicator (hardness HBN) depending from the factors and the interaction between them.

Final Equation in Terms of Coded Factors it is:

$$Hardness = +92.20 + 3.57 *A + 5.84*B - 6.75 *A*B - 4.66*A^2\ 6.66*B^2$$

Final Equation in Terms of Actual Factors it is:

$$Hardness = -945.98637 +9.10519* \text{ A Temperature } +41.54021*B \text{ Time } -0.15000* \text{ A Temperature } * \text{ B Time } -0.020722* \text{ A Temperature}^2 \ -0.74028* \text{ BTime}^2$$

b) Response surface method (RSM)

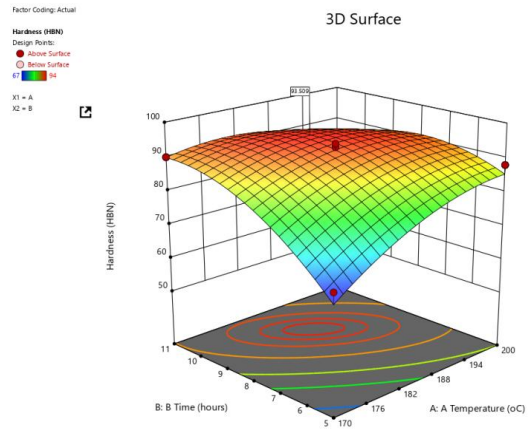

Fig. 7 *The response surface (3D) plot of Hardness vs Time-Temperature*

c) Isocontours of the Indicator of Process (hardness, HBN)

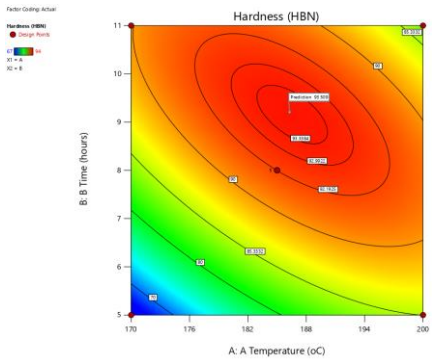

Fig. *The contour plot of Hardness (HBN) vs Time-Temperature*

d) Effects of interaction between factors *(temperature-time)*

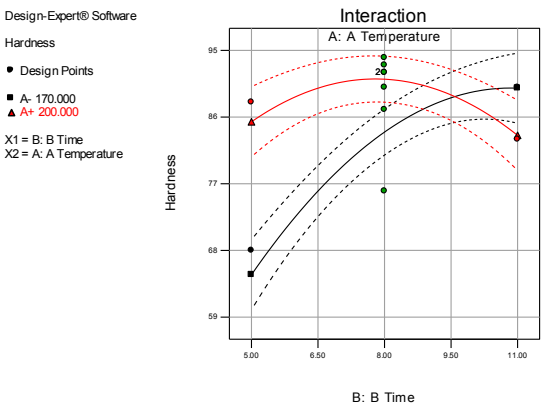

Fig. 9 *Interaction between factors*

7. Conclusions

1. In this paper we have presented the methodology for the planning and analysis of the experiment for the case RSM-CCD applied in artificial aging of aluminum alloys.
2. Careful planning of the experiment ensures that the results are obtained with the right expectation, within low probability errors (p-values), with a minimum number of tests.
3. The RSM-CCD method provides in addition to the 3D graphical representation of the response surface also:

- *Mathematical model* of the dependence of the process indicator on the factors taken in the study
- The *effect of the interaction between the factors* and what is more important:
- *Isocontours* of the indicator depending on the factors within the studied limits.
- We consider the latter especially important for industrial operators as it serves them as a ***technological card*** for process management.
- We hope that this paper will be useful for various researchers who aim to optimize the parameters of a process, as we are convinced that it will serve us in future work to optimize the parameters of artificial aging of various connections of aluminium.

8. Acknowledgment

The author gratefully acknowledges Polytechnic University of Tirana and Laboratory of Materials Science for supporting this research project; University of Lille France, for disponibility of software Design-Expert and Prof. Assoc. Dervish Elezi for professional advices.

9. Conflict of interests

The author would like to confirm that there is no conflict of interests associated with this publication and there is no financial fund for this work that can affect the research outcomes.

10. References

1. Handbook for Experimenters Version DX13.00 (2020)
2. https://www.statease.com
3. Manuale practico per realizzare, Disegni degli Esperimenti Version DX7
4. M.Kumar, M.M.Baloch, M.I.Abro, S.A.Memon; Effect of Artificial Aging Temperature on Mechanical Properties of 6061 Aluminum Alloy; Journal of Engineering and Technology, Vol.38,No.1, 31-36,; p-ISSN:0254-7821,E-issn:2413-7219 January (2019)
5. D.Elezi "Lecture-*Bases of process design*" Polytechnic University of Tirana; (2015)
6. Somsak Kaewploy, Chaiyoot Meengam "Determination of Optimal Parameters for Diffusion Bonding of Semi-Solid Casting Aluminium Alloy by Response Surface Methodology" MATEC 26, 02001 Web of Conferences ACMME pp.01-05 (2015)
7. P.Puspitasari , D.I. Tsamroh , M.Achyarsyah , B.Bandanajaya and D. Puspitasari; Multistage artificial aging optimization for tensile properties of Duralium using Response Surface Method (RSM); MATEC Web of Conferences 204, 00007 ; IMIEC (2018)
8. K.Dehgani, A.Nekahi, M.Mirzaie "Using response surface methodology to optimize the strain aging response of AA5052"MSE A527 ; 7442-7451 (2010)
9. M.Voncina, K.Kresnik, D.Volsak, J.Medved "Effects of homogenization of Aluminium Alloy EN AW 8006" Metals; (2020)
10. J.Hirsch "Annealing of Aluminium and Its Alloys; ASM Handbook, Vol 4E: Heat treating of nonferrous alloys, ASM International, Materials Park, pg.137-147, (2016)

Influence of the transfer function of the data classification process in a two - layer neural network

Bojan Vasovic[1], Ivan Garvanov[2]

[1]Academy of Professional Studies Southern Serbia, Leskovac, Serbia
[2]University of Library Studies and Information Technologies, Sofia, Bulgaria
bojan.vasovic@yahoo.com
i.garvanov@unibit.bg

Abstract: *This paper analyses the influence of transfer function choice and learning rate on a multilayer neural network in the classification process. The neural network is implemented in the Java programming language.*

Keywords: *Transfer Function, Neural Network, Data Classification, Characters Recognition*

1. Introduction

Artificial neural networks (ANNs), usually simply called neural networks (NNs), are computing systems vaguely inspired by the biological neural networks that constitute animal brains.

Neural networks learn (or are trained) by processing examples, each of which contains a known "input" and "result", forming probability-weighted associations between the two, which are stored within the data structure of the net itself. The training of a neural network from a given example is usually conducted by determining the difference between the processed output of the network (often a prediction) and a target output. This is the error. The network then adjusts its weighted associations according to a learning rule and using this error value. Successive adjustments will cause the neural network to produce output which is increasingly similar to the target output. After a sufficient number of these adjustments the training can be terminated based upon certain criteria. This is known as supervised learning.

Such systems "learn" to perform tasks by considering examples, generally without being programmed with task-specific rules. For example, in image recognition, they might learn to identify images that contain cats by analyzing example images that have been manually labeled as "cat" or "no cat" and using the results to identify cats in other images. They do this without any prior knowledge of cats, for example, that they have fur, tails, whiskers, and cat-like faces. Instead, they automatically generate identifying characteristics from the examples that they process.

2. Elements of a Neural Network

Input Layer: This layer accepts input features. It provides information from the outside world to the network, no computation is performed at this layer, nodes here just pass on the information(features) to the hidden layer.

Hidden Layer: Nodes of this layer are not exposed to the outer world, they are the part of the abstraction provided by any neural network. Hidden layer performs all sort of computation on the features entered through the input layer and transfer the result to the output layer.

Output Layer: This layer brings up the information learned by the network to the outer world.

Definition of activation function: Activation function decides, whether a neuron should be activated or not by calculating weighted sum and further adding bias with it. The purpose of the activation function is to introduce non-linearity into the output of a neuron.

We know, neural network has neurons that work in correspondence of weight, bias and their respective activation function. In a neural network, we would update the weights and biases of the neurons on the basis of the error at the output. This process is known as back-propagation. Activation functions make the back-propagation possible since the gradients are supplied along with the error to update the weights and biases.

A neural network without an activation function is essentially just a linear regression model. The activation function does the non-linear transformation to the input making it capable to learn and perform more complex tasks.

3. Network Architecture

A neural network with l layers is observed (Fig. 1). Inputs x_1, $x_2, \ldots, x_{\mathrm{nl}}$ are connected to the first layer neurons. Each connection corresponds to the weight $w_{\mathrm{i,j}}$. Each neuron represents a processor unit where neuron input to n1 is calculated as:

$$z_1^1 = w_{1,1}^1 x_1 + w_{1,2}^1 x_{2+} \ldots + w_{1,n1}^1 x_{n1} + b_1^1 \quad (1)$$

respectively, the input to the first layer *i*-th neuron is:

$$z_i^1 = \sum_{i=1}^{n2} w_{1,i}^1 x_i + b_i^1 \quad (2)$$

An artificial neuron may have an independent component which adds an additional signal to the transfer function. This component is called bias (b_i). This component has a value of 1, so if the weight w_0 is introduced, then the sum (2) can be simplified with

$$z_i^1 = \sum_{i=0}^{n2} w_{1,i}^1 x_i \text{ with } x_0 = b. \quad (3)$$

The output from the first layer *i*-th neuron, which is the input for the second layer neurons is:

$$a_i^1 = f(z_i^1) \quad (4)$$

The output from the neural network is calculated in the for-loop. For-loop is often slow to perform when it comes to processing large data sets, so the solution is to vectorize these equations.

For the architecture shown, the matrix equation can be generalized as follows:

$$Z = WX^T + b \quad (5)$$

$$A = f(Z) \quad (6)$$

The f function is called the transfer function. This function should provide a nonlinear complex functional mapping between the inputs and desired data target outputs.

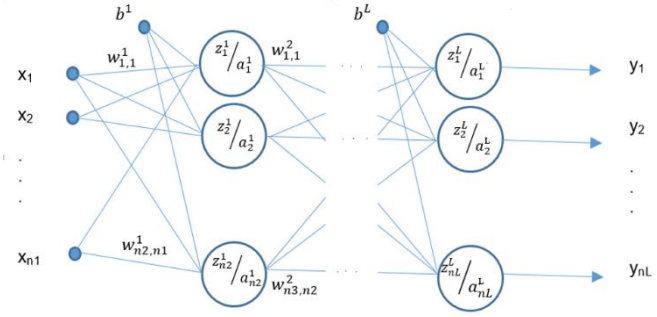

Fig. 1 *Neural network*

The most commonly used transfer functions are: Linear, Sigmoid and Hyperbolic tangent. The distinctive output of a single bias input linear neuron is shown in Figure 2 (a).

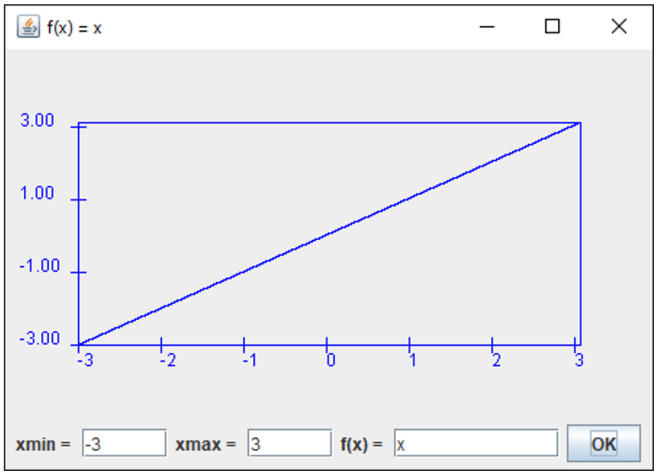

a) Linear

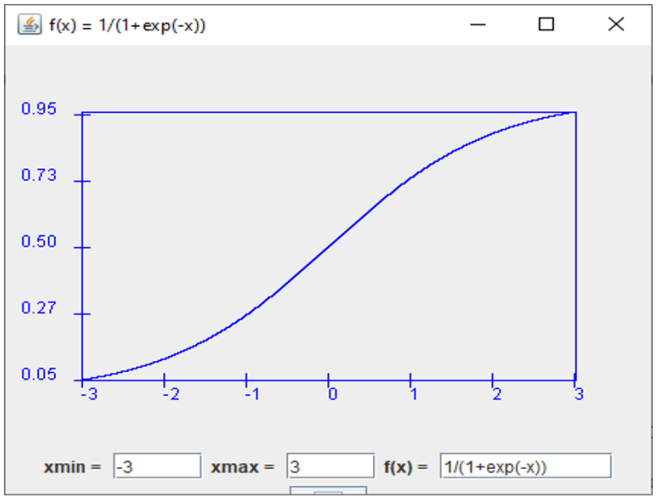

b) Sigmoid

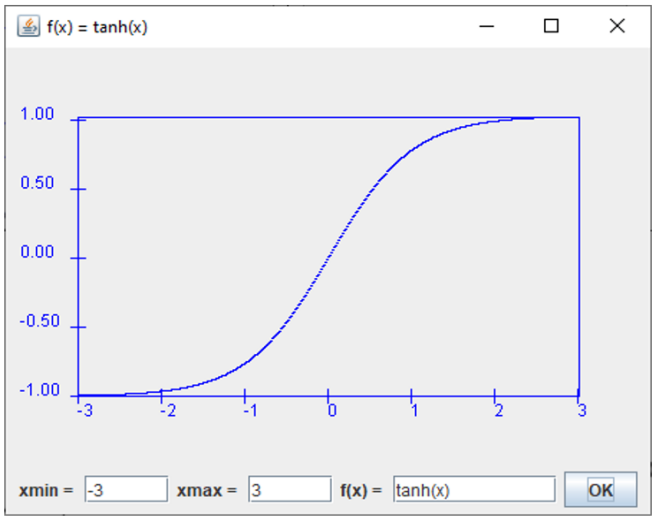

c) Hyperbolic tangent

***Fig. 2** Transfer functions*

The sigmoid function is shown in Figure 2 (b). This transfer function takes an input, which can have any value between plus and minus infinity, and gives an output in the range of 0 to 1, according to the expression:

$$f(x) = \frac{1}{1+e^{-x}} \tag{7}$$

Hyperbolic tangent function is shown in Figure 2 (c).

$$f(x) = \frac{e^{x}-e^{-x}}{e^{x}+e^{-x}} \tag{8}$$

In paper [1], several possibilities of using transfer functions of different types in neural networks are presented, as well as regularization of large networks with heterogeneous nodes and constructive approaches. Paper [2] aims to analyze the influence of the selection transfer function and training algorithms on neural network flood runoff forecast. Sigmoid function, used in this paper is described in paper [3].

4. Algorithm Backpropagation

Rummelhart [4] proposed an algorithm inspired by the gradient method and was called backpropagation. Based on the gradient method, the output error should be returned to the previous layers, find the influence of individual weights on the obtained error and determine the weight gain in individual layers.

The goal is to minimize the overall error. We can now calculate the error for each output neuron using the error function and sum them to get the total error:

$$J = -\frac{1}{m}\left[\sum_{i=1}^{m}\sum_{k=1}^{nL} y_k^i \log(h_w(x^i))_k + (1-y_k^i)\log(1-(h_w(x^i))_k\right] \tag{9}$$

Where y_k^i is the desired output for the *i*-th training set and the *k*-th class from the neural network, and $h_w(x^i)$ is the output from the *i*-th layer, so it is the actual result of the network.

The error in the last layer is:

$$\delta^L = \frac{\partial J}{\partial z^L} = \frac{\partial J}{\partial z^L} * \frac{\partial a^L}{\partial z^L} = a^L - y \tag{10}$$

Backpropagation allows calculations of δ^l for each layer, and then with the help of these errors the values of the real interest $\frac{\partial J}{\partial w_{ij}^l}$, are calculated, respectively the influence of the weights of each layer on the total error.

The error of neurons in layer l can be expressed as follows:

$$\delta^l = (w^l)^T \delta^{l+1} \odot f'(z^l) \tag{11}$$

Here $\odot$ represents the Hadamard's product operator. Hadamard's product of two matrixes is very similar to the matrix's addition, the elements corresponding to the same row and column of given matrices are multiplied by each other to form a new matrix.

The influence of each layer weights on the total error is:

$$\frac{\partial J}{\partial w^i} = \Delta W_i = \delta^{l+1}(a^l)^T \tag{12}$$

The influence of each layer bias on the total error is:

$$\frac{\partial J}{\partial b^l} = \Delta B_i = \delta^{l+1} \tag{13}$$

New weights and bias are calculated as:

$$W_i = W_i - \alpha * \Delta W_i \tag{14}$$

$$\mathrm{B}_i = B_i - \alpha * \Delta B_i \tag{15}$$

The parameter α represents the learning rate. Learning rate is a small positive value that controls the magnitude of the parameters change at each run. Learning rate controls how quickly a neural network learns a problem.

5. Implementation

The base classes in the system are Neural Network and Layer, which should implement a general neural network model. Auxiliary class Matrix is also used, which implements basic operations with matrices. The Layer class is presented in the Figure 3.

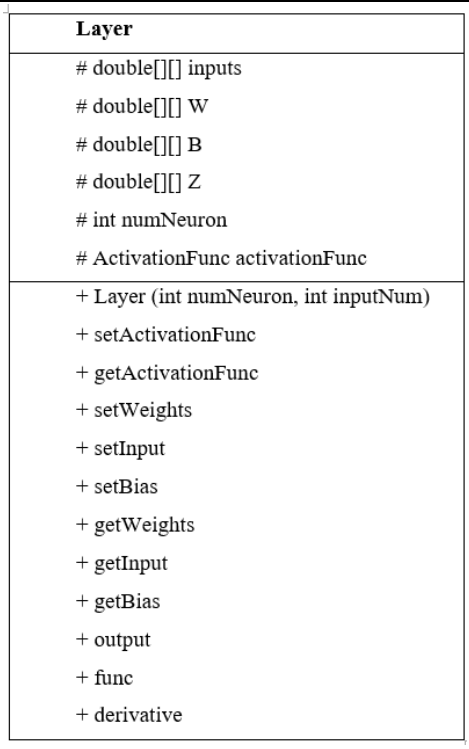

***Fig. 3** UML model of class Layer.*

Parameter NUMBER_LAYERS defines the number of layers and it is placed inside constructor of class Neural Network, where the numbers of neurons and number of entries in each layer are also defined by numNeurons and inputNum. Matrix desiredInputs defines the inputs to the neural network, and the matrix desiredOutputs the desired outputs.

```
int NUMBER_LAYERS = 2;
int numNeuron[] =  {15,10};
int inputNum[]  = {25,15};
private double[][] desiredInputs;
private double[][] desiredOutputs;
private List<Layer> layers = new
ArrayList<Layer>(NUMBER_LAYERS+1);
private List<double[][]> W = new
ArrayList<double[][]>(NUMBER_LAYERS+1);
private List<double[][]> B = new
ArrayList<double[][]>(NUMBER_LAYERS+1);
```

Lists layers, W and B represent the neural network elements (Figure 1) and they are initialized inside the constructor. Initialization is followed by neural network training in the training method. The number of iterations is determined by the variable NUM_ITERATION, and the weights are adjusted by the backpropagation algorithm according to the previously defined description.

```
double[][] dApom = null;
if(error_type == ERROR1)
{dApom=Matrix.sub(layers.get(NUMBER_LAYERS).out
put(),desiredOutputs);}
else if(error_type == ERROR2){
dApom=Matrix.sub(Matrix.div(Matrix.sub(1.0,desiredOut
puts),Matrix.sub(1.0,layers.get(NUMBER_LAYERS).out
put())), Matrix.div(desiredOutputs,
layers.get(NUMBER_LAYERS).output()));}
double[][] dZpom = Matrix.hadamardProduct(dApom,
layers.get(NUMBER_LAYERS).derivative(layers.get(NU
MBER_LAYERS).getZ()));
double[][] dWpom = Matrix.div(Matrix.mul(dZpom,
Matrix.T(layers.get(NUMBER_LAYERS).getInput())),
m); ///
double[][] dBpom = Matrix.div(dZpom, m);
dA.set(NUMBER_LAYERS, dApom);
dZ.set(NUMBER_LAYERS, dZpom);
dW.set(NUMBER_LAYERS, dWpom);
dB.set(NUMBER_LAYERS, dBpom);
```

m is the number of training data;

```
m = desiredInputs.length;
```

Then, the total error is calculated using the error method:

```
public static double error(int brojKlasa, int m, double[][]
y, double[][] a ){double J = 0.0;
for(int i = 0 ; i < m; i++){
for(int k = 0; k < brojKlasa; k++){
J=J+(y[i][k]*Math.log(a[i][k]))+(1-y[i][k])*Math.log(1-
a[i][k]);}}
return (-1.0/m) *J;}
```

The influence of weights on the neurons error in the layer layer (layer = NUMBER_LAYERS-1; layer >0; layer--) can be expressed as follows:

```
double [][] dA2 =
Matrix.mul(Matrix.T(layers.get(layer+1).getWeights()),
dZ.get(layer+1));
double[][] dZ2 = Matrix.hadamardProduct(dA2,
layers.get(layer).derivative(layers.get(layer).getZ()));
double[][]dW2;
if (layer == 1){
dW2 = Matrix.div(Matrix.mul(dZ2,(desiredInputs)), m);}
else{dW2 =
Matrix.div(Matrix.mul(dZ2,Matrix.T(layers.get(layer).get
Input())), m);}
double[][]dB2 = Matrix.div(dZ2, m);
dA.set(layer, dA2);
dZ.set(layer, dZ2);
dW.set(layer, dW2);
dB.set(layer, dB2);
```

At the end of each iteration, new weights are determined for each layer, considering the alfa learning rate. Weight gain and new weight and bias values by layers are obtained:

```
for(int layer = 1; layer < NUMBER_LAYERS+1;
layer++){
double[][] W1 =
Matrix.sub(layers.get(layer).getWeights(),
Matrix.hadamardProduct(alfa, dW.get(layer)));
double[][] B1 = Matrix.sub(layers.get(layer).getBias(),
Matrix.hadamardProduct(alfa, dB.get(layer)));
W.set(layer,W1);
B.set(layer,B1);}
for(int layer = 1; layer < NUMBER_LAYERS+1;
layer++){
layers.get(layer).setWeights(W.get(layer));
layers.get(layer).setBias(B.get(layer));}
```

Regularization was not used in the implementation.

6. Results

A set of ten characters is used to test the network. Each character is represented by a 5x5 matrix, so the neural network has 25 inputs and ten outputs. Also, the network contains one hidden layer that has 45 neurons.

```
int numNeuron[] =  {45,10};
int inputNum[]  = {25,45};
```

For the network training process, the test data shown in Figure 4 are used. The Figure 4 also shows the desired outputs, for the given training data.

We see that each letter is represented by a 5x5 matrix (Figure 5). Matrix elements have a value of 0.0 or 1.0, depending on the appearance of a given character

Fig. 4 *Training data*

After the training, the network testing was made for the input data, which represent the letter B, with intentionally introduced noise (Figure 6).

A	B	C	D	E
0 0 1 0 0	1 1 1 1 1	0 1 1 1 1	1 1 1 1 0	1 1 1 1 1
0 1 0 1 0	1 0 0 0 1	1 0 0 0 0	1 0 0 0 1	1 0 0 0 0
0 1 0 1 0	1 1 1 1 0	1 0 0 0 0	1 0 0 0 1	1 1 1 1 0
1 1 1 1 1	1 0 0 0 1	1 0 0 0 0	1 0 0 0 1	1 0 0 0 0
1 0 0 0 1	1 1 1 1 1	0 1 1 1 1	1 1 1 1 0	1 1 1 1 1
F	**G**	**H**	**I**	**J**
1 1 1 1 1	0 1 1 1 1	1 0 0 0 1	0 0 1 0 0	1 1 1 1 1
1 0 0 0 0	1 0 0 0 0	1 0 0 0 1	0 0 1 0 0	0 0 0 0 1
1 1 1 1 0	1 0 0 1 1	1 1 1 1 1	0 0 1 0 0	0 0 0 0 1
1 0 0 0 0	1 0 0 0 1	1 0 0 0 1	0 0 1 0 0	1 0 0 0 1
1 0 0 0 0	0 1 1 1 0	1 0 0 0 1	0 0 1 0 0	0 1 1 1 0

Fig. 5 *Characters*

1 0.7 1 1 1
1 0.3 0 0 1
1 1 1 0.9 0
1 0 0 0 1
1 1 1 1 1

Fig. 6 *Test data*

The results shown in Figure 7 show that the network correctly performed the classification and recognized the letter B, since only the second element of the vector has a value of 1.0, and all other elements are approximately equal to zero.

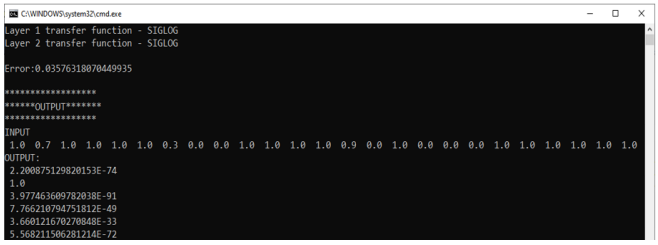

Fig. 7 *Results*

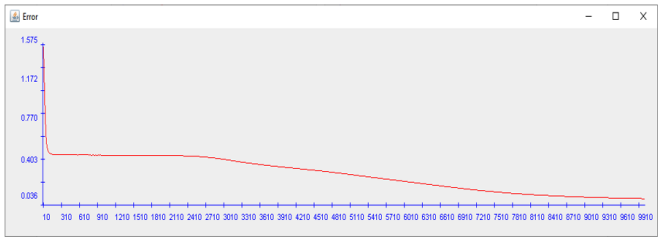

Fig. 8 *Dependence of the total error on the number of iterations*

Fig. 9 *Results for a neural network with two hidden layers*

In the case of a neural network, which has two hidden layers and which uses the tangent hyperbolic transfer function, the results are shown in Figure 9 and 10.

```
int numNeuron[] =  {45,25,10};
int inputNum[]   = {25,45,25};
```

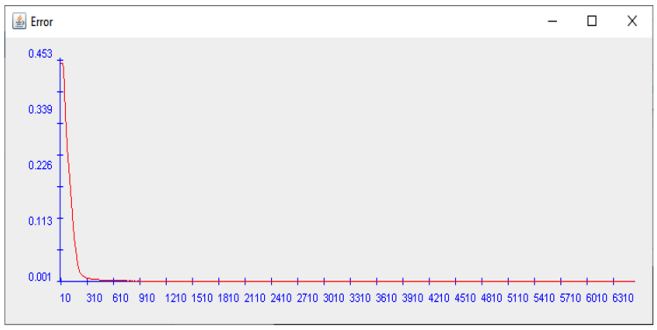

Fig. 10 *Error for a neural network with two hidden layers and Hyperbolic tangent transfer function*

7. Conclusion

This paper presents the neural network implementation into Java programming language. The implementation is generally performed for an arbitrary network having L layers and with the indicated number of neurons in each layer. The sigmoid function was used as a transfer function in the first example and tangent hyperbolic in second. A 10x25 matrix was used to train the net. Each row in the matrix represents a letter measuring 5x5. A matrix of desired outputs is also given. Network testing shows that the network correctly classifies the data and minimizes the error after some 300 iterations (Figure 10), in case of a neural network that has two hidden layers. In the case of a network with one hidden layer, the convergence is a bit slower. In the example, regularization was not used, so if the number of selected parameters is too large [5], the neural network may begin to describe noise, which may result in useless parameter adjustments.

Acknowledgment

This work is supported by: National Science Fund at the Bulgarian Ministry of Education and Science Project: "Synthesis of a dynamic model for assessing the psychological and physical impacts of excessive use of smart technologies", KP-06-N 32/4/07.12.2019.

8. References

1. Duch, W., Jankowski N, (2001). Transfer functions: hidden possibilities for better neural networks. 9th European Symposium on Artificial Neural Networks, Bruges, Belgium.

2. Maca P., Pech P., Pavlasek J., (2014) Comparing the selected transfer functions and local optimization methods for neural network flood runoff forecast. Mathematical Problems in Engineering. https://doi.org/10.1155/2014/782351

3. Yonaba, H., F. Anctil, and V. Fortin. (2010). Comparing sigmoid transfer functions for neural network multistep ahead streamflow forecasting. Journal of Hydrologic Engineering 15(4). DOI: 10.1061/(ASCE)HE.1943-5584.0000188

4. Rumelhart, D. et. al. (1996). Backpropagation: The basic theory. In P. Smolensky, M. C. Mozer, and D. E. Rumelhart(eds.) Mathematical Perspectives on Neural Networks. Erlbaum: NJ, 533-566.

5. Garvanova, M., Ivanov, V. (2020). Quality assessment of defocused image recovery algorithms. 3rd International Conference on Sensors, Signal and Image Processing, Prague, Czech Republic, doi: https://doi.org/10.1145/3441233.3441242.

Разработване на подход за параметричен метасинтез на експлоатационни показатели на пътищата от РПМ на България на основата на сателитни данни

Стоянка Иванова*, Евелина Иванова
Университет по архитектура, строителство и геодезия, София, България
siva_fce@uacg.bg altera1979@abv.bg

Резюме: *Обширни и детайлни сателитни данни за разнообразни параметри на нашата планета се натрупват вече няколко десетилетия и дават възможност за изучаване на промените на земната повърхност в развитие. Една значителна част от тези данни са налични за свободно ползване с приемлива резолюция и могат да се използват за широк спектър от изследователски проекти в разнообразни научни направления. Така лесно могат да се проследяват активни процеси, предизвикани от изменението на климата и влияещи върху обектите на инфраструктурата. В настоящата разработка се разглежда подход за параметричен метасинтез на експлоатационни показатели на пътищата от РПМ на България, базиран на достъпни сателитни данни за атмосферата, енергийния баланс, растителността, повърхността на планетата и др. Концепцията предполага разработване на многопластова взаимосвързана структура от данни: векторно описание на пътищата, с данни като топография (надморска височина), вариации и аномалии в температурата, албедо, снежна покривка, активни пожари и др., като основа на система за бъдещ метасинтез.*

Ключови думи: *САТЕЛИТНИ ДАННИ, ТРАНСПОРТНА ИНФРАСТРУКТУРА, ИНФОРМАЦИОННИ ТРАНСПОРТНИ СРЕДСТВА*

1. Въведение

Обширни и детайлни сателитни данни за разнообразни параметри на нашата планета се натрупват вече няколко десетилетия и дават възможност за изучаване на промените на земната повърхност в развитие. При своето движение около планетата много сателити изпращат постоянно изображения на земната повърхност с висока резолюция в различни дължини на електромагнитните вълни. Тези данни се натрупват с цел бъдещи анализи [1].

Една значителна част от тези данни са налични за свободно ползване с приемлива резолюция и могат да се използват за широк спектър от изследователски проекти в разнообразни научни направления.

Богатството от данни за две десетилетия по месеци, седмици и дни позволява да се проследяват активни процеси, предизвикани от изменението на климата и влияещи върху човешката дейност, в частност – върху обектите на инфраструктурата.

Префиксът „meta-“ (от гръцки произход) означава „по-всеобхватен“ или „надхвърлящ“ [2]. В научната литература понятието *метасинтез* е въведено от Atkins et al [3]. Той обединява качествени данни, за да формира нова интерпретация на научното поле. Не трябва да се бърка с мета-анализ, който проверява хипотеза, използвайки количествени данни. Метасинтезът генерира преди всичко нови теории и хипотези, които подлежат на проверки, тестове и сравнение с резултатите от изпитване.

Целта на настоящата разработка е да изгради подход с потенциално широко приложение за параметричен мета-синтез на експлоатационни показатели на пътищата от РПМ на България, базиран на достъпни сателитни и наземни данни за атмосферата, енергийния баланс, растителността, повърхността на планетата и др.

2. Структура на системата за метасинтез

Концепцията предполага разработване на многопластова взаимосвързана структура от данни, която комбинира векторни данни за пътищата, с растерни набори данни като топография (надморска височина), вариации и аномалии в температурата, албедо, снежна покривка, активни пожари и др., като основа на система за бъдещ метасинтез. Опростена структура на обработваните данни на системата за метасинтез може да видите на фиг. 1. Тя се състои от три основни групи пластове – с растерни, с векторни и с точкови данни. Основните данни в тях се трансформират, чрез взаимодействие помежду им, в производни данни чрез различни алгоритми в системата за метасинтез.

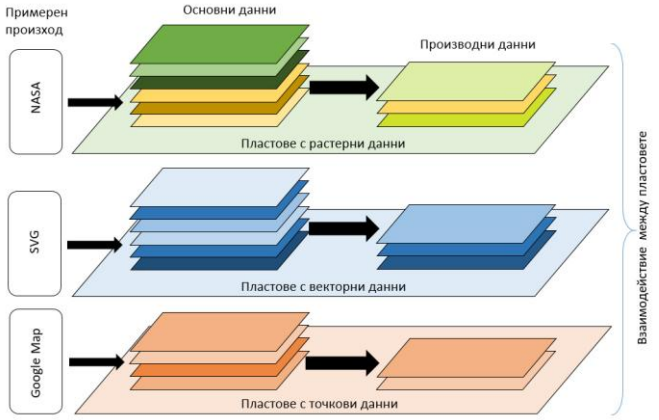

Фиг. 1 *Структура базата данни на системата за метасинтез, състояща се от три основни групи пластове – с растерни, с векторни и с точкови данни.*

2.1. Първични източници на данни

Една свободно достъпна популярна база данни, подходяща за използване в първата версия на системата, се предлага в NEO – NASA Earth Observation website [4]. Примерни карти с резолюция 1° са показани на фиг. 2. По-нататък отново ще се върнем на тази база данни.

Друга подобна база данни, макар и организирана по друг начин, е Power Data Access Viewer [5], отново на NASA. Интерес представлява и друг източник на сателитни данни – LandViewer [6] - инструмент за сателитно наблюдение, който позволява търсене, обработка и получаване на ценна информация от сателитни данни за справяне с реални бизнес проблеми. Значима информация, свързана със соларни данни, температури и др. параметри се предлагат в PVGIS [7] – онлайн база данни, разработена от Joint Research Centre (JRC) в Испра, Италия, по поръчка на Европейската комисия. Тази ГИС предоставя часови и месечни соларни и други данни за цяла Европа с резолюция 1 км. Както е споменато в сайта на PVGIS [8], новата JRC-PVGIS база данни е конструирана на основата на сателитни измервания в периода 1998 – 2016 г. [7], предоставени от Climate Monitoring Satellite Application Facility (CM-SAF), с времева стъпка 1 час и пространствена резолюция 1’30” ≈ 2.5 км. Базата данни PVGIS-CMSAF покрива същата площ, както и Meteosat satellite: Европа, Африка и части от Южна Америка [9].

За пилотната версия на системата е избрана свободната база данни на NEO – NASA Earth Observation website [4], чиито данни са обобщени в 5 области: Atmosphere, Energy, Land, Life,

Ocean. От своя страна всяка област включва от 10 до 20 набори от данни.

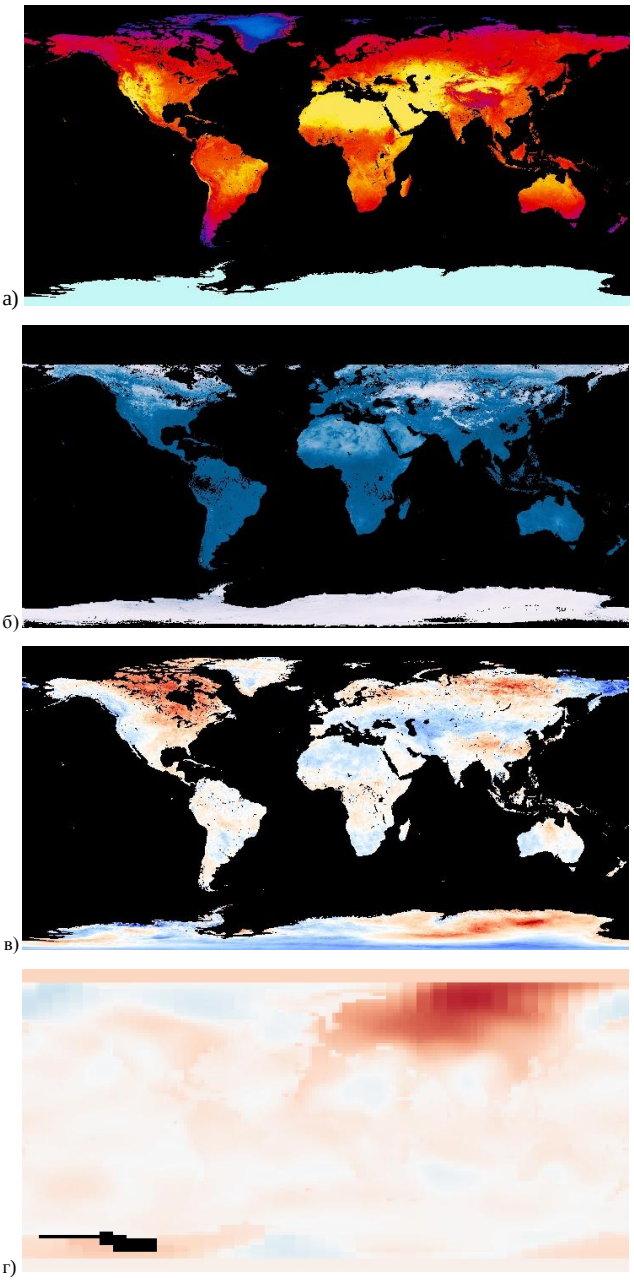

Фиг. 2 Примерни карти, илюстриращи набори данни в NEO – NASA Earth Observation website [4] с резолюция 1°: а) дневни температури на земната повърхност през август 2021 г.; б) албедо на земната повърхност през януари 2015; в) температурни аномалии на земната повърхност през нощта за октомври 2021 г..; г) глобални температурни аномалии през февруари 2020 г.

Всеки набор от данни има следните характеристики:

- Резолюция (разделителна способност) – тя варира от 1° до 0.1°. Колкото по-голяма е резолюцията на един набор данни, толкова по-голяма е таблицата, в която се записва.
- Периодичност – 1, 8, 16 дни, или месец. При по-кратките периоди е възможно в набора да липсват данни за някои фрагменти от земната повърхност, заради липсата на поглед към тях от наблюдаващите сателити. Данните са кумулативни, получават се от наслагване на изображения при всяко прелитане на сателита над наблюдаваната територия.
- Продължителност на наблюдението – най-старите набори от данни са от 2000 г., а най-новите – от миналия месец. Някои набори включват сериозни количества регулярно записвани данни, а други – само по няколко записа в определена година.
- Формат на данните – достъпни са в матричен числов формат (CSV) и в графичен формат (JPG, PNG, GeoTIFF) – цветни или в сивата гама.

2.2. Алгоритми

Проектът включва създаване на софтуерна черупка (shell) на многопластова структура от набори данни с различен контекст. Пластовете могат да бъдат растерни (карти, 15K за територията на България при 0.1° резолюция – фиг. 3), векторни (2D траектории на пътища, например в SVG формат, фиг. 4) и точкови (напр. населени места). От своя страна пластовете с растерните данни могат да се класифицират по следните начини:

- основни и производни (основни са входните данни, а производните са тези, които могат да бъдат генерирани на тяхна база чрез усредняване, търсене на екстремуми, интерполиране и екстраполиране).
- моментни и обобщени за изминали и/или бъдещи периоди с различна продължителност.

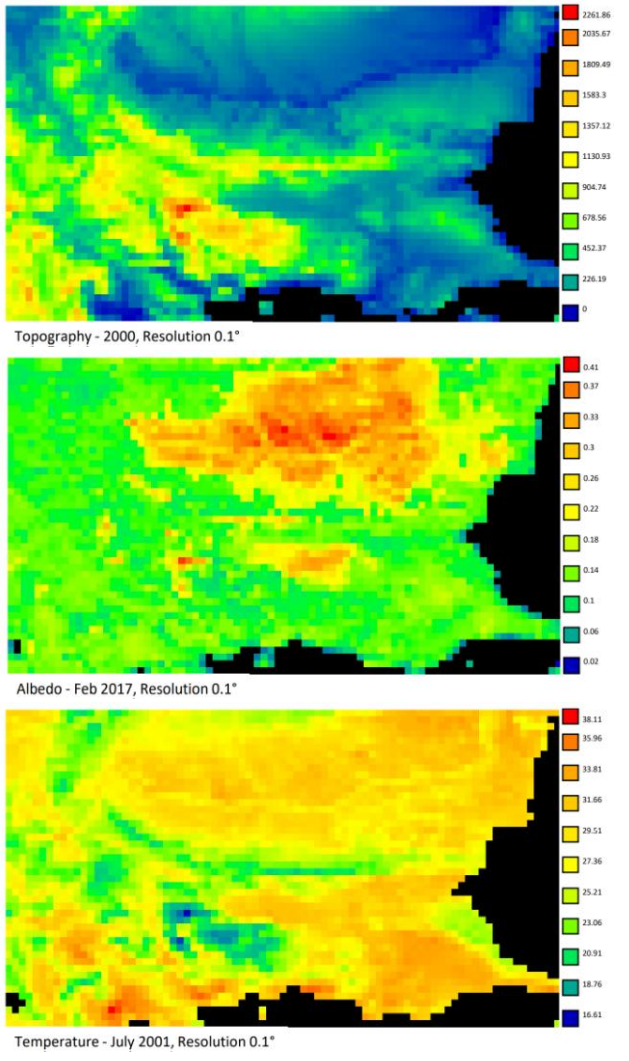

Фиг. 3 Примерни карти на територията на България, илюстриращи входните данни, извлечени от базите данни на NEO – NASA Earth Observation website [4] с резолюция 0.1°: а) топография (надморски височини); б) албедо на земната повърхност през февруари 2017 г.; в) среднодневни температури през юли 2001 г. Размер на матрицата – 81 × 46 клетки. Изображенията са генерирани в прототипа на системата.

Растерните данни са представени във вид на матрици с определена резолюция. Специален проблем, който трябва да се реши, е съчетаването на данни с различна резолюция, отнасящи се за един и същи период, но от различни източници.

Примерни пластове от производни данни могат да съдържат:

- Екстремални и аномални стойности на определени климатични и други параметри за територията на страната;
- Средни стойности на тези параметри;
- Отклонения от средните стойности на параметрите;
- и др.

Необходимите алгоритми за описаните действия с данни се базират на познания, свързани с извличане на данни за конкретна територия (фиг. 3) и обобщаване на налични данни за изминали периоди, а също така и могат да включват елементи на изкуствен интелект (предварително обучени невронни мрежи) за предвиждане на променящи се параметри, които са от значение за пътната инфраструктура – заледяване, падане на мъгли, намалено сцепление, натрупване на снежни преспи и др.

2.3. Компонента на пътната инфраструктура

Поддръжката на пътната инфраструктура е в основата на експлоатационната годност на трасетата, която осигурява целогодишна непрекъснатост на трафика, при висок потенциал на пътна безопасност. За съществуващата пътна инфраструктура на България това е комплексен процес, който включва обследване на текущото състояние на пътя с прилежащите му съоръжения и принадлежности, оценка на постъпилите данни и избор на мероприятия за възстановяване на повредите, дефектите и щетите, които са констатирани при инспекцията.

Съгласно записаното в „Стратегия за развитие на пътната инфраструктура в Република България 2016 – 2022 г.“ [10], състоянието на настилките по републиканската пътна мрежа, определено съгласно действащата “Методика за измерване и оценка на повредите по пътните настилки” (отчита вида и количеството на съществуващите повреди, измерени и оценени спрямо общата повърхност на трасето), е обобщено в Таблици 1 и 2.

Таблица 1: *Данни за състоянието на настилките по класове пътища от РПМ в километри в края на 2015. Източник: АПИ – ИПМ [10].*

	АМ	I клас	II клас	III клас	Пътни връзки	Общо км
Добро	501,4	1678,5	2059,7	3576,5	189,5	8005,6
Средно	145,3	882,6	973,9	3129,6	96,7	5228,1
Лошо	90,3	403,5	989	4852,4	20,2	6355,4
Общо	737	2964,6	4022,6	11558,5	306,4	19589,1

Таблица 2: *Данни за състоянието на настилките на общинските пътища. Източник: АПИ – ИПМ [10].*

Състояние на настилките	Дължина в км
Добро	3157
Средно	3841
Лошо	8748
Без трайна настилка	2690
Обща дължина	17169

В нашата страна стандартна практика при анализа на постъпилите данни от обследването е да се акцентира върху качество на проектиране и изпълнение, което въвежда базовите нива на качество на бъдещите трасета с определено заложено ниво на експлоатационна годност и пътна безопасност. Респективно оценките се извършват по методики, в които традиционните подходи на оценка се основават на установените щети [10] и очакваните разходи за възстановяване. Значително по-малко се залага на анализ, който да се основава на причините за направените констатации, като включва елементите на вътрешно взаимодействащата система път – превозно средство – ландшафт-климатични фактори.

Фиг. 4 *Карта на пътната мрежа на територията на България във векторен SVG формат (с включени двумерни координати). Източник: Ikonact – Wikimedia [11].*

При ново проектиране и при проектите за възстановяване няма практика дълготрайността и експлоатационната годност допълнително да се валидират спрямо данни за особеностите на околната среда. Все пак, предвид широкия годишен и географски спектър на климатични въздействия в България, добра практика може да се окаже допълването на анализите за регистрираните повреди и дефекти с данни за климатичните условия на околната среда. Тази идея е особено актуална в условията на скокообразно изменение на елементите на климата, респективно резонно е да се търси такова зониране и типизиране на основни повтарящи се проблеми при основните конструктивни елементи на пътищата. Това важи с особено голяма сила в Европа, която по последни данни се затопля по-бързо от останалата част на света [12] (дотук с 2.2° повече в сравнение с прединдустриалните нива).

Логично е да се очаква реална зависимост между засиленото въздействие на даден климатичен компонент и степента и вида на настъпилите повреди и дефекти и/или установените случаи на принудително нарушаване на непрекъснатостта на трафика. Разработената система може да допринесе за доказване на такива зависимости.

Елементи на околната среда като слънчева радиация, количество на валежите, температурни инверсии (екстремално високи/ниски температури или широк температурен диапазон в рамките на денонощия), снеговалежи в условията на високо скоростен вятър, може да предпоставят ускоряване и/или усложняване на процесите, които увреждат заложените експлоатационни показатели на пътната инфраструктура. Наличието на такива процеси, би довело до по-чести ремонтно-възстановителни дейности, непредвидени прекъсвания на трафика (при снегонавяване през зимния период) и влошени показатели на трасетата от гледна точка на пътна безопасност.

Системи от типа на разглежданата в тази статия, могат да способстват за въвеждането на климатично зониране на участъците от републиканската и общинска пътни мрежи, при които се налагат чести ремонти, нарушаване на пробега и увеличаване броя на пътнотранспортните произшествия. Отчитането на климатични компоненти като мъгла, снеговалеж, вятър, температурни инверсии като самостоятелно повтарящо се явление или в комбинация помежду им за даден транспортен участък, ще повлияе избора на системи за

превантивно осигуряване на непрекъснатостта на трафика и безопасността на участниците в движението [13, 14]. Това е от особено висок приоритет при висококоростни пътища от републиканската пътна мрежа, където правилният подбор на организационни мероприятия и предпазни елементи би трябвало да обезпечи в голяма степен редукцията на честотата на инцидентите и прекъсването на пробега по направленията. Освен това към момента различни сектори в държавата разполагат с частична информация за такива участъци, а информацията е недостатъчна и/или недостъпна за останалите институции, които имат вменено задължение към мерките за обезпечаването на трафика в страната.

Анализът на практики от чуждестранен опит и от други сектори показва, че внедряването на такъв тип технологични регистратори може да повлияе положително чрез ускоряване на достъпа на институциите до събраната информация, респективно това би трябвало да подобри управлението на процесите по поддръжката на пътната инфраструктура и тези по управление на трафика. Може да се очаква, че по-нататъшното развитие на такава система ще осигури база данни, която е достъпна в реално време за всички участници в управлението на процесите в транспортната инфраструктура и в частност на пътната.

Подобни подходи ще подпомогнат и изпълнението на Директива 2010/40/ЕС [15], която третира въвеждането на информационни транспортни системи за всички видове транспорт и особено за автомобилния. В България прилагането на информационни и комуникационни технологии по приоритетните области на директивата е крайно затруднено, поради значителния финансов и технологичен ресурс, който е необходим, за да обслужат минимум скоростните пътища. Това води до ситуацията, информационни транспортни системи да се залагат в отделни единични участъци от РПМ [16]. Крайният резултат е, че темповете на изграждане на системите за контрол и информация в нашата страна са много бавни (към 2019 година бяха изпълнени 321 пребroителни пункта и само 9 заснемащи метеорологични станции по националната пътна мрежа [17]).

В такава ситуация, при която новите стандарти могат да се залагат ограничено, използването на бази данни, основаващи се на метасинтез, може успешно да определи места (участъци), които се нуждаят в по-висока степен от други от информация в реално време и мерки по превенция на потенциални транспортни събития. Респективно на база на тази обратна връзка може да се планират по приоритет за бъдещите пунктове с елементи на информационни транспортни системи там, където ще са най-полезни, за да се постигнат завишени нива на пътна безопасност, екологичност и трафик удовлетвореност.

4. Заключение

В настоящата публикация е описан проект за бъдеща система за параметричен метасинтез на експлоатационни показатели на пътищата от РПМ на България, базиран на достъпни сателитни данни за атмосферата, енергийния баланс, растителността, повърхността на планетата и др. Концепцията предполага разработване на софтуерна обвивка (shell) на многопластова структура от данни: векторно описание на пътищата, с данни като топография (надморска височина), вариации и аномалии в температурата, албедо, снежна покривка, активни пожари и др., като основа на система за бъдещ метасинтез. Разгледани са потенциални източници на данни, възможни приложения на получените резултати и насоки за бъдещото развитие на системата.

Разбира се, очаква се прилагането на резултатите от параметричен метасинтез в съответни подсектори на транспортната инфраструктура, да се отрази положително в посока на подобряване на експлоатационните ѝ показатели. В тази връзка се изискват последващи изследвания, с които да се верифицира степента на приложимост на системата.

5. Литература

1. G. P. Obi Reddy, Surendra Kumar Singh. Geospatial Technologies in Land Resources Mapping, Monitoring and Management. Springer (2018)
2. Wikipedia – Meta. Available at: https://en.wikipedia.org/wiki/Meta
3. Atkins S, Lewin S, Smith H, et al. Conducting a meta-ethnography of qualitative literature: lessons learnt. BMC Medical Research Methodology. (2008); 8:21.
4. NEO – NASA Earth Observation website. Available at: https://neo.sci.gsfc.nasa.gov/
5. Power – data access viewer. Available at: https://power.larc.nasa.gov/data-access-viewer/
6. LandViewer website. Available at: https://eos.com/products/landviewer/
7. PVGIS. 2017. Photovoltaic Geographical Information System. Available at: http://re.jrc.ec.europa.eu/pvg_tools/en/tools.html
8. PVGIS. 2017. Photovoltaic Geographical Information System. Available at: http://re.jrc.ec.europa.eu/pvgis/apps4/PVlargesystem_en.html
9. Huld, T., Müller, R., Gambardella, A. A new solar radiation database for estimating PV performance in Europe and Africa. Solar Energy 86 (2012), pp. 1803–1815.
10. МРРБ и МТИТС, Стратегия за развитие на пътната инфраструктура в Република България 2016-2022 (2016).
11. Wikimedia: Карта на транспортната мрежа на България в SVG формат, Ikonact. Available at: https://commons.wikimedia.org/wiki/Category:SVG_road_maps_of_Bulgaria#/media/File:Bulgaria_roads_map_bg.svg
12. Pultarova, T. Europe is warming faster than the rest of the world and scientists are puzzled, 11.11.2021. Available at: https://www.space.com/europe-climate-warming-faster-than-world
13. С. Иванова, Д. Митева, Изследване на проблема със снегонавяването по автомобилните пътища в България. Оценка на ефективността на инсталация от PV-панели при вариантни решения на защитни непреместваеми съоръжения, Годишник на УАСГ, том 53 (3), 715-732 (2020)
14. Е. Иванова, Д. Марков, С. Мижорски, Изследване на проблема със снегонавяването по автомобилните пътища в България. Оценка на ефективността срещу снегонавяване на вариантни решения на защитни конструкции от съоръжения с инсталация от PV-панели, Годишник на УАСГ, том 53 (3), 733-753 (2020).
15. Директива 2010/40/ЕС на Европейския парламент и на Съвета от 7 юли 2010 година относно рамката за внедряване на интелигентните транспортни системи в областта на автомобилния транспорт и за интерфейси с останалите видове транспорт. Достъпно на: https://eur-lex.europa.eu/legal-content/BG/ALL/?uri=CELEX%3A32010L0040
16. Златанова, С. Изграждат Интелигентни транспортни системи на АМ „Струма“, 20.09.2021 г. Достъпно на: https://bnr.bg/blagoevgrad/post/101529490
17. Интервю с Яко Пилософ: В какво трябва да се инвестира, за да се развият Интелигентните транспортни системи в България. Достъпно на: https://www.kontrax.bg/bg/inteligentni-transportni-sistemi

Tensile strength and dimensional variances in parts manufactured by sla 3D printing

Ognen Tuteski, Atanas Kočov

"Ss. Cyril and Methodius" University in Skopje, R. Macedonia - Faculty of Mechanical Engineering

ognen.tuteski@mf.edu.mk; atanas.kochov@mf.edu.mk;

Abstract: *With the rise of additive manufacturing (AM) technologies, a numerous limitations in conventional manufacturing have been circumvented. Additive manufacturing uses layer-by-layer fabrication of three-dimensional physical models directly from a computer-aided design (CAD) model. The CAD design is transformed into horizontal cross-section layers that are stacked together in physical space until the physical model is completed. This process can be used to directly manufacture tools for injection molding or for any other technology that requires a specific cavity shape to produce a part. This is referred to as Rapid Tooling (RT) and one of the up and coming AM technologies is the resin based stereolithography (SLA).*

An increasing number of companies are starting to develop desktop machines that utilize this technology and their low cost and high speed changes the design workflow. As a printing technology, SLA creates parts with a smooth surface finish which is ideal for applications such as investment casting for developing jewelry or rapid tooling for injection molding.

The development of rapid tools using SLA usually requires more rigid materials which can withstand higher temperatures and stresses and part models that need to have more accurate dimensions in order for a precise part to be produced from that specific tool. Even though models created by SLA have more isotropic characteristics compared to other 3D printing technologies, there are still some variations linked to the process parameters. This paper covers how orientation of the model on the build plate impacts the part accuracy and the tensile strength of the models. The effects of different post-processing procedures after SLA printing are also taken into consideration, since most resins need to be UV cured after 3D printing in order to achieve maximum mechanical strength.

This paper gives designers and engineers better understanding on the final properties of the models and the tolerances that have to be taken into consideration when designing parts intended to be manufactured via SLA 3D printing.

KEYWORDS*: ADDITIVE MANUFACTURING, 3D PRINTING, TENSILE STRENGTH, STEREOLITHOGRAPHY, SLA*

1. Introduction

In regard to prototyping and small series production, the advancements in additive manufacturing have made great strides and have changed the way we approach new products development. The limitations of industrial machines like purchase costs, maintenance fees and technical expertise are more or less circumvented by the introduction of desktop 3D printing mainly based on the FDM (Fused Deposition Modelling) and SLA (stereolithography) technologies.

SLA 3D printing in particular has created major opportunities for designers and engineers to evaluate more options and iterations of their designs since the print resolution of that technology can be up to 25 µm thus offering more precision and finer details on the models.

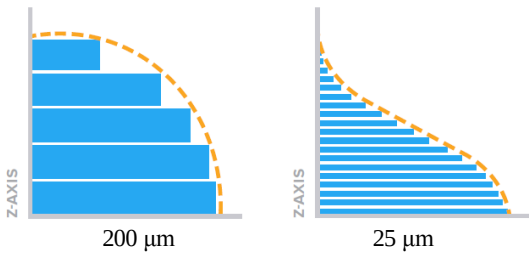

Fig. 1.1 *Layer thickness on surface finish– schematic representation (Source: [5])*

The surface finish on SLA compared to FDM while printing is also different and this is due to the way the layers are built.

In FDM, the build material is a prefabricated filament that is wound up and stored in a cartridge from which it is continuously fed to the extrusion head. In the head, the material it is partly molten by an electric heating system and extruded through a nozzle that defines the string diameter that nearly equals the layer thickness. Usually, string diameters range from 0.1 mm to 0.4 mm. The platform moves in z- direction and defines the layer thickness, as the material is squeezed on the top of the partly finished part [7]. This mainly limits the possible surface quality that is possible to be achieved using this manufacturing technology.

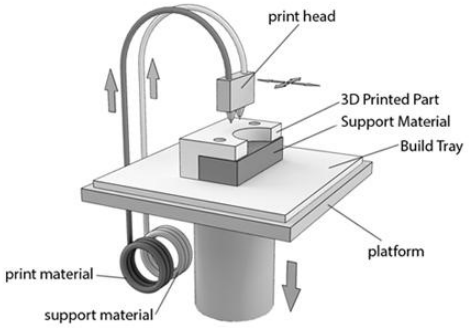

Fig. 1.2 *Fused Deposition Modeling (FDM) – Schematic (Source: https://www.dddrop.com)*

SLA on the other hand, is not only the oldest but also still one of the most detailed additive manufacturing process and delivers parts with very good surfaces and fine details. The parts are created by local polymerization of the initially liquid monomers. Initiated by a UV-laser beam, the polymerization turns the liquid into a solid, leaving a scaled solid layer. The laser beam is directed by a galvo-type scanning device that is controlled according to the contour of each layer. A typical machine can be seen in Fig. 2.3, left. After the build, the part is cleaned and finally fully post-cured in a UV chamber (postcuring oven). [7]

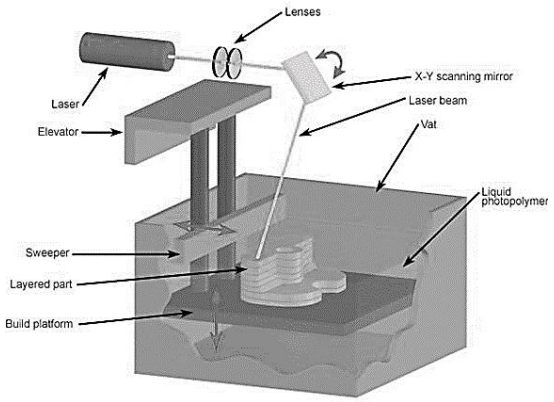

Fig.1.3. *Stereolithography (SLA) – Schematic (Source:http://www.custompartnet.com)*

Even though, SLA is the older technology, the affordability of FDM 3D printers, mostly due to their simpler design and cheaper parts has made them more widespread so most research on the influence of part orientation on strength is done on that technology. The need to post-process the SLA parts with UV curing also adds another level of complexity. The UV curing and furthermore any additional thermal post-processing causes some shrinkage on the part that needs to be taken into consideration when designing parts for assembly.

The surface quality of the printed parts is also mainly dependent on the part orientation during printing. The surface quality doesn't only affect the visual properties but also the roughness of the finish which is important in certain application of 3D printed parts.

For example, one of the most common sources of failure in molding inserts produced with SLA 3D printing has been described as the result of the molded parts features contacting the core inserts, thus causing these features to break during ejection [1]. This is due to the friction forces between the molded plastic and the inserts. Low tool strength especially at elevated temperatures has been cited as a contributory factor to failure and an FEA model on proper draft selection has been covered in the research of Harris et.al [2]. This means that the proper orientation of the models during printing not only influences appearances but has other implications depending on the application in question.

Furthermore, the process by which a layer is created has a dramatic impact on the quality and physical properties of the final part. A part printed at 100 micron layers on an FDM printer looks different from a part printed at 100 micron layers on an SLA printer, because of the way the layers are built.

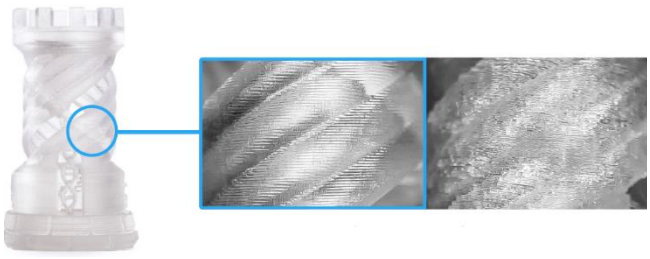

Fig. 1.4. *100 µm resolution print; SLA parts (left) have a better surface finish than FDM prints (right). (Source: [4])*

The aim of this article is to provide engineers and designers with some information about the influence of various part orientations and their influence on the strength properties of parts printed using the SLA technology. Since the experiment is done on multiple specimens

2. Mechanical strength depending on the 3D printing technology

There are a lot of different factors that need to be taken into consideration when preparing a part for 3D printing, especially if that part is supposed to withstand higher stresses. Among them is the orientation of the model on the build plate and minimizing overhangs that require supports. The orientation of the parts on the build plate is extremely important for the mechanical properties because they tend to vary with respect to direction. When building a part using any additive manufacturing technology the main parameter that determines the final physical properties is the way layer adhesion is achieved which differs from technology to technology. This anisotropic behavior is already pretty researched when it comes to FDM 3D printing but when it comes to SLA, the mechanical properties are more uniform.

2.1. Anisotropy in FDM parts

Since FDM 3D printing is based on building with extruded plastics, layer adhesion is achieved by mechanical bonds. The final part is produced from multiple linear layers and will have anisotropic properties regardless of its orientation on the build plate.

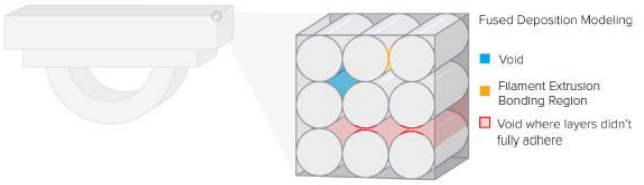

Fig. 2.1. *Composite matrix of a FDM part – Schematic (Source: [4])*

FDM 3D printers form layers by depositing lines of PLA or ABS. This process means that layers are not bonded together as strongly as the lines (filament extrusion) themselves; there are voids in between the rounded lines and it's possible that layers may not fully adhere to one another. [4]

On figure 2.1 it's shown that the surfaces of each layer are not completely adhering to one another. Even when the previous layer is still heated, the new layers only have partial adhesion and as a result the final part is anisotropic and has a smaller density compared to the parts produced with other polymer processing technologies like injection molding.

For this reason it is extremely difficult to obtain a completely enclosed and waterproof part with FDM 3D printing because there are always microscopic gaps in the porous matrix of the part. When bonds are considered at the molecular level, clear differences appear between the intermolecular forces in each extruded line and the bonding forces that bind the individual layers together. Each individual polymer extrusion line is composed of fairly rigid and intertwined high-strength polymer chains. As additional lines are extruded to or above the previous extrusion, it is almost impossible to establish equal contact between the previously applied plastic and therefore locations with lower strength and stiffness appear.

This means that if the direction of extrusion of the filament is taken into account, the final printed part will have the highest strength in the direction of the extruded lines, and its mechanical properties will be lower in the directions in which the interface regions of the part are oriented. Namely, these are the two axes normal to the direction of the extruded line.

The conclusion from this phenomenon is that the parts obtained with FDM technology of additive manufacturing are anisotropic, have different mechanical characteristics in different directions and their build plate orientation has a great importance on their functionality, especially in cases when they are to be used as functional parts and should withstand some load.

2.2. Anisotropy in SLA parts

In the SLA additive manufacturing technologies where the material is a liquid photopolymer resin there are almost no differences between the chemical bonds between the molecules of each separate layer and the neighboring layers.

While the model is being built, the monomer of the resin form covalent bonds between each other forming each layer. Because the polymerization process is not fully finished and the part is kept in a so called "green state"

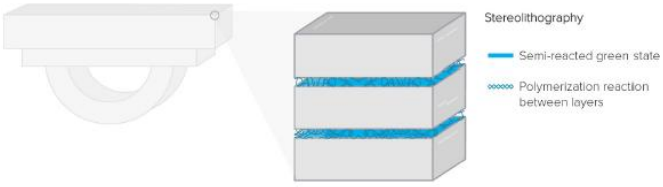

Fig. 2.2. *Continuous polymer matrix of a SLA part – Schematic (Source: [4])*

In this "green state", the material still has free molecular strains that can be bonded to the next layer during printing. While forming each subsequent layer the polymerization reaction includes strains from the previous layers and this way covalent chemical bonds are formed in both the axial and transversal directions.

This means that on a molecular level, practically there shouldn't be any difference between the Z axis and the XY plane due to the chemical bonds and each part produced with this technology can be seen as a singular molecule.

Despite the pronounced isotropy in the theoretical consideration of the SLA 3D printing process, some previous research has shown that there are still some mechanical differences depending on the orientation of the models. These differences, although insignificant, are mostly caused by small deviations in the movements of the printer along the X, Y and Z axes.

The influence of model orientation on the mechanical strength of printed parts has been examined in the research of Barclift and Williams [10], Cazon et. al [9] and in the Formlabs internal study [4]. [9] and [10] used the Stratasys PolyJet technology, while [19] used a Form2 SLA printer.

3. Methods

3.1. Tensile test

A tensile test is the most fundamental type of mechanical test where a testing sample is subjected to uniaxial tension until failure.

The tensile test of each specimen was done according to the guidelines in the standard EN ISO 527-2:1996. The 1BA test specimen used and its dimensions are shown in Figure 3.1.

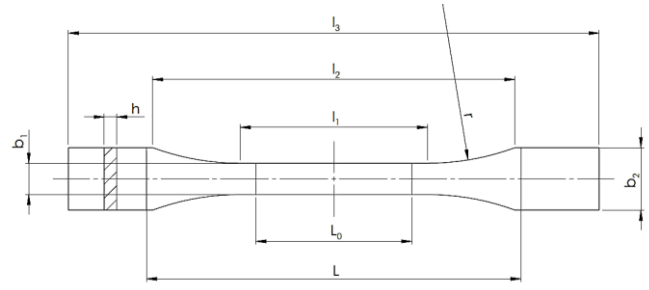

Type of specimen [mm]		1BA
l_3	overall length	≥75
l_1	length of narrow parallel-sided portion	30 ± 0,5
r	radius	≥30
l_2	distance between broad parallel-sided portions	58 ± 2
b_2	width at ends	10 ± 0,5
b_1	width of narrow portion	5 ± 0,5
h	thickness	≥2
L_0	gauge length	25 ± 0,5
L	initial distance between grips	l_2 +2

Fig. 3.1 *1BA tensile testing specimen (Source: [9])*

Each specimen was printed on a Formlabs Form2 SLA 3D printer using the HighTemp resin. Each specimen was later washed for 6 min in an isopropyl alcohol bath and then UV cured for 120 minutes at a temperature of 80°C, as per the recommendation found in the Formlabs datasheet.

There were 8 different orientation tested (as shown in Fig 3.2 and 3.3) with 3 specimens in each group (24 total):

1. Horizontal orientation (flat) (x-y)
2. Horizontal orientation (flat) (y-x)
3. Horizontal orientation (on the side) (x-y)
4. Horizontal orientation (on the side) (y-x)
5. Vertical orientation (flat) (x-y)
6. Vertical orientation (flat) (y-x)
7. 45° inclination (x-flat)
8. 45° inclination (x-side)

The test was one on a Shimatzu Autograph AGS-X series machine with a load cell capacity of 10 kN with a crosshead speed of 1 mm/min.

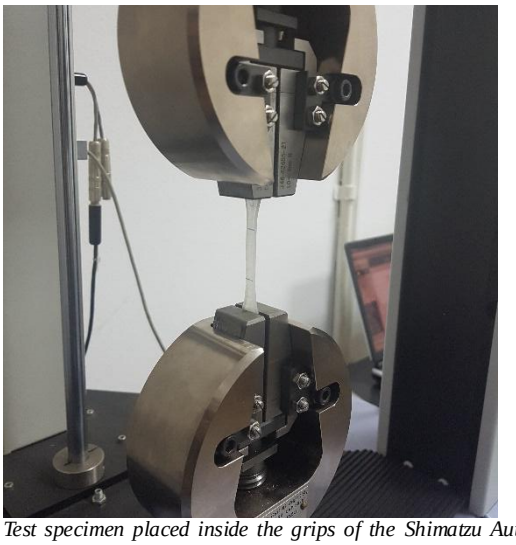

Fig. 3.2 *Test specimen placed inside the grips of the Shimatzu Autograph AGS-10kN*

From each of the test pieces the ultimate tensile stress was calculated as:

$$\sigma_m = \frac{F}{A_0}$$

where F is the force and A_0 is the starting cross-section area (b x h) of 10 mm^2.

From each of the test pieces the relative strain was calculated as:

$$\varepsilon = \frac{L - L_0}{L_0}$$

where L_0 is the initial gauge length of 25 mm and L is the length that corresponds with σ_m.

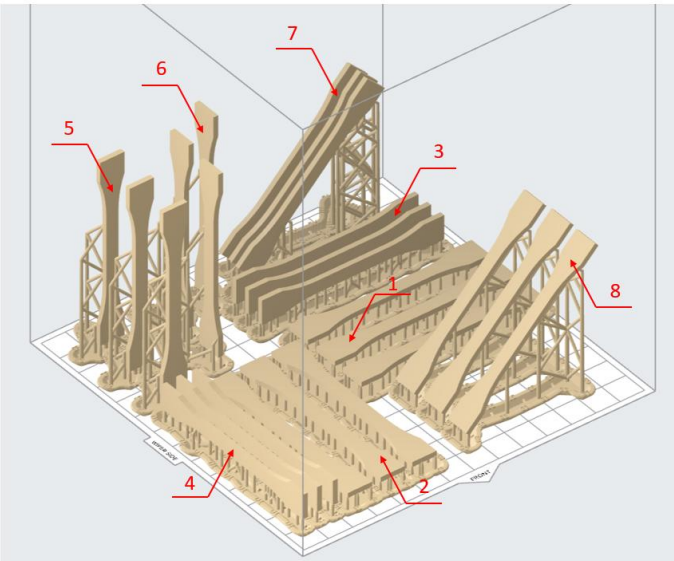

Fig. 3.3 *Different orientation of the test pieces in the Formlabs PreForm slicing software*

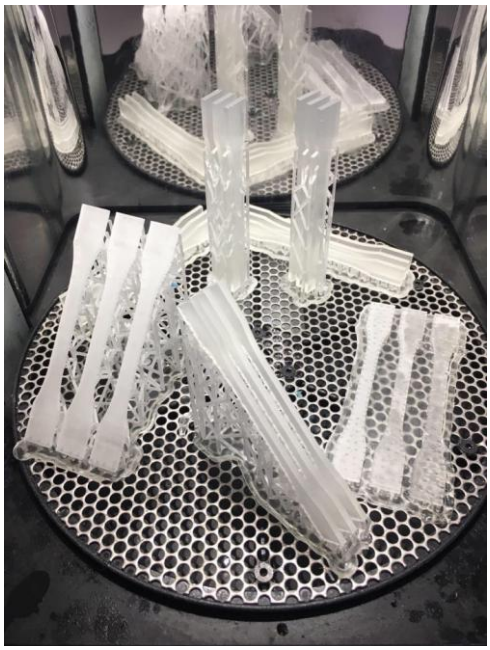

Fig. 3.4 *Different orientation of the test pieces during curing*

All experimental results from the tensile testing are shown in table 4.1 and are plotted on the histograms in figures 3.5 and 3.6 together with the standard error that is within 92% confidence interval. The results show a slight anisotropy in the mechanical strength with the highest UTS being measured in the specimens from group G that are oriented with a 45 degrees inclination on their flat side.

As far as the elongation at break, the High Temp resin is fairly brittle so only a small elongation and strain was measured with almost no plastic deformation on the parts.

3.2. Dimensional variations

Since the mechanical test is done on 24 different speciments, the 5 linear dimensions shown in Fig. 3.5 of each of the specimens were measured. This totals 120 measurements of different linear dimensions. Each measurement was taken 3 times at 3 different points and an average of the 3 measurements is presented for each dimensional control in table 3.2.

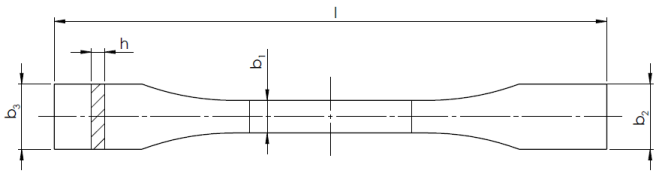

Measurements for dimensional control	
l	overall length
h	thickness
b_1	width of narrow portion
b_2	width at end 1
b_3	width at end 2

Fig. 3.5 *Measurements for dimensional control*

The standard deviation for all controlled dimensions is around 0,1 except the one for the largest measurement (overall length l) that is 0,270. However the % error for all measurement is below 1% as shown in Fig. 3.7

4. Conclusion and further research

Using SLA 3D printing technologies it is possible to produce extremely fine detail in the parts. The detail of these prints is in part determined by the models orientation during printing. The orientation also influences the surface finish that is important in certain applications like 3D printing molds for casting or injection molding.

This is especially important when the application involves printing with photopolymeric resins that need additional thermal postprocesing aside from the standard UV curing like the HighTemp Formlabs resin. Specifically with the HighTemp resin, the heat treatment raises the maximal heat deflection temperature of the material but it influences the mechanical characteristics like the strength and max elongation as well. If the resin is used for production of injection molding inserts, this has to be taken into account during the design process.

Despite the relative isotropic nature of the layer binding during SLA there are still some variances in strength (up to 10 %) in different print orientations.

Further research into the topic can be done by using different materials and test the strength according to different level of curing. As for the dimensional testing of the tolerances, the reaserch can be expanded to cylindrical surfaces, holes and interaxial dimensions.

Table 3.1: *Tensile testing results for the 24 specimens depending on the printing orientation*

	Ultimate tensile stress [MPa]	Ultimate tensile stress - Mean	Standard deviation	Relative strain [%]	Relative strain Mean	Standard deviation
A: Horizontal orientation (flat) (x-y)	39,00	**39,19**	**0,33**	4,56	**4,56**	**0,00**
	39,57			4,56		
	39,00			4,56		
B: Horizontal orientation (on the side) (x-y)	47,92	**44,04**	**7,62**	8,68	**7,53**	**2,67**
	35,27			4,48		
	48,95			9,44		
C: Horizontal orientation (on the side) (x-y)	36,09	**39,67**	**3,15**	4,48	**5,15**	**0,86**
	40,96			4,84		
	41,97			6,12		
D: Horizontal orientation (on the side) (y-x)	46,17	**42,24**	**3,43**	7,68	**6,03**	**1,49**
	40,60			5,60		
	39,94			4,80		
E: Vertical orientation (flat) (x-y)	49,45	**50,22**	**1,00**	8,44	**8,53**	**0,35**
	51,35			8,92		
	49,87			8,53		
F: Vertical orientation (flat) (y-x)	34,30	**39,70**	**4,67**	5,96	**7,11**	**1,14**
	42,31			8,24		
	42,47			7,12		
G: 45° inclination (x-flat)	58,95	**56,90**	**1,84**	8,80	**8,67**	**0,14**
	55,39			8,52		
	56,37			8,68		
H: 45° inclination (x-side)	33,60	**39,09**	**8,68**	4,24	**5,17**	**1,41**
	34,57			4,48		
	49,09			6,80		

Table 3.2: *Dimensional variances results for the 24 specimens depending on the printing orientation*

	l overall length [mm]	h thickness [mm]	b_1 width of narrow portion [mm]	b_2 width at end 1 [mm]	b_3 width at end 2 [mm]
A: Horizontal orientation (flat) (x-y)	74,49	2,15	4,98	9,91	9,95
	74,44	2,15	4,92	9,78	9,81
	74,39	2,18	4,87	9,87	9,87
B: Horizontal orientation (on the side) (x-y)	74,53	2,15	4,88	9,86	9,91
	74,5	2,14	4,92	9,83	9,89
	74,57	2,14	4,91	9,83	9,87
C: Horizontal orientation (on the side) (x-y)	74,5	1,95	5,05	10,08	10,07
	74,45	2,03	5,1	10,12	10,1
	74,45	1,99	5,05	10,16	10,12
D: Horizontal orientation (on the side) (y-x)	74,55	1,87	5,13	10,06	10,03
	74,51	1,87	5,08	10,02	10,06
	74,61	1,86	5,1	10,06	10,05
E: Vertical orientation (flat) (x-y)	74,61	2,02	5,11	10,05	10,11
	75,22	2,07	5,01	10,09	10,3
	75,22	2,07	5,01	10,09	10,3
F: Vertical orientation (flat) (y-x)	74,62	2,13	4,88	9,84	9,86
	74,61	2,1	4,86	9,87	9,87
	74,6	2,03	4,87	9,91	9,93
G: 45° inclination (x-flat)	74,95	2,02	4,82	9,88	9,86
	75,02	1,98	4,87	9,86	9,88
	75,04	1,95	4,88	9,89	9,86
H: 45° inclination (x-side)	74,98	1,85	4,84	9,85	9,83
	75,02	1,84	4,89	9,86	9,85
	75,07	1,86	4,87	9,86	9,91
Standard deviation	**0,272**	**0,114**	**0,100**	**0,115**	**0,141**

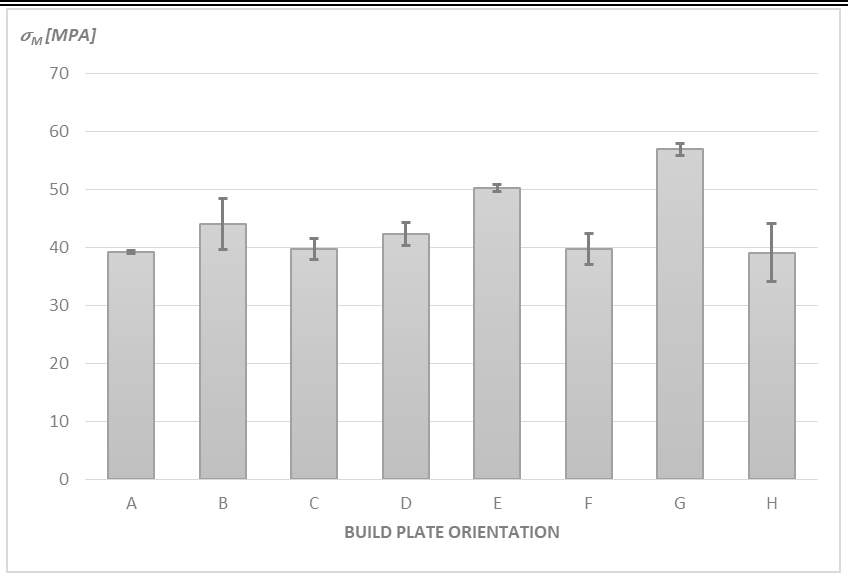

Fig. 3.5 *Mean ultimate tensile stress*

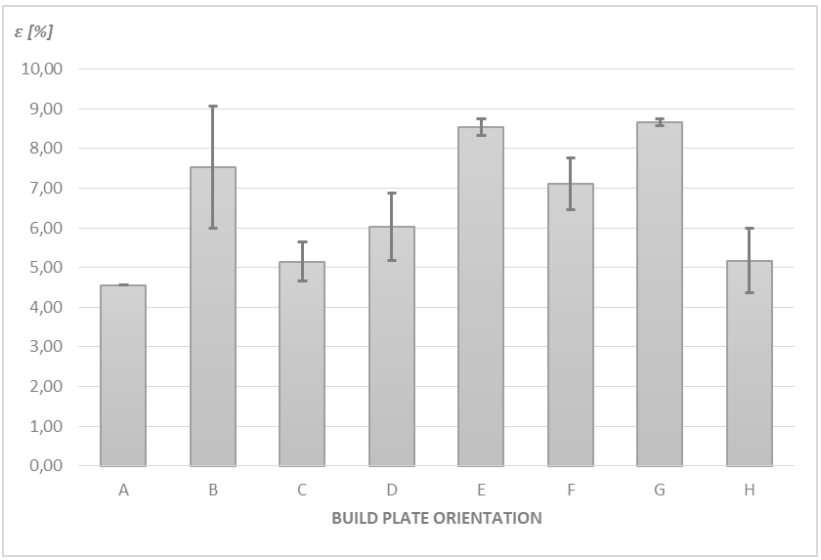

Fig. 3.6 *Mean relative strain*

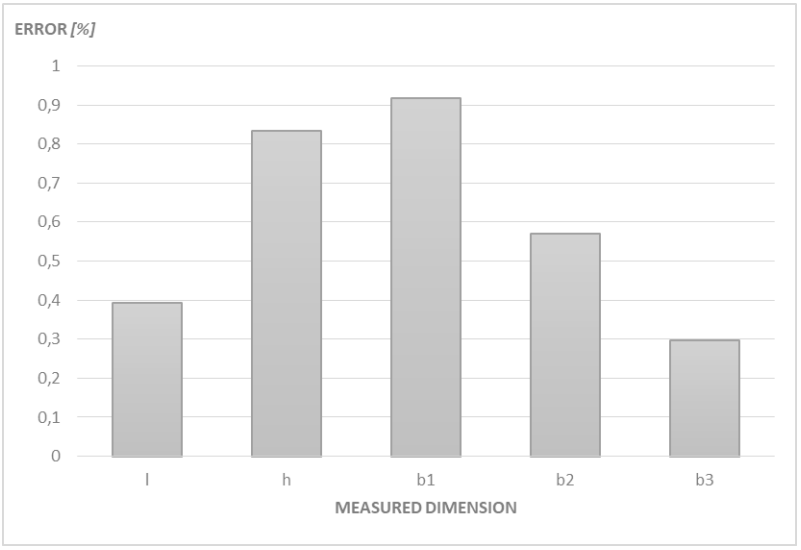

Fig. 3.7 *Measured dimensional error*

5. References

[1] Jacobs, P. F., 1996, Recent advances in rapid tooling from stereolithography. Proceedings of the 2nd National Conference on Rapid Prototyping and Tooling Research, Buckinghamshire College, UK.

[2] R. Harris , N. Hopkinson , H. Newlyn , R Hague & P. Dickens (2002): Layer thickness and draft angle selection for stereolithography injection mould tooling, International Journal of Production Research, 40:3, 719-729

[3] FORMLABS WHITE PAPER: 3D Printing with Desktop Stereolithography, June 2015, formlabs.com

[4] FORMLABS WHITE PAPER: Validating Isotropy in SLA 3D Printing, August 2020, formlabs.com

[5] FORMLABS WHITE PAPER: Introduction to Desktop Stereolithography, March 2015, formlabs.com

[6] Ziemian, Constance & Sharma, Mala & Ziemian, Sophia. (2012). Anisotropic Mechanical Properties of ABS Parts Fabricated by Fused Deposition Modelling. 10.5772/34233.

[7] Andreas Gebhardt. 2011. Understanding Additive Manufacturing. Hanser Publications, Cincinnati

[8] EN ISO 527-2:1996 Determination of tensile properties of plastics

[9] Aitor Cazon, Paz Morer and Luis Matey (2014). PolyJet technology for product prototyping: Tensile strength and surface roughness properties; Proc IMechE Part B: J Engineering Manufacture, Vol. 228(12) 1664–1675

[10] Barclift MW and Williams CB. Examining variability in the mechanical properties of parts manufactured via PolyJet direct 3D Printing. In: Proceedings of the international solid freeform fabrication symposium, Austin, TX, 6–8 August 2012. Texas: University of Texas, 2012.

[11] Ziemian, Constance & Sharma, Mala & Ziemian, Sophia. (2012). Anisotropic Mechanical Properties of ABS Parts Fabricated by Fused Deposition Modelling. 10.5772/34233.

Capability of micro-milling in machining of difficult-to-cut materials

Branislav Sredanovic[1,*], Djordje Cica[1], Stevo Borojevic[1], Sasa Tesic[1], Davorin Kramar[2]
University of Banjaluka, Faculty of Mechanical Engineering, Banja Luka, Bosnia and Herzegovina[1]
University of Ljubljana, Faculty of Mechanical Engineering, Ljubljana, Slovenia[2]
branislav.sredanovic@mf.unibl.org

Abstract: *The trend of using micro-parts in modern industry puts new tasks for contemporary production technologies. If these parts are made of difficult-to-machine materials, machining problems become more complicated. On the other hand, the requirements go towards manageable and stable production processes, reduction of the processes number, reduction of the machining cost, using of clean technologies, etc. Use of mechanical solid tools in engineering materials micro-machining, many problems occur, such as: high machined surface roughness of the, tool deflection, intensive tool wear, etc. These problems lead to difficulties in establishing adequate process models, and thus the ability to control of micro-milling process and it's including in smart processes and smart factory concepts. This paper presents the possibilities of using micro-milling in the difficult-to-process materials machining. The phenomena in micro-cutting are analysed, as well as the output machinability indicators (surface roughness, tool wear, etc.). As a conclusion, guidelines and technological frameworks for the application of micro-milling in practice are given.*
Keywords*: MICRO-MILLING, DIFICULT-TO-CUT MATERIALS, ANALYSIS, MACHINABILITY*

1. Introduction

The contemporary development of industry, in accordance with the Industry 4.0 guidance, leads to the neediness for miniature parts and assemblies developing. Miniature assemblies and parts can be found in many branches of industry (gear systems, micro-actuators, micro-combustion device, micro-robots, micro-tools, mechanical components of sensors, components of measuring devices, etc.), but medicine also (micro medical devices, surgical tools, lenses, etc.). Such a wide range of different miniature products creates a huge market value, with a value of several billion dollars per year, and with constant growth [1, 2]. Like all other fields of industry, micro-production is on global market competition that results on strong demands to the production cost reducing. Also, the micro-parts industry is pressed by global guidance to reducing pollution and production waste, the using of renewable resources, etc. Any further development of this type of products and industry, must be within the sustainable production framework [3].

The micro-part is defined as part that has two perpendicular dimensions under 1 mm [4]. The main initiators of micro-parts development and productions are the automotive, military and aerospace industry, medicine, and energy sector. These industries are not focused on producing of micro-parts only, but also on producing of micro geometric shapes on macro-parts (Fig. 1). A wide range of different micro-parts, has conditioned the use of a wide range of engineering materials, such as: metals, glass, plastics, composites, special materials, etc. In micro-technologies, in addition to the general micro-part materials properties, other properties become important, such as: properties of each type of materials structure grain, properties of structure grain borders, elasticity, electrical conductivity, magnetism, tendency of surface layers to adhesion, surface reflectivity, etc. There are very complex processes and phenomena that weren't characteristic and significant in machining processes on macro-level. All of the above points to complex micro-level industry processes on: construction, machining, measurement and manipulation.

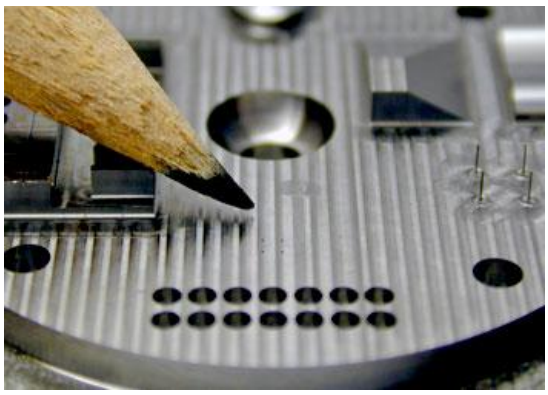

Fig. 1 *Micro-forms on metallic part [5]*

In this paper, the possibility of using solid tool processes in the machining of micro-parts functional surfaces is presented. Focus of analysing is machining of difficult-to-cut materials. In next, micro-production technologies were qualified, basic process phenomena were described, the advantages and disadvantages are listed. On next, analysis of experimental measurements was performed. The aim of the paper is to create the basis guidance for micro-machining process modelling, for the purpose of machining process adequate control and monitoring. It should be noted that micro-machining processes are advanced processes, which are part of Industry 4.0. However, all mentioned is prerequisite for incorporating and using these technologies into the smart factory framework, which is derived from Industry 4.0 concept.

2. Micro-machining technologies

Micro-production technologies can be divided in two groups: micro-system technologies (MST) and micro-engineering technologies (MET) [6]. The first one is focused on productions of micro-electro-mechanical systems (MEMS), on example: computer components, sensors, electronic devices, etc. There are production processes based on etching, electronic and ion beam machining, photolithography, etc. The micro-engineering technologies are focused on production of mechanic micro-parts or micro-forms, such are: micro-surfaces, micro-holes, micro-channels, micro-shafts, micro-gears, micro-chambers, micro-valves, etc. The production processes of mentioned micro-parts can be based on: additive processes (micro-casting, and 3D printing processes), thermal processes (electro-discharge machining, laser beam machining, etc.), or mechanical processes (micro-cutting, micro-forming, non-conventional micro-machining). Subgroup of micro-cutting processes include: micro-turning, micro-drilling, micro-milling, and micro-grinding (Fig. 2).

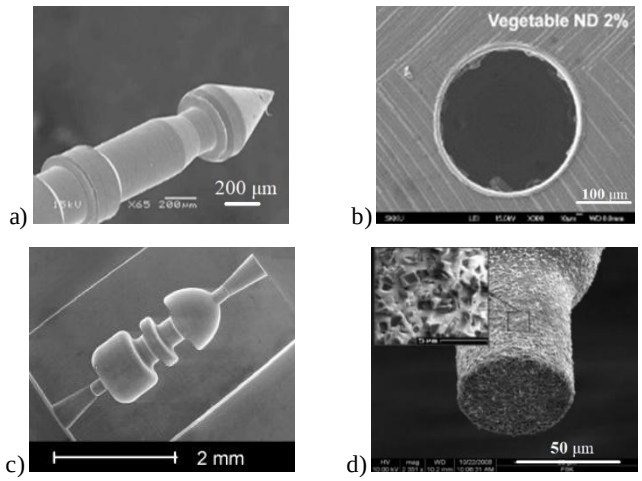

Fig. 2 *Micro-parts produced by mechanical micro-cutting: a) micro-turning, b) micro-drilling, c) micro-milling, and micro-grinding tools [7-10]*

3. Micro-milling of metallic materials

Generally, micro-cutting technologies are used for machining of functional surfaces on micro-parts or micro-forms. According to the type of workpiece material, micro-cutting processes are divided into two types: hard micro-machining (hardened steels, super alloys, glass, etc.) and soft micro-machining (aluminium, brass, plastic, graphite, etc.). As the cutting wedge penetrates in the workpiece material, complex processes occur in the chip forming zone, which are characteristic for micro-cutting. Unlike cutting process and chip forming of workpiece material at the macro level, in the cutting process and chip forming at the micro level, the relationship between geometric and process parameters has a great influence on output parameters and machinability indicators. This relations is described by "size effect" [3, 7]. The size effect is the situation when the rank values of geometric parameters, on example radius of cutting edge (r_c), or crystalline grain size (g_s); and the rank values of cutting process parameters, such are cutting thickness (h), are in the same value range.

Depending on the ratio of the mentioned values, some characteristic cases of workpiece material removing mechanism by cutting wedge, can be defined: a) plugging, b) plugging and cutting and c) dominant cutting (Fig. 3). Each of the material removing mechanism cases is not constant during the machining time. This is due to the cutting tool wedge wear, the change of cutting edge geometry, the workpiece material crystalline structure non-homogeneity, elastic and plastic deformation of workpiece material, dimensional deformation of cutting tool body, cutting process kinematics (on example in milling), etc.

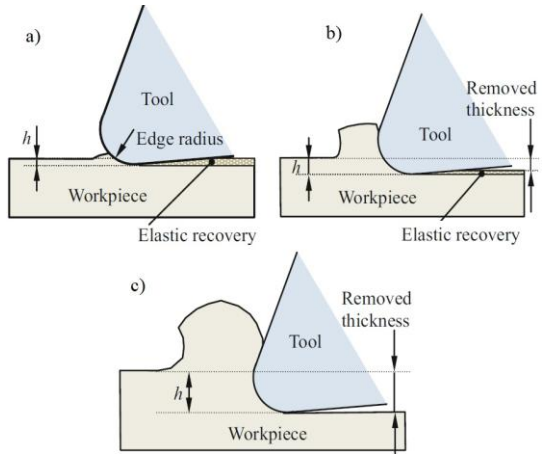

Fig. 3 *Material removing mechanisms n micro-cutting [11]*

In papers [1 - 5], investigation on solid-tool based machining of different metallic materials and machinability was given. Different authors analyzed various metal cutting processes and its possibilities in micro-part machining [7 - 10]. Also, influence of size effect on process performances was investigated by Bissasco et al [3], and Chae et al. [11]. Influence of cutting parameters, cutting tool coatings in micro-milling of Inconel 718 was investigated by Ucun et al. [12]. They concluded that specific coatings on cutting tool are given the best surface roughness. Experimental analysis of micro-milling of super-alloys Inconel 718 and Ti6Al4V, with 0.8 mm diameter flat-end milling tool, was performed by Kuram and Ozcelik [13]. Lu et al. [14] investigated residual stress on micro-parts surface. They performed analysis and comparison of simulated and experimental measured data, which given on micro-milling of Inconel 718. In study [15], Lu et al. investigated machined surface roughness consideration of cutting tool wear, during micro-milling of Inconel 718. There was investigated influence of cutting tool coatings on tool wear and surface roughness. Modelling of micro-milling process by FEM was performed by Thepsonthi and Ozel [16]. In this study, FEM model constants was adopted by micro-milling of Ti-6Al-4V alloy by cBN coated cutting tool. Influence of cutting parameters on process performances, in five-axis micro-milling and deep hole drilling in nickel-titanium alloys, was investigated by Biermann et al. [17]. During investigation of micro-milling process of Ti-6Al-4V, Jaffery et al. [18] are performed statistical analysis on influence of process parameters on machinability indicators. Krishnan and Mathew [19] performed studies on cutting tool wear in micro-milling of Inconel 718. There was investigated behavior of newest cutting tool coatings and its influence on cutting tool performance and machined surface roughness. Similar studies were performed by Atif et al. [20]. They investigated effect of cutting tool coatings and cutting parameters on part quality indicators.

Machining of complex geometry micro-parts made of difficult-to-machining materials (hardened tool steels, super alloy, etc.), leads to the complication of the micro-cutting process. There is an increase of the cutting forces value and deforming of milling tool, more generated heat and more intense abrasive and adhesive cutting edge wear, and etc. As mentioned earlier, micro-milling process are used to machining of functional complex surfaces on micro-parts. If difficult-to-cut workpiece materials are there, main problems is obtaining high shape accuracy, dimension accuracy, satisfactory machined surface roughness, but also a low machining cost. In order to build the efficient control and monitoring of the micro-milling process, it is necessary to perform an analysis of process capability. The aim is obtaining appropriate machinability indicators, and enable possibility of adequate cutting process output parameters modelling.

4. Experimental analysing and discussing

Experimental run were performed on three axis high speed micro-milling machining centre Sodick MC430L, which placed in Laboratory for cutting on FME Ljubljana (Fig. 4). As cutting tool was used flat end mill cutter SECO, TiAlN layer coated. Tool has diameter is 600 µm, corner radius 0.05 mm, and extra-long neck 8 mm. There is two flute, with maximum cutting depth of 0.8 mm, and helix revolution angle is 7.25°.

Fig. 4 *Micro-forms on metallic part [3]*

Experiment runs was performed in channel milling, with different milling process parameters. Workpiece was nickel-chromium super alloy Inconel 718 (53% Ni, 19% Cr, 18% Fe, 5.1% Nb, 3% Mo, 1.1% Ti, 1% Co, 0.5% Al, 0.35% Si and 0.08% C), with tensile strength 1350 MPa, and hardness 40 HRc. It used in responsible parts for mechanisms which work in extreme mechanical and thermal conditions, regard to excellent oxidation and high temperature resistance. During micro-milling of channels, MQL was used as lubrication technique. The channel depth corresponded to the depth of cutting. Experimental plan was adopted as full factorial plan, with two changeable milling parameters: depth of cutting a_p (mm), and feed per tooth f_z (mm/tooth), on three level each. It was given nine experimental runs with different parameter combinations without repeat. Cutting speed was constant v_c = 40 m/min, and width of milling a_e = 0.6 mm.

After each experimental run machined surface roughness at channel bottom was measured. Measuring of surface roughness was performed on Alicona Infinite Focus optical scanning device.

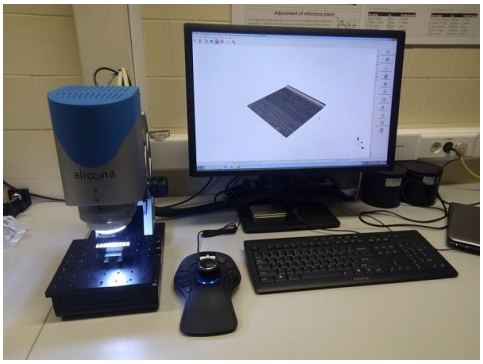

Fig. 5 *Surface scanning on Alicona optical measuring device*

Results of arithmetical mean height of surface roughness (R_a) for machining with different cutting parameters combination were shown on Fig. 6. The highest surface roughness, was on channel that machined with depth of cutting of 0.03 mm, and feed per tooth of 0.018 mm. As theoretical expected, minimal machined surface roughness was obtained when machining with minimum parameter values - depth of cutting of 0.01 mm and feed per tooth 0.008 mm. Observing the diagram and the values for some process parameters combination, it can be noticed that the increase of input process parameters is not accompanied by the increase of machined surface roughness values. This is more pronounced for lower process parameters values. As opposed to machining at the macro level, previous noted occurrence is due to the size effect. It occurred because the cutting process parameters values were close to the cutting tool radius. In that case, the workpiece material plunged with the cutting tool wedge. Also, there may be cases that the values of the parameters were close to the size of the crystal grains in the material of the workpiece, and material removal occurred at the structure grain boundaries.

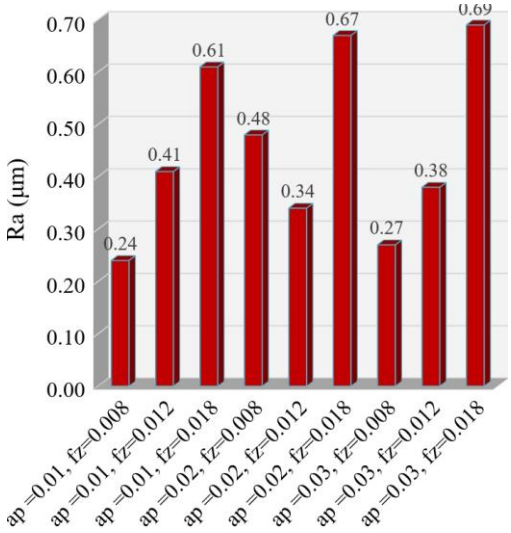

Fig. 6 *Surface roughness of micro-milled channel bottom [3]*

Based on the input cutting parameters and measured data, machined surface roughness modelling was performed. For it, Design Expert 7 software was used. For mathematical model formulation, based on RSM method, software was proposed 2FI (model with parameters interaction) versus Quadratic model. Based on statistical indicators, a modified model with one interaction and one square parameter was formed. The coefficients of the mathematical model were calculated using the least squares method. Statistical analysis was performed by ANOVA. Based on statistical parameters p-value and f-value, as significant parameters the feed per tooth was determined, while the depth was noted as less significant process parameter. Model mathematical formulation for prediction of arithmetical mean height of surface roughness is given as:

$$R_a = 0.546 + 1.333 \cdot a_p - 58.333 \cdot f_z + 3500 \cdot f_z^2 \quad (1)$$

Based on measured data and values calculated by mathematical formulation, statistical analysis was noted average values of 0.45, and standard deviation of 0.088. Model is significant, that noted by p-values is 0.023. Signal to noise ratio is 6.0, and regression coefficient R^2 is 0.83. Based on this, can be concluded that mathematical model for prediction of machined surface roughness is adequate at least. Based on it, RSM graph is formed, and showed on Fig. 7. Based on presented graph, can be concluded that machined surface roughness increases by exponent function with increasing of feed per tooth. Machined surface roughness increase by linear function with increasing of depth of cutting. From the graph shape it can be seen that the earlier explanations of the results variation on low range process parameters, partially included and observed by presented model only. For that reason, a slightly lower regression coefficient was obtained.

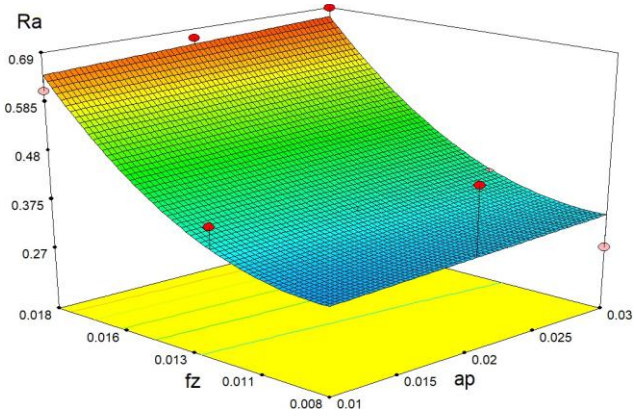

Fig. 7 *Surface roughness model response*

The machined surface roughness increases during machining time. The change of the machined surface roughness was measured at the beginning and at the end of the cutting tool wear monitoring. At the beginning of machining average surface roughness value was 0.34 µm, and at the end of the monitored machining time it was 0.49 µm. This is due to cutting tool wear, as a consequence of adhesion, diffusion and abrasion wear mechanisms. The cutting tool wear in micro-cutting of metals is intensive due to the pronounced size effect. Measuring of cutting tool was performed on Alicona Infinite Focus optical scanning device, also. Cutting tool wear is monitored via parameter, such as the cutting edge radius, because it is directly related to the appearance of the size effect (Fig. 8). Thus, the chip removal mechanism during machining time can be changed from chip separation to the plugging effect.

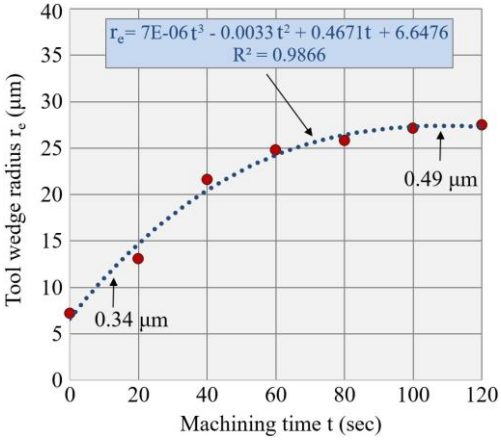

Fig. 8 *Increase of surface roughness during machining time*

5. Conclusions

This study presents the basics of micro-technologies used in the processing of metallic micro-parts. Based on of available literature sources, technologies and methods are classified, and their technological frameworks are summarized. In this paper, the main focus was on mechanical micro-cutting methods, due to the phenomena associated with the size effect, different chip removal mechanisms, and consequential problems in achieving the appropriate machined surface quality and dimensional in terms of economical machining process. Experimental analysis was performed on micro-milling of super-alloy Inconel 718, due its difficulties in machining, and as one of irreplaceable engineering material in modern constructions which exposed to extreme exploitation conditions. Experimental analysis included machined surface roughness measurement, analysis of measured data, and formation of the predictive model of the arithmetical mean height of surface roughness. In addition, there was monitored of surface roughness increasing during machining time due to cutting tool wear. A mathematical model was obtained, and statistical analysis using the ANOVA method and full factorial experimental plan was performed. On the other hand, a lack of formed mathematical model into describing of the arithmetical mean height of surface roughness value was noted. This changes in depending on some combinations of input parameters, which caused by size effect.

However, the obtained results and analysis indicate that micro-milling is one of the machining methods, which can gives the appropriate machined surface roughness on micro-parts made of Inconel 718. Future research will go in the direction of analysing the micro-machinability of other super-alloys. Artificial intelligence (AI) will be included in the micro-cutting process modelling, in line with the Smart factory framework and Industry 4.0 guidelines. Previous research has shown that AI modelling method can give much more accurate models and adequate describing of complex phenomena.

6. References

1. D. Dornfeld, S. Min, Y. Takeuchi: Recent advanced in mechanical micromachining, Annals of CIRP, **55 (2)**, 745-768 (2006).
2. M.A. Camara, J.C.C. Rubio, A.M. Abrao, J.P. Davim: State of the art on micromilling of materials, a review, J Mater Sci Technol **28 (8)**, 673–685 (2012).
3. G. Bissacco, H.N. Hansen, L. De Chiffre: Size effects on surface generation in micro milling of hardened tool steel. Annals of CIRP, **55 (1)**, 593-596 (2006).
4. F. Schneider, J. Das, B. Kirsch, et al.: Sustainability in ultraprecision and micro machining: a review, Int. J. of Precis. Eng. and Manuf. - Green Tech. **6**, 601–610 (2019).
5. "State of the art micromachining CNC service" by 3D Industries, Inc. Web site: https://3dind.com/micro-machining/. Accessed: 04.11.2021.
6. E. Brinksmeier, O. Riemer, R. Stern: Machining of precision parst and microstructures", *Proc. of 10th International Conference on Precision Engineering (ICPE)*, Yokohama, Japan, 3-12 (2001).
7. M. A. Rahman, M. Rahman, A. S. Kumar, H. S. Lim: CNC microturning: an application to miniaturization, Int J Mach Tools Manuf **45(6)**, 631-639 (2005).
8. J.S. Nam, P.H. Lee, S.W. Lee: Experimental characterization of micro-drilling process using nanofluid minimum quantity lubrication, Int J Mach Tools Manuf **51(7)**, 649-652 (2011).
9. C. Brecher, C. Wenzel, R. Klar: Characterization and optimization of the dynamic tool path of a highly dynamic micromilling machine, CIRP J Manuf Sci and Tech **1(2)**, 86-91, (2008).
10. J. C. Aurich, J. Engmann, G. M. Schueler, R. Haberland: Micro grinding tool for manufacture of complex structures in brittle materials, CIRP Annals - Manuf Tech **58(1)**, 311-314 (2009).
11. J. Chae, S. S. Park, T. Freiheit: Investigation of micro-cutting operations, Int J Mach Tools Manuf **46**, 313–332 (2006).
12. I. Ucun, K. Aslantas, B. Gockce, F. Bedir: Effect of tool coating materials on surface roughness in micromachining of Inconel 718 super alloy. P I Mech Eng B-J Eng **288(12)**: 1550-1562 (2014).
13. E. Kuram, B. Ozcelik: Optimization of machining parameters during micro-milling of Ti6Al4V titanium alloy and Inconel 718 materials using Taguchi method. Proc I MechE Part B: J Engineering Manufacture **231(2)**, 228–242 (2017).
14. X. Lu, Y. Lu, F. Wang, C. Zhao: Research on surface residual stress of micro-milling nickel-based superalloy Inconel 718. Int J Nanomanufacturing **12(1)**, 82 – 92 (2016).
15. X. Lu, Z. Jia, H. Wang, L. Si, X. Wang: Surface roughness prediction model of micro-milling Inconel 718 with consideration of tool wear. Int. J. of Nanomanufacturing **12(1)**, 93 - 108 (2016).
16. T. Thepsonthi, T. Ozel: Experimental and finite element simulation based investigations on micro-milling Ti-6Al-4V titanium alloy: Effects of cBN coating on tool wear, J Mater Process Tech **213**, 532– 542 (2013).
17. D. Biermann, F. Kahleyss F, E. Krebs E, T. Upmeier: A study on micro-machining technology for the machining of NiTi: five-axis micro-milling and micro deep-hole drilling, J Mater Eng Perform **20(4-5)**, 745-751 (2010).
18. S. H. I. Jaffery, M. Khan M, L. Ali, P. T. Mativenga: Statistical analysis of process parameters in micromachining of Ti-6Al-4V alloy, Proc IMechE Part B: J Eng Manuf **230(6)**, 1017–1034 (2016).
19. N. A. Krishnan, J. Mathew: Studies on wear behaviour of AlTiN-coated WC tool and machined surface quality in micro endmilling of Inconel 718. Int J Adv Manuf Technol **110**, 291–307 (2020).
20. M. Atif, M. K. Gupta, T. Mikołajczyk, D. Y. Pimenov, K. Giasin: Effect of tool coating and cutting parameters on surface roughness and burr formation during micromilling of Inconel 718, Metals **11(1)**, 1-18 (2021).

Acknowledgement

This paper is results of activities on interstate bilateral project, in cooperation between Department for management of production technologies at FME Ljubljana and Department for production and computer aided technologies at FME Banja Luka. The project is supported by ministries and governments of Republic of Slovenia and Republic of Srpska.

Sequential development of integrated remote-control Smart Home/Office systems

Georgi Kolev*
University of Chemical Technology and Metallurgy, Bulgaria
*georgi.i.kolev@abv.bg

Abstract: *An integrated smart home system for monitoring and management of the elements of the working environment or at home in Home Assistant platform and is integrated with a voice assistant (Google Assistant) has been developed. It allows monitoring and control of various parameters of the environment, determination of geolocation, tracking the state of the connected devices, provides ascertainment of conditions or constraints during the implementation of logical algorithms or actions, etc. The developed integrated system solves the problem of using various interface applications, communication protocols and standards by integration of all its elements in one Application Programming Interface (API) and simultaneously expanding its scope through integration with a voice assistant (Google Assistant). The development of a dataset of interoperable rules integrated in the Smart Home/Office system should be done function by function. This paper is directed toward the sequential development of integrated remote-control Smart Home/Office systems by adding additional functionality to the already developed integrated system.*
Keywords*: SMART HOME/OFFICE, INTERNET OF THINGS, HOME ASSISTANT PLATFORM, VOICE ASSISTANT.*

1. Introduction

An integrated smart home system for monitoring and management of the elements of the working environment or at home in Home Assistant platform [1] and is integrated with a voice assistant (Google Assistant) has been developed [2, 3]. The structure of the Smart Home/Office system is based on the concept of the Internet of Things (IoT), which includes connectivity of devices and actuators, as well as the presence of Wireless Sensor Network (WSN). It allows monitoring and control of various parameters of the environment, determination of geolocation, tracking the state of the connected devices, provides ascertainment of conditions or constraints during the implementation of logical algorithms or actions, etc. The developed integrated system solves the problem of using various interface applications, communication protocols and standards by integration of all its elements in one Application Programming Interface (API) and simultaneously the system is expanding its scope through its integration with a voice assistant (Google Assistant). The functions of the system include performing actions by request from the users, but also predefined (default) values and actions. The development of a dataset of interoperable rules integrated in the Smart Home/Office system should be done function by function. This paper is directed toward the sequential development of integrated remote-control Smart Home/Office (SH/O) systems by adding additional functionality, including intelligent data analysis, to the already developed integrated system. This process can continue without limitation in time as far as the imagination of the designer and/or the users reaches.

2. Integrated Smart Home/Office system

Depending on the specific operational function, both connected devices or actuators and sensors can be used in the operation of the system to detect the presence or absence of certain conditions, followed by appropriate specific actions. They are realized on the basis of the logical algorithms introduced in the system. The general view of the developed integrated system [4] is presented in Fig. 1. The most frequently used data on the condition of the home and the members of the household are presented there. All objects included in the current integrated SH/O system are over 100, and historical data about them can be traced for a given period of time through the option "History" (Fig. 2).

The built system also includes services available through Home Assistant as presented in Fig. 3 estimation of the time for driving between two points - for example, from to the office, based on the Waze application. Other possibilities are creating a calendar with tasks or a list of purchases available to all members of the household (Fig. 1).

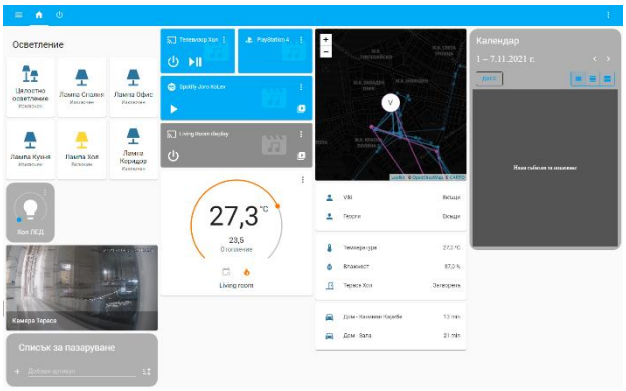

Fig. 1 *Google Home synchronized integrated system.*

Fig. 2 *Historical data.*

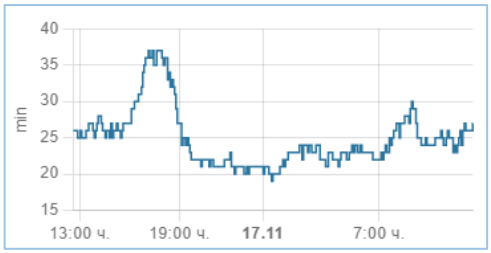

Fig. 3 *Estimation of travel time by car between home and office – Waze [5].*

The functions of the system include performing actions on request by users, but also on predefined values and actions. The development of a set of data from interoperable rules integrated into the Smart Home system must be performed function by function. The structure of a standard interoperable rules can be represented as follows:

"If Condition (& Condition2,…), THEN Action (Action2,…)"

"IF Condition11 (& Condition12,…), then IF Condition21 (& Condition22,…), ……THEN Action (Action2,…)"

The conditions can be set by the user (directly or in time) or depending on the values obtained from the sensors (Sensor-based Linked Open Rules). When analyzing the patterns of the behavior

of the inhabitants of the Smart Home from the collected data, it is possible to offer additional built-in functions [4].

The MQTT (Message Queue Telemetry Transport) protocol is used to ensure the connectivity of the elements in the integrated system and the connected applications, for which many implementations are available. This is a two-way communication protocol through which connected devices can publish data from sensors and at the same time receive configuration information or control commands.

3. Functionality and structure of SH/O system

The presented in the current paper integrated SH/O system integrates the following general functions [2-4]:

- Security – video surveillance, sensor monitoring, fire and flood detection;
- Comfort – remote and/or intelligent control of lighting, curtains, switching on and off appliances, control of video and audio equipment, TV, PlayStation, temperature control – air conditioning, heaters and central heating;
- Healthcare – measurement of environmental indicators – temperature, light, pressure, humidity, CO_2 content, dust, smoke, alarms or reminders for medications;
- Energy consumption and efficiency – consumption of electricity and heat (central heating).
- Indoor care – cleaning, ventilation, air purification and humidification, pet feeding.
- Activities organizer – calendar of events and tasks (individual and common), shopping list, traveling information (Waze), suggestions for spending the holiday time;
- Information – information from the connected mobile phones – geolocation, activities, settings, state of the batteries, sensor data, Wi-Fi connection, data transfer quantity etc.; news, weather information, data storage of historical data from all connected objects, sensor data acquisition and processing.
- Voice control integration – the voice communication is realized through the application for Android – Google Assistant, which is connected to Google Home. On the other hand, the open source Home Assistant application developed on the local server (Raspberry Pi) is synchronized via an API with Google Home.
- Remote access and management.

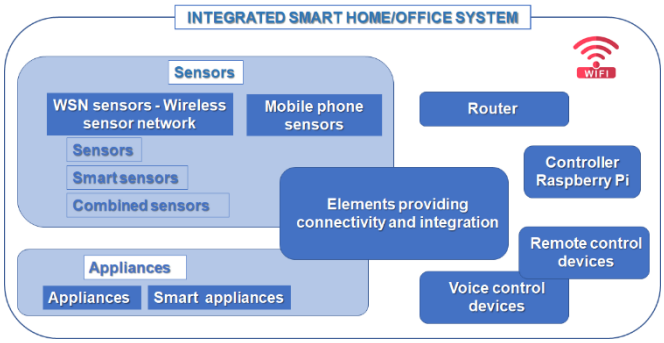

Fig. 4 *Integrated SH/O system elements (devices).*

The described functionality of the integrated system can be successfully applied both in home and in office environment. Each individual project is developed according the individual requirements from the users, connected with their needs, the object specifications – apartment, house, office, their location size, already build or in process of designing or building etc., the selection of its elements and the estimation of its cost.

An overview of the elements integrated in the SH/O system is presented in Fig. 4. Description of the elements can be found in [2, 3].

4. Sequentially expanding of the integrated SH/O system functionality

In order to include additional functions to the developed integrated SH/O system the shown in Fig. 5 algorithm should be followed. Here three cases will be considered:

- Integration of new smart device;
- Development of new function without adding new elements;
- Development of new function, when not all elements are available in the SN/O system.

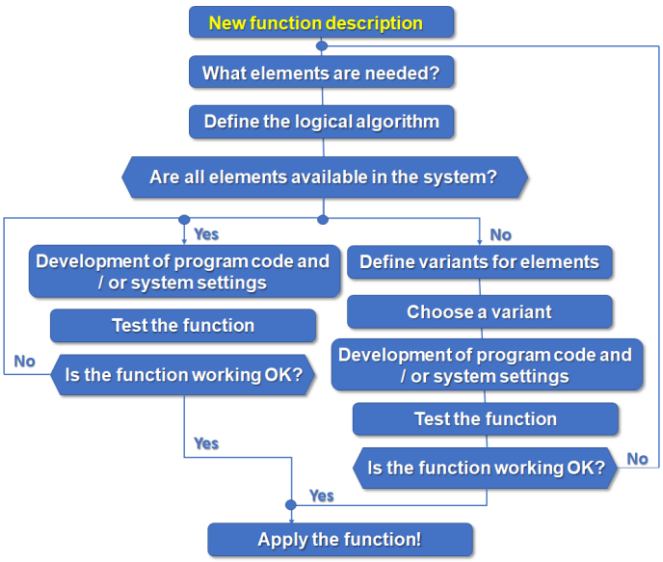

Fig. 5 *Algorithm for new function implementation.*

If a smart device – Canon TR500 series printer must be integrated in the system it should be connected to the Wi-Fi network during the installation of the driver, then the Home Assistant finds the new compatible with the system device, sends notification and the new device can be configured and added to the elements of the SH/O system. This allows the system and the user to monitor the state of the printer, the rate of toner consumption over time and notify the user(s) in advance when the toner reaches predefined level in order to avoid the situation shown in Fig. 6.

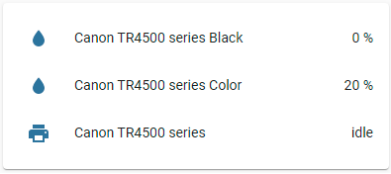

Fig. 6 *State of Canon TR500 series printer.*

As an example for the development of a new function without adding new elements here will be considered the possibility to set the time of for a meeting or an appointment outside the office/home, or waking up in the morning or preparing to go to go work according to the traffic and setting time to prepare (pre-defined time before leaving). In order to set such notification a script defining the arrival time, the time needed for preparation and the target location should be written. That is why it is convenient for repeated actions, like waking up in the morning for work.

The developed function, which uses Waze [5] service for estimation of driving time (*Td*) between two locations, works as it is shown in Fig. 7. For example, the employee should be at the office from 9:00 h. Then the arrival time can be set to *Ta* = 8.55 and the time for preparation is *Tp* = 30 minutes. If the estimated time by Waze is also *Td* = 30 min, then "Notification 1" or the predefined actions (like turning on the lights, playing music, etc.) should be started within the time interval 7:52 ÷ 7:58 a.m. and the "Notification 2" stays in order that the traffic changes and correspondingly the estimated time. If the estimated time for driving

changes to 35 min, then the second notification (or predefined actions) should be started in the time interval 8:14 – 8:20 a.m. The tolerances depend on the frequency of updating of Waze service in the system (current time for update of Waze service is 5 minutes).

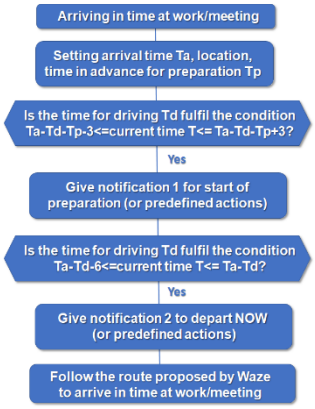

Fig. 7 *Algorithm of arriving in time function.*

The considered here function, which will need additional elements, is a function, which aims to locate if the employee is in the office and if she/he is in her/his workplace. In this case all the elements are not present in the integrated SH/O system (Fig. 5).

The available function is geolocation by GPS in the mobile phones of the connected devices (Fig. 8). In work environment using this function is connected with the availability of business mobile phones of the employees, that can be integrated in the company integrated system, with the knowledge and agreement of the employees.

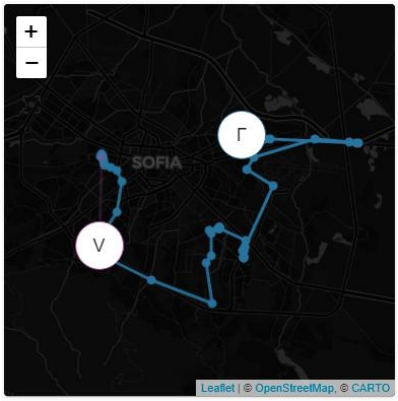

Fig. 8 *Geolocation determined by GPS in a mobile device.*

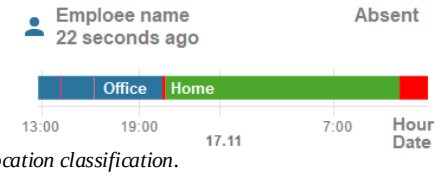

Fig. 9 *Geolocation classification.*

The classification in this case can be done – "in the office" and "out of the office" (Fig. 9).

Another solution, based on Bluetooth connection, is presented in Fig 7. It includes TUYA Bluetooth Gateway and GPS trackers. If the tracker comes into the range of the Bluetooth Gateway it will be registered in the system and the employee can be considered as located in the office. There are different models of trackers and gateways and an appropriate solution should be chosen, depending the size of the office, the number of employees etc. The chosen TUYA Bluetooth Gateway ensures connectivity to the Wi-Fi network and to the SH/O system, besides of Bluetooth devices (trackers), but also of the devices, that use Zigbee communication protocol.

Fig. 8 *TUYA Bluetooth Gateway and GPS trackers.*

The other part of the function is connected with the location of the employee on her/his workplace. This question depends on the type of work of the employees and is not necessarily connected only with the efficiency of the work process, but also can indicate the time the employees sit without movement on their computers (workplaces). In the COVID-19 pandemic the time people, including children, stay behind the computers drastically increases. It is important to add some motion and interruption of the work process in order to let the body and eyes rest.

The integrated SH/O system in this case can register the time spend on the workplace and also can send notification to the employees to interrupt their work for a while and have a rest.

The detection for this function can be done with one or two PIR sensor per employee (Fig. 9), depending on the number of people in the office. The suggested solution is placing the sensor below the desk plate and measurement of the time without movement after registering motion. The suggestion is that, if no motion occurs in the period of 5 minutes, for example, the employee has left his/her workplace.

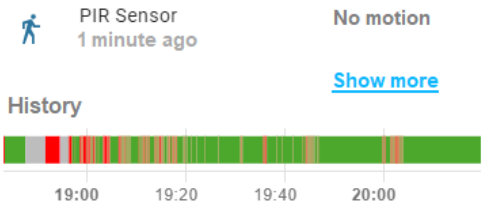

Fig. 9 *PIR sensor historical data.*

In our case the solution with Geolocation, determined by GPS in a mobile device, is appropriate and chosen for realization.

5. Conclusions

This paper is directed toward the sequential development of integrated remote-control Smart Home/Office systems by adding additional functionality, to the already developed integrated system.

Three cases of sequentially expanding of the integrated SH/O system functionality are considered: integration of new smart device, development of new function without adding new elements and development of new function, when not all elements are available in the SN/O system.

The process of the sequential development of integrated remote-control Smart Home/Office systems can continue without limitation in time as far as the imagination of the designer and/or the users reaches.

Acknowledgements

The research was conducted within the framework of the National Science Program "Information and Communication Technologies for a Digital Single Market in Science, Education and Security (ICTinSES)", funded by the Bulgarian Ministry of Education and Science.

References

1. Home Assistant. http://www.home-assistant.io
2. G. Kolev. Electrotechnica & Electronica, **56**, 2021, (accepted)
3. G. Kolev, E. Koleva. Proc. of 29th Int. Symposium "Management of Energy, Industrial and Ecological Systems", (*Bankya, Bulgaria*) 2021. (in Bulgarian)
4. G. Kolev, E. Koleva, L. Koleva. Science. Business. Society, **5** (3), p. 112-115, (2020)
5. Waze. https://www.waze.com/

Investigation of bending strength and modulus of elasticity of a new type of black locust plywood for construction

Asen Hristov[1*], Valerii Naidenov[1], Lilyana Koleva[2]

Institute of Mechanics, Bulgarian Academy of Sciences, Bulgaria[1]
University of Chemical Technology and Metallurgy, Bulgaria[2]

[*]a.n.hristov@abv.bg

Abstract: *The mechanical properties bending strength and modulus of elasticity in bending of a new type plywood for construction, based on black locust wood, have been investigated in relationship with the bonding technological factors. The experimental investigation is based on an optimal composite design with four control factors – temperature, pressure, bonding duration and specific glue consumption. Regression models describing the dependence of bending strength and modulus of elasticity in bending on the investigated technological bonding parameters are estimated. The obtained experimental and model-based results are analysed and discussed.*
Keywords*: CONSTRUCTION, WOOD, PLYWOOD, BENDING STRENGTH, MODULUS OF ELASTICITY IN BENDING, MATHEMATICAL MODELING, BLACK LOCUST (ROBINIA PSEUDOACACIA).*

1. Introduction

Wood is one of the most popular and widely used building materials, with the construction sector being the largest consumer of wood and timber. Its use as a building material is exclusively due to the large number of the positive properties of wood materials [1-4]: relatively low bulk density, easy machinability, significant compressive and tensile strength, low thermal conductivity and others. Last but not least are the positive environmental aspects and the possibility for recovery and renewal of wood resources.

At the same time, the plant origin of wood determines many disadvantages - anisotropic structure, hygroscopicity and the associated variability of shape and size, resistance to various biological attacks and the ability to burn. The modern woodworking industry has accumulated centuries of experience in solving the problems of wood deficiencies. On the one hand, technologies have been developed to protect and modify wood in order to increase its durability and reduce its hygroscopicity and flammability, as well as to increase some of its strength characteristics. The other increasingly fast-growing direction, which eliminates the shortcomings of wood and adds new properties, is the development of wood composite materials, which are increasingly used in construction.

Such wood composite material is plywood, which is most widely used in construction. The main tree species on which plywood production in Bulgaria is based in recent years are poplar and beech. The stocks of raw materials of these types, suitable for plywood production, are constantly decreasing, and at the current rate of exploitation of the forests, the stocks of beech will disappear in the next 2-3 decades, and the stocks of poplar are already running out. This makes it necessary to look for opportunities for the production of plywood from other wood species, from which there are stocks of wood. Such a tree species for our country is the black locust (*Robinia pseudoacacia*), from which there are significant stocks of wood, which so far do not find wide economic application.

The main goal of the present work is to determine the modulus of elasticity in bending and bending strength and to investigate the influence of the main technological bonding factors on these two indicators for a new type of plywood for construction, made of black locust wood.

2. Experimental results and analysis

The materials needed for the research were black locust veneer with a nominal thickness of 2.2 mm and water-soluble phenol-formaldehyde adhesive. These materials were used for the production in laboratory conditions of six-layer, black locust, waterproof plywood for construction with a nominal thickness of 12 mm.

The current investigation aims to establish the influence of the main technological factors in bonding on the modulus of elasticity in bending and bending strength.

The first factor (z_1) is the temperature of the press platens. The range of its variation was determined according to the manufacturer's recommendations in the interval from 120˚C to 160˚C.

The second factor (z_2) is the specific pressure. The interval of its variation was determined by recommendations in the specialized literature. The levels of variation are 1 MPa, 1.5 MPa and 2 MPa.

The third factor (z_3) is the duration of plywood pressing. The range of its variation was determined according to the recommendations of the adhesive manufacturer and from the recommendations for the duration of plywood pressing given in the specialized literature. The levels of variation are as follows: 8 min; 11 min and 14 min.

For fourth factor (z_4) is the specific glue consumption (specific cost). The range of its variation was determined according to the recommendations of the adhesive manufacturer and from the recommendations for specific glue consumption given in the specialized literature. The experimental region for the specific glue consumption is from 100 g/m^2 to 200 g/m^2.

The chosen experimental design was optimal composite design [5] with four control factors: temperature of press plates, pressure, specific glue consumption and duration of pressing. The number of experimental runs in the experimental design is 24. Additional (repeated) three experiments have been made at the central point of the design, where all factors are set equal to the values in the middle of their variation region. Six measurements the mechanical properties of obtained black locust plywood plates the modulus of elasticity in bending (y_1) and bending strength (y_2) are performed for each experimental run and the results are averaged. Thus, the total number of conducted measurement tests is 162.

Table 1. *Data from repeated observations.*

	Elasticity in bending y_1	Bending strength y_2
Mean value	14218.70 N/mm^2	124.86 N/mm^2
St. deviation	458.39 N/mm^2	8.27 N/mm^2

The results for the means and the standard deviations from the repeated experimental runs in the at the central point of the design at constant levels of the process parameters: the temperature of the press platens z_1 = 140 ˚C, specific pressure z_2 = 1.5 MPa, duration of plywood pressing z_3 = 11 min and specific glue consumption z_4 = 150 g/m^2 are presented in Table 1.

The determination of the modulus of elasticity in bending and bending strength was performed according to the standard BDS EN 310: 1999 Wood based panels: Determination of the modulus of

elasticity in bending and bending strength [6]. This European Standard describes the method for determining the modulus of elasticity in bending and bending strength of wood - based panels with a nominal thickness equal to or greater than 3 mm.

3. Model-based investigation results

Regression models are estimated the modulus of elasticity in bending (y_1) and bending strength (y_2) of the produced black locust plywood plates as a function of the temperature of the press platens (x_1), the specific pressure (x_2), the duration of plywood pressing (x_3) and the specific glue consumption (x_4) in coded in the region [-1 ÷ 1] units [7]. The relation between coded (x_i) and natural (z_i) units can be expressed by the equation:

$$x_i = (2z_i - z_{i,max} - z_{i,min})/(z_{i,max} - z_{i,min}). \quad (1)$$

where $z_{i,max}$ and $z_{i,min}$ are the maximal and the minimal values, determined by the experimental regions of each of the investigated process parameters. The regression models, together with the determination coefficients are presented in Table 2.

Table 2. *Regression models.*

	Regression models	***R^2, %***
y_1	$y_1 = 12002.53 - 1052.90x_1 - 193.13x_2 + 774.01x_4 - 1577.36x_1^2 + 903.95x_3^2 + 1111.56x_4^2 - 297.49x_1x_2 + 211.18x_3x_4 + 259.65x_1x_4 + 1273.47x_1x_2^2 - 256.87x_1x_2x_4 - 569.71x_1^2x_4$	90.92
y_2	$y_2 = 138.70 - 12.06x_1 + 4.40x_4 + 6.88x_1^2 - 18.38x_4^2 - 4.55x_1^2x_2 + 3.11x_2x_3 + 2.88x_2x_4 + 13.28x_1x_2^2 - 3.61x_1x_2x_3 + 4.72x_1x_2x_4 + 2.20x_2x_3x_4$	85.94

The goodness of fit tests and the values of the determination coefficients show good prediction characteristics of the estimated models. They can be used for the choice of appropriate process parameters under given technological requirements for the modulus of the elasticity in bending (y_1) and the bending strength (y_2) during the production of black locust plywood.

The estimated regression models are used for the investigation of the dependencies of the modulus of the elasticity in bending (y_1) and the bending strength (y_2) of the produced black locust plywood plates as on the variation of the process parameters: the temperature of the press platens (z_1), the specific pressure (z_2), the duration of plywood pressing (z_3) and the specific glue consumption (z_4), visualized on the contour plots in Fig. 1 – Fig. 4.

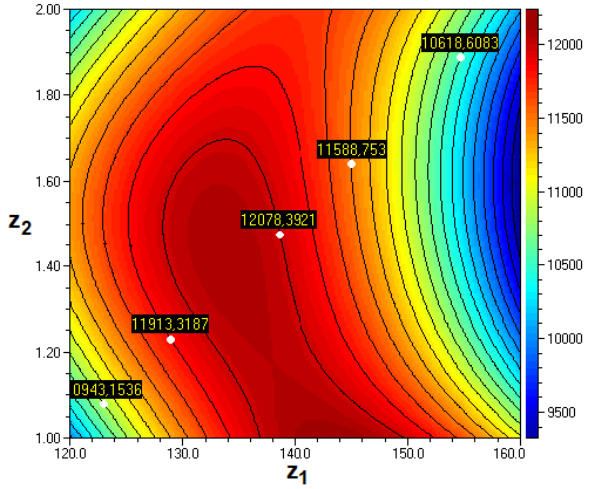

Fig. 1 *Contour plot of the bending elasticity (y_1) vs. the temperature of the press platens (z_1,˚C) and the specific pressure (z_2, MPa) for z_3 = 11 min and z_4 = 150 g/m^2.*

In Fig. 1 the contour plot of the elasticity in bending (y_1) as a function of the temperature of the press platens (z_1,˚C) and the specific pressure (z_2, MPa), for constant values of the duration of plywood pressing (z_3) and the specific glue consumption (z_4): z_3 = 11 min and z_4 = 150 g/m^2. It can be seen that under the specified conditions, the factor with larger influence is the temperature of the press platens (z_1). The region, where the maximal values of the elasticity in bending (y_1) can be obtained for temperatures of the press platens (z_1) in the region from 132˚C to 146˚C and specific pressure values below 1.6 MPa.

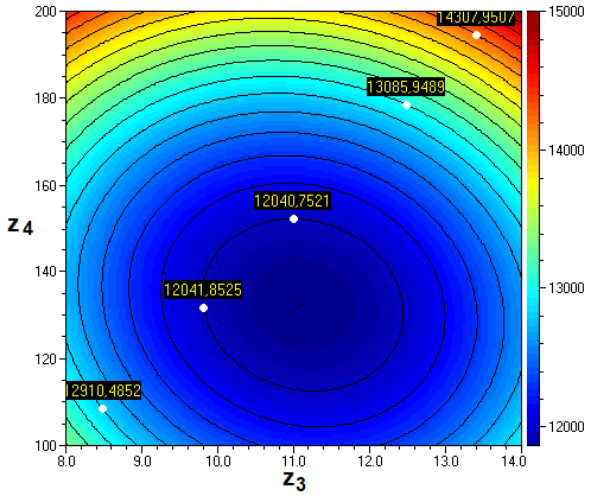

Fig. 2 *Contour plot of the bending elasticity (y_1) vs. the duration of plywood pressing (z_3, min) and the specific glue consumption (z_4, g/m^2), for z_1 = 140 ˚C and z_2 = 1.5 MPa.*

Fig. 2 presents the contour plot of the bending elasticity (y_1) as a function of the duration of plywood pressing (z_3, min) and the specific glue consumption (z_4, g/m^2), for constant values of the temperature of the press platens and the specific pressure, z_1 = 140 ˚C and z_2 = 1.5 MPa. It can be seen that the highest values of the bending elasticity are obtained for the highest values of the specific glue consumption z_4 > 190 g/m^2 for the set by factors z_1 and z_2 conditions.

The contour plot of the dependence of the bending strength (y_2) on the temperature of the press platens (z_1,˚C) and the specific pressure (z_2, MPa) for constant values of the duration of plywood pressing (z_3) and the specific glue consumption (z_4): z_3 = 11 min and z_4 = 150 g/m^2 is presented in Fig. 3. The maximal values of the bending strength in this case are obtained for lowest values of the temperature of the press platens around 120˚C and specific pressure in the region 1.3 ÷ 1.5 MPa.

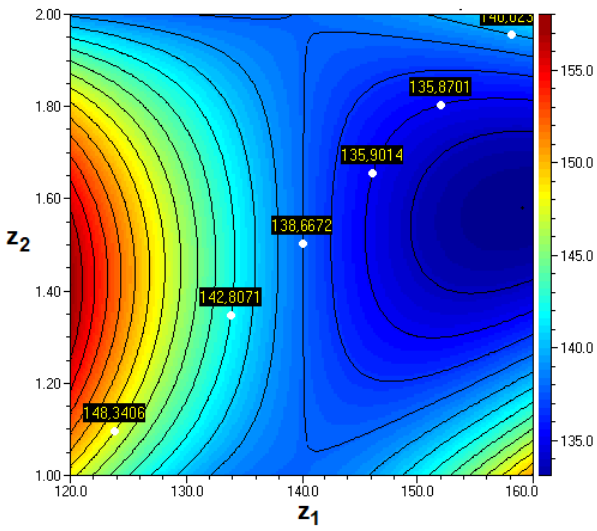

Fig. 3 *Contour plot of the bending strength (y_2) vs. the temperature of the press platens (z_1,˚C) and the specific pressure (z_2, MPa) for z_3 = 11 min and z_4 = 150 g/m^2.*

In Fig. 4 is presented the contour plot of the bending strength (y_2) vs. the duration of plywood pressing (z_3, min) and the specific glue consumption (z_4, g/m^2), for constant values of the temperature of the press platens and the specific pressure, z_1 = 140 ˚C and z_2 =

1.5 MPa. It can be seen, that under the set conditions, the bending strength (y_2) is not dependent on the duration of plywood pressing (z_3, min), while the choice of the specific glue consumption (z_4, g/m^2) is important and for obtaining the maximal values of the bending strength, the specific glue consumption should be set in the region 150 ÷ 160 g/m^2.

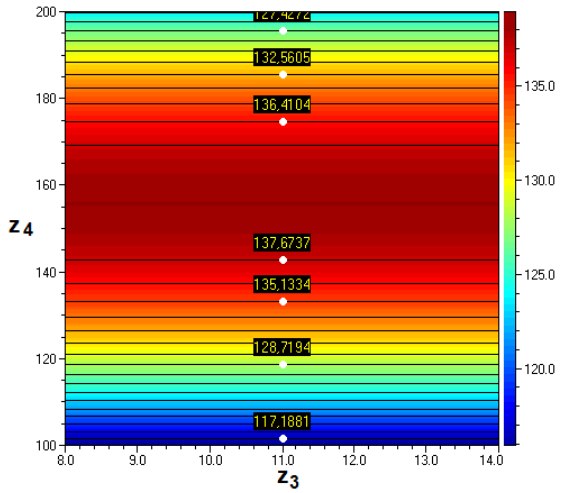

Fig. 4 *Contour plot of the bending strength (y_2) vs. the duration of plywood pressing (z_3, min) and the specific glue consumption (z_4, g/m^2), for z_1 = 140 °C and z_2 = 1.5 MPa.*

From the obtained investigation results is seen that the changes of all factors influence the values of the investigated mechanical properties - the modulus of elasticity in bending (y_1) and bending strength (y_2) of the produced black locust plywood plates. The choice of optimal regimes should be performed at defining concrete technological requirements for all quality characteristics simultaneously.

Experimental studies on the modulus of elasticity in bending and bending strength for construction black locust plywood bonded with phenol-formaldehyde adhesive confirm the patterns and trends of previous studies on the same properties but for black locust plywood [bonded with urea-formaldehyde]. Both indicators depend very much on the wood species from which the plywood is made, and in both studies the respective black locust plywood is superior in values to the respective beech and poplar plywood. This is due to the higher mechanical properties of black locust wood, compared to the same for beech and poplar. Technological factors in gluing also have a decisive influence on the values of the two indicators, as the temperature of the press platens and the specific glue consumption are formed as slightly more important for the final results.

4. Conclusions

The current investigation aims to establish the influence of the main technological factors in bonding on the modulus of elasticity in bending and bending strength.

For the experimental investigation an optimal composite design is realized with four control factors: temperature of press plates, pressure, specific glue consumption and duration of pressing. The number of experimental runs in the experimental design is 24 and 3 additional experiments have been made at the central point of the design. Six measurements the mechanical properties of obtained black locust plywood plates the modulus of elasticity in bending (y_1) and bending strength (y_2) are performed for each experimental run. Thus, the total number of conducted measurement tests is 162.

Regression models for the modulus of elasticity in bending (y_1) and bending strength (y_2) of the produced black locust plywood plates are estimated as a function of the temperature of the press platens (x_1), the specific pressure (x_2), the duration of plywood pressing (x_3) and the specific glue consumption (x_4). The obtained dependencies of the two quality characteristics on the process parameters are used for investigation and prognostication.

Research confirms the good prospects for the introduction of this new type of plywood in construction.

Acknowledgements

The authors want to thank for financial support from the National Science Program "Information and Communication Technologies for a Digital Single Market in Science, Education and Security (ICTinSES)", funded by the Bulgarian Ministry of Education and Science.

References

1. G. Blaskova, Properties and use of black locust wood. *Furniture and woodworking industry* (Sofia) 3 (2000)
2. G. Blaskova, *Wood Science* (Publishing house at LTU, Sofia, 2003)
3. P. Panayotov and team, Report on the topic: "Comparative studies of the properties of the wood of the straight black locust Robinia pseudoacacia forma rectissima and the traditionally used white acacia Robinia pseudoacacia L.". MES, FSI at LTU-Sofia, PSIL for wood modification, Sofia, (2004)
4. A. Hristov, Sci. researches of the Union of Scientists in Bulgaria - Plovdiv. Series C. Tech. and Technol., **V**, Balkan Conf. of Young Scient. (Plovdiv) 39-46 (2005)
5. I. Vuchkov, *Experimental research and identification* (Technique, Sofia, 1990)
6. BDS EN 310: 1999 "*Wood-based panels. Determination of the modulus of elasticity in bending and bending strength*".
7. *QstatLab home page*: http://www.qstatlab.co.uk/eng/index.html

Анализ на дефектите, получени при производство на стомана и стоманени изделия

инж. Миглена Панева[1], инж. Петър Панев[1], доц. Любен Ключков[2], проф. Димитър Карастоянов[1]
Bulgarian Academy of Science, Sofia, Bulgaria[1]
Technical University Sofia, Bulgaria[2]
m.paneva7@gmail.com, panevv@gmail.com, dimikara@abv.bg

***Резюме**: В настоящата статия е представена технологията за производство на стомана, получените полуфабрикати и процесът на тяхната преработка. Разгледани са най-честите причини, които водят до дефекти при трансформацията от суровинния материал до неговото внедряване в производството на изделия от тръби. Факторите се делят на три вида: породени в следствие на първичната технология по производство на стоманата, дефекти породени от човешка грешка или дефект в следствие на неправилна работа на оборудването или неговото дефектиране. Проследено е поведението на метала от производството до крайният вид на произведеният детайл.*
***Ключови думи**: СТОМАНА, ПОЛУФАБРИКАТИ, ДЕФЕКТИ, ПРОИЗВОДСТВО*

1. Въведение

В металургията всичко започва от суровините: желязна руда и кокс. При традиционните технологии от тях в доменните пещи се излива чугунът. След това от този чугун се произвежда стомана и стоманени полуфабрикати – сляби, блуми, кръгли, квадратни и заготовки тип „греда". В някои случаи полуфабрикатите се произвеждат без да преминават доменна обработка. За тази цел са необходими електрически дъгови пещи, в които като основна суровина се използва скрап от черни метали и директно редуцирано желязо [1, 2].

Всички полуфабрикати от стомана първо се обработват по метода на горещото валцуване. Това означава, че пластичната деформация се извършва на специални валцови машини, т.е. те се прекарват между две валцови ролки, при което формата на изходната заготовка се променя. В този случай температурата на материала трябва да бъде по-висока от температурата на рекристализация на стоманата. При това металът е много горещ – в повечето случаи температурата му в началото на валцуването надвишава 1100°C, а в края е най-малко 900°C [3]. На фигура 1 е представено изображение на процес на леене на метал, а на фигура 2- процес на горещо валцуване на метал в прокатен цех на завод „Стомана Индъстри" АД, гр. Перник, България.

***Фиг.1** Леене на метал*

***Фиг. 2** Горещо валцуване [4]*

Целта на настоящата работа е да се представи как се получават дефекти, възникнали в процеса на работа от леенето на метал до неговото внедряване в производството до реализирането на метални тръбни изделия и къде да се внимава, за да бъдат избегнати.

2. Дефекти, получени при производството на стомана

Когато производството на стомана е нискокачествено, шлаката е лоша, вискозитетът на стопената стомана е голям, течливостта е лоша, шлаката не може да плава, а в стоманата има много неметални включвания. Когато степента е сериозна, се формират ивиците и дупките.

Повърхностните дефекти на продуктите с метални ленти могат да имат първопричина, създадена в процеса на леене и на горещо валцуване, чрез кухини и вдлъбнатини [5]. Първоначалният размер и съотношението на повърхностните елементи са критични параметри, които определят дали те ще бъдат елиминирани чрез процеса на валцуване [6].

2.1. Натрупване на железен оксид

Дефектите са забелязани, с лентовидни или люспести черни петна, разпределението не е еднакво, а дълбочината на пресоването е различна. Такива железни листове са трудни за измиване в процеса на байцване, а ямите се образуват, когато железните окиси паднат.

2.2. Разслояване на лентата

Този дефект се получава при процеса на леене на метала, кога има разлика в температурите.

Проявата на дефекта се забелязва най-често чак след достигането му до процеса студено валцуване, където след изтъняване на слоя якостта става по-ниска и това доста често води до скъсване на рулона в проблемният участък.

Това от своя страна може да доведе до много неблагоприятни последици за оборудването, а именно навар на работните валци или отлюпване на парче от тях.

3. Дефекти, причинени при производството на полуфабрикатите горещо валцувани рулони

3.1. Разлика в дебелините в началото, средата и края на рулона

Температурата и скоростта на охлаждане на всяка част от горещо валцованата лента са различни, т.е. температурата и скоростта на охлаждане на главата, средата и опашката по дължината на лентата и ръба и средата на ширината им е различна по време на горещото валцуване. В следствие на неправилно горещо валцуване се получава така наречения дефект "вълна" (Фиг.3), а в по-тежки случаи „кораб" което затруднява последващите операции на байцване и студено валцуване. На фиг. 4 е показано байване на рулон, който е без „вълна" [7, 8].

Фиг. 3 Пулса с дефект „вълна"

Фиг. 4 Пулса без „вълна"

3.2. Лошо байцване

Режимът на байцване не е подходящ, когато например концентрацията на киселината е ниска, температурата на киселината е ниска, скоростта на байцване е твърде бърза, времето за байцване е недостатъчно. Когато повърхността на горещо валцованата намотка не е равномерно окислена след байцването при изсушаване на лентата не се отстранява напълно оксида на повърхността (Фиг.5). На фиг. 6 е представено как изглежда добре байцван рулон.

Фиг. 5 *Байцван горещо валцуван рулон с недотрав (окис по повърхността на рулона)*

Фиг. 6 *Добре байцван рулон*

4. Дефекти, причинени при производството на полуфабрикатите студено валцувани рулони

4.1. Емулсионно петно

Отгрятата повърхност на стоманената ламарина има неправилен цвят или петно в черен или кафяв оттенък (Фиг. 7).

Причините могат да бъдат следните:

1. Емулсията не се изчерпва на изхода на валцовия стан и се карбонизира при нагряване и образува петна;
2. При малко налагяне на обдухващото устройство на изхода на клетката на валцовия стан се задържа емулсия и образува петна при нагряване;
3. След като пещта е запалена, времето за предварителна продувка е недостатъчно и емулсията се карбонизира до образуване на петна при нагряване.

4.2. Окислен цвят

Повърхността е окислена (Фиг.8) и нейният цвят постепенно преминава от тъмно синьо в страни до светло синьо, кафяво и бледо жълто, наричани общо окислен цвят.

- Когато капакът за отгряване не е плътно затворен и навлиза кислород, стоманеният рулон се окислява;

4.3. Мустаци по външните витки на рулона

Мустаците се получават в следствие на износени ножове за надлъжно разкрояване на горещо и студено валцувани рулони.

При лош разкрой на студено валцувани щрипси е невъзможно производството на тръби, поради невъзможност от заваряване на двата края.

Фиг.7 *Емулсионно петно*

Фиг. 8. *Окислен рулон*

Фиг.9. *Мустаци по рулона*

5. Дефекти при производство на тръби

За качествено произведени тръби и профили от стомана е необходимо да се проследяват множество от параметри, които да отговарят на изискванията на клиента, както и на стандартите за производство.

Едни от най-важните параметри за правилна форма и добър външен вид са следните:

- Праволинейност

При криви тръби и профили няма как да се сглобят детайлите от едно изделие.

- Диаметър и дебелина

Почти всички детайли са част от общо изделие и при разминаване в диаметъра и дебелината те не могат да се окомплектоват.

- Здрав заваръчен шев

При лош заваръчен шев (Фиг. 10), детайла загубва своята първоначална форма (Фиг. 11) и губи възможността да се внедри в изделието. Застъпеният заваръчен шев няма естетическа форма и при последваща операция боядисване той става видим, което е недопустимо.

- Ръжда

В следствие на ниска концентрация на емулсията на тръбните линии и нейното замърсяване с хидравлично масло се появява корозия по тръбните изделия.

- Транспортни повреди
- Дупки и наранявания (Фиг. 12)
- Смачквания (Фиг. 13)

Фиг.10. *Лош заваръчен шев*

Фиг.11. *Спукан заваръчен шев*

Фиг. 12. *Нараняване по детайла*

Фиг.13. *Смачкване на детайл*

6. Заключение

След направения анализ на технологията по време на производството на стомана и преработката на полуфабрикатите са класифицирани следните групи дефекти:

1) Възникнали по време на производството на стомана: вдлъбнатини, дупки, железен окис, разнодебелинност, „вълна“, разлояване на лентата;
2) Възникнали в следствие на преработка на полуфабрикатите горещо и студено валцуван рулон: недотрав, оксиден окис, емулсионно петно, мустаци;
3) Дефекти на крайният продукт: лош заваръчен шев, наранявания, смачквания, липса на праволинейност и неправилна форма в геометрията на изделието, ръжда.

През целият етап на преработка на стоманата е необходимо стриктното спазване на всички правила, норми и стандарти. Това би намалило до минимум появата на дефекти. Един метод, представляващ проследяване на безразушителни дефекти е компютърната томография. Този метод може да допринесе за намаляване на скрити дефекти [9]. Ако въпреки това такива бъдат установени, това може да доведе до прекомерни разходи за производителя и загуба на работни часове на производството.

Благодарности:

Изследването в настоящата статия е осъществено с подкрепа по линия на средства за задочни докторанти – 2021 г.

7. Литература:

1. METINVEST HOLDING LLC, https://metinvestholding.com/bg/media/news/chto-takoe-goryachekatanij-staljnoj-prokat-i-kak-on-proizvoditsya
2. S. Moir, J. Preston, *Surface defects—evolution and behaviour from cast slab to coated strip*, **125** (2002), pp. 720-724
3. Jianhui steel, China http://m.bg.hnjhsteel.com/info/cold-rolled-sheet-roll-common-defects-chara-34653981.html
4. Завод „Стомана Индъстри“ АД, гр. Перник, България
5. H. Yu, X. Liu, X. Ren, *Behaviour of longitudinal cracks on slab surfaces in V-H rolling processes*, Steel Res. Int., 2 (2008), pp. 537-544, 10.2374/SRI07SP066-79-2008-xx
6. M.Nioia, S.Celottob, C.Pinnaa, E.Swartb, H.Ghadbeigia, Journal of Materials Processing Technology, Volume **249,** November (2017*), Surface defect evolution in hot rolling of high-Si electrical steels*, Pages 302-312
7. S. Shainu, T.K. Roy, B.K. Dey, R.K. Sharma, N.C. Gorain, S. Dhar, C.V. Sastry, *Study on Slab Surface Defects and Generation of FeO Type Slivers in Hot Rolled Coils Tata Steel Ltd*., Jamshedpur (2008)
8. S.-L. Lee, J. Choi, *Deformation analysis of surface defect on hot rolling by 3-D FEM simulation*, Rev. Metall. Cah. Inf. Tech., 105 (2008), pp. 127-135, 10.1051/metal:2008025
9. Ivanchev I., Stoimenov N., Sokolov B., *Testing of Concrete by Contactless Non-Destructive Tomographic Method*, IEEE XXX International Scientific Symposium 'Metrology and Metrology Assurance' 2020 (MMA 2020), 7-11 September Sozopol, Bulgaria, (2020), E ISBN:978-1-7281-9719-7 pp. 1-6, doi: 10.1109/MMA49863.2020.9254250.

Методика за анализ на метално пробно тяло чрез спектрален апарат

Миглена Панева[1], Петър Панев[1], Любен Клочков[2]
Bulgarian Academy of Science, Sofia, Bulgaria[1]
Technical University Sofia, Bulgaria[2]
m.paneva7@gmail.com, panevv@gmail.com

Резюме: *В настоящата статия е описано откритието на понятието спектрален анализ и областите, в които намира широко приложение. Пояснена е целта на прилагането на този метод и неговата важност. Описана е апаратурата, с която е най-подходящо да се извърши анализ на метално пробно тяло за проверка на входящите материали, осигуряващи качеството в процеса на преработка на горещо валцувани рулони до крайният продукт на готови изделия. Представена е методиката стъпка по стъпка за анализиране на метално пробно тяло от подготовката на пробното тяло до завършване на процеса по установяване количеството на всички химични елементи, които могат да бъдат изследвани..*
Ключови думи: *СПЕКТРАЛЕН АНАЛИЗ, ПРОБНО ТЯЛО, АПАРАТУРА, ХИМИЧНИ ЕЛЕМЕНТИ*

1. *Въведение*

Спектралният анализ е открит през 1859 г. от Г. Кирхоф и Р. Бунзен, преподаватели по химия и физика в една от най-старите и най-престижни образователни институции в Германия - Университета на Хайделберг на име Рупрехт и Карл. Те доказват, че всеки химичен елемент има свой характерен спектър. Това позволява впоследствие да се създаде разновидност на елементния анализ — атомният спектрален анализ, с който може количествено да се определя съдържанието на различни елементи в проба от веществото чрез разлагането им до атоми или йони в пламъка или в електрическата дъга. Спектралният анализ е съвкупност от физични методи за количествено и качествено определяне на състава на веществата чрез изследване на техните спектри. Съотношението между състава на дадено вещество и електромагнитния спектър, излъчен или погълнат от него, позволява спектралният анализ да се използва като чувствителен, относително лесен и бърз метод в научните изследвания, в промишлеността и други области. Над 30 % от всички анализи се извършват чрез този аналитичен метод [1, 2]. Чувствителността на тези прибори е толкова по-голяма, колкото по-мощен е постоянният магнит. Пропорционално на напрегнатостта на магнитното поле расте и резонансната честота, която е необходима за възбуждане на ядрата. Тя служи като мярка за класа на прибора. Спектрометрите от среден клас работят с честота 60 MHz (при записване на протонни спектри); приборите от по-висок клас работят с честота 90,180, 360 и повече MHz.

В спектралният анализ се използват така наречените спектрални апарати. Основните елементи на всеки такъв апарат са източник на светлина, която се изследва, средство за разлагането ѝ и регистриращо устройство. Той е основен метод за изследвания и анализи в астрофизиката, екологията, медицината, промишлеността и металургията за определяне чистотата на състава на металите и сплавите.

Целта на настоящата работа е да се изгради методика за анализиране на метално пробно тяло, като то се съобразява с вида на апарата и начина на подготовка на пробните тела. Основната цел на използване на спектралния апарат е безпроблемният контрол на качеството и проверка на входящите материали, осигуряващи качеството в процеса на преработка на горещо валцувани рулони до крайният продукт на готови изделия.

2. *Използвана апаратура*

За целите на направеният анализ е използван апарат за спектрален анализ Bruker Q2 ION [3]. На фиг.1 е представен лекият и компактен преносим апарат, който чрез своята оптична система AAC (активна компенсация на околната среда) за работа между 10 и 45 ° C компенсира топлинните отклонения и осигурява максимална аналитична стабилност без термично кондициониране. Това е универсална многоматрична система чрез искрови емисии за цялостна проверка на входящите материали и осигуряване на качеството на металните сплави. Основните му приложения и метални матрици включват мед, алуминий и желязо в по-малки леярни, инспекционни компании, рециклиране на метали и производители на метали.

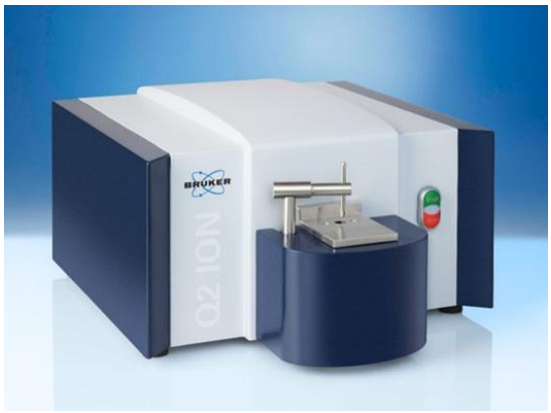

Фиг.1. *Спектрален апарат Bruker Q2 ION [3]*

Той е избран, защото дава бърз анализ на твърдите метални проби, включително положителна идентификация на материала, сплави и сортиране на материали и съчетава лекота на използване с лесна преносимост и ниски експлоатационни разходи.

2.1. *Начин на работа*

Начинът на работа протича чрез поставяне на пробата върху свещта и натискане бутона за стартиране. Пълният състав на тествания метал или метална сплав се получава за по-малко от 30 секунди и полученият резултат се сравнява със световната база данни за референтни сплави.

2.2. *Основни предимства*

- Чрез пакетите за аналитични решения (ASP) е възможно калибрирането на всички групи сплави;
- Нуждата от поддръжка на искровата стойка е минимална и с нисък разход на аргон;
- ELEMENTAL.SUITE предоставя лесно и функционално използване за информацията. ELEMENTAL.SUITE софтуер включва база данни за анализ и интерфейси към функциите на библиотеката MS Office Grade;
- Използва се софтуер Windows за лесна обработка на данните;
- Използва се технологията ClearSpectrum за усъвършенствана деконволюция на спектрите и за по-добра чистота и прозрачност (Фиг.2).

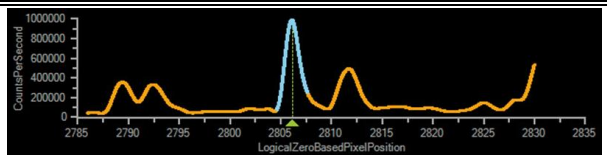

Фиг. 2. *Детектор с технология ClearSpectrum [3]*

3. Методика за провеждане на спектрален анализ на метално пробно тяло

В металургията, при преработката на горещо валцувани рулони (ГВР) в тръбни изделия е много важно да се знае какъв е химичният състав на суровината, защото от там се определя целият режим на работа [4-8]. При закупуването на горещо валцуваните рулони, доставчикът задължително предоставя сертификати за качество, в които е описано дадената марка стомана с какви механични и химични показатели е тя. От тези документи може да се изготви режима на работа за последващите трансформации на рулона. Но след направена проверка на данните доста често има разминаване в показателите, което води до неправилно определяне режима на работа при термоотгряване след студено валцуване на рулоните. Съответно и получените механични показатели на отгретите рулони не отговарят на зададеният стандарт, което води до пренасочване на метала ако е възможно или повторното отгряване, което води до забавяне на поръчката и допълнителни разходи. Именно поради тази причина е толкова важна проверката на всеки един ГВР преди задаването на режим за работа.

Правилната подготовка на металното пробно тяло е от съществено значение за бързата и точна проверка на химичният състав чрез тестването му със спектрален апарат. Пробното тяло от ГВР е във вид на тънка плочка (~2,0÷3,0 mm), поради естеството на тестваният продукт- лента, навита на руло. Минималните размери трябва да бъдат 10x10 mm, заради отворът, които подава искровият пламък. Най-благоприятните размери са 30x30 mm.

Етапи на тестване на плоско метално пробно тяло:

1. Поради окисния слой (окалина), образуван по време на производството на ГВР е невъзможно директното тестване на метала. Той ще покаже неверен резултат, което ще обезсмисли тестването на метала. Съществуват два метода на почистване на пробното тяло:

   - Първият е да се вземе пробно тяло след байцване (почистване с киселина) на целият рулон и после да се отреже на гилотинната ножица пробно тяло;

   - Вторият е да се отреже пробно тяло директно от ГВР и да се зачисти ръчно или чрез потапяне в киселина и после във вода или да се шлайфа с шкурка до премахване на окалината.

2. След идеалното почистване на повърхността на металното пробно тяло е необходимо почистването му със спирт за отстраняване на шлайфаните частици и други замърсявания.

3. Много е важно плоската плочка на пробното тяло да няма кривини, защото ако не прилепне добре върху работната повърхност, няма да има добър контакт и може да се получи неверен резултат. Също така при лошо прилепване на пробното тяло се получава просвет към отвора, което води до голям шум по време на прогаряне и опушване на пробното тяло.

4. След вече подготвено пробно тяло се пристъпва към стартиране на спектралният апарат, включване на компютъра, стартиране на програмата QMatrix, Quantron за анализ и развъртане на крана за аргона.

5. Желателно е преди калибриране или тестване да се направи продувка на системата на спектралния апарат с аргон, за да се прочисти от останали сажди. Аргона, които се използва за горене се свързва чрез маркуче към състемата, а от нея също излиза такова за отвеждане на изгорелите газове и сажди, потопено в бутилка с вода.

6. Ако програмата не е използвана повече от месец или при съмнение, че са неверни данните от последното измерване е необходимо да се направи калибриране на спектрите. За тази цел се използват еталоните, за нисковъглеродна- Re 12/132 и високовъглеродна- RN 19/38 стомана, за да се калибрира апарата за всички честоти. От падащото меню се избира стандартизация по метод Fe110NEW за калибриране на измервания на железни изделия(Фиг.3, 4).

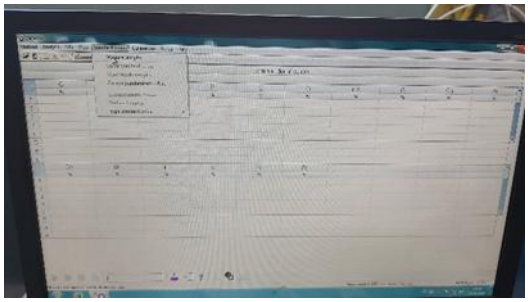

Фиг. 3. *Стандартизиране на програмата*

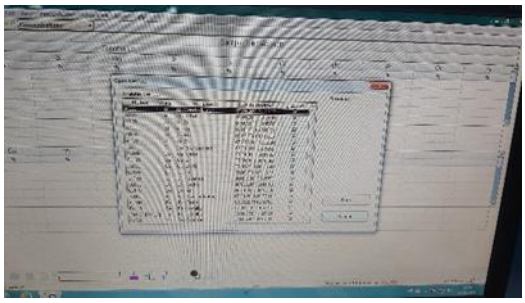

Фиг. 4. *Избор на метод Fe110NEW*

Измерваните елементи са: C; Si; Mn; P; S; Cr; Mo; Ni; Cu; Al; Co; Nb; Ti; V; W; Fe; в проценти, %. При започване на стандартизацията се прави проверка на изместването на спектрите, показано на Фиг. 5.

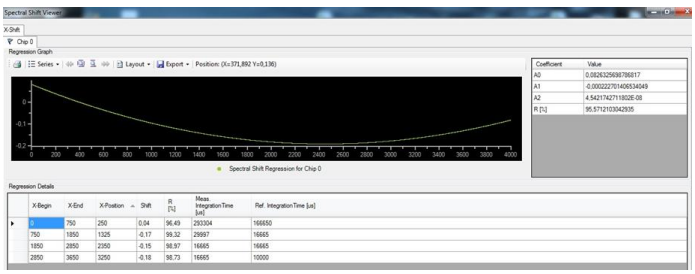

Фиг. 5. *Проверка за изместване на спектрите*

Правят се по 3 измервания на всеки от еталоните, след което програмата изчислява новите стойности на спектрите за всеки елемент. Прави се проверка със справочник. При близки резултати, стандартизацията се приема, а при голямо отклонение се прави отново до

получаване на удовлетворяващи стойности. Тестват се еталоните за определяне на количеството на всеки елемент в %, за да се провери дали отговарят на сертификата. При съответстващи резултати се пристъпва към измерване на пробните тела.

7. Измерването на железните пробни тела става, чрез стартиране на програмата QMatrix, Quantron и задаване на метод Fe110NEW (Фиг. 6). Въвежда се номера на всяка нова проба в ID полето. Поставя се пробата върху отвора на работната плочка и се поставя върху нея отворения свещник (Фиг.7), които се мести нагоре-надолу, налявонадясно и се позиционира според размера на пробното тяло.

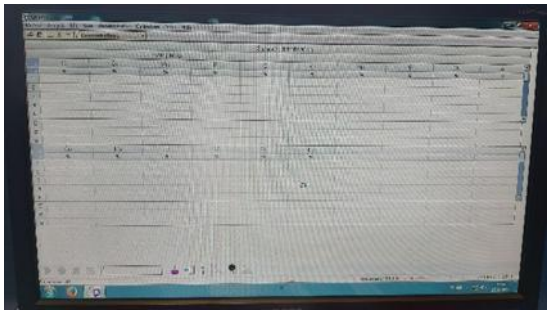

Фиг. 6. *Програма QMatrix, Quantron*

Фиг.7. *Здрав, отворен свещник*

Правят се от 3 до 5 измервания на всяко пробно тяло. По инструкция на доставчика, при резултат много по-различен от останалите се елиминира и не участва в осредняването на измерените стойности. Резултатите се изпращат в Exel таблица за по-лесна обработка на данните. Таблицата съдържа датата и часът на направеният анализ, методът, по който е определен химичният състав на пробното тяло и съдържанието в проценти на всеки елемент.

8. От направените измервания може да се направи анализ за режима на термообработка.

4. Заключение

След направен обстоен анализ на изследването чрез спектрални апарати се установи, че този метод дава информация от съществено значение за опознаване и осъвършенстване на процесите на работа. На база на натрупан опит в провеждането на спектрален анализ на метално пробно тяло е съставена методика, която се използва в металургията, при преработката на ГВР в тръбни изделия. Тя е необходима, за да могат да се правят бързи и точни количествени анализи на химичният състав на суровината, защото от там се определя целият режим на работа.

Благодарности:

Изследването в настоящата статия е осъществено с подкрепа по линия на средства за задочни докторанти – 2021 г.

5. Литература:

1. Киркова Е. Обща Химия. София, Унив. изд. „Св. Климент Охридски“, (2001). с. 436.
2. Добри Лазаров, „Неорганична химия“, (2019), УИ "Св. Климент Охридски", ISBN:9789540738192
3. Bruker, https://www.bruker.com/en/products-and-solutions/elemental-analyzers/optical-emission-spectrometers/q2-ion.html
4. Балевски А., Металознание. Изд. „Техника”, София, (1975) (5-то издание).
5. Будуров Ст., Спасов Т.. Увод в химията на твърдото тяло. Университетско издателство „Н. Рилски“, Благоевград, (1997), ISBN: 954-680-080-5.
6. Феликс Н., Арсов Я.. Планиране на експеримента в технологията на металите. Изд. „Машиностроение”, Москва, изд. „Техника”, София, (1981).
7. Zlateva, G., Martinova Зл., Microstructure of Metals and Alloys. An Atlas of Transmission Electron Microscopy Images. CRS Press, Taylor & Francis Group, (2008), ISBN: 978-1-4200-7556-4.
8. Арсов, Я.Б. Стоманени отливки. Изд. „Техника”, София, 1974.

Recovery of sulfur dioxide from flue gas for sulphuric acid production

Kamila Jóźwiak[1,*], Krzysztof Czajka[1]
Wroclaw University of Science and Technology, Poland[1]
kamila.jozwiak@pwr.edu.pl

Abstract: *The paper presents a review of the literature relative to the flue gas desulfurization methods for sulphuric acid (H_2SO_4) manufacturing. The covered topics include wet and dry methods. Particular attention has been paid to the desulfurization of the flue gas from the copper smelting industry that can lead to a generation of SO_x rich streams resulting in high profitability of H_2SO_4 production.*
Keywords*: SO2, H2SO4, DESULFURIZATION, COPPER, SMELTING INDUSTRY*

1. Introduction

Economic activity, especially production, affects the environment by introducing substances into the air, water, soil or ground. These emissions cannot always be avoided, but a special care has to be taken to minimize them in accordance with the law. This means that an appropriate permit must be obtained for the introduction of substances or energy into the environment, and sometimes appropriate methods of preventing or reducing emissions must be applied.

Desulfurization is mostly associated with the treatment of boiler flue gases and waste gases from crude oil processing, sulfuric acid production and smelting/ metal processing. It is aimed at converting SO_2 into a substance easy to remove both from the gas and from the treatment system. These operations result in the recovery of sulfur in the form of commercial products or the generation of sulfur waste. In the literature may be found different techniques of desulfurization, however, due to techno-economic problems and difficulties in scaling-up from laboratory to industry level, only a few of them have found wide appliances.

The aim of this paper is to review the methods of gas desulphurization, with particular emphasis on technologically mature methods enabling sulphuric acid production from boiler flue gases and waste gases from crude oil processing, smelting and metal processing or sulphuric acid production.

2. Overview of available wet methods

These methods are implemented using a scrubber located in the flue gas duct (upstream of the chimney). As a result of contact with water or a solution, the purified gases are cooled to a temperature of about 365 K, since the stack temperature is about 420 K. The most important issue in these methods is the concentration of SO_2, since sulphur recovery in the form of H_2SO_4 can be carried out when SO_2 + SO_3 > 0.3% v/v. Several important facts should be taken into consideration, namely:

- purified gases must be heated before being directed to the chimney,
- few methods are able to provide the required degree of desulphurization in a given range of concentrations,
- removing water from a product is expensive.

The choice of method is determined by the degree of desulfurization.

The lime method

The method is based on absorption and chemical reaction of SO_2 in a suspension of lime or limestone. The CaSO_3 and CaSO_4 in the form of sludge or wet solid in most cases is waste. According to [2] it is believed that once the lime methods have been properly adapted to the conditions in metallurgy and optimized, they may prove to be crucial for this industry. The conditions in the stack are favorable for the formation of SO_3 and sulfuric acid from flue gases. When the concentration of SO_3 drops below the dew point temperature, a reaction occurs with the vapor H_2O and forms H_2SO_4 in the form of droplets. These droplets are diluted to an equilibrium concentration. An important aspect in any project is the costs incurred, thus in this case the best solution is to mix the purified gases with a corresponding volume of hot, untreated flue gas stream taken from the boiler or precipitator. Also important is the amount of heat that must be applied to heat the purified gases to prevent condensation prior to emission from the stack and to ensure adequate lift and dispersion in the atmosphere. This property is due to the physicochemical characteristics of the flue gases and the design of the chimney and the conditions of dissipation.

Magnesium regeneration method

This is one of the desulfurization methods, in which hydrated (IV) and (VI) magnesium sulfates and unreacted MgO are obtained. The separated solid products are dried and then calcined at temperature 1080-1300 K. As a result of this operation, MgO is regenerated and SO_2 is recovered. The dry waste gas from calcination contains about 5-15% v/v of SO_2 which is used to produce H_2SO_4. Despite the many different details of this method, such as the use of activators, blocking the interior of the apparatus with a deposit of solid or regeneration of the absorbent, it has found many applications in metallurgical processes. Like many technological processes, it has certain limitations, e.g. high corrosion and erosion risks or the necessity of proper dedusting. Nowadays, this method is most popular in the Czech Republic and the USA [4].

The Cat-OX method

In metallurgy, there are many methods to desulfurize flue gases that have been developed by industry companies. The Cat-OX method, developed by Monsanto, involves oxidising SO_2 to SO_3 using a catalyst V_2O_5 catalyst at a temperature of 700-750 K, followed by cooling of the gases and absorption of H_2SO_4. The resulting H_2SO_4 is already an 80% product. Unfortunately, the Cat-OX method, has proved to be another method that poses great corrosion problems. At the very beginning of the operation it requires a thorough preliminary purification of the gas, generating huge economic costs.

Lurgi-Sulfacid method

The next company to implement a desulfurization method is Lurgi-Sulfacid, which uses a layer of activated carbon sprinkled with water. The end product is only 10-20% H_2SO_4. The method is used in the removal of SO_2 of waste gases from chemical and metallurgical processes when the concentration of SO_2 is ≥ 2% v/v [2].

Degussa absorption method

According to the method developed by Degussa, SO_2 is sprinkled with an oxidized water in a separate column. The process makes possible to reduce the concentration of SO_2 in the flue gas to about 20 mg/Nm^3. In this method it is obtained 70% H_2SO_4.

Solinox method

Solinox regenerative desulfurization is based on absorption of SO_2 in liquid ethylene glycol esters, followed by desorption of SO_2 by means of elevated temperature, pressure reduction or gas stream desorption. The aim of the method is to reduce sulphur dioxide emissions by means of a waste-free and highly efficient installation. The sulfur dioxide-treated inlet gases leave the absorption zone through a stack bottom isolating the liquid circuits and enter the sorbent residue backwash zone. Although the sorbent vapours have a very low vapour pressure at this point, due to the large amount of gases and the entrainment of the liquid droplets by the gases, sorbent losses cannot be neglected. The low temperature of the water for leaching the sorbent residue caused by the low gas inlet

temperature and the water evaporation is compensated in the heat exchanger. The treated inlet gases are discharged to the atmosphere via a chimney [1]. Solinox installation works i.a. KGHM Legnica Copper Smelter.

Microbiological reduction of SO_2

One of the most interesting methods is microbiological reduction of SO_2 developed by the Paques-Hoogovens company from the Netherlands. The whole process is carried out in three cycles, consisting of absorption of SO_2, bioreaction with SO_2 and separation of elementary sulphur. Absorption SO_2 is characterized by the production of H_2S, which is oxidized to sulphur in a biologically controlled environment. The whole operation takes place in a settling tank where the sulfur suspension is concentrated. This suspension is subjected to dehydration in a vacuum filter. In order to obtain high quality sulphur, it is subjected to thermal refining. The desulphurization degree of this method is up to 98% [3].

BIPOLAR electrolytic process

Stuffer Technology has implemented the BIPOLAR electrolytic process, which proceeds in two stages. In the first stage, a column filled with rings or saddles made of a material with good electrical conductivity, e.g. phosphosilicon alloy with 12% Si content, is used for absorption of SO_2 in an aqueous solution of sulphuric acid. In the second stage, by electrolysis of sulphuric acid (IV) at a potential of about 0.6 V, it is oxidized to acid (VI) with release of hydrogen. As a result, 40-48% sulfuric acid is obtained, depending on the conditions of the process.

3. Overview of available dry methods

As the name suggests, dry desulphurization methods proceed in dry state i.e. in gas-solid system/ waste products/ utility desulphurization products. They are characterized by adsorption on solid sorbents - metal oxides or activated carbon and absorption with chemical reaction with simultaneous drying of desulfurization products. Dry methods in comparison to wet methods allow to avoid problems connected with pH control, settling of solids in the apparatus, accumulation of liquid waste or heating of purified gases.

Sorption of SO_2 on solid sorbents

In the FW-BF (Foster Wheeler Bergbau, Forschung) method, SO_2 is adsorbed in a mobile layer of active coke, at 400 K, from a dusted flue gas. In this case, if the plant contains a so-called RESOX node, in which the reducer SO_2 anthracite or coke oven gas is the reducer, the desulphurisation product is a concentrated stream of SO_2 or elementary sulphur. As a result, the formed sulphuric acid diffuses from the pores to the liquid layer on the particle surface, from where it is washed out with demineralised water to obtain sulphuric acid (VI) of 10-20% concentration. This method has found recognition in metallurgical processes, because it enables the removal of SO_2 from waste gases. Sorbents in this method are oxides of Mn, Fe, Cu, Co, Zn and others. Due to the significant rate of the reaction with SO_2, the method provides satisfactory economic results. It should be remembered, however, that this method requires the use of adsorption units of large dimensions [2]. Recently there were developed methods that allow the use of activated carbons produced from unburned carbon for the purpose of FW-BF [4-5].

Another oxide that deserves attention is CuO, because due to the its catalytic action, SO_2 oxidises to SO_3. An important element during adsorption is the decrease in efficiency with time and the decrease in mechanical strength of the granules. At higher temperatures Cu i SO_2 is regenerated by means of H_2, CO or light hydrocarbons. This operation takes place at temperatures not exceeding 680 K due to minimization of hydrogen consumption and better copper activity. Desulphurisation efficiency based on sorption SO_2 on CuO is over 95%. Despite the high investment cost, this process has great potential for practical applications.

Desulphurisation by spray drying

Absorption with chemical reaction SO_2 in droplets of alkaline solution occurs simultaneously with spray drying. Unreacted reactants, or desulfurization products, are released as powder. The reactants in this process are solutions of soda or $Ca(OH)_2$. $Ca(OH)_2$ is the most applicable due to insolubility of desulphurization products in water. SO_2 contained in the gas, is absorbed on the surface of droplets, penetrates into the interior, undergoes oxidation and reacts with $Ca(OH)_2$ to form calcium sulfite and sulfate. As a result of water evaporation, the flue gas temperature drops to 10-20 K above the dew point temperature of 333-344 K. Physical changes in the droplets of the suspension have a great influence on the desulfurization rate, through oxidation SO_2 in the liquid phase of the droplets [6].

A similar phenomenon can be observed in smog formation and "acid rain" processes. Therefore, in order to achieve a high desulphurization rate with low sorbent consumption, the process should be carried out at a temperature close to the adiabatic saturation temperature of the waste gases. Better efficiency is also ensured by recirculation of part of the separated solids due to increased contact surface area of the reactant phases in the dryer and faster formation of solid phase nuclei, increasing the utilization rate of $Ca(OH)_2$. This is a very expensive process and any by-product is not economically viable.

4. Summary

A comparative analysis between the methods requires taking into account many aspects, such as the demand for reagents and energy, operation and maintenance, waste collection and neutralization, as well as the costs incurred, which to a large extent determine the realization of the process. Process efficiency is an indicator thanks to which it is possible to visualize the effectiveness of the actions taken. When this value is compared in dry methods, in which a higher stoichiometric sorbent ratio is required to achieve the same levels SO_2 and at the same time are considerably more expensive, it can be concluded that the process is not very cost-effective [7].

However, due to the many times higher cost of the reagent $Ca(OH)_2$ than $CaCO_3$, dry methods are preferred for desulfurization of flue gases from combustion of low-sulfur coals. In addition, due to the elimination of large volumes of slurry streams and the heating of treated gases, the energy requirement is significantly lower. From the practical point of view, in the industry, the key is the facilitated operation with reduced maintenance, due to the elimination of many nodes and apparatuses or blocking of the interior of the apparatus with deposits or reduced corrosion, this method is mainly preferred in the processes of gas purification from smaller emission sources. However, the role of environmental protection development is crucial in today's investments, metallurgical and chemical processes and, above all, in industry. Constantly changing environmental laws and EU standards regulate the level of emissions without regard to both investment and economic costs. Therefore, each branch of the economy uses the tools that are the most necessary for it and at the same time duly effective.

References

1. G. Wielgosiński, R. Zarzycki, *Technologie i procesy ochrony powietrza* (PWN 2018)

2. W.M. Lewandowski, R. Aranowski, *Technologie ochrony środowiska w przemyśle i energetyce* (PWN 2016)

3. J. Warych, *Oczyszczanie gazów procesy i aparatura* (Wydawnictwo Naukowo – Techniczne 1998)

4. A.M. Kisiela-Czajka, S.A. Hull, A. Albiniak, Investigation of the activity of unburned carbon as a catalyst in the decomposition of NO and NH_3, Fuel (Guildford), 2022, vol. 309, art. 122170, s. 1-14.

5. A.M. Kisiela-Czajka, K. Czajka, W. Moroń, W. Rybak, Cz. Andryjowicz, Unburned carbon from lignite fly ash as an adsorbent for SO2 removal, Energy, 2016, vol. 116, pt. 3, s. 1454-1463.

6. J. Konieczyński, *Ochrona powietrza przed szkodliwymi gazami – metody, aparatura i instalacje* (Wydawnictwo Politechniki Śląskiej 2004)

7. R. Janka, *Zanieczyszczenia pyłowe i gazowe – Podstawowe obliczenia i sterowania poziomem emisji* (PWN 2014)

Optimization of electron beam lithography processing of resist AR-N 7520

Elena Koleva[1,2*], Ivan Kostic[3], Lilyana Koleva[1], Katia Vutova[2], Irina Markova[1], Anna Bencurova[3], Anna Konecnikova[3], Robert Andok[3]

University of Chemical Technology and Metallurgy, Bulgaria[1]
Institute of Electronics, Bulgarian Academy of Sciences, Bulgaria[2]
Institute of Informatics, Slovak Academy of Sciences, Slovak Republic[3]

[*]eligeorg@uctm.edu

Abstract: *This work presents experimental and theoretical investigation of exposed and developed negative electron resist AR-N 7520 profiles using electron beam lithography system ZBA23 (Raith) at variation of the exposure doses and pre-defined exposure pattern. Several overall geometry quality criteria for the shape of the developed resist profile cross-sections are defined. Empirical models are estimated for the dependence of overall geometry characteristics of the obtained resist profiles on the exposure dose. These overall quality characteristics are used for defining of technological requirements for the formed profiles and for obtaining optimal regimes by multicriterial optimization.*
Keywords*: ELECTRON BEAM LITHOGRAPHY, EMPIRICAL MODELLING,MULTICRITERIAL OPTIMIZATION.*

1. Introduction

Electron beam lithography (EBL) is a key technology for the fabrication of advanced integral circuits and devices of electronics, photonics and nanoengineering. The experimental investigations and the computer simulation of the processes of electron exposure and development of the resist profile in EBL are very important for the optimization of this expensive technology process. The reasons connected with the expensive equipment used in microelectronic fabrication, the use of sophisticated materials and the long chain of sequential steps required to obtain the desired micro and nano-structures.

Nowadays the goal of EBL production process is reaching the critical dimensions of 50-150 nm [1] with the necessary quality and reproducibility of the obtained microstructures. In this region, the desired dimension of the fabricated microstructures within reasonable tolerances cannot be obtained without a deep knowledge of the process and a precise choice of processing parameters. In the sub-500 nm region, it is very important that the desired relief profile of the developed resist to be produced by a proper choice of optimal process parameter settings [2, 3].

In this work experimental investigation of exposed and developed negative electron resist AR-N 7520 profiles using EBL system ZBA23 (Raith) is performed at variation of the exposure doses and pre-defined exposure pattern. Other EBL process parameters, that influence the shape of the obtained resist profiles and are kept constant during the experiments are: electron energy, development time, initial resist thickness, etc. Several overall geometry quality criteria for the shape of the developed resist profile cross-sections are defined. Empirical models are estimated for the dependence of overall geometry characteristics of the obtained resist profiles on the exposure dose. These overall quality characteristics are used for defining of technological requirements for the produces profiles and for obtaining optimal regimes by multicriterial optimization.

2. Experimental results

The EBL process is conducted in two basic steps: exposure of the electron resist (positive, negative, chemically amplified, multilayer) by an electron beam using pre-defined pattern of exposed zones and development of the resist with an appropriate developer (depending on the resist) for production of desired microstructures.

Experiments were performed using EBL system ZBA23 (Raith) with the variable-shaped electron beam cross-section at 40 keV electron energy [3-5]. Thin film of the negative electron beam resist AR-N 7520 (Allresist) with the thickness of 480 nm was prepared by spin coating on GaAs substrate. The development was conducted with AR 300-47 developer for 60 seconds. The resist thickness measurements were carried out using the standard profilometer technique (Alphastep equipment). A high-resolution scanning electron microscope Quanta FEG 250 (FEI) was used for dimension measurements of resist profiles at the magnification of ×200 000 [5].

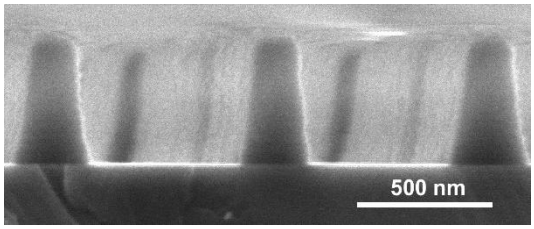

Fig. 1 *Profile of line grating with L/S 100/ 700 nm at exposure dose 340 μC/cm².*

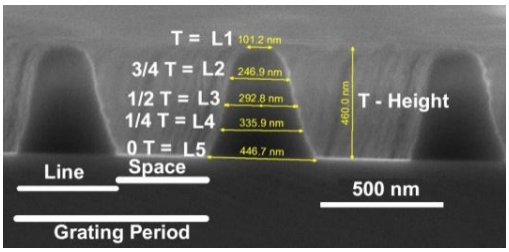

Fig. 2 *Measurement dimension details of AR-N 7520 resist profiles.*

Several single lines with a width of 100 nm and a distance between them of 700 nm are exposed with different exposure doses. After development gratings are obtained and Fig. 1 presents the obtained structure in the case of 340 μC/cm² exposure dose. The overall height of the profiles in AR-N 7520 resist after development is marked by T (Fig. 2) and its values are different depending on the exposure doses. The widths of the lines L_i after development were measured at different resist depths: $L_1 = T$, $L_2 = ¾\ T$, $L_3 = ½\ T$, $L_4 = ¼\ T$ and $L_5 = 0T$ (at the substrate surface) (Fig. 2) and for different exposure doses Q.

In order to investigate the influence of the exposure dose on the geometry of the developed after exposure profiles in the resist, experiments applying 13 exposure doses in the region from 250 μC/cm² to 470 μC/cm² are performed. The realized experimental points are visualized in Fig. 3. The values of the overall height T for different exposure doses (in red) and the resist thickness levels L_1 to L_5 for a given exposure dose, corresponding to one resist profile and five measurement of the obtained line width (in blue for exposure dose of 320 μC/cm²) are presented (Fig. 3). The experiments for 250 μC/cm² and 320 μC/cm² are repeated three times. The overall number of produced structures is 17, and the performed measurements of the line widths at different resist thicknesses and exposure doses are 84.

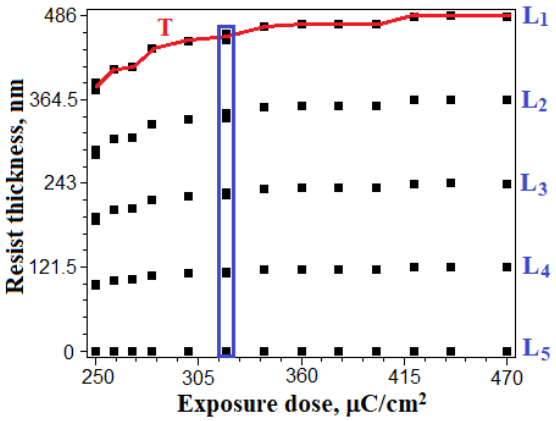

Fig. 3 *Experimental design.*

Several overall geometry quality parameters are defined: T – overall height of the developed resist profile, m - average line width at exposure with a certain dose (determined as the arithmetic mean of the individual line widths at different resist depths L_i – Fig. 2), σ – the standard deviation of the line widths obtained at exposure with a given exposure dose and δ - the difference between the line widths L_5-L_2 at resist depth $0T$ (at the resist-substrate interface) and ¾ T. The results concerning these parameters are presented in Table 1.

Table 1. *Overall geometry quality parameters, depending on the exposure doses.*

№	Q, μC/cm²	T, nm	m, nm	σ, nm	δ, nm
1	250	386	110.7	53.58	83
2	260	410	135.6	66.60	86
3	270	414	146.6	66.91	77
4	280	440	154.0	67.02	93
5	300	450	180.0	66.40	93
6	320	455	204.4	72.36	82
7	340	472	216.8	75.49	93
8	360	475	219.0	75.76	94
9	380	476	228.4	83.60	122
10	400	476	257.4	122.27	233
11	420	486	290.4	152.92	316
12	440	487	359.6	259.91	564
13	470	486	377.2	274.91	603

Three repeated observations are obtained at two of the exposure doses: 250 μC/cm² and 320 μC/cm². The mean values m_i and the standard deviations σ_i of the measured line widths for a given exposure dose give an idea about the repeatability of the results. The mean line width values and the standard deviations are estimated at different resist depths: $L_1 = T$, $L_2 = ¾\ T$, $L_3 = ½\ T$, $L_4 = ¼\ T$ and $L_5 = 0T$ (at the substrate surface) and are presented in Table 2.

Table 2. *The mean line width values and the standard deviations for exposure doses of 250 μC/cm² and 320 μC/cm².*

Q, μC/cm²	Param.	L_1	L_2	L_3	L_4	L_5
250	m_{250}	31.67	85.67	124.33	143.33	168.67
	σ_{250}	2.89	6.66	7.37	11.02	17.62
320	m_{320}	86.33	194.67	224.33	239.67	277
	σ_{320}	5.13	5.51	8.02	6.11	6

3. Regression models

Regression models are estimated for the defined overall geometry quality parameters as a function of the exposure dose coded in the region from (-1) to 1 units (x). The relation between coded x and natural units Q [μC/cm²] in this case can be expressed by the equation:

(1) $$x = (Q - 360)/110.$$

The regression models, together with the determination coefficients values are presented in Table 3.

Table 3. *Regression models.*

	Regression models	R^2, %	R^2_{adj},%
T	$Y_T = 471.13 + 22.55x + 27.19x^3 - 35.12x^4$	98.45	97.93
m	$Y_m = 218.17 + 93.56x + 100.72x^2 + 45.24x^3 - 73.64x^4$	98.36	97.54
σ	$Y_\sigma = 71.08 + 108.58x + 210.98x^2 - 116.48x^4$	95.75	94.34
δ	$Y_\delta = 88.21 + 269.63x + 553.41x^2 - 300.67x^4$	96.87	95.83

The goodness of fit tests and the values of the determination coefficients show good prediction characteristics of the estimated models. They can be used for the choice of the exposure dose settings under given technological requirements.

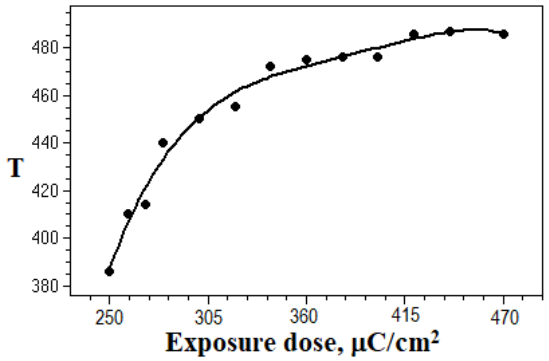

Fig. 4 *Overall height of the developed resist profile T vs. the exposure dose Q.*

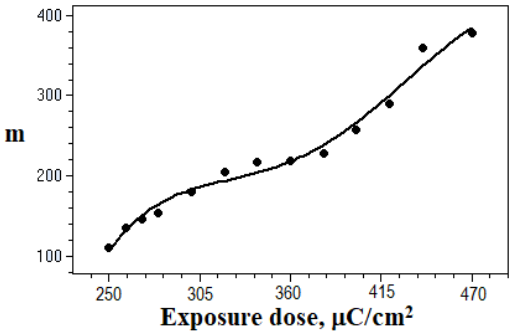

Fig. 5 *Mean line width m vs. the exposure dose Q.*

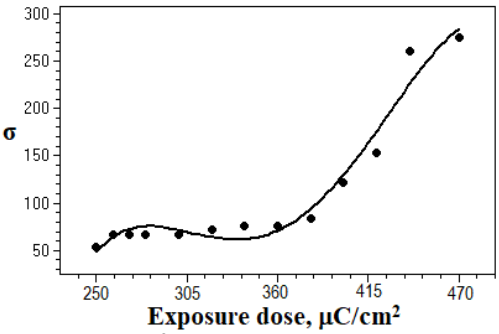

Fig. 6 *Standard deviation of the line widths σ vs. the exposure dose Q.*

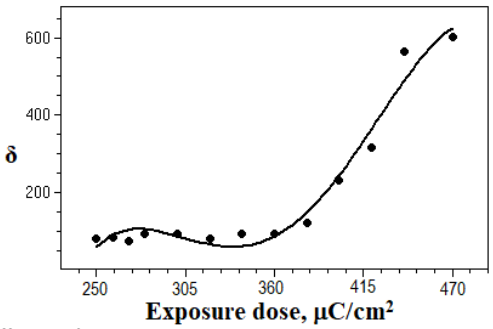

Fig. 7 *Difference δ between the line widths L_5-L_2 vs. the exposure dose Q.*

In Fig. 4 – Fig. 7 are presented plots of the experimental results (signed with dots) and the estimated by the regression models

(Table 3) for the resist profile geometry characteristics: the overall height of the developed resist profile (Fig. 4), the average line width (Fig. 5), the standard deviation of the line widths (Fig. 6), and the difference between the line widths L_5-L_2 (Fig. 7).

Based on the obtained results the following conclusions can be made:

- All the investigated overall geometry quality parameters depend on the exposure dose;
- The overall height T of the developed resist profile for the lower exposure doses (320 μC/cm^2) differs considerably from the initial resist thickness;
- The estimated regression model for the mean width of the resist profile m can be used for choosing the dose of exposure settings, depending on the technological requirements for the width of the resist profiles;
- The standard deviation of the line widths, obtained at exposure with a given dose, is connected with the variation between the line widths L_i at different resist depths and can be considered as considerable for exposure doses above 380 μC/cm^2.
- The difference between the line widths L_5-L_2 at resist depths 0T (at the substrate) and ¾ T for exposure doses below 380 μC/cm^2 can be considered as approximately constant.

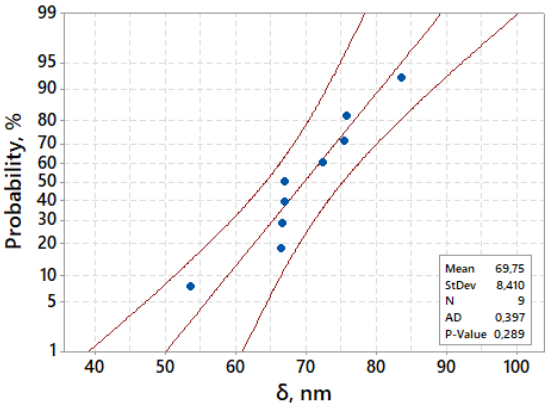

Fig. 8 *Normal probability plot for the difference δ between the line widths L_5-L_2.*

In Fig. 8 the normal probability plot for the difference δ between the line widths L_5-L_2 for exposure doses in the interval 250-380 μC/cm^2 is presented. The hypothesis test is performed by Anderson-Darling criterion and shows that the distribution is normal, since the estimated probability p = 0.289 for accepting the hypothesis is larger than the critical value p = 0.05.

This result shows that the overall criterion difference δ between the line widths L_5-L_2 is not influenced significantly by the exposure dose Q and can be estimated by its mean value $\bar{\delta}$ = 69.75 nm for the exposure dose interval 250-380 μC/cm^2. For these exposure doses the sidewalls of the developed resist profiles are most near to vertical for the resist depths between 0T (at the resist / substrate interface) and ¾ T.

4. Multicriterial optimization

The estimated in section 3 regression models give prediction for all the investigated overall geometry quality parameters when the exposure dose is set to a certain value. The multicriterial optimization task in this case is connected with the fact that under certain tolerance limits for the mean value of the linewidths (m), corresponding to a tolerance interval of the exposure doses Q, the simultaneous fulfilling of the opposite requirements for the other geometry parameters (T, σ, δ) must be done.

Since the desired optimal directions for the overall geometry parameters are different, compromise solutions should be found. By implementation of the statistical software QstatLab [6] and genetic algorithm, Pareto-optimization is realized under the following requirements:

> Mean line width m: $m \rightarrow maximum$, $130 \leq m \leq 150$ nm;
> Overall height of the developed resist profile T: $T \rightarrow maximum$;
> Standard deviation of line widths σ: $\sigma \rightarrow minimum$;
> Difference δ between the line widths L_5-L_2: $\delta \rightarrow minimum$.

Table 4. *Pareto-optimal solutions.*

№	Q, μC/cm^2	T, nm	m, nm	σ, nm	δ, nm
1	260.67	407.40	133.53	67.62	96.08
2	262.97	411.32	138.36	68.95	98.94
3	259.82	405.91	131.67	67.06	94.83
4	268.20	419.48	148.22	70.91	102.79
5	264.62	414.00	141.64	69.72	100.54
6	265.97	416.13	144.21	70.24	101.58
7	267.23	418.04	146.50	70.65	102.33
8	263.90	412.86	140.24	69.40	99.90

Part of the obtained compromise Pareto-optimal solutions are presented in Table 4. These solutions simultaneously fulfil the set of technological requirements. All the obtained optimal exposure doses presented in table 4 can be chosen, thus making compromise with the set requirements to different extend for each single case. The property of the Pareto-optimal solutions consists in the following: if each two solutions are compared, at least one of the quality parameters in one of the solutions will have worse value than that in the other solution.

5. Conclusions

This work presents experimental and theoretical investigation of exposed and developed AR-N 7520 negative electron resist profiles using EBL system ZBA23 (Raith) at variation of the exposure doses and pre-defined exposure pattern. Several overall geometry quality criteria for the shape of the developed resist profile cross-sections are defined. Empirical models are estimated for the dependence of overall geometry characteristics concerning the obtained resist profiles on the exposure dose. These overall quality characteristics are used for defining technological requirements for the formed profiles and for obtaining optimal regimes by multicriterial optimization.

The region of the exposure doses, for which the sidewalls of the developed resist profiles are most near to vertical for the resist depths between 0T (at the resist/substrate interface) and ¾ T is defined as 250-380 μC/cm^2.

Acknowledgements

The research was conducted within the framework of the project KP-06-N27/18, funded by the National Fund "Scientific Investigations", with the support from the Bulgarian Academy of Sciences and the Slovak Academy of Sciences (Bilateral grant agreement between BAS and SAS) and from the mobility project SAS-BAS 2021-2022 of the Slovak Academy of Sciences, and from the Ministry of Education of the Slovak Republic and the Slovak Academy of Sciences under the Contract No. VEGA 2/0119/18.

References

1. K. Vutova, G. Mladenov, Microelectronic Engineering, **57-58**, 349-353 (2001)
2. E. Koleva, G. Mladenov, Vacuum, **77**, 4, 361-370 (2005)
3. E. Koleva, K. Vutova, I. Kostic, J. of Phys. Conf. Ser., **1089** (1), 012015 (2018)
4. R. Andok et al., Proc. 9th Int. Conf. ASDAM 2012 (*Smolenice, SR*) (*Piscataway: IEEE*) 287-290 (2012)
5. I. Kostic, K. Vutova, E. Koleva, A. Bencurova, A. Konecnikova, R. Andok, J. of Phys. Conf. Ser. 2021. Proc. Int conf. VEIT'21 (accepted)
6. QstatLab home page: http://www.qstatlab.co.uk/eng/index.html

Electron Beam Melting and Refining of Copper

Asya Asenova-Robinzonova[1], Lilyana Koleva[1,*], Elena Koleva[1,2,**], Vania Vassileva[2], Katia Vutova[2]
University of Chemical Technology and Metallurgy, Bulgaria[1]
Institute of Electronics, Bulgarian Academy of Sciences, Bulgaria[2]
*sura@uctm.edu, **eligeorg@uctm.edu

Abstract: *Experimental results for the quality of electron beam melting and refining of pyro-refined copper samples are analysed by an empirical model estimation approach. Investigation of the influence of the process parameters – melting power and time of refining on the removal efficiency of specific impurities, overall removal efficiency and material losses is performed.*
Keywords*: ELECTRON BEAM REFINING, COPPER, REMOVAL EFFICIENCY, MATERIAL LOSSES, ELECTRON BEAM MELTING*

1. Introduction

Copper (Cu) is one of the most important metals used in modern life and up to 50% of Cu production is used for making cables, heat exchangers, vacuum equipment, etc., and about 40% is used for production of different alloys with: Zn, Sn, Al, Ni and other valuable metals, which are needed for a number of industries.

The electron beam melting and refining (EBMR) of metals and alloys in vacuum is done using electron beam as a heating source. The aim of the metallurgical refining processes is the removal of metallic impurities and reduction of non-metallic components from the raw material. The increasing demand for purity of the produced materials has led to the use of water-cooled copper crucible in furnaces during EBMR, where the initial material is melted, refined and re-solidified without pollution at using a ceramic pot, and thus EBMR method is superior to the refining methods of the conventional metallurgy [1, 2].

In this paper, investigation of the influence of the process parameters – melting power and refining time on the refined quality characteristics – the removal efficiency of specific impurities, overall removal efficiency and the material losses, is performed based on empirical model estimation.

2. Response surface methodology

Response surface methodology is a group of mathematical and statistical procedures used in fitting an empirical model to the experimental data obtained in relation to an experimental design [3]. Regression models or the polynomial models of some order, giving an adequate functional relationship between a response of interest y (performance characteristic) and a number of associated control (or input) variables (process parameters) $x_1, x_2, \ldots x_m$, are estimated:

$$\hat{y}(\vec{x}) = \sum_{i=1}^{k} \hat{\theta}_i f_i(\vec{x}), \quad (1)$$

where $\hat{\theta}_i$ are the estimates of the coefficients in the regression model.

The natural values of the factors (z_i) in the regression models are coded in the region [-1 ÷ 1] and the relation between the coded (x_i) and the natural values (z_i) is given by:

$$x_i = (2z_i - z_{i,max} - z_{i,min})/(z_{i,max} - z_{i,min}), \quad (2)$$

where $z_{i,min}$ and $z_{i,max}$ are the corresponding values of the minimum and the maximum of the process parameters during the experiment.

3. Experimental conditions

Electron beam melting and refining (EBMR) of Cu was performed using 60 kW equipment with one electron gun and a water-cooled copper crucible with diameter of 60 mm. The vacuum pressure in the melting chamber was in the range 5-8×10^{-3} Pa.

Two EBMR process parameters are varied in order to investigate the EBMR process of copper - z_1 is the electron beam power and z_2 – the refining time. The values of the electron beam powers were: 7.5 kW, 10 kW and 15 kW, while the refining times were set to different values in the range between 3 and 30 minutes [4, 5]. Fifteen experiments were performed for different combinations of these process parameters. The measured quality characteristics are the following: the removal efficiency of Sn (y_1, %), removal efficiency of Ag (y_2, %), removal efficiency of Zn (y_3, %), overall removal efficiency (y_4, %) and the material losses (y_5, g).

4. Estimation of regression models

The dependencies of the quality characteristics of the refined Cu: y_1 – the removal efficiency of Sn [%], y_2 – the removal efficiency of Ag [%], y_3 – the removal efficiency of Zn [%], y_4 – the overall removal efficiency [%] and y_5 – the material losses [g] on the variation of the process parameters: z_1 – the melting power [kW] and z_2 – the refining time [min] are estimated.

They are presented for coded in the region [-1 ÷ 1] values of the process parameters in Table 1, together with the square of the multiple correlation coefficient R^2 and the square of the adjusted multiple correlation coefficient R^2_{adj}. The values of both coefficients are high (maximum 100 %) and the estimated models can be considered as good enough for prediction and investigation.

Table 1: *Regression models.*

	Regression models	R^2 *[%]*	R^2_{adj} *[%]*
$\hat{y}_1(\vec{x})$	$99.388388 + 0.96370857x_1 + 0.08831581x_2 - 0.3525x_1^2 - 0.09437149x_1x_2$	99.89	99.84
$\hat{y}_2(\vec{x})$	$97.442395 + 0.05581727x_1 - 0.03479241x_2 - 0.15916955x_1x_2$	95.01	93.64
$\hat{y}_3(\vec{x})$	$94.047439 - 7.8928562x_2 - 7.120348x_1x_2 - 6.641097x_1x_2^2$	73.97	66.87
$\hat{y}_4(\vec{x})$	$98.759141 - 4.3757779x_2^2 - 3.1445406x_1x_2 + 4.3840616x_1^2x_2 + 4.2965256x_1x_2^2$	80.73	73.02
$\hat{y}_5(\vec{x})$	$9.638259 + 8.4167181x_1 + 7.4642417x_2 + 6.5539856x_1x_2$	99.99	99.99

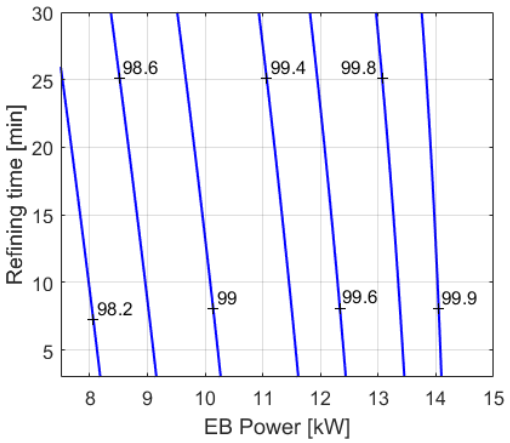

Fig. 1 *Contour plot of the removal efficiency of Sn – y_1, depending on the variation of the melting power (z_1) and the refining time (z_2).*

The obtained by QstatLab [6] regression models for the investigated quality characteristics are used for the investigation of the process of electron beam refining of Cu.

In Fig. 1 – Fig. 3 contour plots of the removal efficiency of Sn – y_1, removal efficiency of Ag – y_2 and removal efficiency of Zn – y_3 depending on the variation of melting power (z_1) and the refining time (z_2) are presented.

From Fig. 1 it can be seen that the removal efficiency of Sn is 99.9%, if the EB power is higher than 14 kW regardless of the chosen refining time in the investigated range.

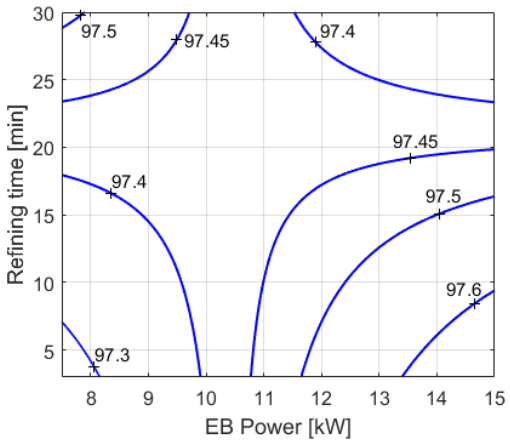

Fig. 2 *Contour plot of the removal efficiency of Ag – y_2, depending on the variation of the melting power (z_1) and the refining time (z_2).*

Fig. 2 shows the contour plot of the removal efficiency of Ag. It can be seen that the removal efficiency is 97.4% or more, but the maximum value (97.6%) is obtained in the range of working regimes where the refining time is less than 6 [min] and the EB power is higher than 14 kW.

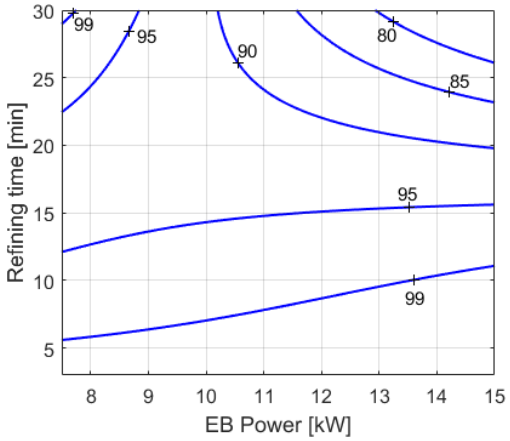

Fig. 3 *Contour plot of the removal efficiency of Zn – y_3, depending on the variation of the melting power (z_1) and the refining time (z_2).*

From Fig. 3 it can be seen that the removal efficiency of Zn can be 99%, if the refining time is equal to 5 min regardless of the chosen EB power or for EB powers higher than 13 kW and refining time less than 8 min.

The contour plot shown in Fig. 4 represents the overall removal efficiency (y_4) depending on the variation of melting power (z_1) and the refining time (z_2). It can be seen that the highest overall removal efficiency can be obtained, if the refining time is in the region from 17 min to 23 min and the EB power is set on its minimal value (less than 8 kW) or the EB power is higher than 14.7 kW and the refining time is more than 20 min.

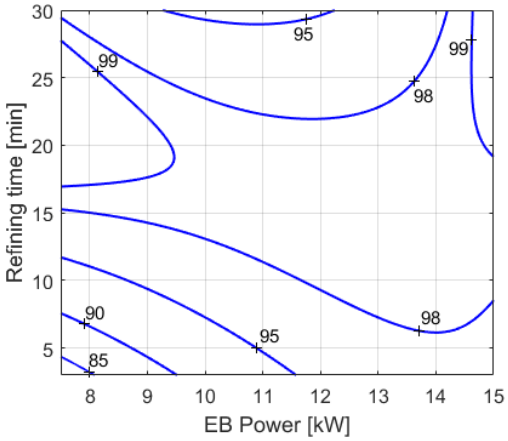

Fig. 4 *Contour plot of the overall removal efficiency – y_4, depending on the variation of the melting power (z_1) and the refining time (z_2).*

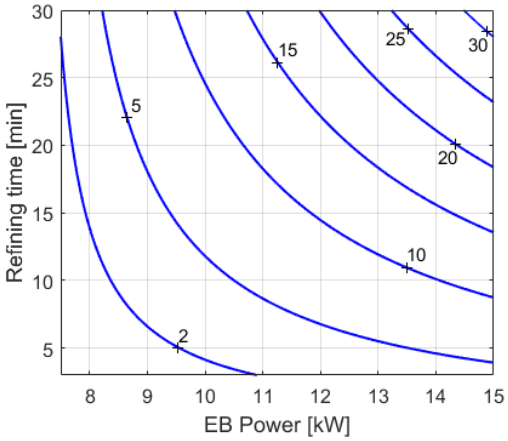

Fig. 5 *Contour plot of the material losses – y_5, depending on the variation of the melting power (z_1) and the refining time (z_2).*

Fig. 5 represents the investigation of the material losses during the process electron beam melting and refining of pyro-refined copper. From the contour plot it can be seen that the losses under 2 g can be obtained, if the EB power is less than 8.5 [kW] and the refining time is less than 7 min.

5. Correlation analysis

Another way to analyze the removal efficiencies of different inclusions is to analyze the coincidence of the refining process parameters in direction of simultaneously removing the inclusions or if a certain set of process parameters favors the refining of one of the inclusions at account of another inclusion. Correlation analysis can answer the question for presence of such correlation between different pairs of inclusions.

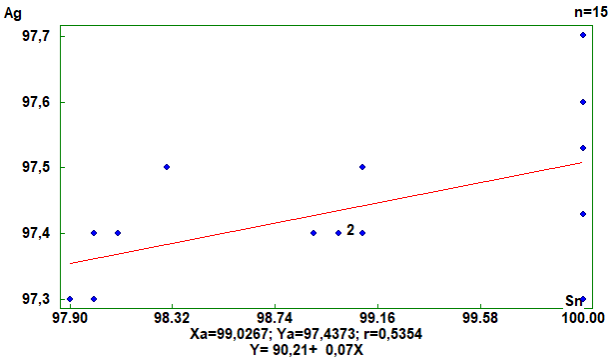

Fig. 6 *Scatter plot of the removal efficiency of Sn – y_1 and Ag – y_2.*

In Fig. 6 – Fig. 8 the scatter plots for the different combinations of inclusion removal efficiencies obtained by QstatLab [6] are presented.

From Fig. 6 it can be seen that there is moderate positive linear relationship between the removal efficiencies of Sn and Ag. The correlation coefficient is r_1 = 0.54 and performed test for significance defines it as a significant correlation. This means, that the choice of EBMR process parameters that favor the refining of Sn will favor the refining of Ag as well.

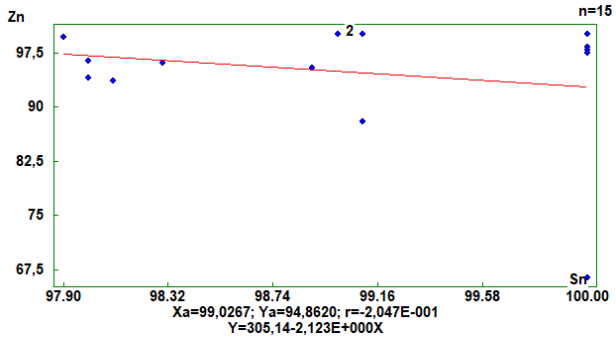

Fig. 7 *Scatter plot of the removal efficiency of Sn – y_1 and Zn – y_3.*

Fig. 7 shows that there is no significant correlation between the removal efficiencies of Sn and Zn. The Pearson linear correlation coefficient is small and insignificant.

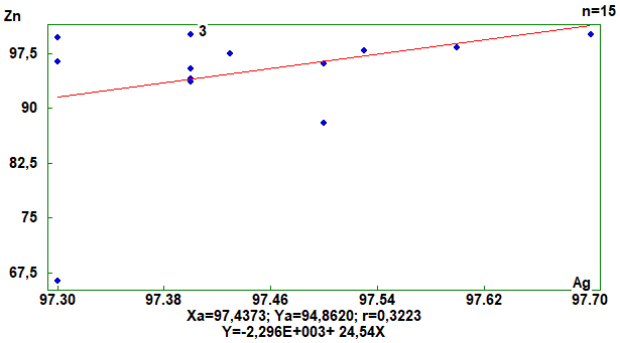

Fig. 8 *Scatter plot of the removal efficiency of Ag – y_2 and Zn – y_3.*

Fig. 8 shows week positive correlation between the removal efficiencies of Ag and Zn – the Pearson linear correlation coefficient is 0.32. After making hypothesis testing for its significance it is proven as insignificant correlation coefficient.

Consequently, the only significant correlation found is between the removal efficiencies of Sn and Ag. The choice of optimal EBMR refining process parameters should be made according the technological requirements for all quality characteristics and compromise solutions should be found that favors the refining of one or another of the inclusions to a certain extend.

5. Conclusions

Regression models for the removal efficiency of specific impurities, overall removal efficiency and the material losses depending on the variations of the electron beam melting and refining process parameters at Cu melting were estimated.

The obtained regression models can be used for future investigation and optimization of the process electron beam melting and refining of pyro-refined copper.

Acknowledgements

The authors want to thank for the financial support of the projects KP-06-N27/18 and DN17/9, funded by the National Fund "Scientific Investigations".

References

1. G. Mladenov, E. Koleva, K. Vutova, V. Vasileva, *Experimental and theoretical studies of electron beam melting and refining, Chapter in a special review book: Practical Aspects and Applications of Electron Beam Irradiation*, (eds.: M. Nemtanu, M. Brasoveanu, publ. Research Signpost/Transworld Research Network) 43-93 (2011).
2. K. Vutova, K. Koleva, G. Mladenov, IREME – spec. Iss. on Heat Transfer, **5**, 257-265 (2011)
3. M. A. Bezerra, R. E. Santelli, E. P. Oliveira, L. S. Villar, L. A. Escaleira, Talanta, **76**, 965-977 (2008)
4. V. Vassileva, K. Vutova, M. Markov. J. of Phys. Conf. Ser. 2021. Proc. Int conf. VEIT'21 (accepted)
5. I. N. Vuchkov, L. N. Boyadjieva, *Quality improvement with design of experiments* (Kluwer Academic Publishers: The Netherlands, 2001)
6. QstatLab home page: http://www.qstatlab.co.uk/eng/index.html

Multicriterial optimization strategies for electron beam grafting of corn starch

Lilyana Koleva[1*], Zlatina Petrova[1], Elena Koleva[1,2**], Mirela Braşoveanu[3], Monica R. Nemţanu[3], Georgi Kolev[1]
University of Chemical Technology and Metallurgy, Bulgaria[1]
Institute of Electronics, Bulgarian Academy of Sciences, Bulgaria[2]
National Institute for Lasers, Plasma and Radiation Physics, Electron Accelerators Laboratory, Romania[3]
sura@uctm.edu*, eligeorg@uctm.edu**

Abstract: *Grafting is the most effective way of modifying and regulating the properties of natural polysaccharides for the production of highly efficient graft copolymers, which have applications as flocculating agents for the treatment of different wastewaters. An experimental investigation connected with the modification of starch by grafting acrylamide with the application of electron beam irradiation is performed. In this paper the implementation of different multi-criteria optimization strategies, solving the problem with the choice between several compromise Pareto-optimal solutions are presented and compared for the process of electron beam grafting of corn starch. The compromise Pareto-optimal solutions are obtained by implementation of genetic algorithm and a set of requirements for the desired reference direction (minimum or maximum) and the constraints of the investigated quality characteristics and their variances under production conditions, which ensure the fulfilment of several goals – economic efficiency, assurance of low toxicity and high copolymer efficiency in flocculation process.*

Keywords*: GRAFT COPOLYMERIZATION, ELECTRON BEAM IRRADIATION, WATER-SOLUBLE COPOLYMERS, STARCH, ACRYLAMIDE, FLOCCULATION PROPERTIES, MULTI-CRITERIA OPTIMIZATION, DECISION MAKING*

1. Introduction

Electron beam (EB) grafting is a process that is able to modify the polymer substrates by implementing radiation-induced graft copolymerization in order to yield water-soluble copolymers for flocculation processes [1-3]. It is widely used to develop a wide variety of ion exchangers, polymer-ligand exchangers, chelating copolymers, hydrogels, affinity graft copolymers and polymer electrolytes, having various applications in water treatment, chemical industry, biotechnology, biomedicine, etc. [4].

Robust or not sensitive to noises and errors engineering approach can be implemented when analyzing experiments during which the variance is non-homogeneous over the factor (process parameters') space and when the noise factors cannot be identified nor an experiment to study them can be conducted [5, 6]. The observations in this case are called heteroscedastic (variance varies with the factor levels). This is the situation, when the analyzed data are obtained under production conditions. In order to estimate the variances of the quality characteristics there are several approaches. In the current investigation the models for the mean values and the variances of the quality characteristics of the product, are estimated by performing repeated observations. Multicriterial parameter optimization in terms of obtaining repeatability of the product parameters and quality improvement at the same time is performed by minimization of variations of the quality characteristics and fulfilling the technological requirements for these characteristics in production conditions simultaneously.

In this paper the implementation of different multi-criteria optimization strategies, solving the problem with the choice between several compromise Pareto-optimal solutions are presented and compared for the process of electron beam grafting of corn starch. The compromise Pareto-optimal solutions are obtained by implementation of genetic algorithm and a set of requirements for the desired reference goals (minimum or maximum) and the constraints of the investigated quality characteristics and their variances under production conditions, which ensure the fulfilment of several goals – economic efficiency, assurance of low toxicity and high copolymer efficiency in flocculation process.

2. Experimental conditions

Experiments for the modification of starch by grafting acrylamide using electron beam irradiation were performed in order to synthesize water-soluble copolymers having flocculation abilities. The synthesis of graft copolymers was performed by two steps: (1) preparation of solutions containing starch and monomer; (2) irradiation of solutions by electron beam.

Step 1: Starch aqueous solutions were prepared by dissolving corn starch in distilled water. Acrylamide was added to starch aqueous solution with further stirring, resulting in various acrylamide/starch (AMD/St weight ratios) homogenous aqueous solutions.

Step 2: Therefore, homogenous aqueous solutions prepared in previous step were exposed to electron beam irradiation. The irradiations were carried out at ambient temperature and pressure by using linear electron accelerators of mean energy of 6.23 MeV with different irradiation doses and dose rates.

The synthesized graft copolymers were characterized by residual monomer concentration, Mr, %; monomer conversion coefficient, Conv., % and intrinsic viscosity, η, dL/g. The variation regions of the process parameters were: for EB irradiation dose (z_1) - 0.65 ÷ 5.50 kGy, the dose rate (z_2) – 0.41 ÷ 1.50 kGy/min and the AMD/St weight ratio (z_3) – 2 ÷ 11.

The dependencies of the mean values and the variances of the product quality characteristics: residual monomer concentration - y_1 (%), monomer conversion coefficient - y_2 (%) and apparent viscosity - y_3 (mPa·s) on the variation of the process parameters: electron beam irradiation dose, electron beam irradiation dose rate and AMD/St weight ratio are estimated.

The estimated mean value $\tilde{\bar{y}}_{ui}$ and $\tilde{s}^2_{ui}$ variance can be considered as two responses at the design points, and ordinary least squares method can be used to fit the models of the mean value and the variance for the quality characteristic [6, 7]:

$$(1) \qquad \tilde{\bar{y}}(\vec{x}) = \sum_{i=1}^{k_y} \hat{\theta}_{yi} f_{yi}(\vec{x})$$

$$(2) \qquad ln\left(\tilde{s}^2(\vec{x})\right) = \sum_{i=1}^{k_\sigma} \hat{\theta}_{\sigma i} f_{\sigma i}(\vec{x}),$$

where $\hat{\theta}_{yi}$ and $\hat{\theta}_{\sigma i}$ are estimates of the regression coefficients, and f_{yi} and $f_{\sigma i}$ are known functions of the process parameters x_i.

The obtained models for the mean values $\tilde{\bar{y}}_j$ and the variance $\tilde{s}^2_j$ for each of the considered $j = 1, 2, ..., m$ quality characteristics are presented and discussed in [4].

3. Multicriterial optimization

In the case of EB induced grafting of corn starch multi-criteria optimization unifying requirements for economic efficiency, assurance of low toxicity and high copolymer efficiency in flocculation process, as well as the repeatability of the obtained results is performed.

The set of defined technological requirements is the following:

- residual monomer concentration: $\tilde{\bar{y}}_1 < 5\% \rightarrow$ assurance of low toxicity;
- monomer conversion coefficient: $\tilde{\bar{y}}_2 > 90\% \rightarrow$ economic efficiency;

- apparent viscosity: $\tilde{\bar{y}}_3$ > 3 mPa·s → copolymer efficiency in flocculation processes.

For the satisfaction of all pre-defined requirements simultaneously the optimization task is set as follows:

$\tilde{\bar{y}}_1$ → minimum, $\tilde{\bar{y}}_1$ < 5%;
$\tilde{\bar{y}}_2$ → maximum, $\tilde{\bar{y}}_2$ > 90%;
$\tilde{\bar{y}}_3$ → maximum, $\tilde{\bar{y}}_3$ > 3 mPa·s;
$\tilde{\sigma}_1^2$ → maximum;
$\tilde{\sigma}_2^2$ → maximum;
$\tilde{\sigma}_3^2$ → maximum.

The implemented for solving the multicriterial optimization task models for the mean values $\tilde{\bar{y}}_j$ and the variance $\tilde{s}_j^2$ for each of the considered *j = 1, 2, ..., m* quality characteristics are presented in [4].

Pareto-optimal compromise solutions are obtained (50 solutions) by applying genetic algorithm and the statistical software QstatLab [8]. Each solution makes some compromise toward some or all quality criteria to a certain extend at the same time. If we compare randomly chosen two Pareto-optimal solutions some of the quality characteristics will have better values, but at least one will be worse. In order to choose one solution from all we need additional analysis. This choice can be done by considering additional criteria (not included in the optimization task), by evaluation based on expert opinion or by definition of an overall function like loss function, desirability function, etc.

In the present work, methods based on reference point strategies optimization are implemented for solving this task. They are compered by estimation of the overall relative error for all best solutions that are obtained.

Optimistic strategy

The *optimistic strategy* is based on the method of the function of losses. This optimization approach is called "optimistic" because the best possible values q_j^{Opt} (*j* = 1, 2, 3, …, *m*) are assigned to the reference (uncompromised) values of the quality characteristic $q_i(x)$. The reference values depend on the required minimum or maximum value for each of the quality characteristics. They are determined from the obtained Pareto-optimal solutions or in this case the differences between the best values and the optimistic reference values are minimized. The generalized function of losses $F^{Opt}(x)$ that has to be minimized is [9]:

$$F^{Opt}(x) = \frac{1}{m}\sum_{j=1}^{m}\left(\frac{q_j^{Opt} - q_j(x)}{\Delta_j}\right)^2, \quad (4)$$

$$\Delta_j = q_{max,j} - q_{min,j}, \quad (5)$$

where $q_j(x)$ is the value for the *j-th* quality characteristic obtained at a given Pareto-optimal solution, $q_{max,j}$ and $q_{min,j}$ are the maximal and minimal values of each characteristic from all obtained 50 Pareto-optimal solutions and are presented in Table 1, together with calculated value for Δ_j. Each reference value q_j^{Opt} is obtained usually for different set of optimal process parameters z_i and cannot be obtained simultaneously.

Table 1: *Goals, reference values and the maximal and minimal characteristic values $q_i(x)$.*

Param.	$\tilde{\bar{y}}_1$ %	$\tilde{\sigma}_1^2$	$\tilde{\bar{y}}_2$ %	$\tilde{\sigma}_2^2$	$\tilde{\bar{y}}_3$ mPa·s	$\tilde{\sigma}_3^2$
Goal	min ↓	min ↓	max ↑	min ↓	max ↑	min ↓
q_j^{Opt}	0.003	0.008	98.689	0.163	5.564	0.163
q_j^{Pes}	4.996	0.136	90.874	3.602	3.359	0.617
$q_{j,max}$	4.996	0.136	98.689	3.602	5.534	0.617
$q_{j,min}$	0.003	0.008	90.874	0.163	3.359	0.163
Δ_j	4.996	0.128	7.815	3.439	2.175	0.454

The best ten optimal solutions obtained by implementation of the Optimistic method are presented in Table 2. They have smallest values of the function of losses $F^{Opt}(x)$ from the arranged in ascending order results from all obtained 50 Pareto-optimal solutions (their numbers are kept in the table). It can be seen that the best result, obtained for $F^{Opt}(x)$ = 0.128 is obtained for Pareto-optimal solution № 10, as well as the optimal values of the process parameters (z_i) at which it can be obtained in production conditions.

Table 2: *Optimal solution by Optimistic strategy.*

№	F^{Opt}	z_1	z_2	z_3	$\tilde{\bar{y}}_1$	$\tilde{\sigma}_1^2$	$\tilde{\bar{y}}_2$	$\tilde{\sigma}_1^2$	$\tilde{\bar{y}}_3$	$\tilde{\sigma}_1^2$
10	**0.128**	**4.7**	**0.6**	**3.9**	**1.4**	**0.06**	**98.2**	**0.95**	**4.09**	**0.19**
9	0.129	4.8	0.6	3.8	1.0	0.07	96.6	0.82	4.39	0.19
43	0.130	4.7	0.6	4.0	1.3	0.06	98.3	0.95	4.01	0.18
28	0.144	5.1	1.1	2.0	3.9	0.02	97.1	0.19	4.99	0.34
22	0.149	5.1	1.1	2.3	3.6	0.03	95.4	0.23	4.78	0.27
39	0.153	4.9	0.6	3.9	1.9	0.07	95.6	0.90	4.22	0.18
2	0.154	5.0	1.0	2.7	3.3	0.02	94.7	0.28	4.61	0.22
30	0.156	5.0	1.1	3.4	3.4	0.02	94.9	0.24	4.61	0.25
6	0.172	4.8	0.6	4.2	1.6	0.06	95.4	1.00	3.95	0.16
18	0.176	5.2	1.1	2.0	4.2	0.03	95.4	0.19	5.15	0.32

Pessimistic strategy

The pessimistic strategy is based on the function of usefulness method. In this strategy the worst possible (among the obtained Pareto-optimal solutions) or the "pessimistic" values q_j^{Pes} (*j = 1, 2, 3, …, m*) are assigned as reference values of the quality characteristic $q_i(x)$, again depending on the required minimum or maximum value for each quality characteristic from Pareto-optimal solutions. The function $F^{Pes}(x)$ that has to be maximized is [9]:

$$F^{Pes}(x) = \frac{1}{m}\sum_{j=1}^{m}\left(\frac{q_j(x) - q_j^{Pes}}{\Delta_j}\right)^2 \quad (6)$$

The best ten optimal solutions obtained by implementation of the Pessimistic strategy are presented in Table 3. They have largest values of the function of usefulness $F^{Pes}(x)$ from the arranged in descending order results from all obtained 50 Pareto-optimal solutions (their numbers are kept in the table).

Table 3: *Optimal solution by Pessimistic strategy.*

№	F^{Pes}	z_1	z_2	z_3	$\tilde{\bar{y}}_1$	$\tilde{\sigma}_1^2$	$\tilde{\bar{y}}_2$	$\tilde{\sigma}_1^2$	$\tilde{\bar{y}}_3$	$\tilde{\sigma}_1^2$
43	**0.571**	**4.7**	**0.6**	**4.0**	**1.3**	**0.06**	**98.3**	**0.95**	**4.01**	**0.18**
28	0.560	5.1	1.1	2.0	3.9	0.02	97.1	0.19	4.99	0.34
10	0.559	4.7	0.6	3.9	1.4	0.06	98.2	0.95	4.09	0.18
18	0.526	5.2	1.1	2.0	4.2	0.03	95.4	0.19	5.15	0.32
22	0.522	5.1	1.1	2.3	3.6	0.03	95.4	0.23	4.78	0.27
42	0.522	4.9	0.5	3.2	2.6	0.12	98.0	0.68	5.29	0.28
23	0.518	5.3	1.0	2.4	4.7	0.05	91.2	0.21	5.47	0.24
2	0.515	5.0	1.0	2.7	3.3	0.02	94.7	0.28	4.61	0.22
1	0.514	5.4	1.1	2.0	4.9	0.03	91.4	0.16	5.53	0.32
49	0. 514	5.2	1.0	2.4	4.5	0.04	92.5	0.21	5.36	0.25

Bracketing approach for multi-criteria optimization

The bracketing multi-criteria optimization strategy combines the optimistic and pessimistic approaches. Here the optimal compromise solution is searched by simultaneously minimizing the under-achievement to the best values (reference values) q_j^{Opt} and maximizing the over-achievement over the required (worst) values q_j^{Pes} [9].

The optimization function that has to be maximized in this case is:

$$F^{Br}(x) = \frac{1}{m}\sum_{j=1}^{m}\left(\frac{q_j(x) - q_j^{Pes}}{\Delta_j}\right)^2 - \frac{1}{m}\sum_{j=1}^{m}\left(\frac{q_j^{Opt} - q_j(x)}{\Delta_j}\right)^2 \quad (7)$$

The best ten optimal solutions obtained by implementation of the Bracketing strategy are presented in Table 4. They have largest values of the function of usefulness $F^{Br}(x)$ from the arranged in descending order results from all obtained 50 Pareto-optimal solutions (their numbers are kept in the table).

It can be seen, that the best result in this case coincides with the best result obtained when the Pessimistic strategy is applied (Pareto-optimal solution №43).

Table 4: *Optimal solution by Bracketing approach.*

№	F^{Br}	z_1	z_2	z_3	$\tilde{y}_1$	σ_1^2	$\tilde{y}_2$	σ_2^2	$\tilde{y}_3$	σ_3^2
43	**2.777**	**4.7**	**0.6**	**4.0**	**1.3**	**0.06**	**98.3**	**0.95**	**4.01**	**0.18**
10	2.750	4.7	0.6	3.9	1.4	0.06	98.2	0.95	4.09	0.18
42	2.647	4.9	0.5	3.2	2.6	0.12	98.0	0.68	5.29	0.28
9	2.361	4.8	0.6	3.8	2.0	0.07	96.6	0.82	4.39	0.19
28	2.359	5.1	1.1	2.0	3.9	0.02	97.1	0.19	4.99	0.34
37	2.291	5.0	0.7	3.2	3.1	0.10	95.9	0.54	5.31	0.25
22	2.099	5.1	1.1	2.3	3.6	0.03	95.4	0.23	4.78	0.27
26	2.069	5.1	0.6	3.2	3.2	0.11	95.4	0.57	5.42	0.26
2	2.049	5.0	1.0	2.7	3.3	0.02	94.7	0.28	4.61	0.22
14	2.026	4.7	0.5	4.6	0.6	0.08	98.0	1.74	3.73	0.19

In order to compare the implemented optimization strategies: *Optimistic and Pessimistic/Bracketing approaches*, the absolute errors are calculated for the best chosen compromise solutions by:

$$\delta_{aj} = \left| q_{j,opt}(x) - q_j{}^*(x) \right|$$

where $q_j{}^*(x)$ is the best value from all Pareto-optimal solutions for the *j-th* quality characteristic, coinciding with the reference point of the optimistic approach. The relative error in this case can be calculated by:

$$\delta_{rj} = \frac{\delta_{aj}}{\Delta_j} * 100\%$$

The calculated results are presented in Table 5.

Table 5: *Comparison of implemented optimization strategies.*

№	$\tilde{y}_1$	σ_1^2	$\tilde{y}_2$	σ_2^2	$\tilde{y}_3$	σ_3^2
q_j^*	0.003	0.008	98.689	0.163	5.564	0.163
Δ_j	4.996	0.128	7.815	3.439	2.175	0.454
$q_{j,opt}$, *Opt*	1.4	**0.06**	98.2	**0.95**	**4.09**	0.19
δ_{aj}	1.397	0.052	0.489	0.787	1.474	0.027
δ_{rj},%	27.96	40.63	6.26	22.88	67.77	5.95
$q_{j,opt}$, *Pes/Br*	**1.3**	**0.06**	**98.3**	**0.95**	4.01	**0.18**
δ_{aj}	1.297	0.052	0.389	0.787	1.554	0.017
δ_{rj},%	25.96	40.63	4.98	22.88	71.45	3.74

From Table 5 can be seen that the implemented strategies give very close results. The only quality parameter, which is a little better for the solution, given by the Optimistic approach, is the result for the apparent viscosity $\tilde{y}_3$, responsible for copolymer efficiency in flocculation processes. All the other criteria values are better or equal for the case of implementation of the pessimistic or bracketing strategies.

4. Conclusions

In this paper, three multicriteria optimization approaches were applies and compared, aiming to simultaneously fulfil the technological requirements for economic efficiency, assurance of low toxicity and high copolymer efficiency in flocculation process, as well as the repeatability of the obtained results.

The implementation of multi-criteria optimization strategies, by definition of one overall optimization criterion, solves the problem with the choice between several compromise Pareto-optimal solutions. Optimistic, pessimistic and bracketing multi-criteria optimization strategies are implemented and compared for the process of electron beam grafting of corn starch.

The comparison of obtained best working regimes of the applied multi-criteria optimization strategies give very close results. The biggest compromise is done with the apparent viscosity $\tilde{y}_3$, responsible for copolymer efficiency in flocculation processes, which is around 70% from the region of the optimal values of obtained Pareto-optimal solutions Δ_3.

Acknowledgements

This research was conducted under the contracts: bilateral joint project between the Bulgarian Academy of Sciences and The Romanian Academy, and KP-06-N27/18, funded by the National Fund “Scientific Investigations”.

References

1. G. Craciun, E. Manaila, M. Niculescu, D. Ighigeanu, Polym. Bull. 1299 (2017)
2. M. R. Nemţanu, M. Braşoveanu, Polymer science: research advances, practical applications and educational aspects, ed. A Méndez-Vilas and A. Solano-Martín (Badajoz: Formatex Research Center) 270-277 (2016)
3. M. Braşoveanu, L. St. Koleva, M. R. Nemţanu, E. G. Koleva, T. P. Paneva. J. of Phys.: Conf. Ser., 1089 (2018)
4. L. Koleva, E. Koleva, M. Nemtanu, M. Braşoveanu, Inter. Sci. J. of Sci. Tech. Union of Mech. Eng. "Industry 4.0", **4**, 2, 48-51 (2019)
5. E. Koleva, I. Vuchkov, Vacuum, **77**, 423-428 (2005)
6. I. N. Vuchkov, L. N. Boyadjieva, *Quality improvement with design of experiments* (The Netherlands, Kluwer Academic Publishers, 2001)
7. S. Najafi, A. Salmasnia, R. B. Kazemzadeh, AJBAS, **5**/9, 1566-1577 (2011)
8. QstatLab home page: http://www.qstatlab.co.uk/eng/index.html
9. S. Stoyanov, Bioautomation, **13**(2), 1-18 (2009)

Improvement of signal quality in CDMA systems on the basis of analysis of correlation properties of pseudo-random sequences

Gherman Sorochin[1], Tatiana Sestacova[1], Vladimir Jdanov[1]
Technical University[1] Chisinau, Republic of Moldova
gherman.sorochin@sde.utm.md, tatiana.sestacova@sde.utm.md, vladimir.jdanov@sde.utm.md

Abstract: *The article presents a continuation of researches in the field of improvement of signal quality in data transmission systems with code division multiple access (CDMA). It is discussed the correlation properties of pseudo-random sequences (PRS) used in the formation of noise-like signals in CDMA systems. The analysis, carried out in MATLAB environment, showed that correlation properties of the Walsh functions derivatives, used for generating PRS, have much better correlation characteristics than the original Walsh functions. Besides, these properties depend on the type of generating function of Walsh functions derivatives. It was justified the advantage of using these signals in the development of CDMA systems in order to improve the signal quality.*
Keywords: *CDMA SYSTEM, NOISE-LIKE SIGNALS, PSEUDO-RANDOM SEQUENCES, AUTOCORRELATION FUNCTION, CROSS CORRELATION FUNCTION, WALSH FUNCTION DERIVATIVE, GENERATING FUNCTION.*

1. Introduction

Sufficient experience in the use of broadband communication systems (BBCS) has confirmed their advantages, such as high resistance to narrowband interference, the ability to operate multiple subscribers in one communication channel, transmission secrecy, high resistance to multipath propagation.

For data transmission systems with code division multiplexing, in comparison with other types of systems, it is possible to reuse (multiple) the frequency resource due to the division of channels not by frequency or by time, but by "form", which allows the simultaneous operation of many subscribers in one and the same frequency band.

Such a system uses pseudo-random sequences (PRS) with specified correlation properties. PRS are widely used to generate noise-like signals (NLS) in communication systems such as DS-CDMA, GPS / Navstar, Glonass, and IEEE 802.11b wireless networks.

2. Theoretical preconditions

The correlation functions of complex noise-like signals are determined by the correlation functions (CF) of the manipulating sequences. Therefore, considering the CF of complex signals, it is sufficient to analyze the correlation functions of the manipulating sequences. Signal decoding on the receiving side is carried out by a correlation receiver, the basis of which is a correlator, which is a series-connected multiplier and an integrator that calculates the cross-correlation function (CCF) of the incoming signal with the PRS stored in the memory.

The most important parameter of the used pseudo-random sequences is their correlation properties [1]. Moreover, on the choice of binary code sequences, i.e., the noise immunity of the entire information system, depend their correlation properties. In addition, the code sequence must be well balanced, that is, the number of ones and zeros in it must differ by no more than one character. The last requirement is important to fulfill by excluding the constant component of the information signal.

The cross-correlation function of two signals $u(t)$ and $v(t)$ is equal to the scalar product $u(t)$ with a copy of $v(t)$ shifted by t_o as a function of the argument t_o:

$$R_{uv}(t_o) = \int_{-\infty}^{\infty} u(t)v(t - t_o)dt. \qquad (1)$$

The cross-correlation function between two discrete signals is calculated by the formula:

$$R_{uv}(n) = \sum_{j=-\infty}^{\infty} u_j \, v_{j-n}. \qquad (2)$$

However, based on the generalized Rayleigh formula, we can write:

$$R_{uv}(t_o) = \frac{1}{2pi} \int_{-\infty}^{\infty} U(w)V^*(w)\exp(jwt_o)dw. \qquad (3)$$

In asynchronous systems, to ensure orthogonality of signals for any t_0 the CCF should be zero. However, due to the linearity of the Fourier transform, this is possible only if $U(w)\cdot V^*(w) = 0$ on the entire frequency axis. Equality of CCF to zero means that two signals are orthogonal for any t_o only if their spectra do not overlap. However, this cannot be achieved in a multiple access system. The consequence of this is the occurrence of inter-user interference, i.e., nonzero response of the receiver of the *k*-th user to the signals of other users [3].

The Walsh functions [7, 8] can be referred to discrete signals with the best CCF structure. Walsh functions were developed in 1923 as a development of the system of Rademacher functions known by that time by adding new functions to it [3,7].

Walsh functions are formed from Rademacher functions using the following relationship:

$$wal_0(\theta) \equiv 1, wal_n(\theta) = \prod_{k=1}^{m} [rad_k(\theta)]^{n_k}, \qquad (4)$$

where n is the Walsh function number, n_k is the value (0 or 1) of the k -th bit of the Walsh function number n, written as m-bit binary Gray code.

Hence it is easy to see that the number of functions in the Walsh system turns out to be equal to $N = 2^m$, where m is an integer. Walsh functions take only two values: +1 and –1, which is a useful property when building circuits on binary digital elements (triggers).

The most common orthogonal system used in multichannel systems with channel division by code are Walsh - Hadamard systems (matrices) of order N = 4k, k is an integer, which are determined by the recurrence rule:

$$W_{2N} = \begin{bmatrix} W_N & W_N \\ W_N & -W_N \end{bmatrix}, \qquad (5)$$

where W_N is the Walsh - Hadamard matrix of order N, and it is assumed that $W_1 = 1$, or in sign form $W_1 = +$.

However, a feature of orthogonal codes is that the orthogonality of these codes is performed only at the "point", i.e., in the absence of time shifts. In real conditions, such situations are not met, orthogonality is violated, which in turn leads to an increase of the level of multiple access interference and the appearance of errors in the processing of input data. Therefore, various methods are used to eliminate these disadvantages.

In order to improve the properties of correlation functions (ACF and CCF), Walsh signal systems often construct so-called derivatives of signal systems [3, 7, 8].

A derivative is a signal, obtained as a result of element-wise (symbol-by-symbol) multiplication of two signals. A system composed of derived signals is called a derivative [3, 7, 8]. Let us consider the essence of the empirical method for constructing derived signal systems, when the Walsh system is used as the initial one (Fig. 1), where each line is a code sequence of the corresponding BPSK signal.

The original Walsh system – Y_{16}

$$y_{16} = \begin{bmatrix} + & + & + & + & + & + & + & + & + & + & + & + & + & + & + & + \\ + & - & + & - & + & - & + & - & + & - & + & - & + & - & + & - \\ + & + & - & - & + & + & - & - & + & + & - & - & + & + & - & - \\ + & - & - & + & + & - & - & + & + & - & - & + & + & - & - & + \\ + & + & + & + & - & - & - & - & + & + & + & + & - & - & - & - \\ + & - & + & - & - & + & - & + & + & - & + & - & - & + & - & + \\ + & + & - & - & - & - & + & + & + & + & - & - & - & - & + & + \\ + & - & - & + & - & + & + & - & + & - & - & + & - & + & + & - \\ + & + & + & + & + & + & + & + & - & - & - & - & - & - & - & - \\ + & - & + & - & + & - & + & - & - & + & - & + & - & + & - & + \\ + & + & - & - & + & + & - & - & - & - & + & + & - & - & + & + \\ + & - & - & + & + & - & - & + & - & + & + & - & + & - & - & + \\ + & + & + & + & - & - & - & - & - & - & - & - & + & + & + & + \\ + & - & + & - & - & + & - & + & - & + & - & + & + & - & + & - \\ + & + & - & - & - & - & + & - & - & + & + & - & + & + & - & - \\ + & - & - & + & - & + & - & - & + & - & + & + & + & + & - & + \end{bmatrix},$$

Walsh derivative system – Π_{16}

$$\Pi_{16} = \begin{bmatrix} + & + & + & + & - & - & - & + & - & - & - & + & - & - & + & - \\ + & - & + & - & - & + & - & - & + & - & - & - & + & + & - & + \\ + & + & - & - & - & - & + & - & - & - & - & + & + & - & - & - \\ + & - & - & + & - & + & + & - & + & + & + & - & + & - & - & + \\ + & + & + & + & + & + & + & + & - & - & - & - & + & + & + & - \\ + & - & + & - & + & - & + & - & + & - & + & - & - & + & - & - \\ + & + & - & - & + & + & - & - & - & - & + & + & + & - & + & + \\ + & - & - & + & - & + & - & + & + & - & + & - & - & + & + & - \\ + & + & + & - & - & - & + & + & + & - & + & - & + & - & + & + \\ + & - & + & - & + & + & + & - & - & + & - & + & + & - & - & + \\ + & + & - & - & + & + & - & + & - & + & + & - & - & + & + & - \\ + & - & - & + & + & - & + & - & + & - & - & + & - & + & - & + \\ + & + & + & + & + & + & + & + & - & - & - & - & + & + & + & + \\ + & - & + & - & + & - & + & - & - & + & - & + & - & + & - & + \\ + & + & - & - & + & + & - & - & - & - & + & + & - & - & + & + \\ + & - & - & + & + & - & - & + & - & + & + & - & + & - & - & + \end{bmatrix}.$$

Fig. 1 *The principle of constructing derivatives of Walsh functions*

The system of signals in Fig. 1, orthogonal at the point t = T_s has, in general, poor properties of ACF and CCF, however, it is very simple from the point of view of signal generation and processing.

A signal is chosen as the generating signal so that the derived system has good correlation properties. As a rule, this is a signal with a good ACF, and it is found with the help of a computer or in another way. In [3], an example of obtaining the derivative of a function (Fig. 1) is given, when M is taken as the generating function - a sequence of the form {+ + + - - - + - - - + - - + -} or in the bipolar representation {+1 +1 +1 -1 -1 -1 +1 -1 -1 -1 +1 -1 -1 +1 -1}.

Obviously, the correlation properties of Walsh functions derivatives will depend on the type of the generating sequence. Let's carry out this analysis.

Consider the correlation properties of Walsh function derivatives if we take as generating functions M - sequence from [3] and de Bruijn sequence with the generating polynomial $f(x) = x^4 \oplus x^3 \oplus 1$. The PRS is obtained by the generator for de Bruijn sequence in the form of a shift register with nonlinear feedback under certain initial conditions (A = 1000) and in bipolar representation have the form: B_1 = +1+1+1-1+1+1-1-1+1-1+1-1-1-1+1.

In this case, the system of Walsh function derivatives will have the form:

$$\Pi_{16} = \begin{bmatrix} + & + & + & - & + & + & - & - & + & - & + & - & - & - & - & + \\ + & - & + & + & + & - & - & + & + & + & + & - & + & - & - & - \\ + & + & - & + & + & + & + & + & - & - & + & - & - & + & - & - \\ + & - & - & - & + & - & + & - & - & + & - & - & + & + & + & + \\ + & - & + & + & - & + & - & + & + & + & + & - & + & - & + & + \\ + & + & - & + & - & - & - & + & - & - & + & + & - & + & + & - \\ + & - & - & - & + & - & + & + & - & - & + & - & - & - & + & - \\ + & + & + & - & + & + & - & - & + & - & - & + & + & + & - & - \\ + & - & + & - & + & + & + & - & + & + & - & + & - & + & + & + \\ + & + & - & + & + & - & + & - & - & - & - & + & - & + & + & + \\ + & - & + & + & - & + & - & - & - & - & + & + & - & - & + & - \\ + & + & + & - & + & - & - & - & + & + & - & + & + & - & - & - \\ + & + & - & + & + & - & - & + & - & + & - & + & - & - & - & + \\ + & - & + & + & - & + & - & - & - & - & + & - & + & + & - & - \\ + & + & - & + & + & + & + & - & + & - & + & - & + & - & - & + \\ + & - & + & - & - & - & - & + & + & - & - & + & - & + & - & + \end{bmatrix}$$

Fig. 2 *Walsh function derivative with generating function in the form of de Bruijn sequence B_1.*

Consider the correlation properties of Walsh functions derivatives (for example, the 2nd and 12th), taken from Fig.1 [3]. The results of calculating the aperiodic (AACF) and periodic (PACF) autocorrelation functions of the selected Walsh function derivatives are shown in Fig. 3 - Fig. 6, respectively.

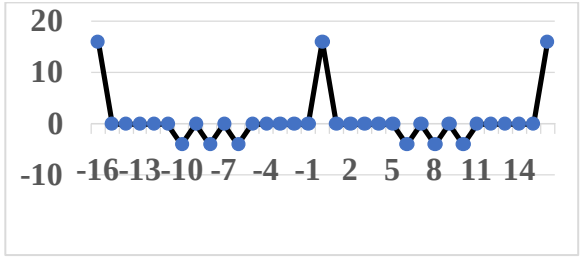

Fig. 3 *PACF of the 2nd derivative of the Walsh functions (Fig. 1)*

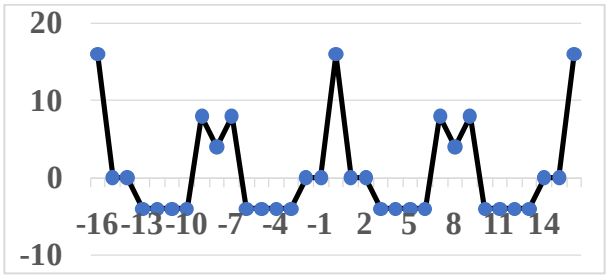

Fig. 4 *PACF of the 12th derivative of the Walsh function (Fig. 1)*

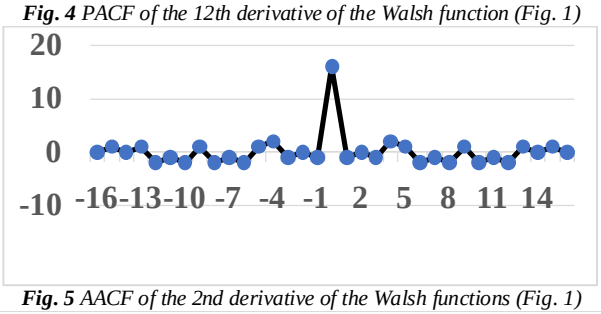

Fig. 5 *AACF of the 2nd derivative of the Walsh functions (Fig. 1)*

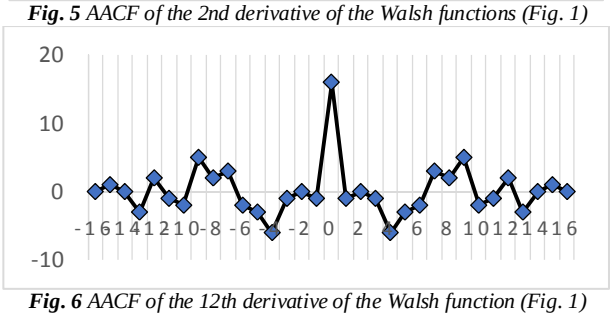

Fig. 6 *AACF of the 12th derivative of the Walsh function (Fig. 1)*

From Fig. 3 - Fig. 6 is seen that considered 16-bit Walsh function derivatives (Fig. 1) have not very good autocorrelation functions. To ensure synchronization during reception, it is necessary to eliminate the influence of side lobes (the suppression coefficient ranges from 2.67 for AAKF 12th and up to 8 for AAKF 2nd Walsh derivative). Similarly, for PACF - from 2 for 12th Walsh derivative and up to 4 for the 2nd Walsh derivative, i.e. the 2nd Walsh function derivative has the best correlation characteristics. For comparison, let us show what form the PACF of the original 2nd Walsh function has.

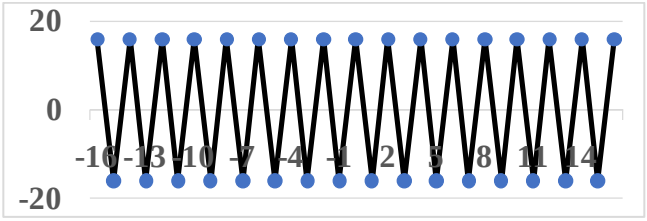

Fig. 7 *PACF of the 2nd original Walsh function (Fig.1)*

Comparative analysis of the PACF of the 2nd original Walsh function (Fig. 3) with the PACF of the 2nd derivative of the Walsh function (Fig. 7) shows that the derivatives of the Walsh function have much better correlation characteristics.

Let us consider the form of the cross-correlation function of the considered Walsh function derivatives. Graphical representation of the CCF is shown in Fig. 8.

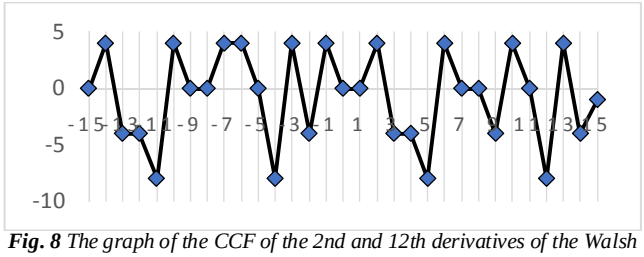

Fig. 8 *The graph of the CCF of the 2nd and 12th derivatives of the Walsh functions (Fig. 1)*

From Fig. 8 it follows that the CCF of Walsh function derivatives can be considered satisfactory, the CCF is more or less uniform, without extreme outliers, and can be used in code division multiplexing systems with the use of solvers that do not respond to CCF outliers within the specified limits.

Let us analyze the correlation properties of the 2nd and 12th derivatives of the Walsh functions with a generating function in the form of a de Bruijn sequence (Fig. 2). The results of calculating the aperiodic (AACF) and periodic (PACF) autocorrelation functions of the selected Walsh derivatives are shown in Fig. 9 and Fig. 8, respectively.

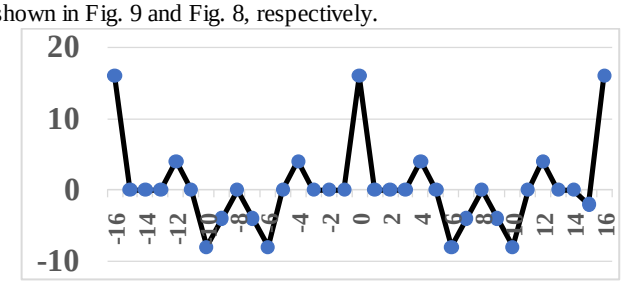

Fig. 9 *PACF of the 2nd derivative of the Walsh functions (Fig. 2)*

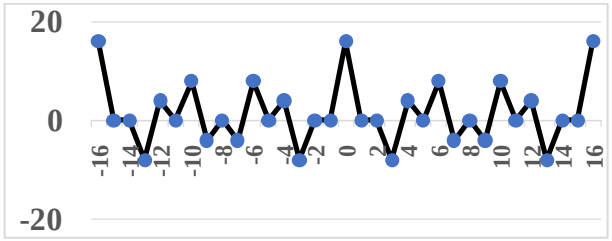

Fig. 10 *PACF of the 12th derivative of the Walsh function (Fig. 2)*

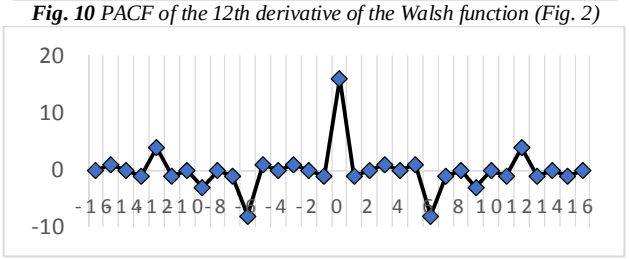

Fig. 11 *AACF of the 2nd derivative of the Walsh functions (Fig. 2)*

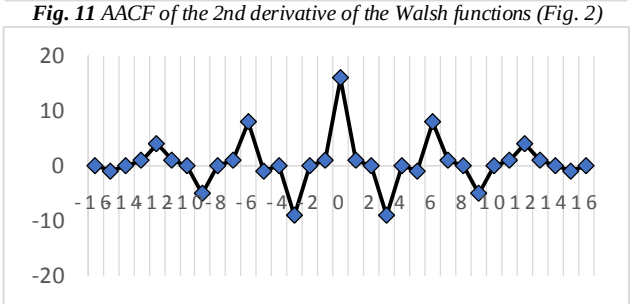

Fig. 12 *AACF of the 12th derivative of the Walsh function (Fig. 2)*

As can be seen from Fig. 9 - Fig. 12, the considered 16-bit derivatives of the Walsh function (Fig. 2) have not very good autocorrelation functions; to ensure synchronization during reception, it is necessary to eliminate the influence of side lobes (the suppression coefficient is the ratio of the amplitude of the maximum ACF peak to the maximum value of the amplitude of the side lobes ranges from 1.78 for AAKF and 2 for PAKF).

When considering the form of the cross-correlation of the considered Walsh function derivatives, was obtained graphical representation of the CCF, shown in Fig. 13.

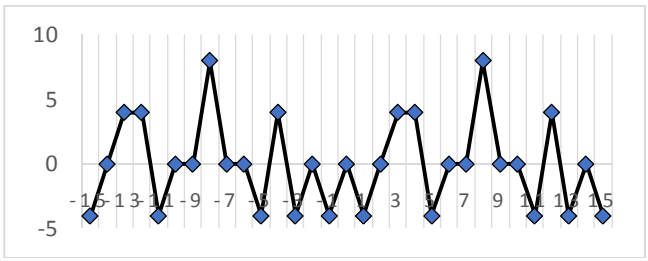

Fig. 13. The graph of the CCF of the 2nd and 12th derivatives of the Walsh functions (Fig. 2)

3. *Experimental data*

Let us analyze the correlation properties of considered above Walsh function derivatives in the MATLAB environment.

For this purpose, there was developed the program which allowed to calculate the aperiodic and periodic correlation functions of two pseudo-random sequences of the same length, given in bipolar form of arbitrary length. The program also allowed to calculate the cross-correlation function of these two sequences. The results of calculating the correlation characteristics are shown in Fig. 14, ..., Fig. 18 respectively.

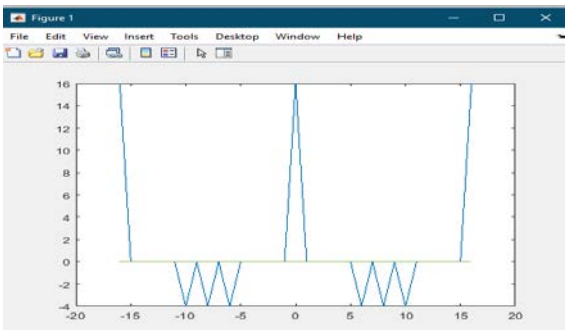

Fig. 14 *PACF of the 2nd derivative of the Walsh functions (Fig. 1)*

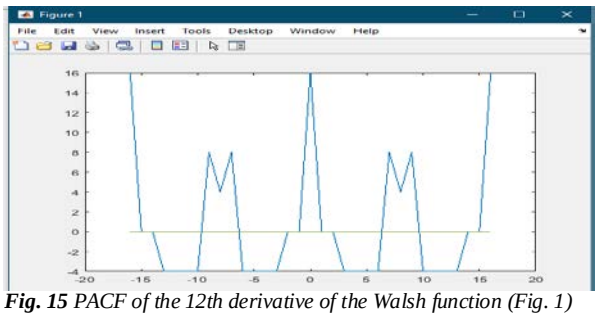

Fig. 15 *PACF of the 12th derivative of the Walsh function (Fig. 1)*

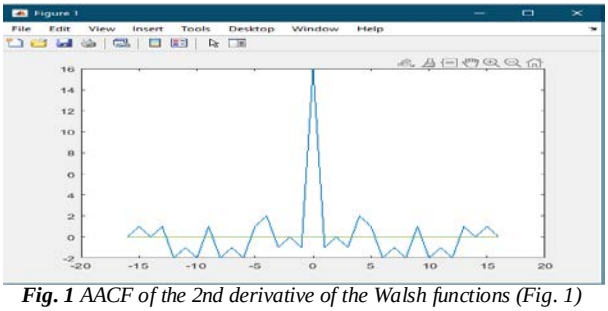

Fig. 1 *AACF of the 2nd derivative of the Walsh functions (Fig. 1)*

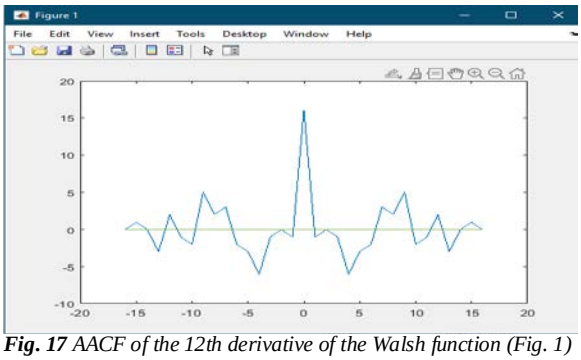

Fig. 17 *AACF of the 12th derivative of the Walsh function (Fig. 1)*

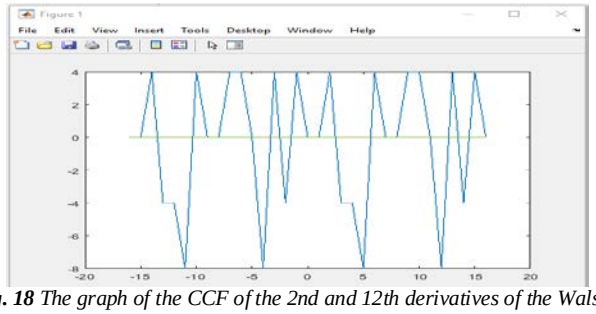

Fig. 18 *The graph of the CCF of the 2nd and 12th derivatives of the Walsh functions (Fig. 1)*

The analysis of Walsh function derivatives showed that in comparison with generating function of de Bruijn sequence, the generating function taken from [3] have better autocorrelation characteristics: the suppression coefficient lies within the limits from 2.67 for the 12th Walsh derivative to 8 for the 2nd Walsh derivative for AAKF and from 2 for the 12th Walsh derivative to 4 for the 2nd Walsh derivative for PACF. Thus, the 2nd derivative of the Walsh function has the best autocorrelation properties.

A comparative analysis of the correlation characteristics obtained analytically (Fig. 3 – Fig. 6, Fig.8) and by modeling in the MATLAB environment (Fig. 14 – Fig. 18) shows their identical form.

4. Conclusion

Analysis of the correlation properties of the studied broadband signals based on the Walsh functions derivatives allows to draw the following conclusions:

1) The correlation characteristics of Walsh functions, that are orthonormal, have good cross-correlation functions, which are equal to zero between two different Walsh functions. However, these functions have such properties only at the point at zero shift. In real conditions, especially in multipath propagation, orthogonality is violated and the cross-correlation function is nonzero. This leads to an increase in the level of multiple access interference and to errors in signal (channel) separation.

2) The correlation properties of the Walsh functions derivatives have much better correlation characteristics than the original Walsh functions.

3) The correlation properties of the Walsh functions derivatives depend on the type of the generating function. It is necessary to choose generating function that obtain the best correlation characteristics (in our case, the derivatives of the Walsh functions with the generating function taken from [2]).

4) The Walsh function derivatives (L = 16 bits) have a large amplitude of the central peak of the ACF, equal to the length of the sequence, but the amplitude of the side lobes slightly increases. This must be taken into account when designing multichannel systems to ensure reliable synchronization of receiving devices when exposed to noise.

5) The large length of the spreading code based on the Walsh functions derivatives allows distributing the signal energy over the spectrum, increasing the noise immunity of the system, providing good protection against unauthorized access, and improving electromagnetic compatibility with neighboring radio engineering systems. But it is necessary to provide special protection measures against sidelobe effects on the processing of input data.

6) The Walsh functions derivatives allow to obtain the required set of different pseudo-random sequences, which are needed for communication systems with code division channels (for example, 64-bit Walsh functions derivatives allow obtaining 64 different pseudo-random sequences, i.e., the same number of independent channels).

Search and design of PRS of arbitrary length is a real practical task. Obtaining all the sequences of the ensemble based on Walsh function derivatives with an analysis of the influence of generating function type on their correlation properties is necessary for the optimal use of considered sequences in the communication system. This, in turn, determines the quality of the communication system, the number of system subscribers, protection against unauthorized access, and, consequently, the economic aspects of systems.

At the same time, these sequences must have certain characteristics such as low threshold of cross-correlation and a pronounced peak of autocorrelation with minimal levels of side lobes, etc. The results can be used in the development of broadband communication systems and information transmission systems with protection from unauthorized access.

5. References

1. T. Sestacova, Gh. Sorochin, V. Jdanov, Analysis of the correlation properties of direct and inverse composite Walsh functions. ISJ *Math.Modeling, "Industry 4.0"*, issue **1,** p. 3 (2021), Sofia, Bulgaria.
2. Л.Е. Варакин, *Системы связи с шумоподобными сигналами*. (М.: Радио и связь, 1985).
3. М.И. Мазурков, *Системы широкополосной радиосвязи*. (О.: Наука и техника, 2009).
4. В.Е. Гантмахер, Н.Е. Быстров, Д.В. Чеботарев, *Шумоподобные сигналы. Анализ, синтез, обработка* (СПб.: Наука и Техника, 2005).
5. W. Solomon, Golomb and Guang, Gong. *Signal Design for Good Correlation*. Cambridge University Press (2005).
6. A.A. Bessarabova, M.D. Venediktov, V.I. Ledovskikh, *Separation of channels by form in broadband information transmission systems: Textbook.* - **2nd** ed. (Voronezh State Tech. University, 2006).
7. Г.И. Никитин, *Применение функций Уолша в сотовых системах связи с кодовым разделением каналов* (СПб.: СПбГУАП, 2003).
8. М.С. Беспалов., В.А. Скляренко, *Функции Уолша и их приложения*. Уч. пособие. (Владимир, Изд-во ВлГУ, 2012).

Fabrication of the Porous Structures with Gradient Thickness of the Struts, by using FDM 3D Printing with Dynamically Changed Parameters during the Printing

Nikola Palic[1,*], Fatima Zivic[1], Vukasin Slavkovic[1], Nenad Grujovic[1]
Faculty of Engineering, University of Kragujevac[1]
palic@fink.rs

Abstract: *This paper deals with 3D printing of porous, functionally graded structures by using Fused Deposition Modeling (FDM). We investigated the printing parameters that can allow printing with gradual infill and challenges associated with this method of printing. We fabricated polylactic acid (PLA) porous structures with variable infill by using FDM 3D printing. Set of the printing parameters for variable infill were investigated: gradient infill and gradient speed and the most successful case is shown. The significant influence of the printer hardware elements was noticed, among which, the worn gear tooth and inadequate extruder feed model can result in inability to print functionally graded lines.*
Keywords*: FUNCTIONALLY GRADED POROUS STRUCTURES; FDM 3D PRINTING; GRADIENT INFILL, DYNAMIC EXTRUSION, PRINTING ERRORS*

1. Introduction

The ability to produce structures/parts with locally variable structure and composition, such as porous, cellular, and lattice structures, is important for scientific and technological advancement in a variety of fields, ranging from tissue engineering [1, 2], bone grafts and dental implants [3, 4] to aerospace engineering [5] and microelectronics [6]. Several approaches have been presented to create these heterogeneous structures [7, 8, 9, 10]. Functionally Graded Materials (FGM) can efficiently mimic the natural structures, such as the bone structure [3, 4], thus providing artificially designed and produced implants closely resembling the natural organs and tissues. Functionally graded additive manufacturing can be realised in different ways [11], whereas additive manufacturing (AM) or 3D printing, offers the most promising possibilities in the FGM design [8, 12, 13]. One of the main benefits of the FGMs is the possibility to tailor mechanical properties of the constructs [14]. However, AM technologies are still associated with certain challenges in producing FGMs [15, 16].

Functionally Graded Materials (FGMs) are heterogeneous materials with tailored composition and structural gradients that have specified qualities in the desired orientation [17, 18, 19]. Functionally Graded Cellular Structures (FGCS) are Cellular Structures that have been functionally graded and are being investigated for a variety of engineering applications [20]. When opposed to totally porous materials, functionally graded porous structures have the benefit of preserving strength close to solid structures [21].

Functional graded materials expands the design space by allowing the engineer to tailor distinct material qualities throughout the different zones within the same element [14]. Objects with FGM structure, in essence, allow engineers to customize its design beyond simply modifying its physical shape to fit design aims and restrictions. FGM structures are challenging to design because it should allow modifications throughout the whole structure volume and is not limited only to topological or the dimensional variations. Such profound structural changes accompanied by the dynamic variation of the structural properties throughout the volume may pose significant complexities, and optimisation techniques are often used, from aspects of the final properties, topological optimization, material distributions, or the fabrication technologies [14, 22]. Furthermore, manufacturing limitations will most likely limit the available design zone and should be taken into account while planning [22].

For components or products with complicated and custom designs, 3D printing is one of the best suited technology, including the low cost Fused Deposition Modeling (FDM) 3D printing [23]. 3D printing of FGMs with broadly and diversely adjustable features in a single 3D printing process has steadily grown in relevance and has been intensively investigated recently, owing to benefits in structural control, resolution, and scalability, among others [16, 24].

Fused Deposition Modeling (FDM) or Fused Filament Fabrication (FFF) is a popular additive manufacturing (AM) technology that may be found in both open-source/low-cost and high-end/industrial AM systems. The typical AM manufacturing method is commonly followed for fabricating heterogeneous components with FDM/FFF [25]. The procedure starts with the creation of 3D models that use CAD software to directly create the desired geometrical form and structure. The geometrical information from these models is then sent to the relevant slicing and route planning software, which creates machine instructions files for the FDM/FFF system. The FDM/FFF technology is then used to create the parts, which are subsequently postprocessed and finalized according to the application [13].

It might be complex to select the printing parameters that will allow the desired porosity and pore size values in the case of a porous structure [20, 26]. The most process variables are related to the machine operation rather than the final form of the final component [20]. Furthermore, final porosity and pore size may deviate from theoretically designed values. Pore size and porosity of structures with gradient infill patterns are measured as a function of the several printing parameters . The influence of the printing parameters is significant, among which the infill values have the prominent role [27]. Application of 3D printing in design and fabrication of porous functionally graded structures are still in research [13, 26], including the investigation on correlation to the resulting material properties [28, 29].

This paper presents the fabrication of porous structures with variable infill by using FDM 3D printing, made of polylactic acid (PLA). We present the parameters of 3D printing for variable printing speed and printing flow and the printed structure with variable infill. We also present the issues in fabrication of such variable structures, related to the 3D printing process.

2. Materials and Methods

The polylactic acid (PLA) sample was created using FDM printer Creality CR-10S5 with purple filament (1.75 mm diameter) as the standard material. A disc with a diameter of 50mm and a height of 3mm serves as the sample (Fig 1a).

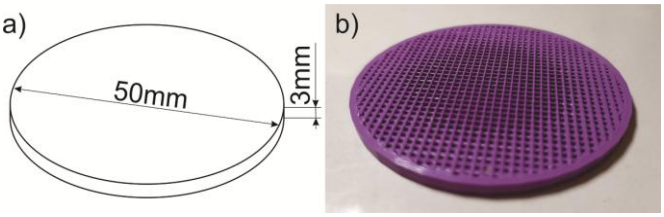

Fig. 1 *(a) schematic view of the printed sample, (b) printed sample*

All of the samples in this study were printed with a 0.4 mm nozzle. We used the printer default parameters, which included 30% infill, the layer height of 0.2 mm, and the printing speed of 20 mm/s. In total, the printing process lasted 29 minutes and 7 grams

of material was used. The printing parameters are given in Table 1. Layer height refers to the thickness of one layer during the 3D printing, while shell thickness refers to the thickness of the outer layers, as the printing head initially passes along the shell line and then fills it with layers. The thickness of the first and the final printing layers that were printed with full fill, regardless of the filling density settings, is referred to as bottom and top thickness. The filling of the specific printing elements is referred to as the infill density. The printing head speed during the printing along a straight line is referred to as the printing speed. The temperature of the nozzle during the printing is referred to as the printing temperature. To minimize the damage of the printed object, that can be caused by the sticking and non-homogenous stress distributions, the sample is printed on a heated plate (with defined bed temperature). Because it makes it easier to remove the final printed sample, raft is used as the support on which the object is directly printed.

Table 1: *3D printing parameters for the standard polylactic acid (PLA).*

Quality	
Layer height	0.2mm
Shell thickness	1.2mm
Enable retraction	Yes
Fill	
Bottom/Top thickness	0mm
Infill density	30%
Infill pattern	Line
Print speed and temperature	
Print speed	20mm/s
Printing temperature	230°C
Bed temperature	50°C
Support	
Support type	None
Platform adhesion type	Raft
Filament	
Diameter	1.75mm
Flow	100%

The sample was not printed with a standard constant infill but with a gradient infill. Gradient filling means that the filling grid volume is distributed unevenly over the sample. Different filler fiber thicknesses may be generated by adjusting the extra print settings inside the Ultimaker Cura software by using the gradient infill plugin. Fig. 2 shows the variation of the fiber thickness along the printing path.

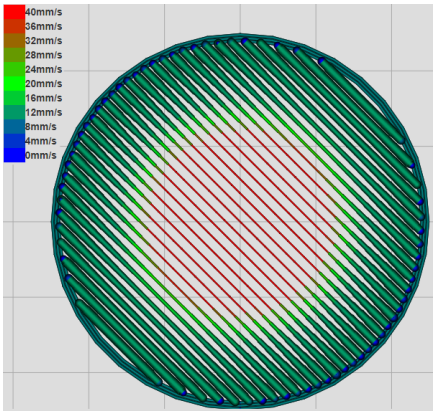

Fig. 2 *The distribution of the fiber thickness in the sample filling, depending on the variation of the printing speed.*

Printing parameters for obtaining variable infill are based on the variation of the printing speed and printing flow. With increasing the printing speed at constant flow, the fiber become thinner, while with increasing the printing flow at constant speed, the fiber become thicker. The distance gradient is a parameter that defines how far from the shell the speed and flow parameters will change. Gradient discretization represents the number of steps on how much the speed and fill parameters will change per gradient distance. 'Max flow' and 'Min flow' are the parameters that set up the limits of the range in which the flow varies during one gradient distance. 'Max over speed' and 'Min over speed' parameters determines the range of the printing speed that is used during one printing cycle. All of the gradient infill parameters are listed in Table 2.

Table 2: *Set of the printing parameters for variable infill*

Gradient infill	
Gradient distance	12mm
Gradient discretization	8
Max flow	350%
Min flow	50%
Short distance flow	350%
Gradient speed	
Max over speed	200mm/s
Min over speed	60mm/s

3. Results and discussion

The goal of the experiment is to leverage extrusion width variability to change the quantity of material that comes out of the nozzle during the printing in a real time. With the current designs and very slight flow alterations, the extruder may deposit more plastic near to the walls and decrease the flow in the middle. It is possible to perform it differently depending on the parameter settings: for example to strengthen the center zones and to make weaker outer zones towards the edges. We made samples that have weaker central zone and the porous structure becomes stronger towards the edges.

The samples were created in the shape of a disk to make it easier to see the effect of the parameters used to control the progressive infill on the sample. The zone of the intense filling of the material around the periphery of the sample is clearly visible in Figure 3a. This zone is 12 mm wide, which is the value of the gradient distance print parameter that has been specified (Table 2). The thickness of the printing lines at the ends and in the center of the sample are shown in Figure 3b. It can be seen that the lines in the central zone are half the thickness of the same printed line at the outer, edge zone. Considering the flow (max flow = 350 percent, min flow = 50 percent) and the speed (max speed 200mm/s, min speed 60mm/s) parameters, it is reasonable to deduce that such difference in fiber thickness might be considerably larger. However, major drawbacks of the lab 3D printers, especially FDM 3D printers, are related to the dimensional accuracy, and the high probability for some hardware elements (e.g. gear tooth) to rather rapidly loose their original performance, thus greatly influencing the final printed structures. For example, if the sliding of the filament occurs without direct feed into the extruder, the printing settings become inconsistent.

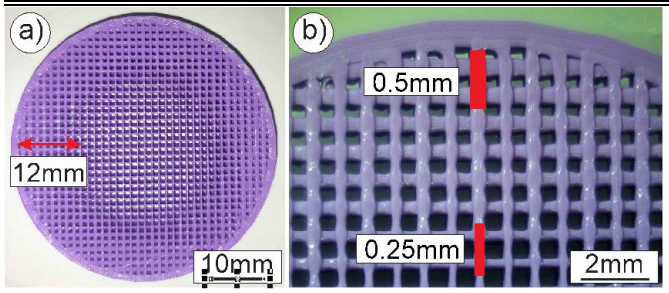

Fig. 3 *Gradient structure of the printed sample with two different magnifications*

Figure 4 shows the change in extrusion width along the diameter line printing direction. This variation of the extrusion width is directly correlated with the width of the printed line and produces its variation as shown in Fig. 3.

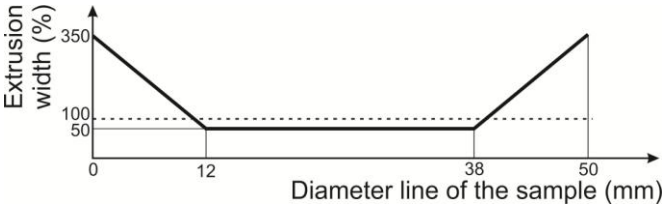

Fig. 4 *Change in extrusion width along the diameter line printing direction*

The success of the gradient infill printing is greatly influenced by the hardware settings and characteristics of the FDM printer. One of the characteristics of the printer that has the greatest influence is the performance of the extruder feed. There are two types of extruders, commonly used in FDM 3D printers: Bowden extruder and direct feed extruder (Fig. 5). Direct feed extruder gives better results because in Bowden extruder the filament is driven from a distance through the teflon tube. The distance that the filament has to travel has a negative influence on variable change of parameters during the printing, since the extruder can lose the ability to immediately apply the variations. Hence, in Bowden extruder, there is a slight delay in variation of parameters that significantly influence the possibility to print the gradient structure. Slightly delayed feed during the changing of the filament push speed produced the tube movement which further influenced delays in change of the fiber thickness, thus producing errors in printed structure: inaccurate change in the thickness of the fiber at the top of the nozzle.

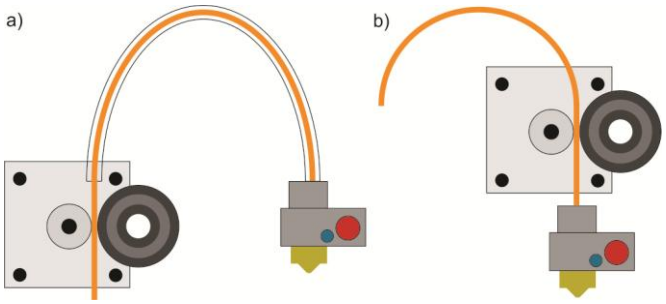

Fig. 5 *The extruder feed models: a) Bowden extruder, b) Direct feed extruder*

Filament slip during the feeding of the extruder is another possible source of error in the printed structure. Filament slip can occur for two main reasons. The first one is the insufficiently strong spring. For the proper filament feed, the spring creates tension and thus allows the gear to push the filament into the extruder. If the spring is weakened, what can occur after a certain time of the printer work, it will not create sufficient tension for the filament to be properly pushed. Another, much more common reason is the wear of the drive gear. In small 3D printers (home printers, fab lab printers), the drive gear is usually made of brass that does not exhibit high wear resistance, especially in harsh environments. Over time, the gear teeth wear out, thus forming worn tracks (channels), along which the filament slides (Fig. 6). This has a negative effect on the printing with standard parameters, and especially significant influence on the printing with a gradient infill. Worn gear teeth cannot efficiently follow the changes in the filament push speed and results in filament slipping, thus producing significant errors in the printed structure. This is especially prominent for the gradient infill printing where, in case of the worn teeth, we obtained structures with significantly different designs from the initially planned ones. Accordingly, we changed this gear element in the printer and used the new one, for the fabrication of the previously showed samples with gradient fill (Fig. 1b), since with the worn gear, it was impossible to produce them.

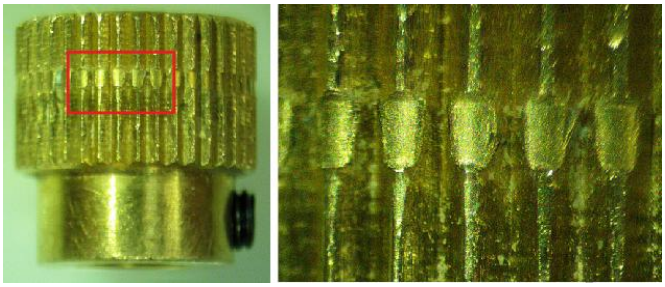

Fig. 6 *Worn brass gear that drives the filament*

4. Conclusion

Porous functionally graded PLA samples were fabricated using 3D printing (FDM) with the printing layer of 0.15 mm and gradient infill of 30%. Gradient infill printing was sucessfuly realised, proven by the functional distribution of the infill line thickness inside the sample structure. A variety of factors influenced the quality of the printed object. Beside the process parameters, the quality of the printer hardware elements essentially determines the behaviour during the printing. For the printing of porous, functionally graded structures, even the small defects in printer hardware can result in inability to print it. For the FDM 3D printing, the most significant influence, was determined to be the worn drive gear and extruder feed model. Further research on the influence of process parameters on the structural and mechanical properties will be realised.

5. Acknowledgement

This paper is funded through the EIT's HEI Initiative SMART-2M project, supported by EIT RawMaterials, funded by the European Union.

6. References

1. F. Hejazi, S. Bagheri- Khoulenjani, N. Olov, D. Zeini, A. Solouk, H. Mirzadeh, *Fabrication of nanocomposite/nanofibrous functionally graded biomimetic scaffolds for osteochondral tissue regeneration*, Journal of Biomedical Materials Research Part A, **109(9)**, 1657–1669, (2021).
2. S. V. Murphy, A. Atala, *3D bioprinting of tissues and organs*, Nature Biotechnology, **32(8)**, 773–785, (2014).
3. M. C. Bottino, V. Thomas, G. M. Janowski, *A novel spatially designed and functionally graded electrospun membrane for periodontal regeneration*, Acta Biomaterialia, **7(1)**, 216–224, (2011).
4. M. Mehrali, F. S. Shirazi, M. Mehrali, H. S. C. Metselaar, N. A. B. Kadri, N. A. A. Osman, *Dental implants from functionally graded materials: Dental Implants from FGM*, Journal of Biomedical Materials Research Part A, **101(10)**, 3046–3057, (2013).
5. J. W. Chua, X. Li, T. Li, B. W. Chua, X. Yu, W. Zhai, *Customisable sound absorption properties of functionally graded metallic foams*, Journal of Materials Science & Technology, **108**, 196–207, (2022).
6. Z. Rahimi, W. Sumelka, S. R. Ahmadi, D. Baleanu, *Study and control of thermoelastic damping of in-plane vibration of the*

functionally graded nano-plate, Journal of Vibration and Control, **25(23–24)**, 2850–2862, (2019).
7. J. M. Lowen, J. K. Leach, *Functionally graded biomaterials for use as model systems and replacement tissues*, Advanced Functional Materials, **30(44)**, 1909089, (2020).
8. N. Oxman, *Variable property rapid prototyping: Inspired by nature, where form is characterized by heterogeneous compositions, the paper presents a novel approach to layered manufacturing entitled variable property rapid prototyping*, Virtual and Physical Prototyping, **6(1)**, 3–31, (2011).
9. B. Kieback, A. Neubrand, H. Riedel, *Processing techniques for functionally graded materials*, Materials Science and Engineering: A, **362(1–2)**, 81–106, (2003).
10. D. Almasi, M. Sadeghi, W. J. Lau, F. Roozbahani, N. Iqbal, *Functionally graded polymeric materials: A brif review of current fabrication methods and introduction of a novel fabrication method*, Materials Science and Engineering: C, **64**, 102–107, (2016).
11. G. H. Loh, E. Pei, D. Harrison, M. D. Monzón, *An overview of functionally graded additive manufacturing*, Additive Manufacturing, **23**, 34–44, (2018).
12. U. Scheithauer, S. Weingarten, R. Johne, E. Schwarzer, J. Abel, H-J. Richter, T. Moritz, A. Michaelis, *Ceramic-based 4d components: Additive manufacturing (Am) of ceramic-based functionally graded materials (Fgm) by thermoplastic 3d printing(T3dp)*, Materials, **10(12)**, 1368, (2017).
13. J. Giannatsis, A. Vassilakos, V. Dedoussis, *A heterogeneous infill technique for fused deposition modeling*, Procedia Manufacturing, **51**, 642–648, (2020).
14. T. S. Lumpe, J. Mueller, K. Shea, *Tensile properties of multi-material interfaces in 3D printed parts*, Materials & Design, **162**, 1–9, (2019).
15. M. Bahraminasab, *Challenges on optimization of 3D-printed bone scaffolds*, BioMedical Engineering OnLine, **19(1)**, 69, (2020).
16. M. Ansari, E. Jabari, E. Toyserkani, *Opportunities and challenges in additive manufacturing of functionally graded metallic materials via powder-fed laser directed energy deposition: A review*, Journal of Materials Processing Technology, **294**, 117117, (2021).
17. M. Naebe, K. Shirvanimoghaddam, *Functionally graded materials: A review of fabrication and properties*, Applied Materials Today, **5**, 223–245, (2016).
18. M. Sathish, N. Radhika, B. Saleh, *A critical review on functionally graded coatings: Methods, properties, and challenges*, Composites Part B: Engineering, **225**, 109278, (2021).
19. R. Ghanavati, H. Naffakh-Moosavy, *Additive manufacturing of functionally graded metallic materials: A review of experimental and numerical studies*, Journal of Materials Research and Technology, **13**, 1628–1664, (2021).
20. Y. Li, Z. Feng, L. Hao, L. Huang, C. Xin, Y. Wang, E. Bilotti, K. Essa, H. Zhang, Z. Li, F. Yan, T. Peijs, *A review on functionally graded materials and structures via additive manufacturing: From multi- scale design to versatile functional properties*, Advanced Materials Technologies, **5(6)**, 1900981, (2020).
21. R. V. Duraibabu, R. Prithvirajan, M. Sugavaneswaran, G. Arumaikkannu, *Compression behavior of functionally graded cellular materials fabricated with fdm*, Materials Today: Proceedings, **24**, 1035–1041, (2020).
22. A. Garland, G. Fadel, *Design and manufacturing functionally gradient material objects with an off the shelf three-dimensional printer: Challenges and solutions*, Journal of Mechanical Design, **137(11)**, 111407, (2015).
23. J. Wang, S. Mubarak, D. Dhamodharan, N. Divakaran, L. Wu, X. Zhang, *Fabrication of thermoplastic functionally gradient composite parts with anisotropic thermal conductive properties based on multicomponent fused deposition modeling 3D printing*, Composites Communications, **19**, 142–146, (2020).
24. X. Zhang, J. Wang, T. Liu, *3D printing of polycaprolactone-based composites with diversely tunable mechanical gradients via multi-material fused deposition modeling*, Composites Communications, **23**, 100600, (2021).
25. N. Palić, V. Slavković, Ž. Jovanović, F. Živić, N. Grujović, *Mechanical behaviour of small load bearing structures fabricated by 3d printing*, Applied Engineering Letters : Journal of Engineering and Applied Sciences, **4(3)**, 88–92, (2019).
26. B. Saleh, J. Jiang, R. Fathi, T. Al-hababi, Q. Xu, L. Wang, D. Song, A. Ma, *30 Years of functionally graded materials: An overview of manufacturing methods, Applications and Future Challenges*, Composites Part B: Engineering, **201**, 108376, (2020).
27. I. Buj-Corral, A. Bagheri, A. Domínguez-Fernández, R. Casado-López, *Influence of infill and nozzle diameter on porosity of FDM printed parts with rectilinear grid pattern*, Procedia Manufacturing, **41**, 288–295, (2019).
28. K. D. Nguyen, C.-L. Thanh, H. Nguyen-Xuan, M. Abdel-Wahab, *A hybrid phase-field isogeometric analysis to crack propagation in porous functionally graded structures*, Engineering with Computers, (2021).
29. P. M. Ramteke, S. K. Panda, N. Sharma, *Effect of grading pattern and porosity on the eigen characteristics of porous functionally graded structure*, Steel and Composite Structures, **33**, 865–75, (2019).

Sterile Manufacturing Quality Control Methods in the Medical Products Industry

Toma Stulgė[1], Rūta Rimašauskienė[1*]
Kaunas University of Technology, Faculty of Mechanical Engineering and Design, Kaunas, Lithuania
toma.gagyte@ktu.edu, ruta.rimasauskiene@ktu.lt

Abstract: *Manufacturing of medical products is a very wide market. Many steps must be taken to ensure that produced product is sterile and safe and efficient to use for the customer. All manufacturing system from production floor to the type of sterilization must comply with required standards and regulatory. Every step of introducing new product to the production to routine production itself must be well documented and justified to be able to release the product to the market for human consumption. This paper presents information of production area requirements for medical devices, sterilization methods and sterilization indicators, briefly overlooks the quality control of such processes and the effectiveness of it.*
Keywords*: STERILE, MANUFACTURING, QUALITY CONTROL, MEDICAL PRODUCTS, STERILIZATION*

1. Introduction

The importance of quality control and inspection in manufacturing of sterile medical devices is exceptionally high. Stardartized procedures and quality control methods must be incorporated into routine production and followed strictly to ensure the best quality product will reach the customer and complaint level for the company will be as low as possible. Sterile medical devices should be sterile because these products are going to be infused directly into the bloodstream or body tissues [1].

Many steps must be taken to produce the sterile medical device. Starting from the qualified production area, validated and verified production processes, appropriate sterilization methods, succesfully passed audits and maintened required certification level. Many standards and requiraments must be fulfilled before succesfuly releasing the product to the market and, for example, ISO 13485 is one the most basic and most commom standard that medical devices manufacturer must follow. This standard basically specifies all requiraments for the Quality Management System for the manufacturer. The manufacturer of medical devices must demonstrate the ability to provide such medical devices and services that meets regulatory and customer requiraments. Besides compliance to ISO 13485, medical devices manufacturers has to comply with many more regulations and guidelines instituted by the FDA, ISPE, EMA, MHRA, and ICH, emphasizing good manufacturing practice and inspection requiraments in the manufacturing of medicinal products [2]. Sam A. Hout studies sterile manufacturing requiraments and fundamentals of aseptic techniques, quality by design, risk assesment, and management in support of sterile operations application [2] in the book "Sterile manufacturing. Regulations, processes, and guidelines".

Country/region	Standards/regulations	Conformity assessment
Australia	ISO13485 or EN46001[a] ISO13488 or EN46002[a]	Government and third party
Canada	ISO13485, ISO13488	Third party
European Union	EN46001[a] or ISO13485 EN46002[a] or ISO13488	Third party
Japan	GMP #40 ordinance GMPI #63 ordinance QS Standard for medical devices #1128 notice	Government
United States	QS (21 CFR part 820)	Government

Fig. 1 *Quality standards [3]*

The word "sterile" usually associates with the meaning that products or devices do not contain any viable pathogens, such as viruses, bacteria, fungi, and other living forms.

Neither visually nor by other means used nowadays, it is possible to quickly and without special research methods determine that one or another product is certainly "sterile". Nowadays, the term "sterile products" is understood to mean that these products or devices have been manufactured and prepared in appropriate ways, in accordance with strict rules and requirements. The necessary measures to ensure quality were used throughout the process, the process itself was controlled, and the results of the process and its control were documented. The concept also includes that the personnel involved in the processes have the necessary qualifications and are properly trained. The overall requirements for sterility are very nicely describe in Medical Device Directive 93/42/EEC points 8.3 – 8.7 and point 13.

The goal of sterile product is usually reached by sterilization or irradiation processes. Sterilization processes are carefully chosen for every type of the product or device as it can have a huge influence on product functionality and safety to the end user. These processes are expected to change used plastic [4], elastomer or other materials properties. Laurence W. McKeen investigates the effect of different sterilization methods on plastics and elastomers. Also, dozens of sterilization methods are reviewed in a very informative and simple way in the book "The Effect of Sterilization on Plastics and Elastomers" chapter 1. Medical devices manufacturers not only carefully choose the sterilization supplier, but also monitors closely the whole process. To ensure that sterilization process is completed successfully sterilization indicators are used widely across the industry. These indicators are used to identify that the procedure used for sterilization is completed and to avoid any confusion [5]. Shruti Moondra reviews the application of different types of sterilization indicators in the book "Sterilization of pharmaceuticals".

Cleanrooms and controlled production environment are a big part of medical devices, especially, sterile medical devices or pharmaceuticals production. The cleanroom environment has many potential sources of contamination, including: operators, equipment, structures, and any surface that can create particles via friction, heat, exhaust, outgassing, and static electricity charge [6]. During active production, millions of particles are generated into the environment. Associates that performs everyday activities in such production areas are considered to be one of the biggest contamination sources. This is the reason why the garment for operators and other personnel [6] must not be comfortable to work, but also be validated and monitored closely. Shih-Cheng Hu and Angus Shiue investigates the importance of validation, testing, penetration and application of the personnel factor for the garment used cleanrooms [6].

In this paper, production area requirements will be reviewed, as also the types of sterilization methods and indicators types. The quality control and effectiveness of sterilization process will be briefly overlooked in chapters 3.1 and 3.2.

2. Production area of sterile medical devices

Sterile medical devices are usually produced in cleanrooms, where environment is controlled. The product itself is usually not sterile immediately after production, but the bioburden level on the surface of such kind devices is significantly lower in comparison with normal production. Cleanrooms are frequently used not only for medical devices or pharmaceuticals production, but also for electronic, micro schemes or anything else that require low viable and non-viable particles concentration in the air.

Air filtration and overpressure are used to lower the particle and microorganism concentration presence in the environment, where production process is ongoing. Overpressure prevents air ingress

into the cleanroom, in this way when personnel is entering the room the particles from the outside does not flow into the room. The air is supplied through HEPA filters and high number of air changes per hour is kept. The biggest contamination in cleanrooms is considered to be people and materials as, in example, skin of a human sheds according the speed of its movement (Fig. 2).

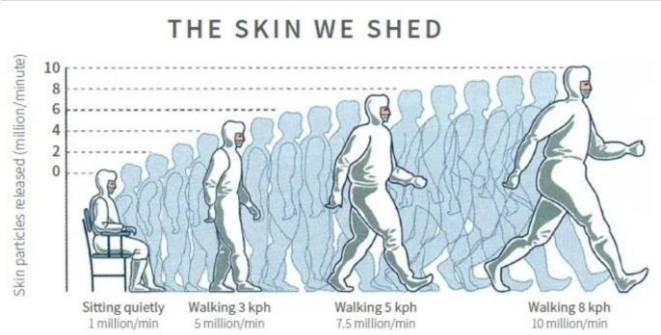

Fig. 2 *Contamination from people [7]*

In the companies where cleanrooms are in operation special procedures are usually in place. Most manufacturers have established cleaning and disinfection procedures, gowning and behavior procedures, environmental monitoring programs, special personnel training programs, pressure monitoring instructions. For cleaning such production areas only approved and appropriate cleaning agents must be used, alternating them between to reduce the risk to develop bacterial resistance. The process of the cleaning must be validated to ensure its effectiveness.

Cleanrooms itself are classified into classes according the airborne particulate cleanliness per ISO 14644-1 standard (Fig. 3)

Table 1 — Selected airborne particulate cleanliness classes for cleanrooms and clean zones

ISO classification number (*N*)	Maximum concentration limits (particles/m³ of air) for particles equal to and larger than the considered sizes shown below (concentration limits are calculated in accordance with equation (1) in 3.2)					
	0,1 µm	0,2 µm	0,3 µm	0,5 µm	1 µm	5 µm
ISO Class 1	10	2				
ISO Class 2	100	24	10	4		
ISO Class 3	1 000	237	102	35	8	
ISO Class 4	10 000	2 370	1 020	352	83	
ISO Class 5	100 000	23 700	10 200	3 520	832	29
ISO Class 6	1 000 000	237 000	102 000	35 200	8 320	293
ISO Class 7				352 000	83 200	2 930
ISO Class 8				3 520 000	832 000	29 300
ISO Class 9				35 200 000	8 320 000	293 000

NOTE Uncertainties related to the measurement process require that concentration data with no more than three significant figures be used in determining the classification level

Fig. 3 *Cleanroom classification [8]*

Before starting normal production, such area must be validated and regularly re-qualificated. Cleanrooms that is classified as 5 class or higher must be re-qualificated to demonstrate compliance with particle concentration limits every 6 months as the lower classes every 12 months. Routine environmental monitoring should be completed to define the limit values for alert and action limits. During such monitoring the room is usually at operation conditions and it must be documented what type of products were produced during testing, number of operating machines and personnel in the room. Microbiological analysis of such monitoring and identification of microorganisms can reveal the true origin of the contamination (air, material, water or people). Different sampling methods can be used to determine the contamination (Fig. 4).

Active air sampling	Passive air sampling (settle plates)	Surface sampling	Hand sampling	Garment sampling
Production, at operation, before starting the production	Indicate particles contamination on the product	Production – NOT on critical points within machine operation	Any time, after sampling disinfection!	Always before the texile garments are changed – before being washed
Dressing room – right after change, when no people are present	Dressing room – during the change	Dressing room – contact plates at/after change, different sampling points	Swabs or contact plates, gloves print	Swabs or contact plates - hands, armpit

AIR: passive or active sampling
PEOPLE: hand swabs, contact plates, clothes
SURFACES: surface swabs, contact plates (RODAC)

Materials & Products: bioburden acc. to documented control plan

Fig. 4 *Sampling methods*

3. Sterilization methods and indicators

Many medical devices and products require sterilization to ensure that they are effective and safe for customer use. Sterility is therefore a critical quality attribute and is essential [9] for these products. Medical device only can be sterile or non-sterile, no partial sterility is impossible. Sterilization of medical devices and products is performed in several different techniques. Nowadays mostly used techniques are these:

- Saturated water vapor sterilization;
- Sterilization with Ethylene Oxide (E.O.) gas;
- Sterilization with low temperature steam and formaldehyde;
- Sterilization with hydrogen peroxide plasma;
- Gamma sterilization;
- Sterilization with dry hot air.

For the control of effectiveness of these sterilization techniques indicators are most widely used. To date, there is no universal indicator of sterilization, which could provide control of the sterilization effectiveness for all types of equipment [10]. Those indicators could be chemical, biological or different data loggers.

The evaluation of chemical indicators (CI) is based on clearly visible discoloration/change of colour after the sterilization cycle is over. But the chemical indicator's colour change only shows that the conditions where CI was positioned were what the indicator was designed to indicate. Therefore, only part of CI are used to evaluate the sterilization process. The possibility of correctly evaluating the effectiveness of sterilization depends on proper selection of indicators and the interpretation of their readings. Unfortunately, none CI could show whether the sterilization was truly effective.

Biological indicators (BI) are the only indicators that provide reliable assessment of the efficiency of the sterilization process. They consist of a culture of bacteria that are highly resistant to the sterilization conditions under particular study. Different BI with different cultures of bacteria is used for every sterilization technique. To acknowledge that sterilized device or product is suitable for use after the sterilization process where BI were used could only be done after the results of BI evaluation have been received. The process of evaluating the readings of BI could take up to 48 – 72 hours.

Data loggers, digital devices that record the physical data of the sterilization process, on the other hand, are relatively new way to control and evaluate the sterilization process. Firstly, the recording of process data (parametric control), was introduced in the industry. Unlike chemical indicators or biological indicators, parametric control provides much more information about the course of the cycle, the sterilization conditions achieved and the duration of the cycle. These loggers can also provide (and provides) information about preparation for sterilization, such as removal of air from the chamber, duration and number of preparation stages for sterilization, etc.. The application of the method in industry has

brought tangible benefits to consumers and significantly increased reliability of sterilized products. After starting using this control technique manufacturers have reduced the risk of placing improperly sterilized products on the market and dispensed the huge quantities of CIs used so far. The application of parametric control resulted in lower product costs and cost to consumers.

3.1. Sterilization process quality control

Quality control methods calls for effective inspection procedures, but product testing may not always be adequate [11] for sterilization process control. The variation of the sterilized product testing methods brings the uncertainty while evaluating results. The most used classical methods of microbiological testing as quality control for sterilized products or devices may not always be the most suitable choice. Results of microbiological testing may show the capabilities of laboratory, its personnel and procedures than sterilization effectiveness itself. For radiation sterilization (gamma sterilization, e-beam sterilization) simple dosimetry may be the key. Since standardized dosimetry is fairly simple, reliable, and reproducible, there is a trend towards using this method for assuring safe product release [11]. In Fig. 5 number of the applications of irradiation dosimetry can be seen.

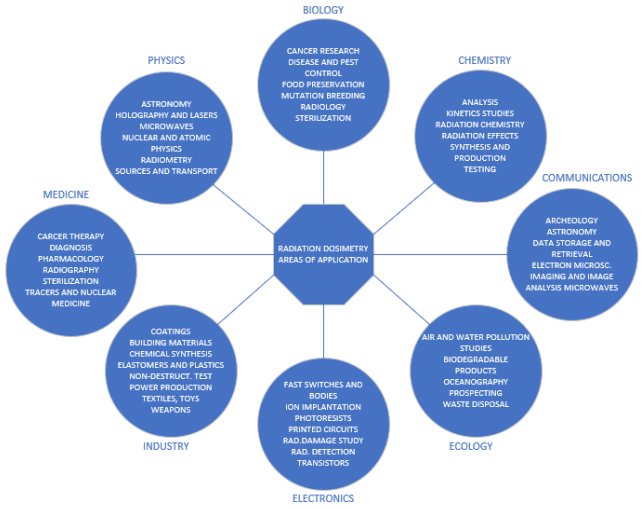

Fig. 5 *Dosimetry areas of application [11]*

The focus on quality control in producing the sterile medical devices can not be only based on QC in sterilization facility, it should be more of a system. The emphasis on quality control only in radiation processing without harmonization it with the other parts of the whole process of manufacture of a final product may not allow a final product to have been of required quality as a whole [12]. Manufacturers usually emphasize validation processes to choose the right type of sterilization and accurate dose, suitable materials of the device.

3.2. Effectiveness of sterilization

When radiation sterilization method is used to maintain sterilization process effectiveness usually dose audits are completed. The frequency of dose audits depends on many factors. In example, average bioburden level, equipment re-calibrations, maintenance of production equipment, change controls of the processes. When larger time interval is defined, proof and strong justification is required.

Bioburden

CFU / device	Method of dose determination	Max. interval dose-audit
≥ 1.5	Any	Quarterly
<1.5	Method 2 or VD max25	Quarterly
< 1.5	Method 1 or VD max15	Monthly
Any	Individual LOT release	Every individual LOT

Fig. 6 *Maintenance of radiation sterilization effectiveness based on bioburden*

ETO sterilization process effectiveness can be maintained by periodic control, justified regular and defined requalification of sterilization process, equivalence assessment. Medical devices that is sterilized by ethylene oxide sterilization method is marked very clearly. Special standards for this method are applicable because ETO is cancerogenic, mutagenic and reproductive toxic. Residuals after this sterilization can cause irritation of skin, eyes, blisters, burns and mutagenic – chromosomal defects.

There is a lot of factors when choosing the right type of sterilization for produce divice, but the comparison between most commom sterilization methods can be seen in Fig. 7.

Characteristic	Irradiation	Ethylene oxide	Steam
Efficiency	Excellent	Excellent	Excellent
Material compatibility	Majority of materials, some are decoloured, becomes brittle, are degraded	Majority of materials, not suitable for non-porous materials, liquids	Some materials, not suitable for temperature sensitive
Mechanism of action	Ionisation, damages in the DNA structure	Alcylation, damages in the DNA structure	Denaturation of proteins
Post-process control	Dose release, parametric	Biological indicators, parametric release	Biological indicators, parametric release
Quarantene	No quarantene (or 2-7 days)	2-7 days, until noEtO residuals are left	No quarantene (or 2-7 days)
Economical aspect	Very good for large and small volumes, high investment	Very good, small investment	Very good, the smallest investment

Fig. 7 *Comparison of the most frequent sterilization methods*

After sterilization medical device or product must be labeled accordingly the sterilization method used (Fig. 8)

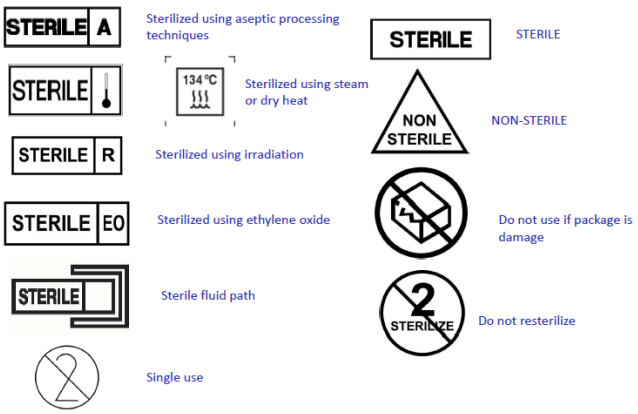

Fig. 8 *Labeling of sterile medical device*

Although, most manufacturers ships already finished product/device to sterilization facility, and it is already labelled as sterile even though it is non-sterile. Some specific restrictions and agreements are used in these situations, and some manufacturers

usually considers to have additional visual indicator on the package so the end user would sure, that the product is sterile.

4. Conclusions

Manufacturing sterile medical devices is strictly regulated by dozens of standards and guidelines instituted by various organization across the world. Various types of sterilization and irradiation methods may be used to sterilize the final product. The method may be chosen carefully according to the use of the product, raw materials that is used to manufacture it and most importantly end user. Different types of indicators could be used throughout the process to assure successful completion. Quality control of the sterilization process must be harmonized with QC in manufacturers facility to ensure the best quality products reaches the customers.

Acknowledgements

Research was funded by a grant (No. S-M-ERA.NET-20-1) (project: “Additive Manufactured Composite Smart Structures with Embedded Fibre Bragg Grating Sensors”, acronym: “AMCSS”) from the Research Council of Lithuania

4. References

1. Manmohan Singhal, MD. Habban Akhter, Devesh Kapoor, Lakshmi Kanta Kanthal, Yashu Chourasiya, Rahul Maheshwari, Anil Pethe, Rakesh K. Tekade. Advancements in sterile products and admixtures. The Future of Pharmaceutical Product Development and Research. Academic Press (2020)
2. Sam A. Hout, Sterile manufacturing. Regulations, processes, and guidelines (2021)
3. M. Gudeppu, S. Sawant, C. G. Chockalingam, & P.S. Timiri Shanmugam. Medical device regulations. Trends in Development of Medical Devices (2020)
4. Laurence W. McKeen, The Effect of Sterilization on Plastics and Elastomers (2018)
5. Moondra, Shruti. Dosage Form Design Parameters. Sterilization of Pharmaceuticals Technology, Equipment, and Validation (2018)
6. Hu, Shih-Cheng; Shiue, Angus. Validation and application of the personnel factor for the garment used in cleanrooms, Building and Environment (2016)
7. https://www.pharmamicroresources.com/2018/02/distribution-of-particles-within.html
8. https://www.pharmaguideline.com/2012/07/overview-of-iso-14644-clean-room.html
9. Fatima Hasanain, Katharina Guenther, Wayne M. Mullett and Emily Craven. Gamma Sterilization of Pharmaceuticals. A Review of the Irradiation of Excipients, Active Pharmaceutical Ingredients, and Final Drug Product Formulations. *PDA Journal of Pharmaceutical Science and Technology* March, 68 (2) 113-137 (2014).
10. Novikova Ye, Indicators of sterilization of medical products. National University of Pharmacy (2020)
11. William L. McLaughlin, Radiation measurements and quality control. , 9(1-3), 147–181 (1977)
12. V. N. Ponomarev, A. A. Molin, V. V. Kalashnikov, Ju. A. Drabkin. QC/QA system in radiation sterilization process on E-Beam irradiation plant, Department of radiation technologies of state research center (2006)

Set up for real time capturing of welding parameters

Deyan Gradinarov[1]
Institute of Metal Science, Equipment and Technology with Hydroaerodynamic Center at Bulgarian Academy of Sciences[1]
dgradinarov@ims.bas.bg

Abstract: *It is presented set up for real time capturing welding parameters – voltage, current and temperature in specific points of welding process.*
Keywords*: REAL TIME, REALT TIME CAPTRING, WELDING PARAMETERS*

1. Introduction

According to the modern requirements for low energy intensity and environmental protection and in the context of declining natural resources, scientists, the business, and the society are looking for ways to meet the growing needs of various industries, from optimizing and improving welding methods to adding additional alloying elements for better weldability.

The welding process is used in almost every area of human activity, and the need products of this process is constantly increasing. With the increase of the responsibility of the welded joints, the requirement for welding quality is also increased.

The welding process is performed according to a pre-approved and validated Welding Procedure. This welding procedure sets the welding technology, welding mode, current, voltage, welding speed, wire feed rate, flux used, type, diameter and tip pre-forming of the welding wire, welding and break time, and other parameters on which the quality and reliability of the welded joint depends. Deviating from them, with a high probability, leads to a decrease in the properties of the welded joint, and hence to defects and damage that increases the risk of injuries and endangering human life and negative environmental consequences.

When welding by an operator, due to a number of factors that cannot be avoided, the welder can deviate from the welding procedure, with the welding process being carried out at welding parameters that differ from the procedure. This leads to the presence of defects - gas and slag inclusions, welding cracks, unexpected change of the main metal properties in the surrounding area, etc. The presence of such defects directly affects the exploitation properties of the manufactured parts and elements by reducing their strength, lifetime, reliability, etc. When applied conscientious control, this leads to wastage, cost increases and waste of resources - metal, welding wire, welding gases and energy. In case of unconscious control - to the direct danger of traumatism, accidents, ecological catastrophes, etc., which directly or indirectly affects the society.

Improving the welding process by the real time control of welding parameters compared to those set in the welding procedure reduces drastically the possibility of defects and thus gives economic and environmental advantages by reducing wastage and consequently consumption of metal, gas, electricity and water to reducing emissions.

The results of the research show that there are numerous studies on the methods and technologies for monitoring and control of the welding parameters, the influence of the parameters on the exploitation properties of the welded elements, the quality determination of the welded joints.

It is studied the influence of the welding parameters in various welding processes and their impact on the quality and performance of the welded joints [1,2,3].

One of the current problems of modern material science is methods for increasing the life cycle of parts with welded joints, which must have both high hardness and strength and low internal stress. It is studied the impact of welding parameters on the morbidity of welded joints [4,5].

There are known studies on welding process optimization methods by control of welding parameters [6,7,8].

There are studies on welding parameters control and welding optimization [9,10] as well as methodologies for determining the parameters in welding processes [11].

There are developed welding parameters parameter control systems [12,13,14].

The analysis of our well-known sources does not give enough clarity to the question: what impact the welding parameters have on the performance of the welded joints and what methodologies should be used to improve the quality of the process.

This leads to the need to acquire new fundamental knowledge about the possibilities, means and rate of improving the quality of the welding processes by real time control of parameters.

A thorough study and determination of the influence of welding parameters on the quality of the process and analysis of the possibilities for quality improvement through real time control is also needed.

2. Set up for real time capturing of welding parameters

The set up has two main parts – welding equipment and measuring equipment. The welding equipment consists of welding torch, which is mounted on mechanical grip. The mechanical grip fixes the torch in one position and removes fluctuations from welder's movements. The mechanical grip is mounted on welding tractor, which moves along and over the welded elements with constant speed. Welded elements are placed on welding table. Next to the welding table are placed the power source that feeds the torch and gas bottle that protects the joint. The measuring equipment consists of capturing module Lincoln Arc Tracker. Arc tracker captures welding current and voltage. It is connected to WiFi Router that transmits the data to laptop. On tripod is placed pyrometer IL 92 that measures contactless the temperature in one point next the welding joint. The pyrometer is connected via USB cable to the laptop. The pyrometer is placed on 1,5 m distance from the measured point. It is developed program with Matlab for capturing the temperature from the pyrometer. Temperature of the process is measured with 8-channel contact thermometer Spider 8. K type thermocouples are connected to the Spider 8 and set in 8 point next the welding joint. Thermocouples are welded to the welded elements. The Spider 8 is connected to the laptop with UBS cable. Temperature is captured by Spider 8 with software Catman.

Il 92 pyrometer was chosen to perform the experiment, which has wide temperatures measurement range, including liquid metals, can be freely measured. The excellent distance / measured spot ratio of 50:1 allows long-distance measurement of small objects, as well as in extreme conditions, e.g.: in the furnace. The characteristics of the device are: measuring range: -50 to 2200^{o}C; accuracy of the device ± 2%; reaction time - 150ms; spectral range - 8-14µm.

The set up functionality is verified with experiment with the following parameters:

- welding current – 210A
- welding volatage – 25V;
- η of the welding source – 0,8;

- welding power – 4200J/s;
- welding speed – 50cm/min;
- welding steel plates 50x5x200mm.

The real time data sequences are shown as follows – welding current on Fig.1 and welding voltage on Fig. 2 from Arc Tracker, temperature from Pyrometer on Fig.3 and from the contact thermometer on Fig.4

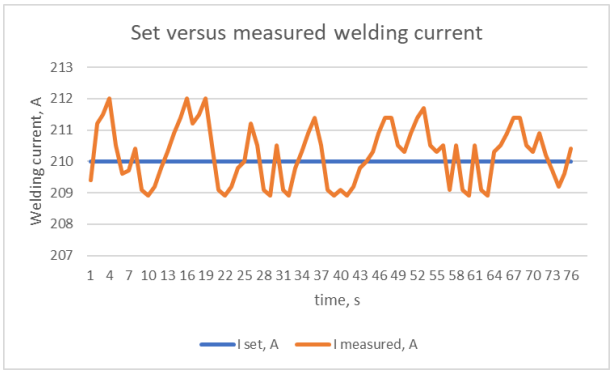

Fig. 1 *Measured welding current by Arc Tracker.*

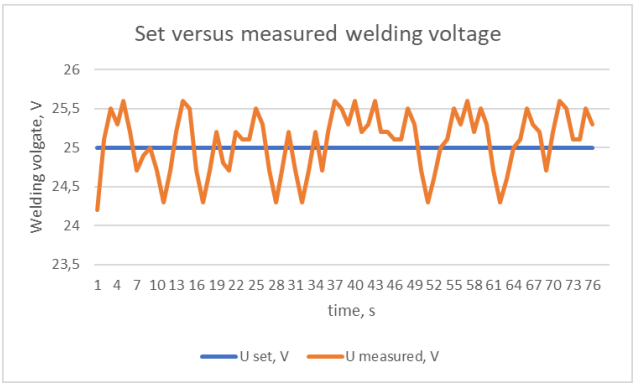

Fig. 2 *Measured welding voltage by Arc Tracker*

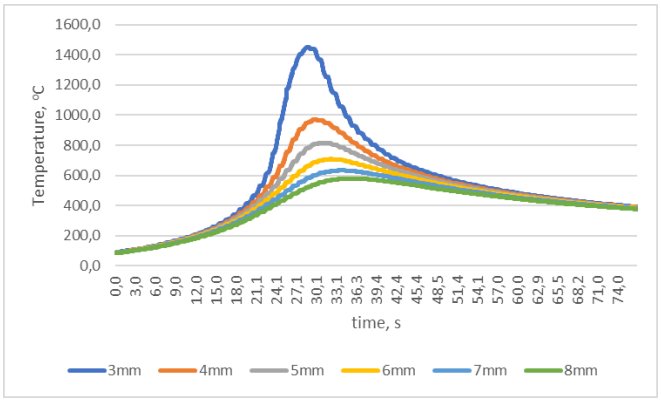

Fig. 3 *Measured contactless temperature by the pyrometer.*

3. Conclusions

It is developed set up for real time capturing of welding parameters – welding current and voltage, contact and contactless temperature in fixed specific points of interest.

Acknowledgments

This work was made possible by a project KP-06-N37/31, funded by the NSF.

All equipment and experimental units used in this work was funded by the European Regional Development Fund within the OP "Science and Education for Smart Growth 2014 - 2020", project CoE "National center of mechatronics and clean technologies", № BG05M2OP001-1.001-0008-C08

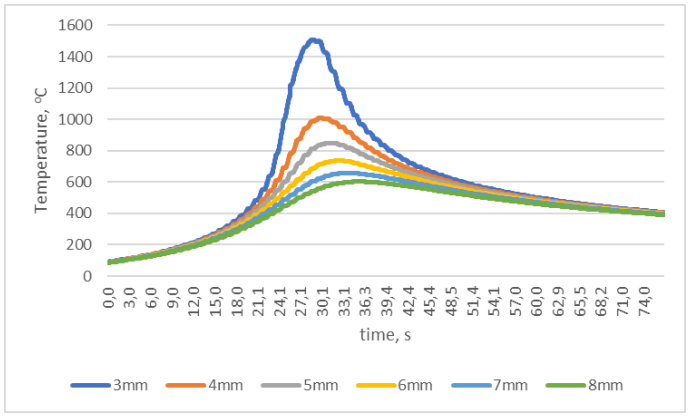

Fig. 4 *Measured contact temperature by Spider 8.*

4. References

1. H. Dong ; M. Cong ; Yu. Zhang; Yu. Liu ; H. Chen, Real time welding parameter prediction for desired character performance, IEEE International Conference on Robotics and Automation (ICRA), 2017
2. E. Karadeniz, U. Ozsarac, C. Yildiz. The Effect of Process Parameters on Penetration in Gas Metal Arc Welding Process. Materials and Design. 28(2):2007; 649–656.
3. P. Tashev, „Modeling of temperature processes in automated TIG welding overlay and samples with plain surface“, Collection of reports, Vth National conference with foreign participation „„Metal science, hydro- and aerodynamics and national security ’2015“, 22 – 23 October 2015, Sofia, ISSN 1313-8308
4. P. Ghosh, S. Gupta, P. Gupta, R. Rathi, Fatigue Characteristics of Pulsed MIG Welded Al-Zn-Mg Alloy. Journal of Material Science. 26(22):1991; 6161–6170.
5. N. Takuo, M. Takashi, K. Katsuhiro, Deformation and Fatigue Characteristics of Large Welded Bellows with Inclined External Edge, Materials Transactions, Vol. 49, No. 6 (2008) pp. 1249 to 1255, 2008 The Japan Society for Technology of Plasticity
6. I. Kim, M. Park, A Review on Optimizations of Welding Parameters in GMA Welding Process, Journal of Welding and Joining, Vol. 36, No. 1, 2018, pp. 65-75, ISSN 2466-2232
7. V. Chauhan, G. Khandoori, A. Kumar, Role of Taguchi Design of Experiment in Optimization of Welding Process Parameters for Different Materials-A Review. International Journal of Advanced Technology & Engineering Research (IJATER). 2014; 146–151
8. D. Kim, M. Kang, S. Rhee, Determination of Optimal Welding Conditions with a Controlled Random Search Procedure. Welding Journal. 2005
9. G. Posch, J. Bruckner, H. Ennsbrunner, INDUSTRY 4.0 IN WELDING, Fronius International, 2017
10. P. Hammersberg, H. Olsson, Proactive Control of Weld Dimensions in Robot MAG Welding. 2013
11. P. Tashev, A. Tasev, M. Manilova, Ya. Lukarski, Methodology for defining technological parameters of resistance welding of cross wires, VIth International Metallurgical Congress, Ohrid 2014
12. https://play.google.com/store/apps/details?id=com.kemppi.arcmobilecontrol&hl=en_US
13. https://www.boschrexroth.com/en/xc/products/product-groups/welding-technology/controllers-with-power-section/mf-system-prc7000/prc7300/prc7300-2
14. http://www.linde-gas.com/en/products_and_supply/welding_safety_products/digital-welding-management/index.html

Points for real time temperature capturing in welding process

Deyan Gradinarov[1]
Institute of Metal Science, Equipment and Technology with Hydroaerodynamic Center at Bulgarian Academy of Sciences[1]
dgradinarov@ims.bas.bg

Abstract: *It is presented experiment for temperature measurement in welding process. It is shown arc interference with measurements and temperature versus distance form arc trajectory. This study will help selecting specific points for measuring temperature in welding process..*
Keywords*: TEMPERATURE MEASUREMENT, WELDING PROCESS*

1. Introduction

Welding process is performed under Welding procedures (WP) in which strictly are defined the welding equipment and parameters. Welding joint quality is determined by following the welding parameters by the operator of the welding process. Variations from set it the welding procedures parameters – welding current, voltage speed, initial heating of the welded elements cause lowering the quality.

Deviation form set in the welding procedure parameters may occur by various reasons – in the equipment, in the materials and in the operator of the process. Some of those lowering welded joint quality reasons may occur during the process and some may be appear and disappear periodically during the process.

For lowering the impact on welding process and welded joints quality of such occurrences in the welding process has to be inserted quality control in real time. Such control is performed by capturing welding parameters such as welding current, voltage, speed or indirect indications as capturing temperature in one or more specific points of interest.

Physical application on welding current and voltage with defined speed heats the welded elements equally in equal other conditions and welding environment. For those reasons temperature control is applicable and used. Temperature control may be contact – mostly by thermocouples placed next to the welding joint or contactless – by pyrometers capturing temperatures focused next to the welding joint.

For better results of temperature control of the welding process thermocouples of the contact measurement and focusing the pyrometer have to be as close as possible to the trajectory of the welding torch along over the welding joint.

Unfortunately, thermocouples cannot be placed too close to the welding arc because of two reasons – the arc itself will damage or destroy the thermocouple and with this will malfunction the temperature capturing system; and melting basin next to the arc will shift or move the thermocouple. This can result in welding the thermocouple into the welding joint making welded detail unusable.

Emitted infrared light will interfere with pyrometer measurement causing false temperature result. In the case of pyrometer temperature measurement, the operator of the process or the welding torch may cause shade obstructing in visibility by the pyrometer. This has to be taken in advance to prevent interruption of the measurement.[1]

2. Experimental set up

The set up has two main parts – welding equipment and measuring equipment. The welding equipment consists of welding torch, which is mounted on mechanical grip. The mechanical grip fixes the torch in one position and removes fluctuations from welder's movements. The mechanical grip is mounted on welding tractor, which moves along and over the welded elements with constant speed. Welded elements are placed on welding table. Next to the welding table are placed the power source that feeds the torch and gas bottle that protects the joint. The measuring equipment consists of capturing module Lincoln Arc Tracker. Arc tracker captures welding current and voltage. It is connected to WiFi Router that transmits the data to laptop. On two tripods are placed pyrometers IL 92 and Trotec TP10 that measure contactless the temperature in two points next the welding joint. The pyrometers are connected via USB cables to the laptop. The pyrometers are placed on 1,5m (Trotec TP10) and 1,2m (IL 92) distance from the measured point. It is developed program with Matlab for capturing the temperature from the pyrometers. Temperature of the process is measured with 8-channel contact thermometer Spider 8. K type thermocouples are connected to the Spider 8 and set in 8 point next the welding joint. Thermocouples are welded to the welded elements. The Spider 8 is connected to the laptop with UBS cable. Temperature is captured by Spider 8 with software Catman.

The two pyrometers Trotec TP10 and IL 92 was chosen to perform the experiment, both have wide temperatures measurement range, including liquid metals, can be freely measured. The excellent distance / measured spot ratio of 75:1 (Trotec TP10) and 50:1 (IL 92) allows long-distance measurement of small objects, as well as in extreme conditions, e.g.: in the furnace. The characteristics of the device are: Trotec TP10 – measuring range: -50 to 1850°C; accuracy of the device ± 2%; reaction time - 150ms; spectral range - 8-14µm[1]; IL 92 – measuring range: -50 to 2200°C; accuracy of the device ± 2%; reaction time - 150ms; spectral range - 8-14µm.[2]

The set up functionality is verified with experiment with the following parameters:

- welding current – 210A
- welding volatage – 25V;
- η of the welding source – 0,8;
- welding power – 4200J/s;
- welding speed – 50cm/min;
- welding steel plates 50x5x200mm.

Contact temperature is measured simultaneously in 8 points (from 1 to 8) placed in a row with distance of 1mm from each other starting at 1mm from the welding torch trajectory to 8mm away from it as shown on Fig.1.

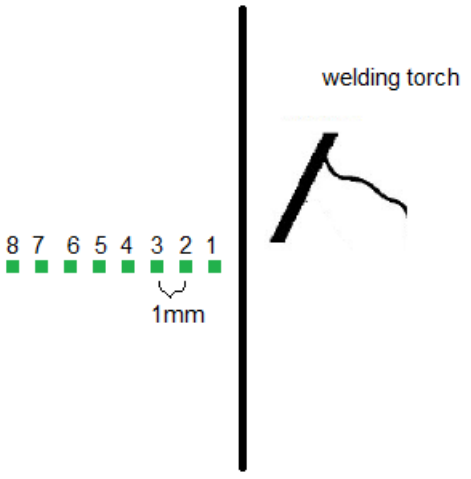

Fig. 1 *Diagram of placement of the thermocouples.*

Contactless temperature is measured simultaneously in 4 runs at 2 points each run placed in a row with distance of 1mm from each other starting at 1mm from the welding torch trajectory to 8mm away from it as shown repeating measurements of the thermocouples. First run is in points 1 and 2, 2nd at 3 and 4, 3rd at 5 and 6, 4th at 7 and 8. Each run is performed at the same experiment parameters.

3. Results

In the contact measurement the thermocouple in the first point is destroyed and in the second point is damaged. Result of thermocouples form point 3 (3mm) to point 8 (8mm) are shown on Fig.2.

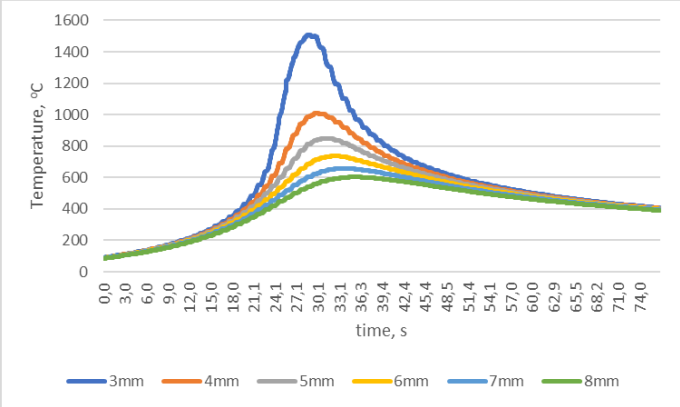

Fig. 2 *Temperature curves from thermocouple 3 (3mm) to thermocouple 8 (8mm).*

In the contactless measurement the first and second points have interference from the welding arc that caused data loss when the torch passed next to the measured points. Result of measured temperature form point 3 (3mm) to point 8 (8mm) are shown on Fig.3.

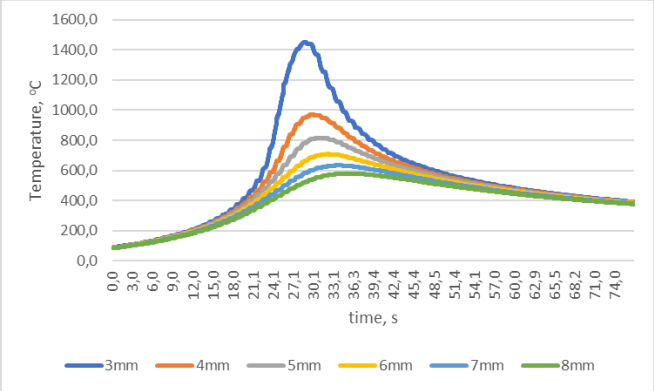

Fig. 3 *Temperature curves from pyrometers from points 3 (3mm) to point 8 (8mm).*

Results from contact and contactless measurements show similar results for the points from 3mm to 8 mm away from the line of welding. Contact measurement show 3-4% higher values of the temperature than contactless. At bot type of measurements point at 1mm and 2mm away of the welding line give false results at the time of welding torch passing or cause malfunction of the measurement system.

The most informative point for this experiment is at 3mm away from the welding line. At this welding parameters temperature in this point is close to the liquidus line and may cause false results if welded with more power.

The point at 4mm away of the welding line is also informative for temperature measurements. If welded with higher power this point would be best for temperature measurement and control of the welding process.

4. Conclusions

It is measured temperature in 8 consecutive points at a line perpendicular to the welding line ate 1mm from each other starting from 1mm away of the welding line.

The point at 1mm and 2mm caused false results in the contactless measurements and measurement system malfunction in the contact measurements.

For these welding parameters the point at 3mm away of the welding line is the best for measurement temperature. Is the welding parameters are higher the point at 4mm would be the best. For further welding powers net point of the sequence would result the best.

Acknowledgments

This work was made possible by a project KP-06-N37/31, funded by the NSF.

All equipment and experimental units used in this work was funded by the European Regional Development Fund within the OP "Science and Education for Smart Growth 2014 - 2020", project CoE "National center of mechatronics and clean technologies", № BG05M2OP001-1.001-0008-C08

5. References

1. Datasheet of pyrometer Trotec TP10
2. Datasheet of pyrometer IL 92

Real time capturing temperature of welding process

Deyan Gradinarov[1]
Institute of Metal Science, Equipment and Technology with Hydroaerodynamic Center at Bulgarian Academy of Sciences[1]
dgradinarov@ims.bas.bg

Abstract: *It is presented real time capturing temperature in specific points of welding process with pyrometer.*
Keywords*: TEMPERATURE MEASUTEMENT, PYROMETER, REAL TIME TEMPERATURE*

1. Introduction

Welding process is performed under Welding procedures (WP) in which strictly are defined the welding equipment and parameters. Welding joint quality is determined by following the welding parameters by the operator of the welding process. Variations from set it the welding procedures parameters – welding current, voltage speed, initial heating of the welded elements cause lowering the quality.

Deviation form set in the welding procedure parameters may occur by various reasons – in the equipment, in the materials and in the operator of the process. Some of those lowering welded joint quality reasons may occur during the process and some may be appear and disappear periodically during the process.

For lowering the impact on welding process and welded joints quality of such occurrences in the welding process has to be inserted quality control in real time. Such control is performed by capturing welding parameters such as welding current, voltage, speed or indirect indications as capturing temperature in one or more specific points of interest.

Physical application on welding current and voltage with defined speed heats the welded elements equally in equal other conditions and welding environment. For those reasons temperature control is applicable and used. Temperature control may be contact – mostly by thermocouples placed next to the welding joint or contactless – by pyrometers capturing temperatures focused next to the welding joint.

The pyrometer is a device that non-contactly measures the temperature of an object, based on the IR light emitted by the object [1]. The main elements of a pyrometer are shown in Fig.1. Infrared light emitted by the heated bodies is focused and transmitted from the optics of the device to a thermosensitive element, which converts the infrared light into voltage, it is transmitted for processing to a microprocessor unit, the information is displayed on a screen in an operator-friendly form. The most important feature of the optics is the viewing angle. It determines how large a spot of the object is observed [2,3,4]

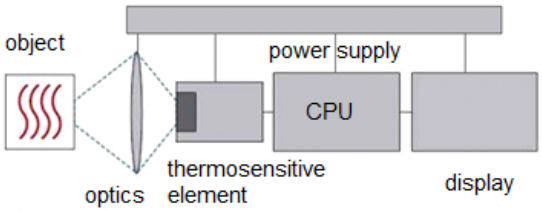

Fig. 1 *Block diagram of a pyrometer [1].*

2. Pyrometer measurement

Pyrometers have advantage over contact thermometers on setting the measurement element on the measured surface of the object. Thermocouples must have good contact with the object while the pyrometer captures infrared light emitted by the object. Disadvantage of the pyrometers is the need of calibration. Emitted infrared light depends of emissivity of the object. It varies with the material of the object, condition of the surface and changes slightly with change of the temperature. Most of the materials has their emissivity known and there are data bases, including on websites of pyrometer's manufacturer, defining emissivity of the needed material. Surface conditions of welded elements are similar for each process or batch and pyrometers has internal correction on emissivity over temperature changes. This helps reducing the calibration process in contactless temperature measurements. For unknown materials and surface conditions are various methods for calibration of pyrometers. The main method is by comparison between contact and contactless measurement. The object is heated to constant temperature and measured with calibrated contact thermometer. Pyrometer is focused on the object and its emissivity is changed while both contact and contactless temperatures are equal. Then the emissivity of this material is considered known.

The set up for contactless temperature measurement consists of welding torch, which is mounted on mechanical grip. The mechanical grip fixes the torch in one position and removes fluctuations from welder's movements. The mechanical grip is mounted on welding tractor, which moves along and over the welded elements with constant speed. Welded elements are placed on welding table. Next to the welding table are placed the power source that feeds the torch and gas bottle that protects the joint. The measuring equipment consists of capturing module Lincoln Arc Tracker. Arc tracker captures welding current and voltage. It is connected to WiFi Router that transmits the data to laptop. On two tripods are placed pyrometers IL 92 and Trotec TP10 that measure contactless the temperature in two points next the welding joint. The pyrometers are connected via USB cables to the laptop. The pyrometers are placed on 1,5m (Trotec TP10) and 1,2m (IL 92) distance from the measured point. It is developed program with Matlab for capturing the temperature from the pyrometers.

The two pyrometers Trotec TP10 and IL 92 was chosen to perform the experiment, both have wide temperatures measurement range, including liquid metals, can be freely measured. The excellent distance / measured spot ratio of 75:1 (Trotec TP10) and 50:1 (IL 92) allows long-distance measurement of small objects, as well as in extreme conditions, e.g.: in the furnace. The characteristics of the device are: Trotec TP10 – measuring range: -50 to 1850^{o}C; accuracy of the device ± 2%; reaction time - 150ms; spectral range - 8-14µm[5]; IL 92 – measuring range: -50 to 2200^{o}C; accuracy of the device ± 2%; reaction time - 150ms; spectral range - 8-14µm.[6]

The pyrometer are started in the mode of continuous measurement and are connected to a computer via a USB port, and their outputs are read with a program developed on Matlab. One pyrometer report is a packet of 17 bytes – two initial FF, the next two bytes represent the current measured temperature with an accuracy of 0.1^{o}C, the last is a closing byte – AA. The measurement time is set in advance by setting an input buffer bytes, which is a multiple of 17. After completing the process, the results are automatically converted to temperature (degrees Celsius), a graphics is drawn, the data is saved in an .xls file, and the graphics - in .jpeg.

The set up functionality is verified with experiment with the following parameters:

- welding current – 210A
- welding volatage – 25V;
- η of the welding source – 0,8;

- welding power – 4200J/s;
- welding speed – 50cm/min;
- welding steel plates 50x5x200mm.

Contactless temperature is measured simultaneously at 2 points placed in a row with distance of 1mm from each other starting at 3mm (Trotec TP10) and 4mm (IL 92) away from the welding torch trajectory. Captured temperature curves in real time are shown on Fig 2 for pyrometer Trotec TP10 and on Fig.3 for pyrometer IL 92.

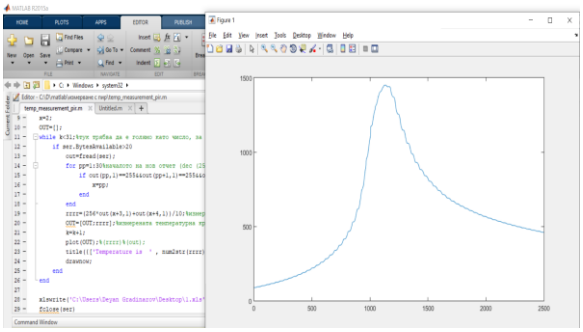

Fig. 2 *Temperature curve measurement pyrometer Trotec TP10 at 3mm away from the welding torch trajectory.*

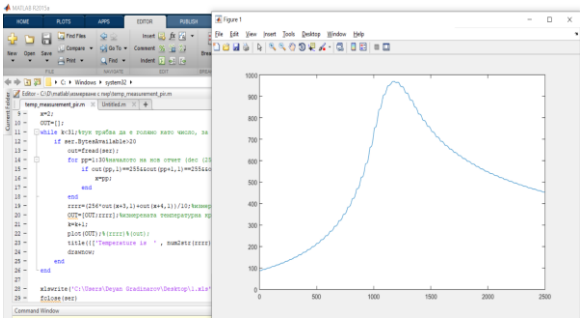

Fig. 3 *Temperature curve measurement pyrometer IL 92 at 4mm away from the welding torch trajectory.*

3. Conclusions

It is shown set up for real time measurement temperature of welding process in specific point if interest with pyrometer.

It is developed program for real time measurement of temperature by various pyrometers of welding process.

Acknowledgments

This work was made possible by a project KP-06-N37/31, funded by the NSF.

All equipment and experimental units used in this work was funded by the European Regional Development Fund within the OP "Science and Education for Smart Growth 2014 - 2020", project CoE "National center of mechatronics and clean technologies", № BG05M2OP001-1.001-0008-C08

4. *References*

1. D. Gradinarov, Yu. Bijev, St. Todorov, “Features and application, of cameras in infrared spectrum”, NDT days 2013, ISSN 1310-3946
2. http://www.flir.com/BG/
3. http://www.bestech.com.au/
4. http://www.lokatork.com/
5. Datasheet of pyrometer Trotec TP10
6. Datasheet of pyrometer IL 92

Real time capturing welding parameters with tracking module

Deyan Gradinarov[1], Yuri Bijev[1]
Institute of Metal Science, Equipment and Technology with Hydroaerodynamic Center at Bulgarian Academy of Sciences[1]
dgradinarov@ims.bas.bg

Abstract: *It is presented real time capturing voltage and current in welding process with module Lincoln Arc Tracker.*
Keywords*: WELDING PROCESS, CURRENT CAPTURING, VOLTAGE CAPTURING, REAL time*

1. Introduction

According to the modern requirements for low energy intensity and environmental protection and in the context of declining natural resources, scientists, the business, and the society are looking for ways to meet the growing needs of various industries, from optimizing and improving welding methods to adding additional alloying elements for better weldability.

The welding process is used in almost every area of human activity, and the need products of this process is constantly increasing. With the increase of the responsibility of the welded joints, the requirement for welding quality is also increased.

The welding process is performed according to a pre-approved and validated Welding Procedure. This welding procedure sets the welding technology, welding mode, current, voltage, welding speed, wire feed rate, flux used, type, diameter and tip pre-forming of the welding wire, welding and break time, and other parameters on which the quality and reliability of the welded joint depends. Deviating from them, with a high probability, leads to a decrease in the properties of the welded joint, and hence to defects and damage that increases the risk of injuries and endangering human life and negative environmental consequences.

When welding by an operator, due to a number of factors that cannot be avoided, the welder can deviate from the welding procedure, with the welding process being carried out at welding parameters that differ from the procedure. This leads to the presence of defects - gas and slag inclusions, welding cracks, unexpected change of the main metal properties in the surrounding area, etc. The presence of such defects directly affects the exploitation properties of the manufactured parts and elements by reducing their strength, lifetime, reliability, etc. When applied conscientious control, this leads to wastage, cost increases and waste of resources - metal, welding wire, welding gases and energy. In case of unconscious control - to the direct danger of traumatism, accidents, ecological catastrophes, etc., which directly or indirectly affects the society.

Improving the welding process by the real time control of welding parameters compared to those set in the welding procedure reduces drastically the possibility of defects and thus gives economic and environmental advantages by reducing wastage and consequently consumption of metal, gas, electricity and water to reducing emissions.

The results of the research show that there are numerous studies on the methods and technologies for monitoring and control of the welding parameters, the influence of the parameters on the exploitation properties of the welded elements, the quality determination of the welded joints.

It is studied the influence of the welding parameters in various welding processes and their impact on the quality and performance of the welded joints [1,2,3].

One of the current problems of modern material science is methods for increasing the life cycle of parts with welded joints, which must have both high hardness and strength and low internal stress. It is studied the impact of welding parameters on the morbidity of welded joints [4,5].

There are known studies on welding process optimization methods by control of welding parameters [6,7,8].

There are studies on welding parameters control and welding optimization [9,10] as well as methodologies for determining the parameters in welding processes [11].

There are developed welding parameters parameter control systems [12,13,14].

The analysis of our well-known sources does not give enough clarity to the question: what impact the welding parameters have on the performance of the welded joints and what methodologies should be used to improve the quality of the process.

This leads to the need to acquire new fundamental knowledge about the possibilities, means and rate of improving the quality of the welding processes by real time control of parameters.

A thorough study and determination of the influence of welding parameters on the quality of the process and analysis of the possibilities for quality improvement through real time control is also needed.

2. Capturing welding parameters – voltage and current

As a capturing module is chosen Lincoln Arc Tracker. With this module we can capture in real time welding current up to 1000A and voltage up to 44V. This module has an ethernet connector to easily connect it in to a local network. The module is combined with software product Power wave manager which captures tracked welding parameters. With this capturing process can be monitored in real time on remote computer.[15]

The set up consists of welding torch, which is mounted on mechanical grip. The mechanical grip fixes the torch in one position and removes fluctuations from welder's movements. The mechanical grip is mounted on welding tractor, which moves along and over the welded elements with constant speed. Welded elements are placed on welding table. Next to the welding table are placed the power source that feeds the torch and gas bottle that protects the joint. Capturing module Lincoln Arc Tracker. Arc tracker captures welding current and voltage. It is connected to WiFi Router that transmits the data to laptop. Connection of the Arc tracker module is shown on Fig. 1.

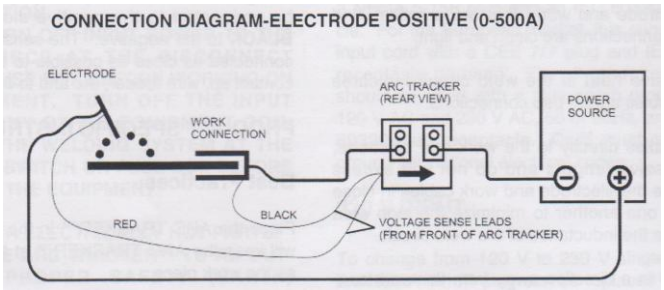

Fig. 1 *Connection diagram of Arc Tracker in the experimental set up.[15]*

The set up functionality is verified with experiment with the following parameters:

- welding current – 210A
- welding volatage – 25V;

- η of the welding source – 0,8;
- welding power – 4200J/s;
- welding speed – 50cm/min;
- welding steel plates 50x5x200mm.

On Fig.2 are shown values of set and measure welding current.

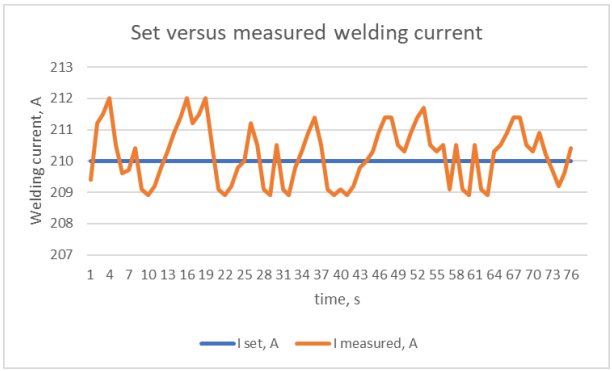

Fig. 2 *Set versus measured welding current curves.*

On Fig.3 are shown values of set and measure welding voltage.

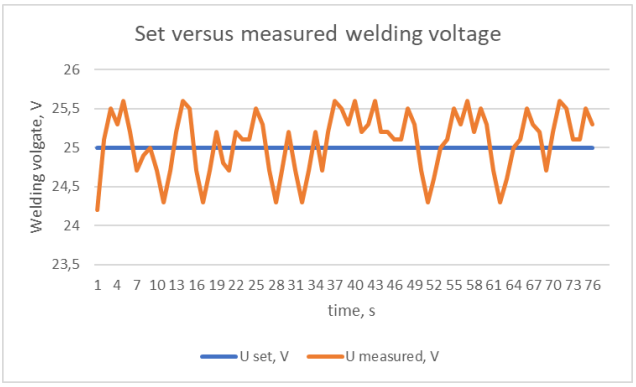

Fig. 3 *Set versus measured welding voltage curves.*

On Fig.4 are shown values of set and measure welding power.

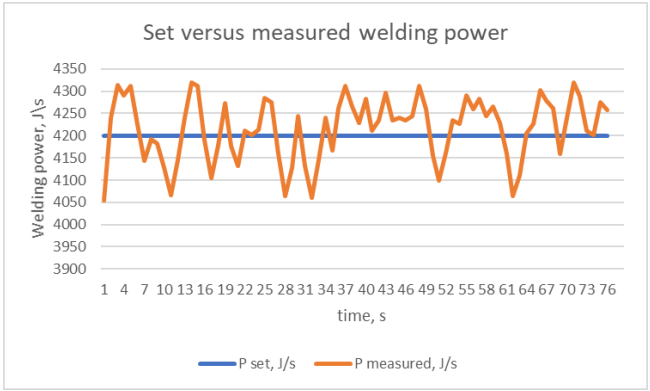

Fig. 4 *Set versus measured welding current power.*

On Fig.5 are shown set versus measured welding current, voltage and power differences.

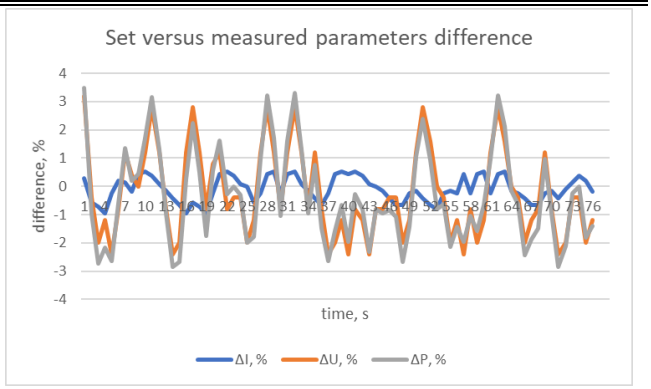

Fig. 5 *Set versus measured welding parameters.*

Measured welding current and voltage don't deviate much from set values. This gives the expectation that the welded joint would be of good quality.

3. Conclusions

It is presented tracking module for real time capturing welding current and voltage during a welding process. Parameters are shown graphically on remote laptop and a warning signal value limitation can be triggered if measured values goes off.

Acknowledgments

This work was made possible by a project KP-06-N37/31, funded by the NSF.

All equipment and experimental units used in this work was funded by the European Regional Development Fund within the OP "Science and Education for Smart Growth 2014 - 2020", project CoE "National center of mechatronics and clean technologies", № BG05M2OP001-1.001-0008-C08

4. *References*

1. H. Dong ; M. Cong ; Yu. Zhang; Yu. Liu ; H. Chen, Real time welding parameter prediction for desired character performance, IEEE International Conference on Robotics and Automation (ICRA), 2017
2. E. Karadeniz, U. Ozsarac, C. Yildiz. The Effect of Process Parameters on Penetration in Gas Metal Arc Welding Process. Materials and Design. 28(2):2007; 649–656.
3. P. Tashev, „Modeling of temperature processes in automated TIG welding overlay and samples with plain surface“, Collection of reports, Vth National conference with foreign participation „„Metal science, hydro- and aerodynamics and national security '2015“, 22 – 23 October 2015, Sofia, ISSN 1313-8308
4. P. Ghosh, S. Gupta, P. Gupta, R. Rathi, Fatigue Characteristics of Pulsed MIG Welded Al-Zn-Mg Alloy. Journal of Material Science. 26(22):1991; 6161–6170.
5. N. Takuo, M. Takashi, K. Katsuhiro, Deformation and Fatigue Characteristics of Large Welded Bellows with Inclined External Edge, Materials Transactions, Vol. 49, No. 6 (2008) pp. 1249 to 1255, 2008 The Japan Society for Technology of Plasticity
6. I. Kim, M. Park, A Review on Optimizations of Welding Parameters in GMA Welding Process, Journal of Welding and Joining, Vol. 36, No. 1, 2018, pp. 65-75, ISSN 2466-2232
7. V. Chauhan, G. Khandoori, A. Kumar, Role of Taguchi Design of Experiment in Optimization of Welding Process Parameters for Different Materials-A Review. International Journal of Advanced Technology & Engineering Research (IJATER). 2014; 146–151
8. D. Kim, M. Kang, S. Rhee, Determination of Optimal Welding Conditions with a Controlled Random Search Procedure. Welding Journal. 2005

9. G. Posch, J. Bruckner, H. Ennsbrunner, INDUSTRY 4.0 IN WELDING, Fronius International, 2017
10. P. Hammersberg, H. Olsson, Proactive Control of Weld Dimensions in Robot MAG Welding. 2013
11. P. Tashev, A. Tasev, M. Manilova, Ya. Lukarski, Methodology for defining technological parameters of resistance welding of cross wires, VIth International Metallurgical Congress, Ohrid 2014
12. https://play.google.com/store/apps/details?id=com.kemppi.arcmobilecontrol&hl=en_US
13. https://www.boschrexroth.com/en/xc/products/product-groups/welding-technology/controllers-with-power-section/mf-system-prc7000/prc7300/prc7300-2
14. http://www.linde-gas.com/en/products_and_supply/welding_safety_products/digital-welding-management/index.html
15. Operator's manual of Lincoln Arc tracker, Lincoln Global Inc. 16.05.2018

Experimental analysis of creep behaviour of solder alloys at near eutectic point by using indentation test

Irida Markja [1,*], Klodian Dhoska[2], Dervish Elezi[3], Heinrisch Oettel[4]
[1,2,3] Faculty of Mechanical Engineering, Polytechnic University of Tirana, Albania
[4] Faculty of Materials Science and Technology, Technische Universität Bergakademie Freiberg, Germany

*imarkja@fim.edu.al ; irida.markja@gmail.com

Abstract: *Eutectic solder alloys are widely used in the microelectronics industry. The phenomenon of creep and its mechanisms are important aspects that influence the performance of solder alloys. During the last two decades, a Pb - solder alloys is fast becoming a reality in lead free electronic products due to harmful caused as toxic material to environment and health, international legislative pressure and marketing. The replacement of Sn - Pb alloys with Sn-Ag-Cu (SAC) alloys needs reliable results for assuring the usage of this solder joints material in electronic industry. In this paper has been studied the creep behaviour of a group of alloy in the system Sn-Ag-Cu (SAC) near the eutectic point. In this research work we have used three different alloy samples which are 95, 5Sn-3, 8Ag-0,7Cu, 96, 5Sn-3, 0Ag-0,5Cu and 95, 46Sn-3, 58Ag-0,96Cu. Indentation technique has been conducted to study the creep behaviour of these three SAC alloys by determining the creep parameters at different temperatures. The temperature used was at room temperature 30°C until 100°C and the stress used was 64MPa-178MPa for the indentation diameter 1 mm and 0.5 mm. The experimental method and results of the creep parameters like activation enthalpy Q, the stress exponent n of the power law model and the parameter of the material A were briefly described in this paper. From the creep curves, constructed for alloys and considered loads, the values of creep stress exponent n were determined for the studied alloys.*

Keywords: CREEP MECHANISMS, SN-AG-CU ALLOYS, CREEP STRESS EXPONENT *n*, INDENTATION TECHNIQUE.

1. Introduction

The purpose of this research work has been focused on the experimental study of the creep behaviour of a solder alloys at near eutectic point and in particular the determination of the reinforcement exponent *n* which is depending on the SAC microstructure.[1,2]

Indentation technique has been applied to study the creep behavior of this SAC alloys by determining the creep parameters at different temperatures. Based on it, the experimental study of the creep behavior through indentation instrument has become a useful technique to explore the dependence on time on the mechanical properties of materials and structures. Furthermore, the usage of the indentation technique is driven by the fact that this method requires minimal amount of study material as well as minimum sample preparation in comparison of the conventional method such as tensile test.

Three different samples such as 95,5 Sn-3,8Ag-0,7Cu, 96,5Sn-3,0Ag-0,5Cu and 95,46Sn-3,58Ag-0,96Cu have been used for determination of the creep behavior of SAC solder alloys at near eutectic point by using indentation test. The temperature used was at room temperature 30°C until 100°C and the stress used was at 64MPa until 178MPa for 1mm and 0.5 mm diameter. A constant load has been applied to the sample surface with a suitable penetrator for a period of time which largely exceeds the duration of the standard hardness test. The experimental method and results of the creep parameters like activation enthalpy Q, the stress exponent n of the power law model and the parameter of the material A were are estimated in this paper.

The goal of our experiments was to determine the creep behavior near room temperature depending on the microstructure of solder alloy Sn-Ag-Cu. The experimental method used was the indentation creep test. Indentation creep has become a useful technique for exploring the time-dependent mechanical properties of materials and structures and its recent advance is driven by the potential applications to small material structures, since the indentation creep experiment is inherently simple, accurate, and require minimum sample preparation (compared with the conventional methods such as the tensile test) [1,3,4].

2. Metallographic preparation of samples and experimental procedures

2.1 Metallographic preparation of samples

The materials were used in this study are Sn based solder alloys: 95,5Sn-3,8Ag-0,7Cu, 96,5Sn-3,0Ag-0,5Cu and 95,46Sn-3,58Ag-0,96Cu. The samples were produce in *Felder GmbH* company in Germany. The samples are prepared accordign to the standart ASTM 26 [5,6].

In figure 1 are presented the diagram for binary composition and the SAC ternary phase diagrame, that we have pointed the chemical positon for our samples and on the table 1 are presented the phase content of SAC ternary phase diagram[7,8].

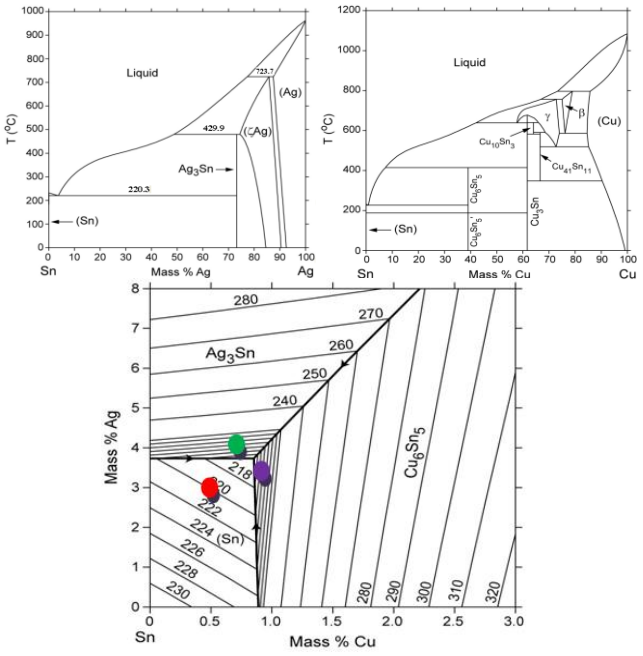

Fig.1 a)*Sn-Cu binary phase diagram ; b)Sn-Ag binary phase diagram ; c) Sn-Ag-Cu ternary phase diagram (Sn-rich corner); d) Sn-Ag-Cu ternary phase diagram [NIST]*

Table 1: *Phase contentof SAC ternary phase diagram*

Phase	*Density*	*Content of elements in phase%*			*Content of phases% mass*	*Content of phases% volume*
		Sn	*Ag*	*Cu*		
β-Sn	*7,31*	*100,00*	*0,00*	*0,00*	*92,65*	*94,14*
Ag3Sn	*9,93*	*26,83*	*73,17*	*0,00*	*4,89*	*3,66*
Cu6Sn5	*8,28*	*60,89*	*0,00*	*39,11*	*2,45*	*2,20*

2.2 Experimental procedures

The main objective in a creep test is to measure how a given metal or an alloy will perform under constant load, at constant temperatures. The indentation creep test (impression test) is schematically illustrated in Fig.2. A flat bottomed cylindrical punch of diameter is pushed into the creep test specimen under an applied pressure F load. The punch diameter used was 1mm, 0.75mm and 0.5 mm with a chemical composition of stainless steel and was used for creep test for temperature in the range 30^0C until 100^0C. The depth of indentation h of the punch is monitored as a function of time. The impression creep curve is derived by plotting the indentation versus time [9, 10,11,12].

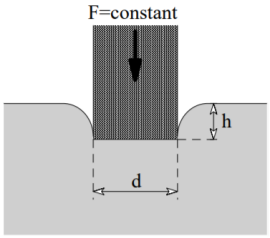

Fig.2 *Schematic of the indentation creep test [NIST].*

3. Experimental results

In SAC alloyes the formation of intermetallic compounds between the primary elements Sn, Ag and Cu in properties of alloys (Ag_3Sn,Cu_6Sn_5,Cu_3Sn). Precipitated particles of intermetallic compounds have a higher strength than the bulk of the material and also improve the fatigue resistance of solder alloys [13,14,15].

The metallographic examinations were carried out with the Neophot 30 light microscope (Carl Zeiss Jena) with a built-in digital color camera (JVC TK-C1381) carried out. The pictures were taken with the standard magnifications 25, 125, 250 and 500 times (figure 3). The microstructure of 95.5Sn-3.8Ag-0.7Cu contains the following ingredients: Base-Sn (1); Ag_3Sn lamellae which were even before thermal treatment near Sn dendrites (2); fine Ag3Sn particles which have been constituents of binary and tertiary eutectic and partially coagulated (3) and thicker Cu_6Sn_5 particles as constituents of ternary and coagulated eutectic (4).

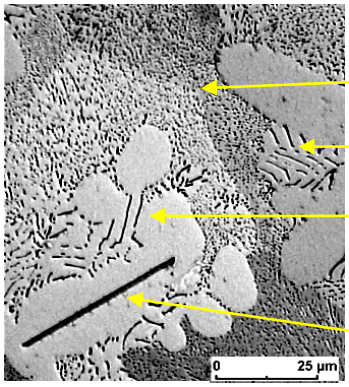

Ternary Eutectic
β-Sn, Ag_3Sn, Cu_6Sn_5;
Binary Eutectic
β-Sn, Ag_3Sn;
Dendrit
β-Sn;
Ag_3Sn

(a)

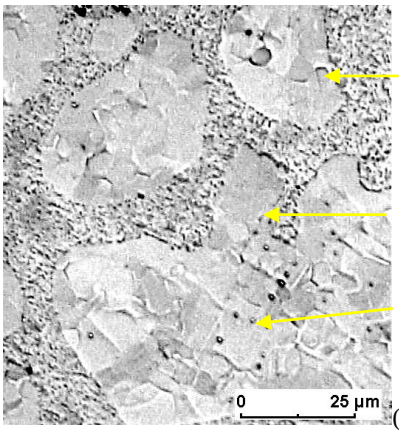

Ternary Eutectic
β-Sn, Ag_3Sn, Cu_6Sn_5;
Binary Eutectic
β-Sn, Ag_3Sn;
Dendrit
β-Sn;

(b)

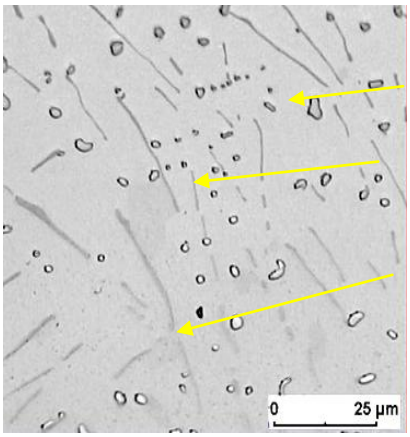

Ternary Eutectic
Ag_3Sn, Cu_6Sn_5;
Binary Eutectic
Ag_3Sn;
Dendrit
β-Sn;

(c)

Fig.3*Microstructure of solder alloys performed with Light Microscope: a) 95.5Sn-3.8Ag-0.7Cu; b) 96.5Sn-3.0Ag-0.5Cu; c) 95.46Sn-3.58Ag-0.96Cu*

The temperature used was in the range 30^0C - 100^0C and the stress used was 64MPa-178MPa for 1mm, 0.75 mm and 0.5mm diameters. The following relations were used for all experiments (Table 2):

Table 2: *The relations used for our experiments: X-h-ε-έ*

X – chronometer value	
h – indentation	h=X/10
ε – deformation	ε = h/d
έ – creep rate	έ=Δh/Δt

The following graphs shows the results obtained from the experiments performed for the samples used in this study, depending on the *creep displacement dependence* **(**Table 3):

Table 3: *The creep displacement for three functions: έ-σ-T*

Creep displacement		*σ*	*Temp*
creep rate vs. deformation	*έ= function (σ)*	*102 MPa*	*TR,*
		77 MPa	*50°C ,*
		64 Ma	*80°C,*
		178 Mpa	*100°C*

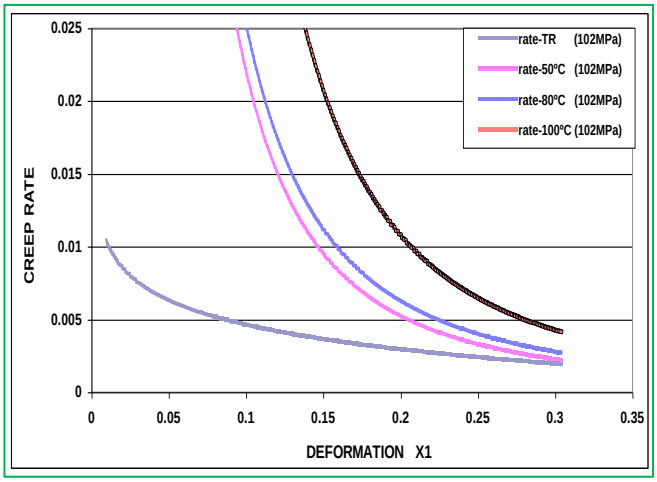

Fig.4 *The graphics show the functions for the dependence of creep rate vs. strain ε=funx(σ) for RT,50,80,100 °C , diameter 1mm and stress 120MPa*

The graph in figure 4 show the dependence of creep rate vs. strain ***ε=f (σ)*** for a load 800gr applied at the different temperature (**RT, 50, 80, 100**), the diameter **d=1mm,** and the stress **σ = 102MPa.**

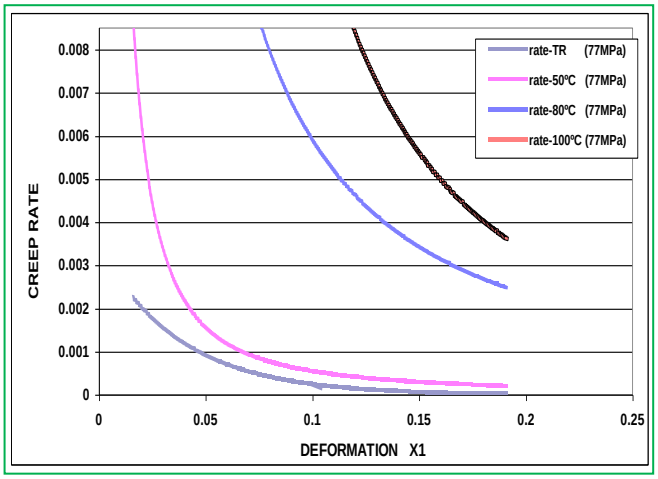

Fig.5 *The graphics show the functions forthe dependence of creep rate vs. strain ε=funx(σ)for RT,50,80,100 °C , diameter 1mm and stress 77 MPa*

The graph in figure 5 show the *dependence* of creep rate vs. strain ***ε=f (σ)*** for a load 800gr applied at the different temperature (**RT, 50, 80, 100**), the diameter **d=1mm,** and the stress **σ = 77 MPa.**

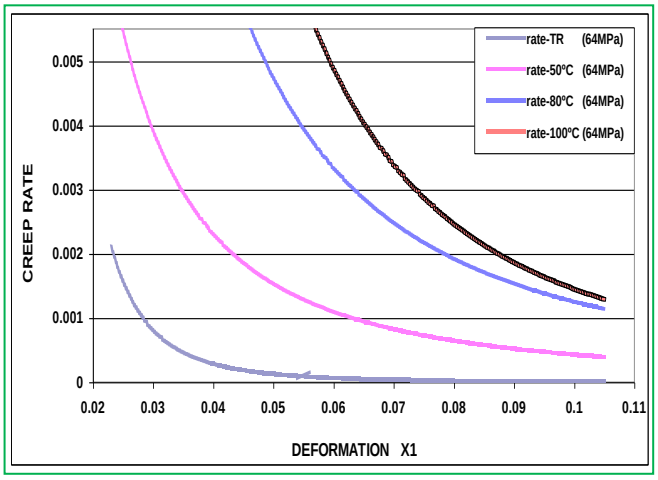

Fig.6 *The graphics show the functions for the dependence of creep rate vs. strain ε=funx(σ)for RT,50,80,100 °C , diameter 1mm and stress 64 MPa*

The graph in figure 6 show the dependence of creep rate vs. strain ***ε=f (σ)*** for a load 800gr applied at the different temperature (**RT, 50, 80, 100**), the diameter **d=1mm,** and the stress **σ = 64 MPa.**

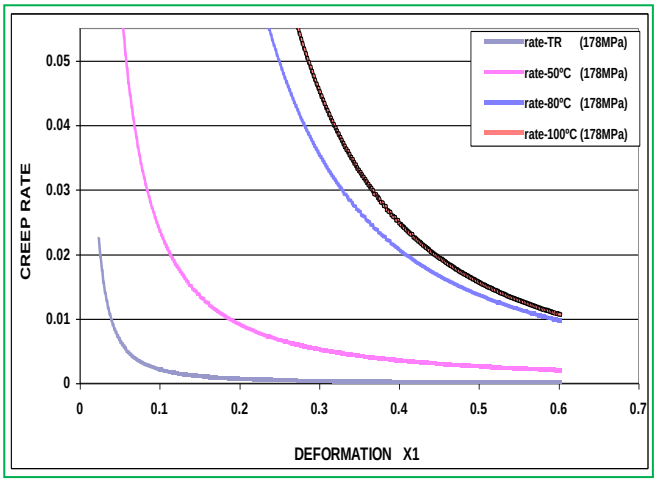

Fig.7 *The graph show the dependence of creep rate vs. strain ε=funx(σ)for RT,50,80,100 °C , diameter 0.5mm and stress 178 MPa*

The graph in figure 7 show the dependence of creep rate vs. strain ***ε=f (σ)*** for a load 800gr applied at the different temperature (**RT, 50, 80, 100**), the diameter **d=0.5mm,** and the stress **σ = 178 MPa.**

4. Discussions and Conclusions

From our experimental study we can draw the following interpretations and conclusions:

1. The realization of the experiments tests of the creep evaluation of the SAC alloys in the laboratory equipment with indentation test. The equipment was initially adjusted for the upper stress limit (with Fe sample) and for the lower stress limit (with Sn sample).

2. For the case of pure Sn sample, the exponent of stress was also evaluated, according to the law of power, which resulted: $n = 2.4$. This value is between the interval which are evaluated from other authors in different study referred to creep behavior SAC (1.8 - 2.8).

3. For the alloy 96,5Sn-3,0Ag-0,5Cu-IIRL we found $n = 6.3$ which can be said to show a higher creep resistance compared to the samples with long-term aging, probably due to intermetallic particles in large quantities that can be in the microstructure.

4. For the alloy 95, 5 Sn-3, 8Ag-0,7Cu we find the exponent $n = 5.6$ for the aging time at 200 ° C of 170 hours, and $n = 7.5$ for the aging times 340 and 510 hours.

5. Even in our study it has been found that with the increase of the applied strain the minimum velocity of creep deformation increases, in the second stage.

6. For a more complete interpretation of the creep behavior of SAC bonds it is necessary that the study proceed with the evaluation of the size of the intermetallic particles as well as the nature of the matrix particleboards.

7. Future work will be focused on the investigation of microstructures of our samples for evaluation of precipitates into the matrix.

10. Acknowledgment

The authors gratefully acknowledge the TU Bergakademie Freiberg, Germany for providing the SAC alloy samples used in this work, part of the project 'Network of Materials Science and Engineering (NMST)' supported by DAAD and Polytechnic University of Tirana for partial funding of this study.

9. Conflict of interests

The author would like to confirm that there is no conflict of interests associated with this publication and there is no financial fund for this work that can affect the research outcomes.

10. References

1. I.Markja, K. Dhoska, D. Elezi, Experimental Study of Creep-behavior by using Indentation Test To Solder Alloys Sn-Ag-Cu near Eutectic'2nd "International Conference "Engineering and Entrepreneurship" Proceedings, Albania Tirana, 10-11 October (2019);

2. K. Dhoska.; J. Kacani.; H. Oettel.; V. Ramaj. Creep Behavior of a Sn-Ag-Cu Alloy Near Room Temperature. In proceedings of the 11th International Research/Expert Conference"Trends in the Development of Machinery and Associated Technology", Hammamet, Tunisia, 05-09 September, pp. 307-310. (2007)

3. A.S.T.M.24, "Metallographic and Materialographic Specimen Preparation" ISBN 978-0-8031-4265-7 (2007)

4. Y. M.Leong.; A.S.M.A. Haseeb. Soldering Characteristics and Mechanical Properties of Sn-1.0Ag-0.5Cu Solder with Minor Aluminum Addition. Materials 2016, 9(7), 522. pp. 1-17.

5. J.Gomez, C. Basaran 'Nanoindentation of Pb/Sn solder alloys; experimental and finite element simulation results' International Journal of Solids and Structures 43 (2006) 1505–1527

6. I. Markja "Diploma Thesis: Experimental study of creep with the indentation test to solder alloys" TUF Germany and PUT Albania (2009)

7. M.E. Kassner, M.T.P.Prado; Fundamentals of creep in metals and alloys; ISBN 0-08-04367-4 Elsevier (2004)

8. https://www.metallurgy.nist.gov/phase/solder/agcusn.html (NIST)

9. https://d-nb.info/1011669226/34

10. K.S. Kim, S.H. Huh, K. Suganuma, "Effects of cooling speed on microstructure and tensile properties of Sn-Ag-Cu Alloys", Materials Science and Engineering, A333, (2002), S. 106-114.

11. C.S. Ohy, J.H. Shim, B.-J. Lee , D.N. Lee, "A Thermodynamic Study on the Ag-Sb-Sn System", Journal Alloys and Compounds 238, (1996), S. 155-166.

12. C.M. Miller, I.E. Anderson, J.F. Smith, „A Viable Tin-Lead Solder Substitute: Sn-Ag-Cu", Journal of Electronic Materials, Vol. 23, No. 7, S. 595- 601; (1994).

13. M.E. Loomans , M.E. Fine, "Tin-Silver-Copper Eutectic Temperature and Composition", Metallurgical and Materials Transactions A, Vol. 31A, S. 1155-1162; (2000),

14. J.Y. Park, C.U. Kim, T. Carper, V. Puligandla, "Phase Equilibria Studies of Sn-Ag-Cu Eutectic Solder Using Differential Cooling of Sn-3.8Ag-0.7Cu Alloys", Journal of Electronic Materials, Vol. 32, No. 11, pp. 1297-1302; (2003)

15. I. Ohnuma, M. Miyashita, K. Anzai, X.J. Liu, H. Ohtani, R Kainuma, K. Ishida, "Phase Equilibria and the Related Properties of Sn-Ag-Cu Based Pb-free Solder Alloys", Journal of Electronic Materials, Vol. 29, No. 10, pp. 1137- 1144, (2000)

MRI compatible robotic device for FUS therapy of canine and feline mammary tumours

Marinos Giannakou,[1a] Nikolas Evripidou,[2b] Anastasia Antoniou[2c], Dr. Christakis Damianou[2d]
MEDSONIC LTD, Limassol, Cyprus[1]
Department of Electrical Engineering, Computer Engineering and Informatics, Cyprus University of Technology, Cyprus[2]

marinosgt4@gmail.com[a]
nk.evripidou@edu.cut.ac.cy[b]
anastasiaantoniou12@gmail.com[c]
christakis.damianou@cut.ac.cy[d]
(Corresponding Author)

***Abstract**: Veterinary medicine has expanded its applications beyond traditional approaches, increasingly incorporating the Focused Ultrasound (FUS) technology in veterinary oncology. A robotic device that comprises a positioning mechanism for navigating a single element spherically focused transducer in four PC-controlled axes has been developed for veterinary FUS applications. Motion is established using piezoelectric motors and monitored by dual optical encoder setups. Sufficient accuracy and repeatability of motion were demonstrated through benchtop and Magnetic Resonance Imaging (MRI) techniques, with an estimated mean positioning error smaller than 0.1 mm. The system was proven safe for operation inside conventional MRI scanners with minimal effect on the overall image quality. Efficient performance of the system was initially validated through extensive ex-vivo studies in tissue-mimicking phantoms and excised tissue. The prototype was then evaluated for its ability to precisely ablate naturally occurring mammary tumours in dogs and cats (n=3). Histological examination with hematoxylin and eosin staining demonstrated well-defined areas of coagulative necrosis in the exposed tumours. No adverse events compromising animal welfare were recorded. Overall, FUS ablation of pet mammary cancer under proper monitoring was proven safe and feasible. Application of this technology in veterinary medicine may help advance knowledge of the analogous human disease, optimize therapeutic protocols, and more rapidly translate research into clinical practice.*
***KEYWORDS**: FUS, MRI COMPATIBLE ROBOTIC DEVICE, MAMMARY TUMOURS, DOGS, CATS*

Robotic device for veterinary applications of MRgFUS

Marinos Giannakou,[1a] Nikolas Evripidou,[2b] Anastasia Antoniou[2c] Christakis Damianou[2d*]
MEDSONIC LTD, Limassol, Cyprus[1]
Department of Electrical Engineering, Computer Engineering and Informatics, Cyprus University of Technology, Cyprus[2]
marinosgt4@gmail.com [a]
nk.evripidou@edu.cut.ac.cy [b]
anastasiaantoniou12@gmail.com [c]
christakis.damianou@cut.ac.cy [d]
*Corresponding Author

***Abstract**: Given the current popularity of Magnetic Resonance guided Focused Ultrasound (MRgFUS) as a promising non-invasive therapeutic modality in modern oncology, a robotic system intended for MRgFUS applications in veterinary medicine has been developed. The positioning mechanism comprises four PC-controlled motion stages dedicated to navigating a single element spherically focused transducer with an operating frequency of 1-3 MHz. The motion in each axis is actuated by a piezoelectric motor and accurately monitored by two optical encoder setups. Experiments carried out in the benchtop setting using a caliper-based method demonstrated highly accurate motion with a mean positioning error smaller than 0.1 mm. Sufficient accuracy and repeatability of motion have also been verified through Magnetic Resonance Imaging (MRI) studies, as well as through visual assessment by performing multiple ablations on a plastic film. In addition, the system was proven MR compatible through a series of specialized quality assurance tests in a 1.5 T MRI scanner and capable of operating inside the scanner without significant effects on the image quality. Its compact design where all the mechanical parts are included in a single enclosure makes it portable and suitable for use in any conventional MRI scanner of up to 7 T field strength. Application of this technology in veterinary medicine will contribute towards optimizing therapeutic protocols and may also provide insights into the analogous human disease. Veterinary validation of the system may lead to its clinical adoption to be used in the treatment of abdominal cancer upon minimal design modification.*

***KEYWORDS**: ROBOTIC DEVICE, VETERINARY MEDICINE, MRGFUS*

Breast mimicking agar/wood powder material for MRgFUS applications

Ms. Andria Filippou[1a], Dr. Marinos Giannakou,[2b] Mr. Nikolas Evripidou,[1c] , Christakis Damianou[1d]
Department of Electrical Engineering, Computer Engineering and Informatics, Cyprus University of Technology, Limassol, Cyprus[1]
MEDSONIC LTD, Limassol, Cyprus[2]

ap.filippou@edu.cut.ac.cy[a]
marinosgt4@gmail.com[b]
nk.evripidou@edu.cut.ac.cy[c]
christakis.damianou@cut.ac.cy[d]
(Corresponding Author)

***Abstract**: A high-quality Tissue Mimicking Material (TMM) is of great value in the process of evaluating emerging Magnetic Resonance guided Focused Ultrasound (MRgFUS) applications. An agar-based TMM doped with wood powder was developed for breast MRgFUS applications. The phantom was designed with the shape of breast tissue using a 3D printed mold. The characterization procedure involved a series of experiments dedicated to estimate the acoustic (attenuation coefficient, absorption coefficient, propagation speed, and acoustic impedance), thermal (conductivity, diffusivity, and specific heat capacity), and MR properties (T1 and T2 relaxation times) of the wood-powder doped material. The optimized TMM containing 2 % weight/volume (w/v) agar and 4 % w/v wood powder demonstrated compatibility with MRI. The estimated attenuation coefficient was close to 0.5 dB/cm/MHz, whereas the acoustic absorption coefficient was about 0.35 dB/cm-MHz. In addition, it was proven that the wood powder concentration enhances the acoustic absorption. The material possessed an acoustic impedance of 1.6 MRayl. The thermal conductivity of the material was estimated at 0.5 W/m.K. Regarding MR properties, the measured relaxation times T1 (844 ms) and T2 (66 ms) were within the range of values found in the literature for soft tissue. Overall, the TMM matched the critical properties of human tissues adequately. Furthermore, experiments using MR thermometry demonstrated the usefulness of this phantom for evaluating ultrasonic thermal protocols.*
***KEYWORDS**: MRGFUS, BREAST MIMICKING MATERIAL, AGAR, WOOD*

Circular economy in metallurgical waste: application of metallurgical waste from ferro-nickel production into eco-friendly composites

Perica Paunović, Anita Grozdanov, Andrea Petanova, Marija Katerina Paunović, Radica Piponska

Faculty of Technology and Metallurgy, Ss Cyril and Methodius University in Skopje – Skopje, North Macedonia
pericap@tmf.ukim.edu.mk

Abstract: *One of the methods in circular economy and reuse of industrial waste is lowering the material cost is replacing components with not so expensive equivalents (mainly waste materials) but the substitution should be still accompanied by fulfilling the material and technical requirements. Metallurgical waste such as fly ash particles and slags are usually generated as an industrial by-product from the ferro-nickel production process and it is recognized as a potential hazard to environment. The main purpose of this work is use of solid waste materials from ferro-nickel industry (fly ash – FA, electric-arc furnace slag – EAFS and converter slag – CS) as a reinforcing component in polymer based composite – eco-friendly, functional geo-membranes.*

Firstly, metallurgical waste materials were modified in acid (HCl) and alkaline (NaOH) medium. The studied composites were produced by film-casting method using polyvinyl chloride (PVC) matrix reinforced by the previously mentioned waste materials. The study of the produced geo-membranes was done related to their: i) morphology and internal structure (SEM observation and FTIR analysis), ii) thermal stability (TG/DTA/DTG analysis) and iii) moisture stability (followed kinetics of swelling was determined and the ultimate rate of swelling after 24 hours).

The studied composites have shown good thermal stability with corresponding low weight losses during thermal measurements. The morphology of the waste materials is of spherical and polygonal not regular shape and uniform. Generally, all the studied composites have shown higher swelling degree than PVC, where the composited reinforced with FA have shown the best performances in adsorption test.

Keywords*: CIRCULAR ECONOMY, FLY ASH, ELCTRIC-ARC FURNACE SLAG, CONVERTER SLAG, GEOPOLYMERS.*

Aknoledgement: This research was supported and performed within the bilateral Project with PR China, "Transformation of industrial waste powders into new functional materials" founded by Ministry of education and science of R. N. Macedonia (No20-6334/1; 29.06.2020).

Functionalization of MWCNT and G with Ag for incorporation in facial masks and filters for protection of Covid 19

Anita Grozdanov, Perica Paunovik
Faculty of Technology and Metallurgy, University Ss Cyril and Methodius in Skopje, Rugjer Boskovic 16, 1000 Skopje

Abstract: *Last two year, the world is faced with the biggest problem - how to protect the life from various viruses, bacteria and other tiny pollutants on submicron scale. Due to the growing field of nanotechnology, and extra-ordinary sorbent properties and capturing efficiency of nanostructures as well as the ability to produce nano-fibers with the dimensions of less than 100 nm, new methods can be used to develop protective masks and filters that can remove tiny pollutants and impurities even at nano-metric or submicron scales. Carbon Nano Structures –CNs and their nanocomposites in polymer nano-fibers are among the most important types of nanostructures for this purpose.*

In this work, we present our results of the structural characterization of functionalized MWCNT and Graphene with Ag ions, aimed for incorporation in facial masks. MWCNT and Graphene were activated with HNO3 and then modified with Ag, in solvent, at room temperature under continuous mixing. Functionalized nanostructures were characterized by TGA and SEM analysis. Modified nanostrucutres were sprayed on the surface of the facial masks and air-filters at room temperature. The obtained results indicate that the modified nanostructures provide higher level of efficiency in the protection.